The Open University

Open Research Online

The Open University's repository of research publications and other research outputs

Modifications of radiofrequency capacitive discharge for deposition of carbon coatings

Thesis

How to cite:

Goruppa, Alexander (2002). Modifications of radiofrequency capacitive discharge for deposition of carbon coatings. PhD thesis. The Open University.

For guidance on citations see FAQs.

© 2002 Alexander Goruppa

Version: Version of Record

Copyright and Moral Rights for the articles on this site are retained by the individual authors and/or other copyright owners. For more information on Open Research Online's data policy on reuse of materials please consult the policies page.

oro.open.ac.uk

UNRESTRICTED

Modifications of radiofrequency capacitive discharge for deposition of carbon coatings

Thesis submitted by
Alexander Goruppa
Mechanical Engineer
for the degree of
Doctor of Philosophy
March 2002

Department of Materials Engineering
The Open University

DATE OF SUBMISSION: 31 MARCH 2002
DATE OF AWARD: 9 DECEMBER 2002

ProQuest Number: 27532766

All rights reserved

INFORMATION TO ALL USERS
The quality of this reproduction is dependent upon the quality of the copy submitted.

In the unlikely event that the author did not send a complete manuscript
and there are missing pages, these will be noted. Also, if material had to be removed,
a note will indicate the deletion.

ProQuest 27532766

Published by ProQuest LLC (2019). Copyright of the Dissertation is held by the Author.

All rights reserved.
This work is protected against unauthorized copying under Title 17, United States Code
Microform Edition © ProQuest LLC.

ProQuest LLC.
789 East Eisenhower Parkway
P.O. Box 1346
Ann Arbor, MI 48106 – 1346

Modifications of radiofrequency capacitive discharge for deposition of carbon coatings

Alexander Goruppa

Abstract

A thesis submitted for the degree of Doctor of Philosophy at the Open University
March 2002

This thesis is an investigation of modifications of RF excited discharge for deposition of carbon coatings. Two separate discharge configurations were examined: an RF capacitive discharge with electron injection and removal by means of an emissive filament and a DC electrode, and an RF discharge with a hollow cathode powered electrode. Plasma characterization was conducted by means of an electrostatic probe and an energy and mass analysis probe. Interpretation of the electrostatic probe data in presence of RF harmonics in plasma has been discussed.

Electron injection and removal has been found to control strongly plasma potential and maximum of ion energy at the grounded electrode, reducing them to less than 10 V or increasing above 90 V accordingly. Related changes of electron temperature and density have been measured, with plasma density being increased up to an order of magnitude by electron injection. This effect has been linked with a regime, when hot filament instigates discharge inside of an electron source.

A model, based on the analysis of electron movement in an RF matrix sheath, has been developed to investigate an effect of the DC electrode on stochastic heating/cooling of electrons in the sheath. It has been demonstrated that an adequate heating of the EEDF tail and cooling of the bulk electrons could be produced by a combined effect of the sheaths of powered and grounded electrodes, assuming the multi-harmonic grounded sheath and non-equal plasma density at the sheath

boundaries.

Another model, based on balance of conduction currents from RF plasma to the electrodes, has been aimed at investigation of discharge potentials. It has predicted correctly variation of time-averaged plasma potential with electron injection and removal.

Deposition experiments were conducted from both discharge configurations. Carbon coatings were analysed by means of Raman spectroscopy and scanning electron microscope (SEM). Raman spectra of coatings from the plasma with injected electrons revealed a polymeric-like nature of the coatings. SEM study of carbon films from the RF hollow cathode configuration demonstrated a wide variety of coating morphology: from porous films, consisting of separate particles, to nucleation of conical, spherical and cauliflower-like carbon phases.

Publications

Parts of the data in this thesis have been presented at the conferences and published in refereed journals:

- A.A. Goruppa and N.St.J. Braithwaite, "The influence of a dc electrode on a capacitively coupled RF plasma", at the 20th Annual Plasma Phys. Conf. of IOP Annual Congress., Brighton, April 1993.
- A.A. Goruppa, C.M.O. Mahony and N.St.J. Braithwaite, "Electrode structure effects in 13.56 MHz Rf plasma" at the 21t Annual Plasma Phys. Conf. of IOP Annual Congress, Brighton, April 1994.
- I.R.McColl, D.M.Grant, S.M.Green, J.V.Wood, T.L.Parker, K.Parker, A.A. Goruppa and N.St.J.Braithwaite, "Low temperature plasma-assisted chemical vapour deposition of amorphous carbon films for biomedical polymeric substrates" in "Diamond and Related Materials", 3 (1994), 83.
- A.A. Goruppa, N.St.J. Braithwaite and D.M. Grant, "Direct electrical control of diamond-like carbon growth by plasma-enhanced CVD" in "Diamond and Related Materials", 3 (1994), 1223.
- A.A. Goruppa and N.St.J. Braithwaite, "DLC from hollow cathode RF plasma", at the the 5th European Conference on Diamond, Diamond-like and Related Materials", Il Ciocco, Italy, September 1994.

Contents

Chapter I "Introduction" 1

1.1 Diamond as engineering materials 1

1.2 Brief history of diamond and diamond-like carbon growth............... 3

1.3 Diamond crystal structure and film morphology............................ 6

1.4 Methods of CVD diamond growth... 8

1.5 Main plasma parameters.. 10

1.6 CVD diamond growth process.. 11

1.7 Diamond-like carbon.. 14

1.8 Advantages and drawbacks of RF discharge for carbon films growth.... 17

1.9 Outline of the research program... 18

Chapter II "Experimental device and plasma characterisation" 20

2.1 Experimental device specification.. 20

2.2 The base plate unit.. 20

2.3 The furnace and the heat shield... 22

2.4 Vacuum RF power line.. 25

2.5 Experimental set up.. 26

2.6 Electrostatic probe and mass and energy analysis diagnostic systems.... 28

2.7 Hydrogen and argon plasma characterisation.............................. 30

2.8 Discussion... 37

2.8.1 Variation of plasma parameters with pressure...................... 37

2.8.2 Brief overview of impact reactions, forming hydrogen species... 40

2.8.3 Formation of water ions in plasma discharge........................ 42

2.9 Conclusion........ 45

Chapter III "RF capacitive discharge with injection and removal of electrons" 46

3.1 Introduction........ 46

3.2 Brief review of previous works on electron injection in plasma........ 46

3.3 Design of the electron source and the discharge volume configuration... 56

3.4 Operation of the DC bias electrode and the electron source........ 60

3.5 Interpretation of data from electrostatic probe........ 67

3.6 Some aspects of ion sampling by the energy-mass analyser........ 73

3.7 Effect of the DC bias electrode on plasma parameters........ 74

3.8 Effect of simultaneous operation of the electron source and the DC bias electrode on plasma parameters........ 77

3.8.1 Impact of electron injection on RF plasma........ 77

3.8.2 DC anode operation during electron injection........ 81

3.8.3 Time of ion transition through the sheath........ 86

3.8.4 Potential structures in RF discharge with electron injection-removal........ 91

Chapter IV "Modeling" 96

4.1 Introduction........ 96

4.2 Modeling of electron interaction with RF sheath........ 97

4.2.1 Model........ 97

4.2.2 Results and discussion........ 101

4.3 Modeling of plasma potential variation, caused by electron injection and removal........ 109

4.3.1 Model........ 109

4.3.1 Results and discussion.. 113

Chapter V "Deposition of carbon films, using various modifications of RF discharge" 116

5.1 Introduction.. 116

5.2 Deposition of carbon coatings from RF discharge with electron injection.. 117

5.2.1 Experimental conditions... 117

5.2.2 Coating characterisation using Raman scattering.................. 117

5.2.3 Technical limitations of the configuration with electron injection and removal for depositing carbon films................ 119

5.3 Deposition of carbon coatings from RF hollow cathode configuration.... 120

5.3.1 Hollow cathode effect.. 120

5.3.2 Experimental configuration of RF hollow cathode discharge for carbon film deposition... 122

5.3.3 Experimental conditions... 124

5.3.4 Results and discussion... 125

5.4 Deposition of carbon coatings from a single hollow cathode 129

5.4.1 Limitation of power in the discharge............................... 129

5.4.2 Experimental configuration and conditions...................... 130

5.4.3 Discussion.. 131

5.4.3.1 Morphology of deposition...................................... 131

5.4.3.2 Composition of deposited crystallites......................... 138

5.5 Conclusion... 141

General conclusion.. 143

Appendix A Electrostatic probe measurements.................................. 145

Appendix B Energy and mass analysis probe.................................... 149

Appendix C Ionization and particle loss model................................ 151

Appendix D Chemical reactions, describing impact collision processes with hydrogen.. 153

Appendix E Electron energy distribution.. 158

Appendix F Model of particle balance, including conduction and displacement currents.. 160

Appendix G Raman spectroscopy.. 168

Appendix H Hollow cathode deposition chamber................................... 169

Appendix I Plasma potential of the hollow cathode discharge.................. 171

References 173

List of Figures

1.1 Diamond-graphite phase diagram in terms of pressure and temperature... 1

1.2 Model of diamond lattice.. 7

1.3 Schematic diagrams of diamond particle morphologies..................... 7

1.4 Cross-section of growing film.. 8

2.1 Schematic diagram of the main vacuum vessel.............................. 21

2.2 Simplified scheme of the heat shield, used for calculations................ 24

2.3 Calculated temperature of the furnace T_1 as the function of the number of shield layers N for various values of emissivity ε......................... 24

2.4 Schematic diagram of the vacuum RF power line........................... 26

2.5 Schematic diagram of the experimental set up............................... 27

2.6 Arrangement of plasma diagnostic systems in the vacuum chamber....... 29

2.7 Probe measurements of plasma parameters in hydrogen discharge with pressure variation.. 32

2.8 Variation of ion composition and IEDF in the H_2 discharge with increasing pressure... 33

2.9 Probe measurements of plasma parameters in argon discharge with pressure variation.. 34

2.10 Variation of ion composition and IEDF in the Ar discharge with increasing pressure... 35

2.11 Mass analysis data for the experimental chamber from the energy and mass analysis probe... 36

2.12 Electron temperature T_e as a function of pressure p in hydrogen discharge... 39

3.1 Schematic diagram of the electron source.................................... 57

3.2 Experimental configuration of the discharge volume: plan and side section.. 59

3.3 Current-voltage characteristics of the DC bias electrode..................... 61

3.4 Plasma potentials of the RF discharge in hydrogen as a function of bias potential of the (a) small and (b) large DC electrode........................ 62

3.5 Current-voltage characteristics of the emissive filament electron source: (a) – linear and (b) – logarithmic scales...................................... 64

3.6 Variation of electron density of the main plasma discharge as a function of the filament emission current... 66

3.7 Probe characteristic.. 68

3.8 Second derivative and natural logarithm of the probe electron current..... 70

3.9 Second derivative of electron current to the probe........................... 71

3.10 Effect of the small (3.14 cm^2) DC anode on plasma parameters of RF discharge in hydrogen at 31 and 51 mtorr.................................... 75

3.11 Variation of plasma parameters with electron injection and removal in hydrogen discharge; RF power – 30 W, pressure – 30 mtorr............... 78

3.12 Variation of plasma parameters with electron injection and removal in hydrogen discharge; RF power – 30 W, pressure – 46 mtorr............... 79

3.13 Ion energy distribution at the grounded electrode in the H_2 discharge (30 mtorr) with electron injection-removal.................................. 82-83

3.14 Ion energy distribution at the grounded electrode in the H_2 discharge (30 mtorr) with electron injection-removal.................................. 84-85

3.15 Variation of IEDF area under the curve as a function of electron injection and removal at (a) – 30 mtorr and (b) – 46 mtorr................. 90

3.16 Schematic time-averaged plasma potential profile in front of the electron source in RF discharge at 30 mtorr.. 92

3.17 Schematic variation of time-averaged potential in the discharge volume between the electron source and the DC anode at 30 mtorr.................. 93

4.1 Space- and time-dependent potentials of the discharge........................ 97

4.2 Time-dependent potential settings, used in the model.......................... 99

4.3 Transformation of maxwellian electrons (T_e = 1.4 eV) during interaction with the matrix grounded electrode sheath over the period of RF cycle... 100

4.4 EEDF and EEPF after interaction of maxwellian electrons with the matrix grounded ((a) and (b)) and powered ((c) and (d)) electrode sheath affected by the positive DC electrode.. 102

4.5 Single and four harmonic potential curves of the grounded electrode sheath... 103

4.6 EEDF (a) and EEPF (b) after interaction of maxwellian electrons with the matrix grounded electrode sheath affected by the positive DC electrode... 104

4.7 EEDF (a) and EEPF (b) after interaction of maxwellian electrons with the matrix powered electrode sheath affected by the positive DC electrode... 104

4.8 Potential and electric field of the powered electrode in single and multiple harmonic cases.. 105

4.9 Trajectories of electrons after the interaction with the matrix sheath of the powered electrode at $\frac{2}{8}\cdot\pi$ of RF cycle.................................. 106

4.10 Trajectories of electrons after the initial interaction with the matrix sheath of the powered electrode at $\frac{2}{8}\cdot\pi$ of RF cycle.......................... 107

4.11 Electrical circuit of the RF discharge with electron injection and removal 110

4.12 Variation of the averaged plasma potential and the self-bias voltage of the powered electrode for the cases of: (a) – DC electrode and (b) – electron injection.. 113

4.13 Time-resolved potentials in the discharge at $\Phi_b = 18.75$.................... 115

5.1 Raman spectra of carbon coatings from the grounded electrode without (a,b) and with (c,d) electron injection in the RF discharge.................. 118

5.2 EEDF of the hollow cathode discharge in helium........................... 121

5.3 Schematic diagram of the RF hollow cathode experimental device......... 123

5.4 SEM micrographs of carbon coatings.. 126

5.5 Raman spectra of coatings from the RF hollow cathode configuration..... 127

5.6 RF powered electrode with a single hollow cathode structure.............. 130

5.7 SEM micrograph of coating for the conditions (D) in the Table 5.2........ 132

5.8 SEM micrographs of the sample substrate for the conditions (E) in the Table 5.2.. 133

5.9 Schematic of substrate transformation.. 134

5.10 SEM micrographs of sample substrates for the conditions (F) and (G) in the Table 5.2... 135

5.11 SEM micrographs of sample substrates with tilt 26° for the conditions (F) and (G) in the Table 5.2.. 136

5.12 Suggested cross-section of a cavity with fence-like formation of crystallites... 137

5.13 SEM micrograph of the tilted (26°) sample for the conditions (F) in the table 5.2... 137

5.14 SEM micrographs of the masked area of the cavity-rich substrate......... 139

5.15 SEM micrograph of the polished substrate.................................. 140

A.1 Current-voltage signal from the tantalum 0.25 mm diameter 5.6 mm length probe.. 146

B.1 Schematic of the EQP300 energy and mass analysis probe.................. 149

D.1 $e + H(1s) \rightarrow e + H^+ + e$ 153

D.2 $e + H_2(X^1\Sigma_g^+) \rightarrow e + H_2^+ + e$ 154

D.3 $e + H_3^+ \rightarrow H + H + H$.. 154

D.4 $e + H_3^+ \rightarrow e + H^+ + 2H$.. 155

D.5 $e + H_2 \rightarrow H^- + H$.. 155

D.6 $H_2^+ + H_2 \rightarrow H_2 + H_2^+$.. 156

D.7 $H_2^+ + H_2 \rightarrow H_3^+ + H$.. 156

D.8 $e + H_2(X^1\Sigma_g^+) \rightarrow e + H(1s) + H(1s)$... 157

D.9 $e + H_2(X^1\Sigma_g^+) \rightarrow e + H(1s) + H^*(2s)$... 157

E.1 EEDF (a) and EEPF (b) of two temperature Maxwellian distribution...... 159

F.1 Equivalent circuit of RF discharge with DC bias electrode................. 162

F.2 Variations of potentials and currents during RF cycles...................... 167

H.1 Hollow cathode discharge chamber after trial deposition experiments..... 169

I.1 Time-resolved potentials in the RF hollow cathode discharge.............. 171

List of Tables

1.1	CVD diamond properties	2
1.2	Methods of diamond film deposition	9
1.3	Properties of DLC materials in comparison with CVD diamond and graphite	13
2.1	Impact reactions, producing various hydrogen species	41
2.2	Ionisation potentials, effective diameters and ionisation cross-sections of selected molecules	43
2.3	Hydronium ions production reactions	44
3.1	Summary of the reviewed publications on electron sources and electron injection	53-55
3.2	Time of ion transition through the sheath (number of RF cycles) and thickness of the sheath at different discharge conditions	88
4.1	Effect of the DC bias electrode on the temperature of the tail electrons after interaction with RF sheath of the powered and grounded electrodes	108
5.1	Deposition conditions	125
5.2	Deposition conditions of the single hollow cathode discharge	130
B.1	Electronic parameters values of the EQP300 analyser	150

Symbols

Symbols	Descriptions	Dimensions
A	surface area, electrode area	m^2
A	surface area in dimensionless form	-
d_{eff}	effective size of plasma	m
E	electric field	$V \cdot m^{-1}$
E_{th}	threshold energy of reaction	V
I	electrical current;	A
I_e	– of electrons, collected by electrostatic probe	
I_{pr}	– of electrostatic probe	
I_{emis}	– of electrons, emitted by filament	
I_{in}	– of injected electrons	
i	instantaneous conduction current;	A
i_e	– of electrons,	
i_{ion}	– of ions,	
i_D	displacement current	
ι	instantaneous conduction current in dimensionless form; subscript A, B or C defines current to a particular electrode	-
j	current density;	$A \cdot m^{-2}$
j_e	- of electrons	
j_i	- of ions	
l	length of electrostatic probe	m
l	distance	m
M_i	ion mass	a.m.u.
m_i	ion mass ($= M_i \cdot m_p$)	kg
n	density;	m^{-3}
n_e	- of electrons	

n_i	- of ions	
P	power	W
P_r	- radiation power	
p	pressure	torr, mtorr
Q	surface charge density	$C \cdot m^{-2}$
r	radius of electrostatic probe	m
S_{loss}	total area of charged particles loss	m^2
s	sheath thickness	m
t	time	s
T_g	gas temperature	K
T_e	electron temperature	V
V	voltage or electric potential;	V
V_p	- plasma potential	
V_{pr}	- potential of electrostatic probe	
V_{fil}	- potential of emissive filament	
V_i	- ionisation potential	
V_{gen}	- amplitude of a sinusoidal signal of RF generator	
$V_{dc\ an}$	- potential of positive DC electrode	
$V_{dc\ bias}$	- self-bias voltage of powered electrode	
$V_{dc\ an}$	- potential of positive DC electrode	
$V_{p\ el}$	- potential of a powered electrode	
$V_{p\ sh}$	- potential of a powered electrode sheath	
$V_{g\ sh}$	- potential of a grounded electrode sheath	
υ	velocity	$m \cdot s^{-2}$
υ_e	- electron velocity	
υ_B	- Bohm velocity	
$\mathcal{V}_{pl}$	volume of plasma discharge	m^3
W	energy	V
x	distance	m

α_R	relative polarisability	-
Γ	particle flux	$m^{-2} \cdot s^{-1}$
ε	emissivity of material	-
σ_{max}	maximum of ionisation cross-section	m^2
Φ	potential (dimensionless)	
τ_{ion}	transition time of ion through a sheath	s
τ_{RF}	RF period	s
ω	cyclic frequency	$rad \cdot s^{-1}$
ω_{ip}	- ion plasma frequency	
ω_{RF}	- RF cyclic frequency	

Physical constants

Symbol	Description	Value
σ	Stefan-Boltzmann constant	$5.67 \cdot 10^{-8}$ W·m^{-2}·K^{-4}
k	Boltzmann constant	$1.38 \cdot 10^{-23}$ J·K^{-1}
m_e	electron mass	$9.11 \cdot 10^{-31}$ kg
m_p	proton mass	$1.67 \cdot 10^{-27}$ kg
e	elementary charge	$1.60 \cdot 10^{-19}$ C
ε_0	permittivity of free space	$8.85 \cdot 10^{-12}$ F·m^{-1}

Acknowledgements

I wish to express my gratitude to the Open University for providing financial support for myself.

Thanks are also due to:

Prof Nickolas Braithwaite , for his supervision and advice, friendship and hospitality, and, most of all, his eternal patience.

Dr Peter Johnson, for help with the modelling part.

Dr Glenn Counsell, for help with the electrostatic probe system.

Prof Gerald Elliot, for his encouragement during this work.

Ted Beaver, Alan Knight and David Sommerville, for their first class technical help.

Naomi Williams, for introducing me to the art of SEM.

Dr Charles Mahony, Dr John Young, Dr Heather Phillips and Dr Abdulkadir Altunogly, for joint work and friendship.

The whole staff of ORU, for support and friendship.

My wife, Lena, for her support and patience for the last eleven years.

This thesis is dedicated to

my mother Nina Ivanovna Goruppa (1936-1994) and

my father Alexander Iosiphovich Goruppa (1934-2002)

for many years of loving care and countless happy memories.

Their lives are celebrated forever in this and all my works.

Chapter I. "Introduction"

1.1. Diamond as an engineering material.

During the last two decades chemical vapour deposition (CVD) of diamond-based films has been one of the most interesting directions in thin film technology. Its popularity originates from the unique combination of physical properties of the materials (Table 1.1) [2]. In contrast with the high pressure high temperature (HPHT) method of growing separate diamond crystals, CVD techniques produce the material in the form of polycrystalline film, expanding significantly application areas of the material. At first it seems that CVD diamond formation at pressures and temperatures as low as 1 Torr and 600°C contradicts the carbon-phase diagram, reproduced from [1] in Fig.1.1. The diagram depicts the various thermodynamic conditions under which carbon exists stably as diamond or graphite. At any fixed temperature graphite will be converted into diamond at a pressure exceeding the equilibrium boundary on which both phases co-exist. At any pressure below the boundary the diamond phase is metastable, so it reverts to graphite. Reversion to graphite proceeds at a rate determined by chemical kinetics. This rate is evidently very slow at room temperature and pressure since diamonds are gemstones of high value. But the diagram, reflecting thermal equilibrium conditions does not imply any restrictions to non-thermal equilibrium approaches in diamond synthesis.

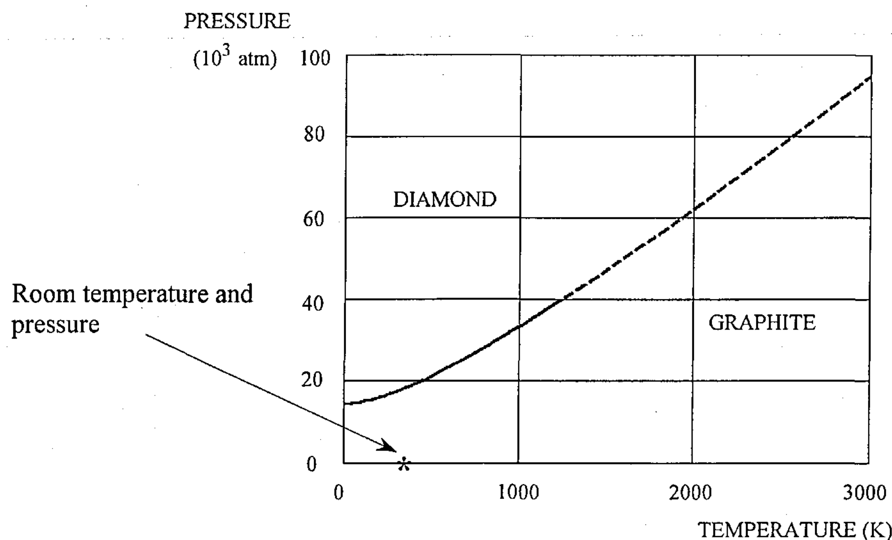

Fig. 1.1 Diamond-graphite phase diagram in terms of pressure and temperature.

CVD diamonds versus competing materials			
Properties of diamond		Comparison with competitors	Possible applications
Vickers' hardness (kg/mm^2)	12000 - 15000	hardest material known	drill bits, polishing material, cutting tools, surgical knives, sintered or brazed diamond compacts.
Coefficient of friction	0.1 (in air)	very low in air; (higher if kept clean under vacuum)	wear resistant coatings on lenses, bearings, tools, or hard disks, sliding parts.
Young's modules (N/m^2)	1.2×10^{12}	twice the value of alumina; highest mechanical strength	stiff membranes for lithography masks, radiation windows, high-end
Sound propagation velocity (km/s)	18.2	1.6×the value of alumina	audio twitter domes, micro-mechanical applications.
Chemical inertness	inert	at room temp. resistant to all acids, bases and solvents	coatings for reactor vessels, sample containers for analytical instruments.
Range of high transmittance (μm)	0.22 - 2.5 and > 6	in the IR orders of magnitude lower than other materials	UV-VIS-IR windows and coatings, spectrometer sample containers, microwave windows, optical
Refractive index	2.41	1.6×the value of silica	interference filters, optical wave guides.
Band gap (eV)	5.45	1.1 for Si; 1.43 for GaAs; 3.0 for β -SiC	passive and active electronics, high power, high frequency
Electron/hole mobility (cm×A/s)	1900/1600	1500/600 for Si; 8500/400 for GaAs	semiconducting devices, wide range thermistors, hot transistors, Schottky diodes, short wavelength lasers,
Dielectric constant	5.5	11 for Si; 12.5 for GaAs	γ - ray detectors.
Thermal conductivity (W/cm/K)	20	value for type IIa natural diamond at room temp. 4 × the value of Cu or Ag	highly efficient, insulating heat sinks for high power or ULSI electronics.
Thermal expansion coeff. (K^{-1})	0.8×10^{-6}	value at room temp. close to silica value of 0.57×10^{-6}	thermally stable substrates, e.g. for X - ray lithography masks, power laser windows.
Luminiscence (μm)	0.44 0.52 (B-doped)	blue luminescence scarce (β -SiC)	blue or green LEDs, detectors.

Table 1.1 CVD diamond properties (from [1])

Low-pressure plasmas, produced in electrical discharges through gases, are by their very nature non-equilibrium media. A diversity of chemical processes can be promoted by them.

The technological potential of such media is reflected in the fact that the majority of diamond and diamond-like carbon (DLC) deposition methods are based on various gas discharge techniques.

1.2 A brief history of diamond and diamond-like carbon growth

The starting point of the scientific approach to diamond study and its synthesis can be traced back to the XVIII century, when A.L.Lavoisier determined that the product of diamond combustion was limited to carbon dioxide. It was not until the beginning of the XX century, when it became possible to look at the atomic structure of material using X-rays, that W.H.Bragg jointly with W.L.Bragg demonstrated that carbon had three allotropic states: cubic (diamond), hexagonal (graphite) and amorphous. Numerous attempts to grow artificial diamond resulted in success fifty years later. In 1953 W.G.Eversole from the Union Carbide corporation (USA) synthesised diamond from carbon monoxide grown on natural diamond crystals at pressures in the range from 53 to 309 atmospheres ($(53-309)\cdot 10^5$ Pa) and temperature in the range from 850 to 1100 °C. Further development of this approach, using only solid precursors, became known as a high pressure and high temperature (HPHT) method. Later the same year diamond was synthesised without pre-existing diamond seeds using HPHT method at Allemana Svenska Electrisia Aktiebologet (ASEA) in Sweden. In 1954 the General Electric Company (USA) independently achieved successful growth of diamond by the HPHT method, which was widely publicised. The typical pressure and temperature of the HPHT method for direct graphite-to-diamond conversion without a metal catalyst are 120 kbar ($120\cdot 10^8$ Pa) and 2000 °C. Subsequent perfection of the HPHT method achieved growth of diamonds as large as 11.1 ct (2.22 g) [3], which corresponds approximately to crystal size of 1cm. The HPHT method effectively uses the rapid chemical kinetics at HPHT conditions to reach the equilibrium state. Further in this chapter only low-pressure synthesis from the gaseous phase will be considered. In 1956 B.V.Spitsyn from the Moscow Physical Chemistry Institute deposited diamond on pre-existing diamond crystal at a pressure of the order $3\cdot 10^{-6}$ torr ($4\cdot 10^{-4}$ Pa). In his

experiments substrates were heated from 800 to 1000 °C, and CBr_4 or CI_4 were used as the source of carbon.

Summarising early successes in diamond synthesis it is obvious to note that major efforts were directed at a replication of the natural geological phenomenon of diamond growth that resulted in domination of the HPHT method. The idea of diamond deposition from the vapour phase was so contradictory to the physical properties of the material that the low growth rates of the first experiments were almost recognised as the method's natural limit; though partly it may be explained by the absence of any open publications. In addition, the unique role of low-temperature plasmas as chemically active media was not yet widely appreciated; that happened in the 70s [4].

The next important advance in the low pressure deposition of diamond was achieved by the group of J.C.Angus at the Case Western Reserve University (USA). Eventually after repeating in the mid 60s Eversole results they came to use of hydrocarbon gases (typically CH_4) in the deposition medium and, subsequently, reached an understanding of the role of molecular, and later atomic, hydrogen in the suppression of graphite deposition. The cyclic process developed by the group in 1970 [5] consisted of two stages. A mixed phase diamond-graphite film was precipitated from thermally decomposed methane in the first stage. In the second stage the graphite deposits were removed by reaction with atomic hydrogen, generated at a hot tungsten foil over which the hydrogen gas stream was passed. An analogous route was devised by the group of Deryagin from the Physical Chemistry Institute in Moscow. The Moscow group also started from confirmation of Eversoles results in the late 60s. Similar to the process developed in USA, Deryagins group used a cyclic method, based on deposition from thermally decomposed methane and subsequent admittance of air for selective etching of graphite phase [6]. Later they came to use of atomic hydrogen during the growth process, resulting in the mid 70s in the deposition of diamond crystals on non-diamond substrates [7]. Another experimental method, called chemical transport reaction technique (CTR), was a continuous etching and

deposition process in hydrogen, that achieved growth rates up to 1 μm/h [8]. At that time little experimental details were revealed. According to J.C.Angus [9], "if open communication had been possible, low pressure diamond technology would have developed about a decade earlier than it actually did".

At the same time, another class of carbon materials started to attract the interest of the scientific community. That was hydrogenated amorphous carbon (α-C:H) or diamond-like carbon (DLC) films. The interest was stimulated by the work of Aisenberg and Chabot from the Whittaker Corporation (USA), published in 1971 [10]. In their experiment, films exhibiting many of the properties of diamond were deposited from a beam of carbon ions, accelerated electrically to the substrate by means of negative bias. In 1976 similar carbon films were deposited by Whitmell and Williamson from AERE Harwell (UK) [11] in a DC plasma and by Holland and Ohja from the University of Sussex (UK) [12] in an RF discharge. Characterising the 60s and 70s stage in CVD diamond deposition it is possible to conclude that a significant step had been made in establishing the most favourable gas components for the deposition process, that is hydrocarbon gases and hydrogen, and an understanding of their function in the deposition process. However, the experimental approach still relied on traditional thermodynamic methods, namely thermal decomposition of gases and cyclic processes. The growth rates achieved by these methods were rather slow.

The start of the modern era in diamond film growth is connected with the research programme at the National Institute for Research in Inorganic Materials in Japan. The programme was initiated by Nobuo Setaka in the mid 70s. In 82, 83 the group published a series of papers [13-16], describing deposition of diamond films by hot filament and microwave methods at remarkably high rates of several μm/h. Gas mixtures were typically 1-2% of methane in hydrogen. The success of the NIRIM group spawned numerous research programs all over the world, which led to the development of various deposition methods [17]. A considerable advancement was made in the understanding and description

of separate gas phase and surface mechanisms of deposition, which are reviewed in [18]. Popularity of the subject has grown to such an extent that since the late 80s annual international conferences on CVD diamond and related materials are held in Europe, the USA and Japan. At the same time a significant progress has been made in research on DLC coatings, resulting in the emergence of commercial products for optical, electronic, wear resistance and biomedical applications [19]. At this period several review monographs have been published, describing properties and applications of natural and synthetic diamond crystals [3], and growth methods, properties and applications of diamond and diamond-like films [20-22].

At the beginning of 90s the choice of the main CVD diamond growth methods was as follows. For low pressure (1-100 torr) there are microwave and hot filament techniques, for high pressure (up to atmospheric) - DC and RF arc jet and flame techniques. By 94 the level of perfection of these methods had become quite high. For example, a 125 kW microwave system, manufactured by the Applied Science and Technology Company (ASTeX) from the USA allows the growth of CVD diamond on a deposition area of 30 cm diameter at a rate of 10s μm/h. The purity of the film is higher than that of natural diamond. In general, the focus of CVD diamond research is shifting from the process itself to the material characterisation and application.

1.3 Diamond crystal structure and film morphology

The basis of the extraordinary properties of diamond is its regular lattice. The lattice structure of natural diamond was determined by W.H.Bragg and W.L.Bragg by means of X-ray diffraction at the second decade of last century. Each carbon atom shares each of its four outer electrons with four other carbon atoms, forming in this way four sp^3 bonds. The combined effect of sp^3 bonds leads to the regular arrangement of carbon atoms in the lattice, pictured in Fig. 1.2. Dots, shown black, represent carbon atoms and are located at the corners of the cube and at the centres of the cube faces. This arrangement is repeated all over the lattice, which is known as face-centred cubic. Those, shown white,

also represent carbon atoms and form another face-centred cubic lattice similar and parallel to the first, but displaced from it. Therefore, the complete diamond lattice consists of two interpenetrating face-centred lattices.

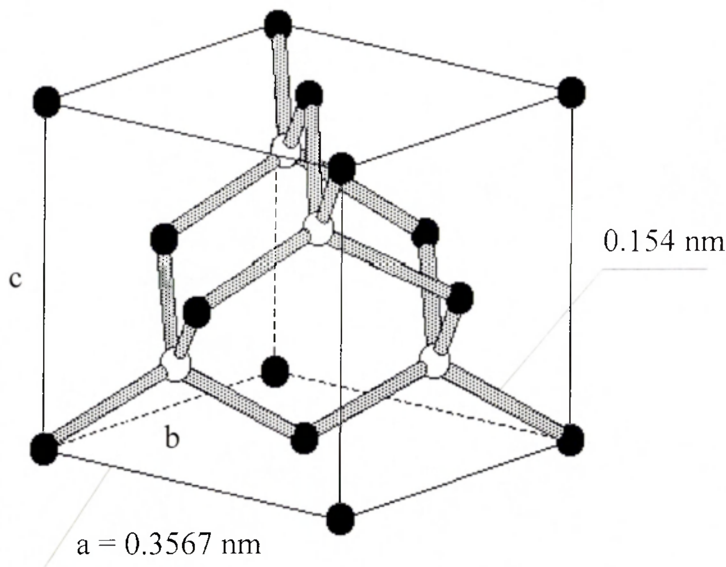

Fig. 1.2 Model of the diamond lattice

CVD diamond growth produces at the initial stage multiple crystallites of various shapes, depicted on Fig. 1.3 [23].

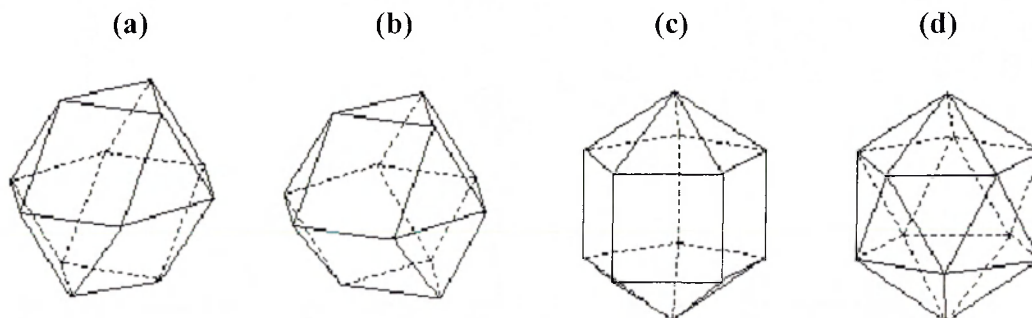

Fig. 1.3 Schematic diagrams of diamond particle morphologies
(a) Cube-octahedron (a single crystal);
(b) Twinned cube-octahedron;
(c) Decahedral Wulff-polyhedron;
(d) Icosahedron.

The growth process leads to the covering of all the substrate by crystallites and the formation of a polycrystalline film. In general, a polycrystalline film exhibits a columnar structure, which is shaped by "evolutionary selection" of microcrystals [24]. Microcrystals with a direction of fastest growth more or less perpendicular to the substrate surface are

more favourable and grow at the expense of microcrystals with different orientation. The selection process is schematised in Fig. 1.4.

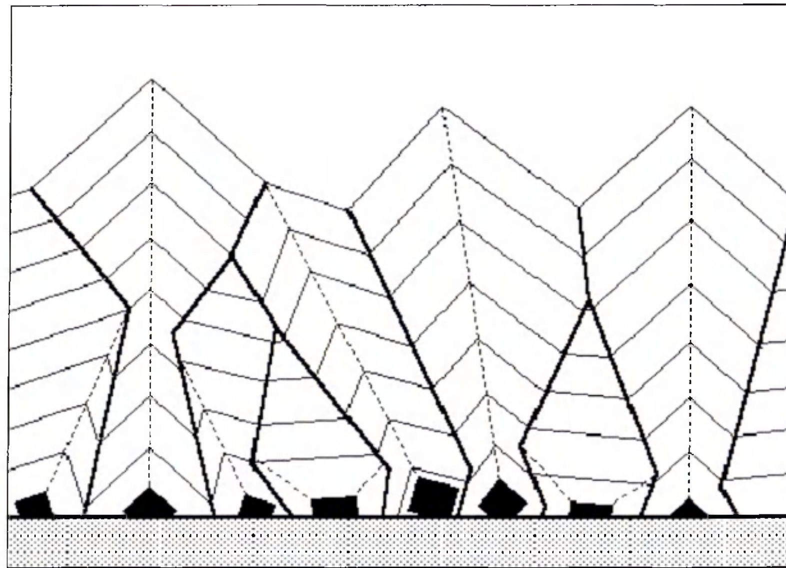

Fig. 1.4 Cross-section of a growing film

Finally grown film can have the following typical morphologies, determined by crystalline faces directed upwards: the {111} triangular faces, the {100} square faces or cauliflower-like small crystalline aggregates. These morphologies have been correlated with the substrate temperature, gas composition and gas flow rate [25].

1.4 Methods of CVD diamond growth.

The growth of diamond films from the gas phase has been performed by a variety of plasma, flame and thermal decomposition methods (Table 1.2). Plasma techniques are commonly referred as plasma enhanced chemical deposition (PECVD) methods. It is difficult to group PECVD methods owing to the wide variety of operating conditions and precursor materials. The most obvious operational parameter for comparison is gas pressure. From the analysis, presented in [17], it has been concluded, that at least for plasma-based methods the growth rate is proportional to gas pressure, while the deposition area is inversely proportional to pressure. The more successful plasma methods, such as those based on microwave discharges, have operating pressure in the range 1-50 torr. Combining high values of deposition area and growth rate requires high power inputs to

Method	Rate (μm/h)	Area (cm^2)	Advantages	Drawbacks
Non-plasma methods				
Combustion flame	30-200	0.5-3	Simple set-up, high growth rate	Poor stability, small area, contamination by torch material
Hot filament	0.3-8	5-900	Simple set-up, large deposition area	Contamination by filament mater., poor filament stability
Plasma-based methods				
DC discharge (low pressure)	<0.1	70	Simple set-up, large deposition area	Bad quality, low deposition rates
DC discharge (medium pressure)	20-250	<2	High rate, excellent quality	Small area
DC plasma jet	930	<2	Highest rate, excellent quality at high power	Contamination by electrode material, high equipment cost
RF (low pressure)	<0.1	100	Scaleable by area	Poor quality, low rate, contamination by electrode material
RF (thermal, 1 atm)	180	2-3	High rate, high quality at high power	Small area, poor stability, high equipment cost
Microwave (0.9-2.45 GHz)	1 (low pres.) 30 (high pres.)	80 5	High quality and stability	Area scaling requires very high power
Microwave (ECR, 2.45 GHz)	0.1	100	Large deposition area	Poor quality, low rate

Table 1.2 Methods of diamond film deposition from [17]

the plasma in order to sustain high power density at the deposition substrate. For example, a microwave reactor, created by "ASTeX Inc", maintains power density up to 177 W/cm^2 at the substrate. It deposits diamond coating up to 30 cm in diameter at rates of up to 50 μm/h.

1.5 Main plasma parameters

In general, a low pressure gas discharge plasma could be defined as a gas media, which contains in addition to atoms and molecules of a background gas products of their ionisation, or negatively and positively charged particles. Typically, electrons are the main carriers of negative charge. The fundamental property of quazineutrality of plasma means that their density n_e is in average equal to the density of particles, carrying a single positive charge, i.e. the density of ions n_i. Ions originate from a process of ionisation, when electron, orbiting atom nucleus, gains sufficient energy from outside to leave the atom. In this way ion-electron pair is created. Because of low mass (proton/electron mass ratio equals 1836) electrons are easily accelerated by electric field, gaining high energy. In the first approximation, electron energy distribution function (EEDF) is described by the Maxwellian distribution (section 4.2.1, chapter IV). Therefore, electron component of plasma can be characterised by a temperature T_e. Normally, electron temperature of low pressure plasma is in the range 1-5 eV (1eV $\approx$ 11600 °C). In difference from electrons, ions can't be accelerated fast by electric field due to their high mass. Their resulting temperature is close to the room one. Consequently, heating of electrons is the channel, through which electric or electromagnetic field passes energy to all the variety of kinetic and chemical processes in plasma volume. Therefore, electron temperature T_e and density n_e are the most important parameters, characterising status of the discharge plasma.

Because of their high energy, electrons run away from ions near the electrode surface, creating a positively charged sheath between plasma and electrodes. Potential across the sheath of the grounded electrode is called plasma potential V_p. Ions are accelerated through the positive sheath towards electrode surface. Their energy is characterised by the ion energy distribution (IEDF) on the electrode surface. Typically, in low pressure radio-frequency (RF) discharge the grounded electrode is larger in area than the powered electrode. As the result, it acquires a time-averaged negative self-bias potential $V_{dc\ bias}$ (Fig. 4.2 in chapter IV). So, ions arriving to the surface of the powered electrode,

have maximum energy $E_i = V_p + V_{dc\ bias}$. Depending upon the net sheath potential, E_i could reach hundreds of Volts. This parameter is important for sputtering, etching or deposition processes on the electrode surface.

1.6 The CVD diamond growth process.

The classical low-pressure CVD diamond growth scheme includes the following main features. First, the concentration of methane in hydrogen makes up just 1-2%. Second, the gas is activated prior to deposition by a hot filament, a gas discharge or a flame. Third, the deposition substrate is heated to temperatures in the range 800-1000 °C. Fourth, the substrate material (typically silicon, molybdenum) and various types of surface pretreatment (scratching) or deposition-state (electrical biasing) provide high nucleation density.

Until nowadays there has not been a single self-consistent theory describing CVD diamond growth because of the complexity and diversity of the chemical and physical processes in the gas phase and on the surface. Nevertheless, several concepts and ideas have been developed to the stage of a clear understanding of various contributing mechanisms.

The general concept developed by the group of Deriagin at the early stage of CVD diamond science [26] was based on the idea that the growth process was controlled by kinetics rather than by thermodynamics. The key element consists of preferential etching by hydrogen atoms of the graphitic phase, which is deposited simultaneously with diamond. Later this theoretical assumption was confirmed experimentally [27]. It was demonstrated that removal of graphite by activated hydrogen was orders of magnitude faster than removal of diamond.

Other roles played by hydrogen have also been revealed. An important function of hydrogen is the stabilisation of the diamond surface. By combining with the dangling bonds of surface carbon, hydrogen keeps the bonds of surface carbon atoms in the sp^3 configuration and prevents surface reconstruction into sp^2 or sp structures, that are

characteristic of graphite and carbides respectively [28]. Hydrogen is further entangled in the maintenance of active growth sites by removing hydrogen from the surface, preventing its massive trapping within the solid [29]. In effect, the surface is kept active by a type of catalytic process in which hydrogen atoms are cycled onto the carbon surface. The chemical desorption of hydrogen from the surface by atomic hydrogen is thermodynamically favoured because of the strength of the H-H bond.

A positive role is played as well by molecular hydrogen. The importance of its excessive concentration is in the suppression of polyaromatic hydrocarbons formed in the gas phase [30], which may be precursors to unwanted sp^2 carbon during the growth process. Along with attachment kinetics hydrogen participates in energy transport processes. Studies of the hot filament reactor environment have shown that a significant amount of energy is transported by decomposition of H_2 and subsequent recombination of H atoms on the surface [31]. For a typical pressure 20 torr the "chemical" or internal energy transport by hydrogen is approximately equal to that transferred "physically" by thermal conduction from the gas. It has been estimated that for each carbon atom added to the diamond lattice there are approximately 10^4 carbon atom recombination events [31].

Gas activation has two main functions in the process: production of precursor carbon species and dissociation of hydrogen. In methane-hydrogen mixtures methyl radicals and acetylene are the most often detected carbonaceous species in the vicinity of the deposition substrate. Many proposed mechanisms of diamond growth are based on the attachment of these species or their ionic products [18]. Dissociation of hydrogen occurs either through thermal decomposition in the case of hot filament and flame techniques or through direct impact between electrons and H_2 molecules in low pressure plasmas. Typical operating temperatures of a tungsten filament are around 2500 °C. For production of atomic hydrogen by direct impact electron should have energy no less than the reaction threshold (or potential):

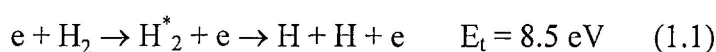

$$e + H_2 \rightarrow H^*_2 + e \rightarrow H + H + e \qquad E_t = 8.5 \text{ eV} \qquad (1.1)$$

Other kinetic reactions between electron and atomic/molecular hydrogen will be described in chapter II, section 2.8.2.

The optimum temperature range 800-1050°C of the growth process is determined from below by the rate of chemi-desorption of hydrogen and from above by graphitisation of the diamond surface. At temperatures below 800°C the formation of active sites by chemi-desorption is slow which leads to a rapid decrease in the film quality. The addition of small amounts of oxygen allows the deposition of good quality film down to 600°C. This occurs because of etching by OH radicals of sp^2 surface carbon together with a decrease in concentration of aromatics in the gas phase owing to oxidation [32].

Nucleation is the initial stage of diamond film formation. It is strongly dependent on substrate material. The general rule for deposition substrates is that nucleation densities are higher on stable carbides or carbide forming substrates (SiC, TiC, WC, Si, Mo, Ti, W, Ta) and on oxygen-containing substrates (SiO_2 and Al_2O_3) than they are on substrates not forming carbides (Cu, Pt, Ni). Most of the materials that not form carbides are considered to have a high diffusivity for carbon, so much that there is a substantial reduction of the carbon concentration at the surface leading to a considerable delay in the onset nucleation [33]. A tiny diamond crystal can survive on the substrate surface only as long as the re-supply of carbon from the feed stock is no slower than the dissolution losses at the interface.

Silicon substrates have proved to be the most popular for basic studies of carbon films. It seems to be the ideal material for study of diamond nucleation and film formation because of similarity of its lattice to that of diamond. But diamond nucleation is very slow on highly polished, defect-free, single-crystalline Si wafers because it takes a long time to transform the surface into silicon carbide. On the other hand, diamond nucleation occurs readily along scratches or sharp fracture edges. So, it has become a common practice to scratch and polish Si wafers with diamond grits or other hard particles, such as SiC, B_4C, c-BN, etc. prior to deposition. This method increases the nucleation density from 10^4 cm^{-2}

up to 10^7 cm^{-2}. There are several hypotheses explaining this phenomenon: residual diamond particles act as nucleation sites; an energetically favourable "sharp edge" mechanism; formation of carbide is speeded at edges and groove walls. Experimental data do not confirm in full any of these hypotheses. Another method that has achieved a nucleation density of 10^{11} cm^{-2} in the early stage of deposition is electrical biasing [34]. A pristine silicon substrate is biased to a voltage of -250 V for 1-2 hours at the initial stage. Afterwards the biasing is removed and normal growth process takes place. The core of this method it thought to be in fast formation of silicon carbide layer in the presence of bombardment by energetic ions. After achieving a nucleation layer thickness ≈90 Å the carbon on silicon carbide surface is free to form critical clusters that are eventually favourable for diamond nucleation.

1.7 Diamond-like carbon

Diamond-like or α-C:H carbon is a cross-linked non-crystalline network of carbon and hydrogen atoms. The structure and properties of DLC materials (Table 1.3) are strongly dependent upon the relative proportion of sp^2- and sp^3-co-ordinated carbon atoms, which in its turn is mediated by the amount of hydrogen present in the film.

A large amount of hydrogen atoms acting only as network terminators permits a considerable fraction of sp^3 carbon bonds. DLC films are prepared by a variety of methods [37]. Schemes have been demonstrated based on ion beams, plasma deposition and laser ablated plasma plumes. All methods are nonequilibrium processes characterised by the interaction of energetic ions with the surface of the growing film. Ions play an important role in forming sp^3 bonding. The commonly used plasma method is RF parallel plate discharge in hydrocarbon gases.

As it has been noted in section 1.5, in low pressure RF discharge in the absence of collisions ion energy on the electrode surface $E_i \approx V_{dc\ bias} + V_p$. At higher pressure, the ion energy has a form of an energy spectrum with a mean value that scales as $V_{dc\ bias} \cdot p^{-1/2}$,

where p is operating gas pressure [38]. For typical pressure 3 Pa (≈ 23 mTorr) $E_i \approx 0.6 \cdot V_b$.

Property	CVD diamond	α-C	α-C:H	Graphite
Crystal structure	Cubic a = 3.561 A	Amorphous sp^3/sp^2 bonds	Amorphous Sp^3/sp^2 bonds	Hexagonal a = 2.47 A
Form	Faceted crystals	Smooth to rough	Smooth	-
sp^3 (%) *	100	30 - 60	up to 95	0
Hardness, Hv	3000 - 12000	1200 - 3000	900 - 3000	-
Density ($g \cdot cm^{-3}$)	2.8 - 3.5	1.6 - 2.2	1.2 - 2.6	2.26
Refractive index	2.41	1.5 - 3.1	1.6 - 3.1	2.15
Band gap (eV)*	5.5	0.4 - 2.5	0.8 - 1.5 1.5-4 (soft α-C:H)	-0.04
Electrical resistivity ($\Omega \cdot cm^{-1}$)	$>10^{13}$	$>10^{10}$	10^6- 10^{14}	0.4
Thermal conductivity ($W \cdot m \cdot K^{-1}$)	1100	-	-	3500
Chemical stability	Inert	Inert	Inert	Inert
Hydrogen content (%)*	0	0	25 - 65	0

Table 1.3 Properties of DLC materials in comparison with CVD diamond and graphite [35]. * - Data taken from [36].

Ion beam methods can produce a high proportion of sp^3 bonds in DLC films with very little hydrogen. α-C films deposited by mass-selected ion beam (MSIB) method have up to 95% of sp^3 bonding [39]. The basic idea, that explaines deposition mechanism from MSIB, is also germane to other types of DLC deposition. The ion flux is reckoned to promote sp^3 bonding through surface densification [40]. The bonding hybridisation adjusts itself to the local density. At low density it is sp^2, at high density it becomes sp^3. High energy ions penetrate the first atomic layer of the film, entering an interstitial position and increasing the local density. As the result of increased density the compressive stress P, which can achieve the value of 15 GPa, transforms the local bonding around the atoms into the bulk bonding of the appropriate hybridisation. Low energy ions, which fail to penetrate, remain at the surface, forming sp^2 bonds.

In plasma based methods carbon is transported to the surface also by radicals in

addition to the charged species. But the main role in the transformation of bonding hybridisation is played by ions. Owing to the electrical structure of low pressure plasmas, ions are considerably more energetic than most of the neutral radicals. For RF plasma there has been suggested a further mechanism considering the low degree of decomposition of the source gas [41]. The major ionic species from source gases methane, acetylene and benzene, detected by mass spectrometry, are CH_3^+, $C_2H_2^+$ and $C_6H_6^+$ respectively [42]. It is supposed that on impact for example the $C_mH_n^+$ ions dissociates into m separate C^+ ions with energy being shared between these daughter ions. As a result, each C^+ ion has an energy E_i/m. Ion bombardment dehydrogenates DLC films by preferential sputtering of weakly bounded hydrogen atoms. This mechanism has a good correlation with experiment. Hydrogen content and sp^3 fraction as functions of self-bias potential $V_{dc\ bias}$ relate to source gas as 1/m. The maximum density of DLC film occurs at about $V_{dc\ bias}$=300 V in methane, 500 V in acetylene and over 1000 V in benzene [40].

Their mixed sp^3/sp^2 structure and hydrogen content places DLC films in between diamond, graphite and polymeric hydrocarbons [43]. Although their properties are poorer than those of diamond, the low cost of production, based on standard deposition equipment, and low deposition temperature rate (room temperature - 300°C) makes DLC a competitive coating in many areas. High hardness and chemical resistance make DLC a good material for wear-resistant coatings on metals and on optical and electronic components. Smoothness of the order 3% for film several tens of nm thick makes them a valuable protecting film for magnetic recording media. Such protecting layers must be less than 50 nm thick (to maintain adequate signal to noise ratio). The high value of electrical resistivity (Table 1.3) of α-H:C films makes them a useful insulator in microelectronics devices. Like α-H:Si films it is possible to dope hydrogenated amorphous carbon films, making them a prospective candidates for semiconductor devices. It appears that DLC films are highly compatible with biological tissue. This biocompatability opens up many opportunities for DLC the area of medical implants [19, 44].

1.8 Advantages and drawbacks of RF capacitive discharge for carbon films growth.

The appeal of low-pressure RF (13.56 MHz) capacitive discharges for carbon film deposition is the availability of fully developed equipment, capable of coating large areas of a wide variety of substrates whether insulators or conductors. This type of discharge is widely used in the microelectronics industry. Its physics and chemistry in various environments has been thoroughly studied during the last three decades. For these reasons a new coating technology based on the capacitive discharge may be applied in industry quite fast and at a low cost. As it has been demonstrated in sections 1.4 and 1.6 RF discharges have completely justified early hopes for the deposition of DLC films yet have had a very poor performance for CVD diamond. This contradictory achievement is closely linked with discharge physics. The self-bias potential $V_{dc\ bias}$, characteristic of the powered electrode, is a valuable feature for the deposition of DLC films (section 1.6), but it is not desirable throughout the growth period of diamond films. In fact, energetic ions ($E_i > 130$ eV) can destroy the diamond lattice, converting sp^3 hybridisation into sp^2. Other drawbacks of the discharge as a medium for diamond growth are its relatively low mean electron temperature and plasma density; at typical pressures 10-100 mtorr they are 1-3 eV and 10^{15}-10^{16} m^{-3} respectively. The mean electron energy is far below the dissociation energy for the hydrogen molecule, which is 8.5 eV. This leads to a quite low amount of atomic hydrogen, produced in the discharge. Its content has been measured to be around 0.8% [45].

For comparison, the microwave discharge (2.45 GHz) has density up to 10^{18} m^{-3} [46] at the pressure $\approx$1 torr. This results in up to 70% of hydrogen dissociated in microwave plasma [47]. The potential drop in the sheath of a microwave plasma is much smaller than that of an RF one. It produces an ion energy flux of the order 20-50 eV. These properties of microwave discharge make it most commonly used for CVD diamond growth.

An important combined parameter reflecting a discharges ability to create high

density plasma is the power density. For CVD diamond microwave discharge it's value is in the range 10-30 $W \cdot cm^{-3}$, whilst for capacitive discharge it is just 0.1-1 $W \cdot cm^{-3}$. In order to increase the value of this parameter it is possible simply to apply more RF power. This leads to even higher $V_{dc\ bias}$ in accordance with $V_{dc\ bias} \sim (P/p)^{1/2}$ [37], where P - discharge power and p - gas pressure. Preserving the value of power and decreasing the reactor volume, which is equivalent to change in the electrode area ratio, can mainly redistribute sheath potentials at the electrodes in accordance with $V_C/V_A = (A_C/A_A)^n$, $1<n<2$, where V_C and V_A are sheath potentials and A_C and A_A are areas for cathode and anode respectively. Increase of power density results in higher values of $V_{dc\ bias}$ equally with higher current to the electrodes, which reflects growth of plasma density. This lack of independent control in the self-bias voltage, consequently ion bombardment energy, and plasma parameters is the crucial limiting feature of RF discharges in CVD diamond growth. So, it is necessary to go outside the frames of the standard RF parallel plate configuration to make it more feasible for CVD diamond growth.

1.9 Outline of the research program.

In order to enhance the scope for making CVD diamond by alow pressure RF plasma route it is necessary to achieve higher levels of density and electron temperature. Electrons are the main vehicles of energy transfer from electric field to ions, atoms and radicals.

A transverse magnetic field of 100-200 G can be used for RF discharge enhancement. It causes a magnetic confinement of electrons, thereby increasing plasma density 2-3 times and decreasing self-bias potential up to 5 times. This scheme is commonly known as an RF magnetron. Its chief disadvantage is a strong nonuniformity of plasma, which may lead in turn to uneven coating.

Another method is plasma enhancement by an electron beam or flux. This approach has been used in 60s to maintain dc glow discharge at the pressure below 20 mtorr. The method of supplying additional electrons is attractive because it opens the way of

controlling plasma parameters, which is not coupled directly to the discharge power, and in the case of RF diode to the self-bias potential. At the same time, it may provide the possibility of fine tuning of energetic electrons, that is crucial for production of atomic hydrogen and methyl radicals.

A third way of plasma enhancement is to confine electrons created by the discharge itself electrostatically using physical boundaries. This is by utilising a "hollow" glow effect, which can be seen at higher pressures within recessed structures of powered and grounded electrodes. Its advantage is in the simplicity of localizing high density plasma.

This work has been aimed at the investigation of RF capacitive plasma, enhanced at lower pressures by the addition of electrons and at higher pressures by the hollow glow effect, with particular attention to applications of the enhanced discharges for carbon film deposition. Studying the effects of these enhancements on the main plasma parameters, such as plasma potential, density and electron temperature, was of a special interest. Plasma characterisation has been performed by such diagnostic techniques as Langmuir probe, energy and mass analysis and emission spectroscopy. A number of carbon film deposition experiments have been done in order to verify specific features of film growth processes in enhanced plasmas.

Chapter II. "Experimental device and plasma characterisation"

2.1 Experimental device specification.

A special experimental device has been developed in order to accomplish the research programme, outlined in the section 1.8. This programme has determined two main requirements of the design. The first one is the high temperature of the deposition substrate, which must be heated up to 1000°C in order to comply with typical diamond deposition regimes. The second one constitutes a specific configuration of the vacuum RF power line, which allows the device to operate at high temperature and over wide pressure range: from 0.01 up to 6 torr. These requirements resulted in a device configuration which included such major units as water cooled base plate, high temperature heater, heat shield and RF line with quartz or ceramic insulation, as depicted in Fig. 2.1.

2.2 The base plate unit.

The design of the vacuum chamber has arisen from the traditional vacuum equipment utilising a glass bell-jar chamber with a rubber ring sealing. The glass bell-jar chamber, marked (1) in Fig. 2.1, has an advantage of a good visual control of any processes inside it and of easy access to units and diagnostics based within the vacuum. In order to prevent the rubber seal from being damaged by heat it was decided to provide the base plate (2) with a water cooling bath (3). Maintaining the base plate near room temperature has also allowed the use of rubber o-ring sealing for multiple ports. This solution has made the vacuum system servicing quite convenient and cheap. Duraluminium was chosen as the material for the base plate because of its high heat conductivity and its machinability. The base plate (2) is a cylindrical plate 330 mm in diameter and 30 mm thick. Another cylindrical plate of smaller diameter was joined on top of it in such a way as to form the cooling bath. A copper disk (4) on the top of the cooling bath, covering almost all the vacuum area of the base plate, is intended for collection of heat flux from the discharge

volume.

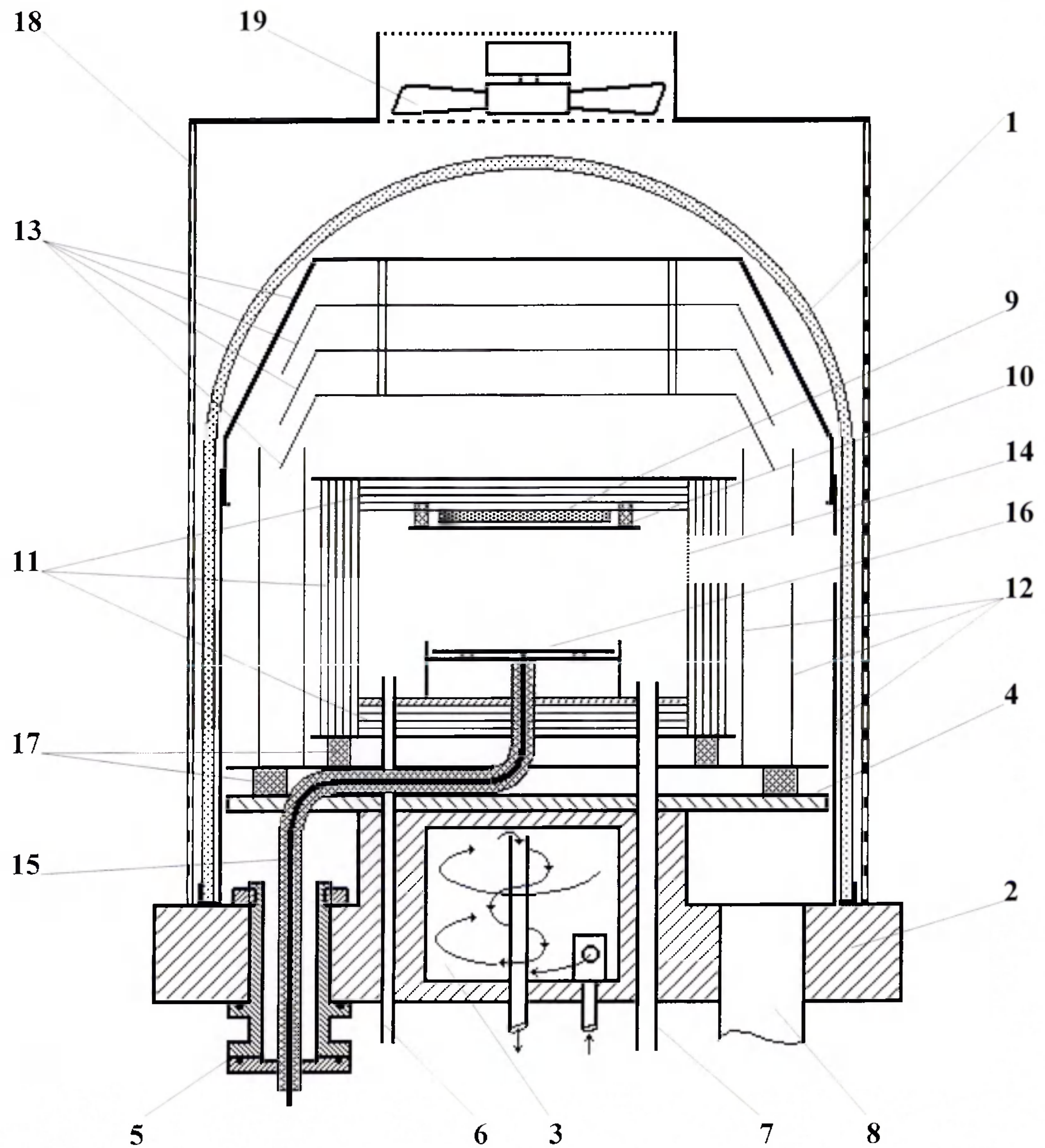

Fig. 2.1 Schematic diagram of the main vacuum vessel

1 - Glass bell-jar
2 - Base plate
3 - Water cooling bath
4 - Copper disk
5 - RF line vacuum leadthrough
6 - Gas input tube
7 - Pressure sample tube
8 - Pumping port
9 - Furnace
10 - Deposition substrate
11 - Heat shield
12 - Outward heat shield
13 - Outward shield lid
14 - Meshed viewport
15 - Vacuum RF power line
16 - Powered electrode
17 - Ceramic spacers
18 - RF shield
19 - Air cooling fan

In this way it protects multiple leadthrough ports positioned in a circle around the cooling bath. In all there are 8 standard 26 mm diameter ports, which are used for RF and DC voltage leadthrough, furnace power supply, thermocouple and electrical probe leadthrough; one port of diameter 40 mm (8) is used for pumping. Additionally, inside the bath wall there are two specialised ports for gas input (6) and pressure measurement (7) tubes, passing directly into the discharge volume. In the cooling bath volume the input nozzle and the output tube are positioned so that they create a circular movement of water. This leads to an ascending spiral flux of water, which provide good convectional heat transfer. Both nozzle and output tube have been manufactured also from duraluminium in order to prevent electrochemical corrosion.

2.3 The furnace and the heat shield.

The typical diamond deposition regime requires heating of the substrate up to 800-1050°C (see section 1.5). For this purpose it was decided to equip the experimental device with a special furnace (9), utilising a heating element "Philips Thermocoax", type SEI15/100. The heating element of this type is capable of achieving the power level 500W and temperature up to 1000°C. It is a coaxial wire with a resistive core, which is separated from the metallic sheath by mineral insulant. The sheath protects the resistive core from interaction with gases filling the chamber. This metal casing of the heating core allows it to be used extensively in multiple deposition runs; whereas a heating wire of bare tungsten would last in a hydrogen medium no more than a few hours. The length of the heating wire hot part is 1 m with the diameter just 1.5 mm. The wire operates from a 50 V AC supply. The heating element was sandwiched between two stainless disks of diameter 80 mm and 3.5 mm thick. It was interleaved with a 1.5 mm stainless steel wire, shaped as a flat spiral by spot-welding to one of the disks. This spiral wire provided additional heat removal from the heating element. The disks of the furnace were fastened together by screws.

Two positions of the furnace in the discharge volume were tried out during deposition experiments. One was just beneath the powered electrode (16), the other - behind the deposition substrate (10), which was opposite the powered electrode. Several runs with the furnace at the first position led to heat and weight overload of the top part of the RF line. This resulted in cracking of the quartz insulation of the RF line. More successful was the second position, where the furnace was fixed to the lid unit of the heat shield. Surface temperatures of the furnace and the deposition substrate were measured by separate chromel-alumel thermocouples.

The heat shield (11) was necessary in order to reduce radiation heat losses from the discharge volume; maintaining in that way the high temperature of the furnace (up to 1000°C) and the deposition substrate. The heat shield scheme was analogous to that one described in Ward and Allen [48]. The heat shield consists of multiple layers of thin metal, which re-radiate both inward and outwards. In [48] a formula was deduced for the radiated power as a function of the furnace temperature and number of shield layers.

$$P_r = \frac{A_1 \cdot \alpha \cdot \sigma \cdot T_1^4}{\beta} \qquad (2.1)$$

where $\beta = 1 + \frac{A_1}{A_2} + \dots \frac{A_1}{A_N}$, $\alpha = \frac{\varepsilon}{2-\varepsilon}$, A_1 and T_1 - area and temperature of the furnace, $A_2 \dots A_N$ - areas of shield layers, ε - emissivity of the layer, σ - Stefans constant. By rewriting (2.1) in the form

$$T_1 = \sqrt[4]{\frac{P_r \cdot \beta}{A_1 \cdot \alpha \cdot \sigma}} \qquad (2.2)$$

it is possible to calculate the furnace temperature as a function of the number of shield layers for various values of emissivity. The idealised scheme of the heat shield, used in calculations, is presented in Fig. 2.2. The diameter of the heat shield was constrained by the glass bell-jar at the upper limit and the electrode and substrate assembly at the lower limit. Further constraints were imposed by the requirement of inserting an electrostatic probe through the heat shield and the need to install the extracting orifice of an energy and

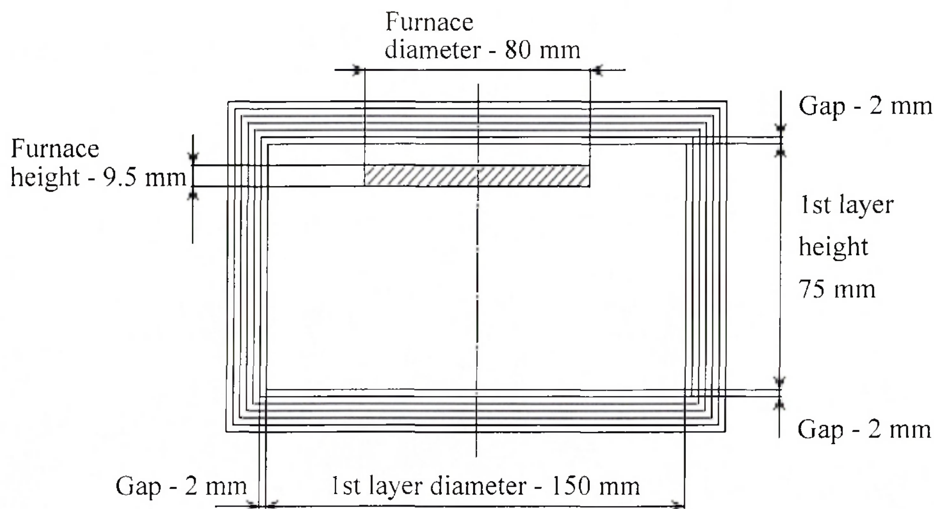

Fig. 2.2 Simplified scheme of the heat shield, used for calculations

mass analyser. The temperature of the furnace is calculated from the formula (2.2) for the shield geometry in the Fig. 2.2 and a furnace power setting of 800 W. Results are presented in Fig. 2.3.

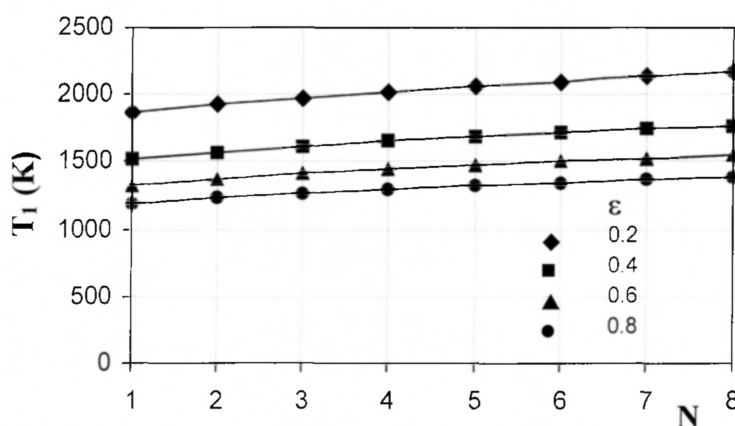

Fig. 2.3 Calculated temperature of the furnace T1 as the function of the number of shield layers N for various values of emissivity ε.

As it is seen from the Fig. 2.3 seven layers of material with an emissivity of 0.4 (e.g. shiny metal) give about 500 degrees margin for the furnace. Even for higher emissivity ($\varepsilon = 0.8$), corresponding to a dark metal surface, the temperature margin is enough to cover part of the required temperature interval 1073-1323 K. In reality the heat shield was made of stainless steel sheet 0.1 mm thick, which after several thermal cycles has changed from shiny metal to various black to grey tints (Appendix H). For convenience of servicing, access of power lines and diagnostics the shield included three parts: the base, the side wall and the lid, with several input ports. This resulted in additional channels of heat loss and

lowered the furnace temperature below 1073 K. In order to maintain the temperature in the required range it has become necessary to make the outward heat shield, marked (12) in Fig. 2.1. Then, the furnace, heated up to 990 °C, maintained temperature of the deposition substrate at 800 °C.

2.4 Vacuum RF power line.

In order to realise high temperature and high pressure features of the experimental device the vacuum part of the RF power line had to satisfy the following requirements. The top end of the line had to withstand temperature up to 1000°C. The insulation and grounded sheath of the line had to allow operation up to 10 torr without electrical breakdown. The line had to be of the staggered shape, marked (15) in Fig. 2.1, because of the off centre position of the vacuum leadthrough. The natural choice of the line concept was a coaxial cable. Two designs were tried out to implement this concept.

The first one has been developed on the base of the quartz tube of internal and external diameters 4.2 and 8.2 mm. The staggered shaping of the tube was done by softening the quartz on butadiene-oxygen torch. The ground casing and the core RF wire were made of copper braids. The hot part of the casing was made of stainless tube. Quartz proved to be an excellent insulating material for RF potential. But the design, utilising a single piece tube, had serious disadvantages. Difficulties of threading of the core wire through the tube knees have constrained it's diameter to 2 mm. This resulted in the position of the core wire inside the tube, changing during thermal cycles of the device. So, it was impossible to make precise measurements of the line impedance. The small inside diameter of the tube has led to complications in fixing the core wire to end connectors.

Overload of the hot part of the line resulted in cracking around the knee, necessitating the making the whole new tube. In order to avoid these systematic problems the second design, depicted in Fig 2.4, was developed. The second design was based on insulation made of ceramic alumina spacers with spherical convex and concave ends,

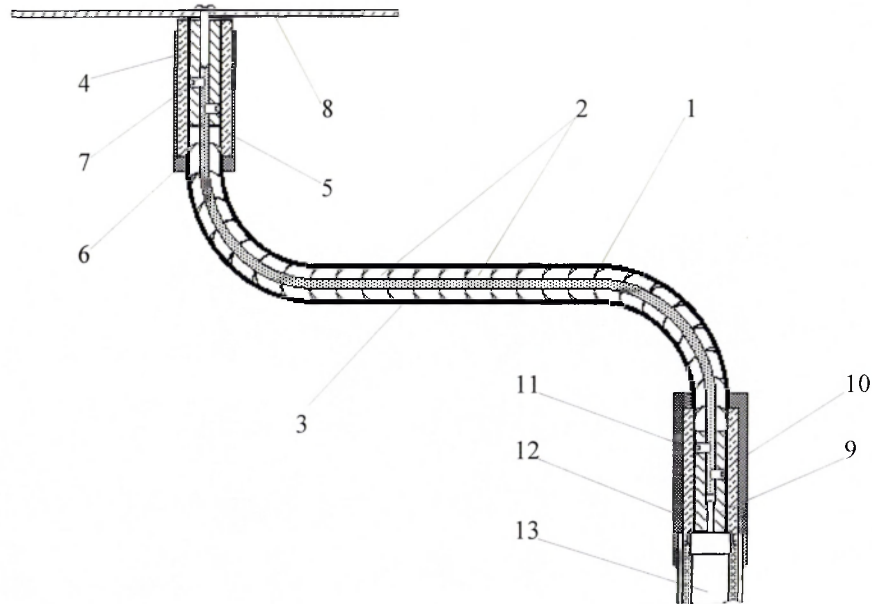

Fig. 2.4 Schematic diagram of the vacuum RF power line

1 -	RF core wire	8 -	Powered electrode
2 -	Alumina insulating spacers	9 -	Stainless steel connector
3 -	Copper tube casing	10 -	Socket set screw
4 -	Stainless steel connector	11 -	Quarts insulating tube
5 -	Quarts insulating tube	12 -	Brass casing
6 -	Stainless steel casing	13 -	Electrical feedthrough based on 6 mm diameter copper rod
8 -	Socket set screw		

which allowed the line to be curved in knees. Ceramic insulators were strung closely on a 2.9 mm diameter copper braid, functioning as the RF core wire. A solid copper tube was used as the grounding casing around ceramic insulators with the gap just 0.2-0.3 mm. Stainless steel end connectors were fastened to the RF wire by socket set screws and electrically insulated by short quartz tubes, which might be easily replaced. The whole line had very small gaps between the grounded sheath and insulators, that provided its reliable operation up to a pressure 6 torr.

2.5 Experimental set up

The vacuum vessel (Fig. 2.1) was connected to a number of systems, forming the assembly of the experimental set up, shown in the Fig. 2.5. The vacuum pumping line is

based on a "Leybold" TRIVAC B mechanical pump and a "Leybold-Heraeus" TURBOVAC 220 turbo pump with the pumping speed 220 l/s. The vacuum line has the main pass with a butterfly valve and a by-pass with a tap valve. The pressure inside the vacuum chamber is measured: in the range 10^{-3}-10^{-7} torr by the "Edwards" CP25-K penning gauge and in the range 10^{-3}-10 torr by a "Chell" MKS 122a baratron. The gas supply line utilises three "Chell" MKS 258 mass flow controllers with ranges up to: 10 sccm for CH_4, 50 sccm for H_2 and 100 sccm for Ar. RF current is produced by an ACG-5 RF (13.56 MHz) generator, which is connected through an MW-5 matching unit and a specially designed high current RF vacuum feedthrough to the vacuum chamber.

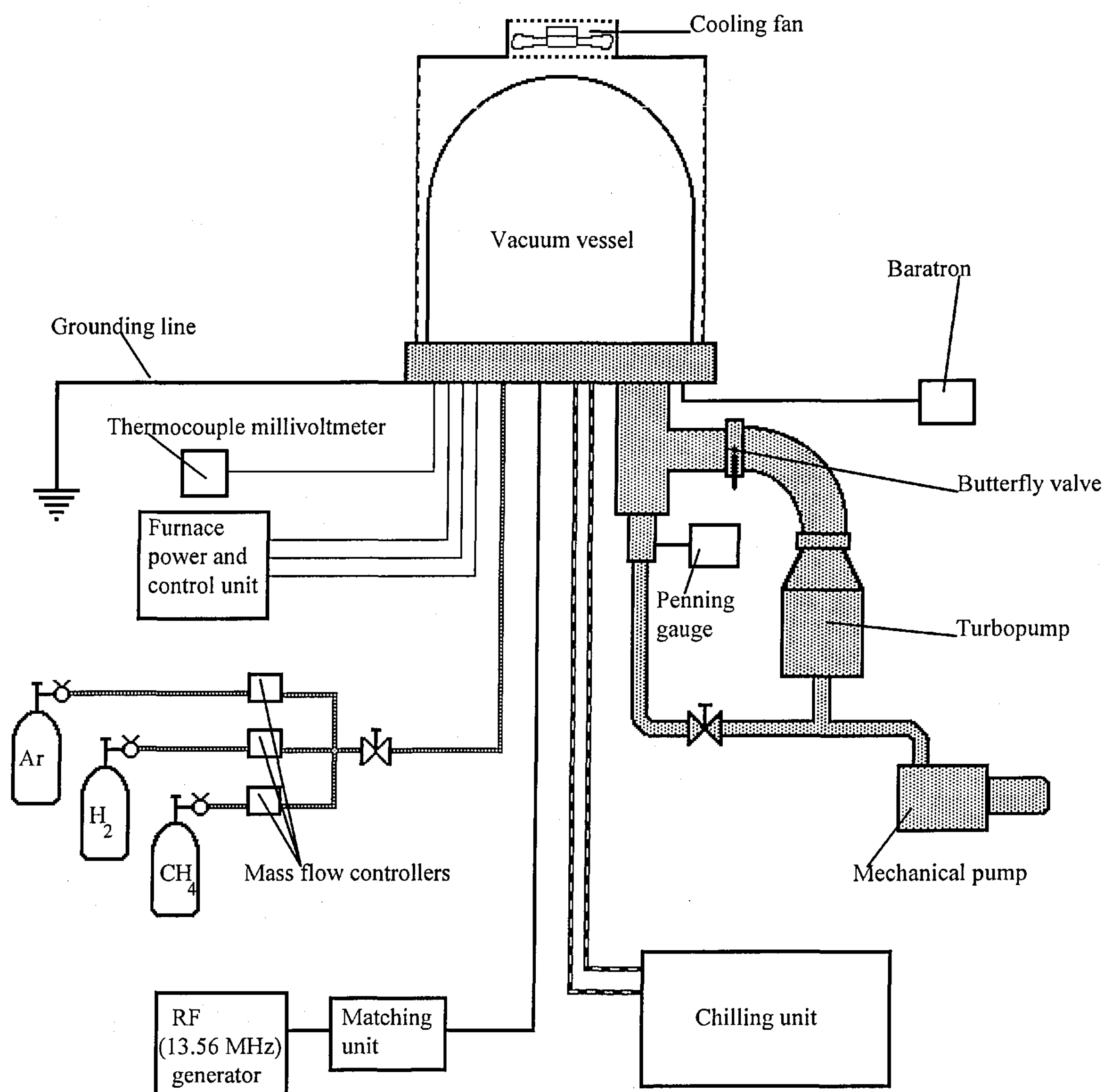

Fig.2.5 Schematic diagram of the experimental set up

The furnace power supply is based on a standard 10 A variac and a WEST 2072 process controller, which allows a preset temperature up to 1300 ± 0.1 °C. Temperature of the furnace, rather than of the deposition substrate, was controlled directly in order to safeguard the heating element from overheating beyond its top limit of 1000 °C. The water cooling of the device is provided by the laboratory cooling system, based on a chiller unit with a cooling capacity 6.7 kW at 15°C water temperature. A special grounding line was made for the device, ending with 1 m steel rod inserted in ground outside the building. During runs with high temperature of the deposition substrate the top part of the vacuum glass bell-jar was air cooled.

2.6 Electrostatic probe and mass and energy analysis diagnostic systems.

Two diagnostics have been utilised for RF discharge plasmas characterisation. The first one is a passive electrostatic (Langmuir) probe, connected to the "AEA Technology" PlasmaProbe acquisition system. The second one is the "Hiden Analytical" energy and mass analysis system. The arrangement of both diagnostics in the vacuum chamber is depicted in Fig. 2.6.

The electrostatic probe design is based on the passive probe approach, described by Annaratone and Braithwaite [49]. The ring reference electrode (6), connected to the probe tip through a 6.6 nF capacitor (8), provides excitation of the tip potential so that it exactly follows the RF fluctuations of the plasma potential. In this way the tip (5) draws only conduction current and no displacement current. The LC filter, formed by the 50 μH chain of inductors (9) and 4.7 nF capacitor (12), has a resonance at ≈ 0.3 MHz. It effectively impedes RF currents and passes only DC or slowly varying signals. As a result the probe characteristic can be interpreted as for DC plasmas without distortions from RF currents. The PlasmaProbe diagnostic system performs automated measurement of current to the probe tip and processing of acquired data. For signal processing the system uses an algorithm based on standard Langmuir probe theories [50]. It provides graphical and

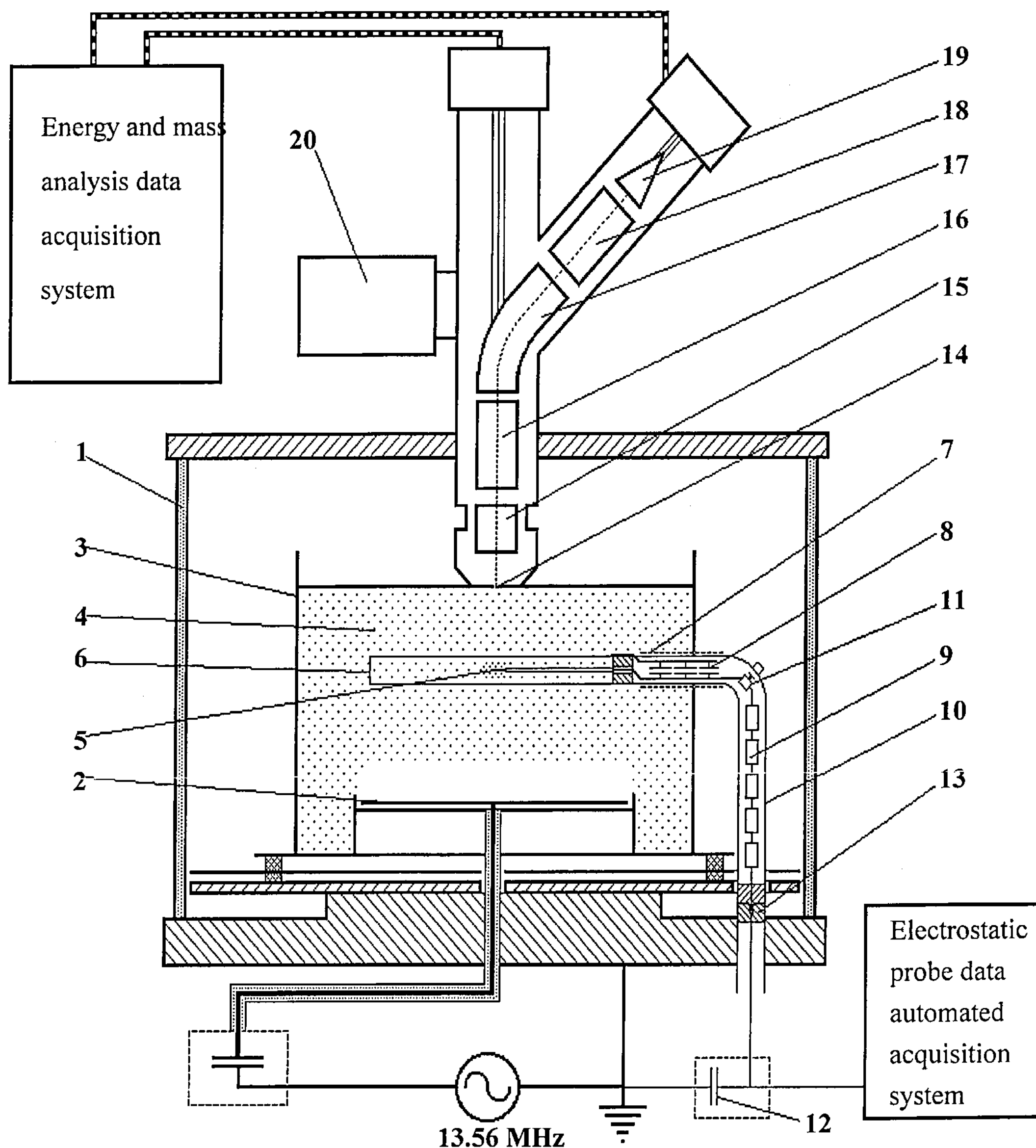

Fig. 2.6 Arrangement of plasma diagnostic systems in the vacuum chamber

(The scale of the diagram is arbitrary)

1 -	Vacuum chamber	11 -	Screwed connector
2 -	Powered electrode	12 -	4.7 nF capacitor
3 -	Grounded (top hat) electrode	13 -	Vacuum seal
4 -	Gas discharge plasma	14 -	50 μm sampling orifice
5 -	Cylindrical probe tip	15 -	Ion source
6 -	Ring reference electrode (side view)	16 -	Ion transfer optics
7 -	RF guard	17 -	Electrostatic deflector energy filter
8 -	Three 2.2 nF capacitors	18 -	Quadrupole mass filter
9 -	Five 10 μH inductors	19 -	Detector
10 -	Glass tube	20 -	Turbo pump

numerical information about the probe current and the main plasma parameters: plasma potential U_p, electron temperature T_e and electron number density n_e (see Appendix A).

The energy and mass analysis diagnostic includes an extraction orifice for sampling ions and neutrals from the discharge volume and electronic blocks for powering the spectrometer and processing acquired signals. The sampling orifice is positioned in the plane of the earthed electrode. Ions from plasmas, accelerated by the potential drop of the sheath, enter the probe through 50 μm aperture, (14) in Fig. 2.6. Inside the probe before reaching a detector (19) ions pass in series through an electrostatic energy filter (17) and a quadrupole mass filter (18). By arranging the status of these filters it is possible to scan particles of specific mass through their energy spectrum or to detect various masses of a given energy (Appendix B). For analysis of neutrals the system has a special ion source (15) behind the sampling orifice, where neutral particles are ionised by electron impact. The two major types of data, produced by the system, are mass spectra of neutrals and energy spectra of ions.

2.7 Hydrogen and argon plasma characterisation.

Before trying various methods of RF plasma modification it was decided to characterise a basic asymmetrical RF discharge. Hydrogen was chosen as the main working gas because of its fundamental importance for diamond film deposition. Argon discharges were also characterised for adjusting diagnostics, being best studied medium of low-temperature plasma.

In order to use simultaneously the electrostatic probe and energy and the mass analysis probe the heat-shield grounded electrode assembly was replaced by a "top hat" grounded electrode (Fig 2.6), made of stainless steel. The "top hat" electrode is identical in size to the inner heat shield: diameter of the side wall - 150 mm, distance from the powered electrode to the top lid - 57 mm. At the centre of the top lid there is a sampling orifice of the energy and mass analysis probe.

The electrostatic probe is inserted through a special port in the side wall with its tip 38 mm above the powered electrode. The probe tip of the length 7.5 mm is made of a 0.25 mm diameter tantalum wire. The Debye length has been calculated subsequently to be 0.2-0.3 mm. So the probe perturbs plasma very little. Measurements of electron temperature, electron density and space potential as function of pressure are shown in figures 2.7 for hydrogen and 2.9 for argon. The pressure range was 30-135 mtorr for hydrogen and 20-105 mtorr for argon at the power 20 and 30 W.

The same figures contain data of DC bias potential of the powered electrode as function of pressure. These measurements were made by a high impedance voltmeter, connected to the pre-filtered and pre-scaled DC bias output of the matching unit.

Data of the energy and mass analysis probe of ion energy distribution function (IEDF) and neutral composition of RF plasma are presented in figures 2.8, 2.10 and 2.11. These experimental results will be discussed in the next section.

In hydrogen discharges a rapid degradation of the electrostatic probe signal was observed below 0.030 torr. This was evident from a strongly distorted second derivative of the signal. The automatic software algorithm, processing probe data, does not recognise any deviations from a perfect probe signal. Consequently, the software could choose for calculation a corrupted part of the probe characteristic. Typically, this led to a spreading of values of the main plasma parameters during repetitive measurements. A method of bypassing this problem, using manual data processing, will be discussed in the next chapter (section 3.5).

Such behaviour of a passive electrostatic probe in RF plasmas is usually caused by a poor compensation of RF potential at the probe tip, which results in passing of RF currents through the probe sheath. Most likely, this problem is a result of higher frequency harmonics, which are generated in plasma at some regimes. In order to tackle this difficulty a reference ring, three times larger in collecting area, has been tested.

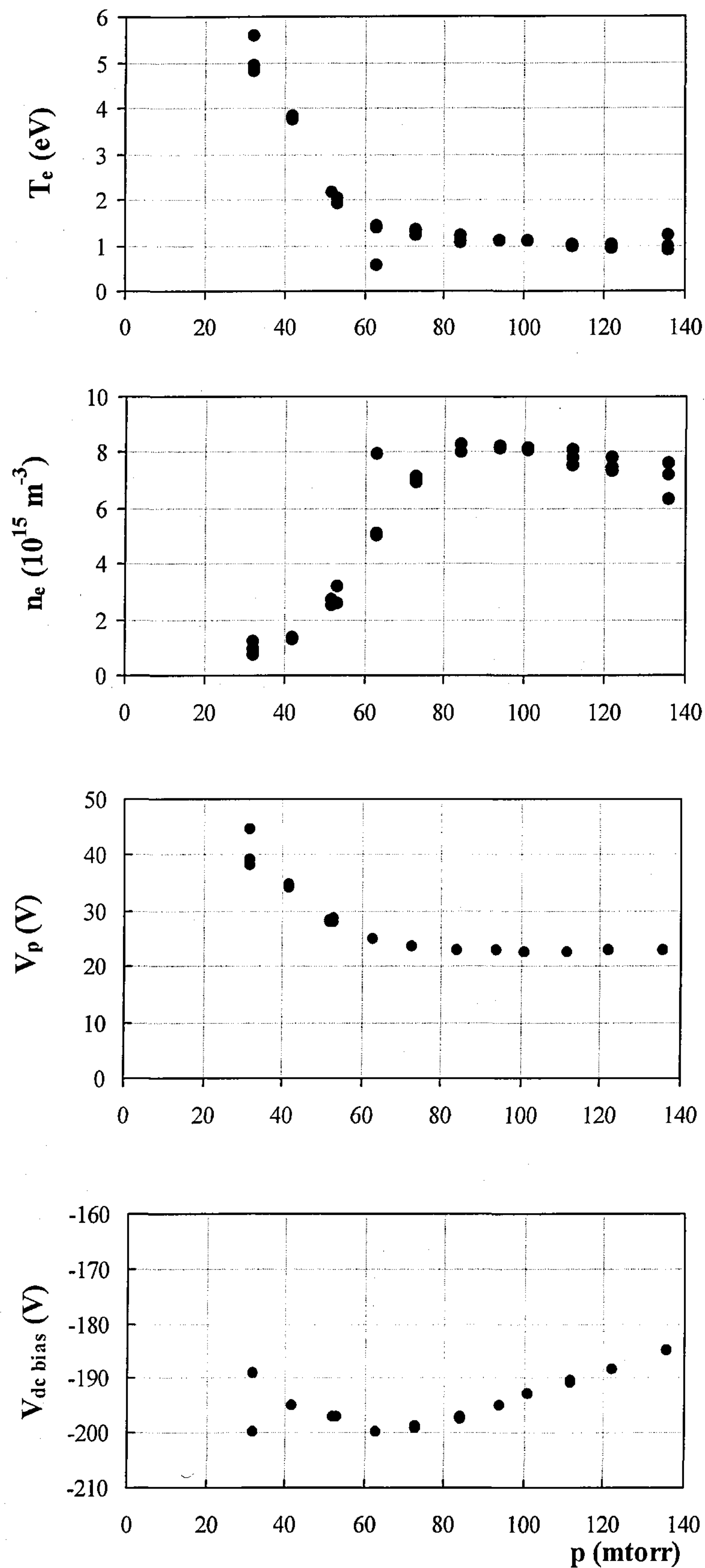

Fig. 2.7 Probe measurements of plasma parameters in hydrogen discharge with pressure variation. Power – 23 W, gas flow – 30 sccm.

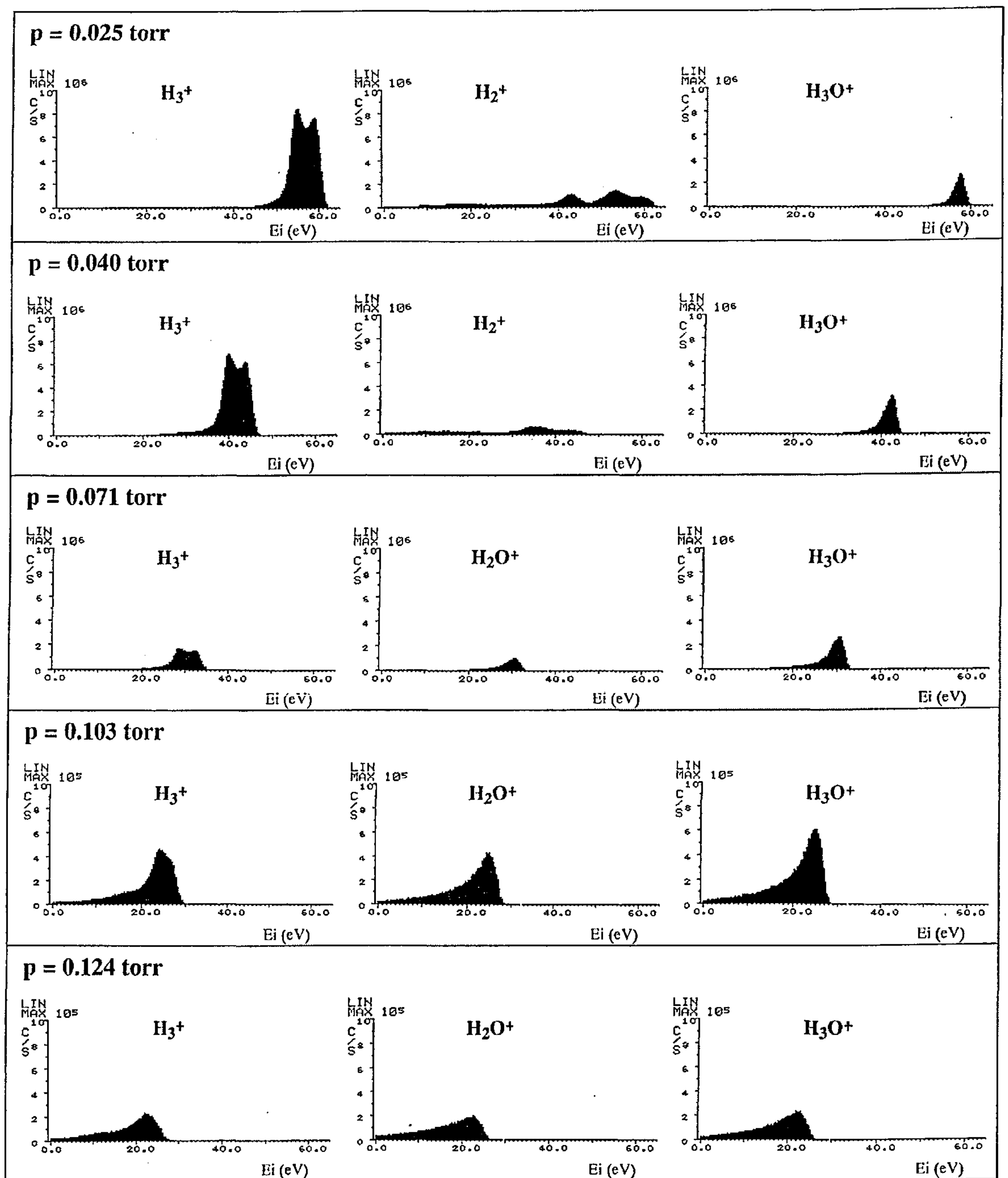

Fig. 2.8 Variation of ion composition and IEDF in hydrogen discharge with increasing pressure (power-30 W). Measurements are taken by the mass and energy analysis probe. Note the different vertical scale.

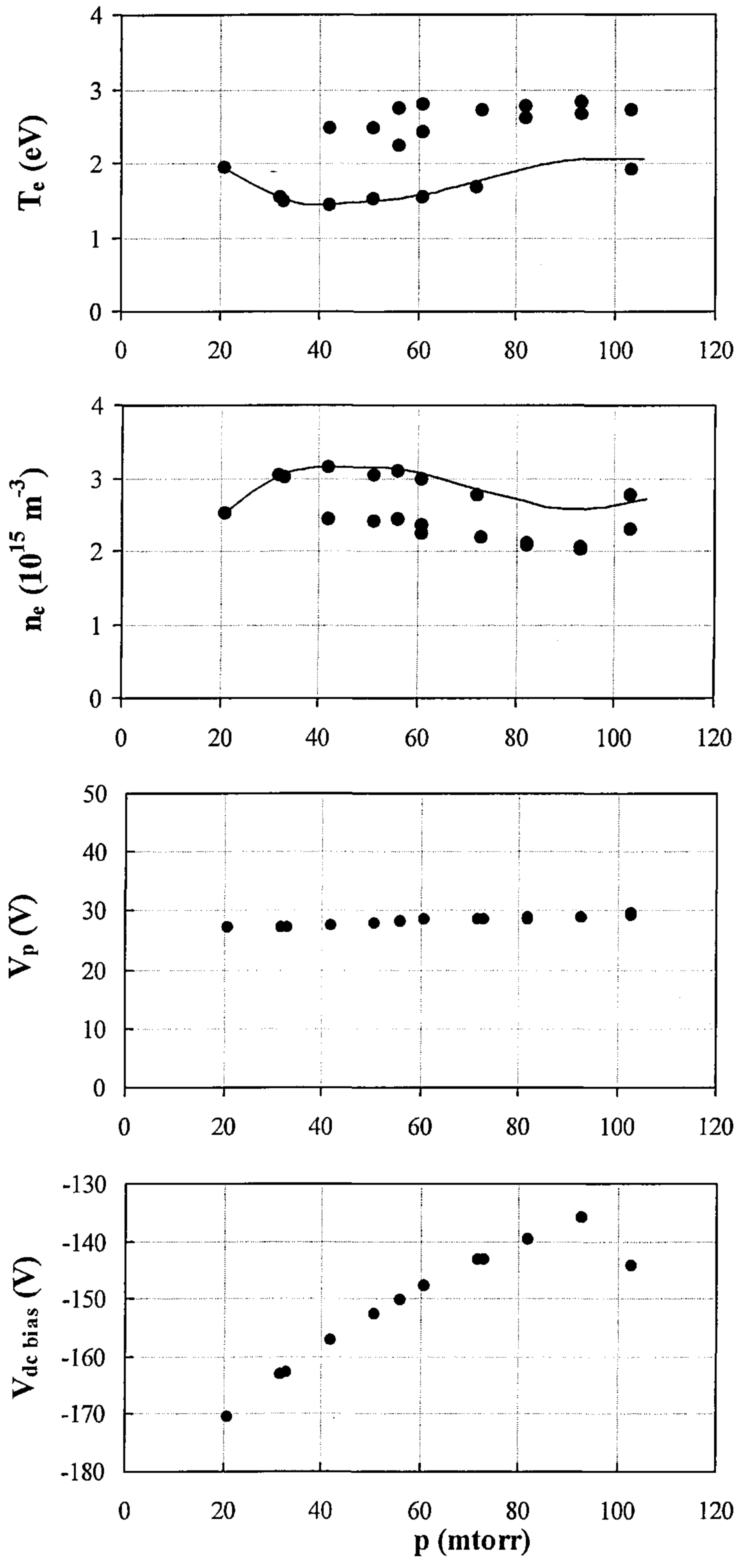

Fig. 2.9 Probe measurements of plasma parameters in argon discharge with pressure variation (power – 20 W, gas flow – 30sccm).

Solid lines on the T_e and n_e graphs distinguish the real data from the one, distorted by RF signal. Typically, RF contamination of the probe signal raises electron temperature values and understates density values. In more details, this problem is described in the section 3.5, chapter III.

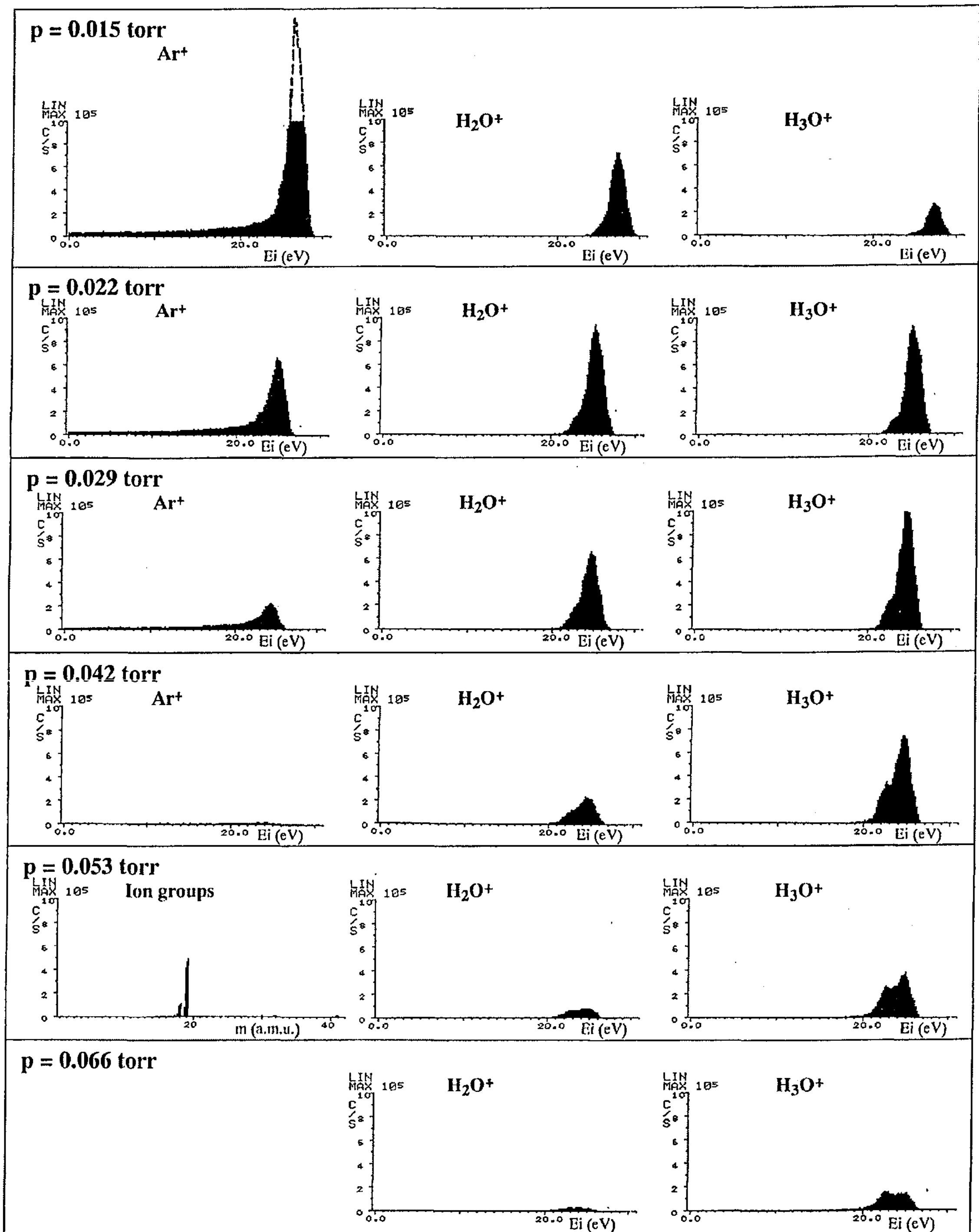

Fig. 2.10 Variation of ion composition and IEDF in argon discharge (power-30 W) with increasing pressure. The chamber has been pre-pumped for 30 h.

Measurements are taken by the mass and energy analysis probe.

Broken line of the Ar^+ IEDF at 0.015 torr depicts the part, which exceeds the chosen vertical scale of the capture screen. The $2 \cdot 10^6$ c/s maximum have been measured separately at the screen with vertical scale 10^6 c/s.

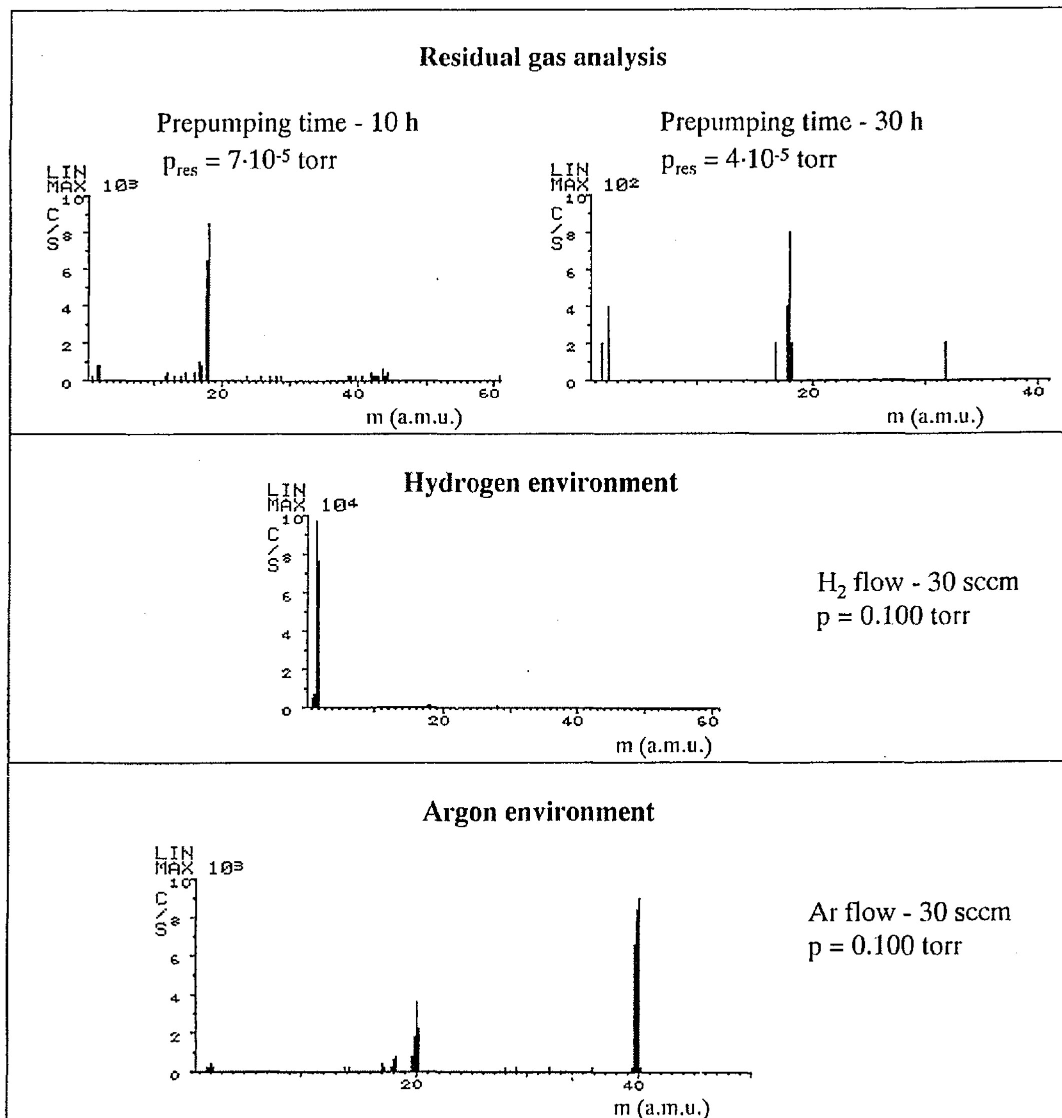

Fig. 2.11 Mass analysis data for the experimental chamber from the energy and mass analysis probe.

It is possible to estimate content of water vapour from the mass spectra of argon environment. Assuming equal sensitivity of the mass analyser to water (17 and 18 a.m.u. peaks) and to argon (20 and 40 a.m.u. peaks), the water vapour density is estimated to be 9%.

The large reference ring did extend probe measurements of acceptable quality down to the pressure 27-28 mtorr in hydrogen. But subsequently the original reference ring was used for the bulk of the experiments reported here, because its smaller vertical size facilitated electron injection.

Typically, with gas flow being at a preset level pressure increase was achieved by throttling the pump line using the butterfly valve (Fig. 2.5). When the gas pressure rises in argon discharges, electron temperature first demonstrates a tendency for a steady decrease (Fig.2.9). But starting from 42 mtorr the values of the electron temperature become scattered. Again, it could be associated with the poor compensation of the probe against higher frequency harmonics. The fact, that they appear with pressure rise, could be linked with a complete substitution of argon ions by water (or hydronium) ions (Fig. 2.10) by 42 mtorr. Most likely, substitution of the major positive charge carrier has changed plasma impedance, generating higher harmonics. The residual water vapour in the chamber (Fig. 2.11) originates from several layers of the heat shield above the base plate ((Fig. 2.1, (4) and (11)), which can not be easily removed. It is impossible to outgas water by heating the chamber because of the inductances, that form probe filter circuit and positioned inside the vacuum vessel. Therefore, the remaining solution is a longer pumping period before starting discharge (Fig.2.11). It gives some effect by delaying the ion substitution in argon discharge up to 50 mtorr.

2.8 Discussion

2.8.1 Variation of plasma parameters with pressure

Basic tendencies of variation of plasma parameters with pressure change agree with commonly known discharge plasma properties. Most data from the probe showed the electron energy distribution to be not to far from Maxwellian, and therefore an electron temperature can be defined.

Plasma potential is determined by balance of electron and ion fluxes to the

grounded electrode surface. At low pressures, where plasma is less dense, energetic electrons can easier escape from quasineutral plasma through the sheath potential barrier. In this way the positive potential of the sheath or plasma potential is created. With increasing pressure such electron escape is impeded by the decline of their temperature. So, plasma potential declines. "Argon" discharges, where hydronium (water) ions completely dominate above 40 mtorr (Fig 2.10), has the opposite tendency (Fig. 2.9). Their increase apparently causes a growth of plasma potential by 3 V at 105 mtorr.

A simple model using a particle balance can be applied to calculate electron temperature for comparison with experimental results. Assuming ions production only by a direct electron-molecule impact and equalising ionisation rates in the plasma volume and losses of charged particles to the surfaces leads to the following formula (Appendix C):

$$T_e \cdot \ln\left(1.651 \cdot 10^{23} \cdot \left(1 + \frac{2 \cdot T_e}{V_i}\right) \cdot T_g^{-1} \cdot M_i^{\frac{1}{2}} \cdot \sigma_{max} \cdot p \cdot d_{eff}\right) - V_i = 0 \qquad (2.3)$$

where T_e - electron temperature (eV), V_i - ionisation potential (V), T_g - gas temperature (K), p - gas pressure (mtorr), σ_{max} - maximum value of ionisation cross-section (m^2), M_i – ion mass (a.m.u.), d_{eff} - effective size of plasma (m). The last parameter is determined as $d_{eff} = \mathcal{V}_{pl}/S_{loss}$ where $\mathcal{V}_{pl}$ - plasma volume (m^3), S_{loss} - total area of charged particles losses (m^2). We assume T_g = 330 K, $\mathcal{V}_{pl} = 1.35\times10^{-3}$ m^3, $S_{loss} = 8.64\times10^{-2}$ m^2. Initially, T_e is calculated, considering H_2^+ ions only: $M_i = 2$, $\sigma_{max} = 1.01\cdot10^{-20}$ m^2, $V_i = 15.4$ eV.

As it can be seen in Fig.2.12 theoretical values (curve (b)) exceed experimental values (curve (a)) 1.7-5 times. Assumption of $M_i = 3$, corresponding to the most numerous hydrogen ion H_3^+, lowers theoretical values just by a few percents (curve (c)). Calculation of the formula (2.3) for water ions ($M_i = 18$, $\sigma_{max} = 4\cdot10^{-20}$ m^2, $V_i = 12.67$ V) produces curve (d), which still exceeds experimental data almost 3 times above 70 mtorr. Finally, curve (e), which coincides with experimental values above 70 mtorr, is obtained for water ion with assumption of hypothetical $V_i = 6.5$ V.

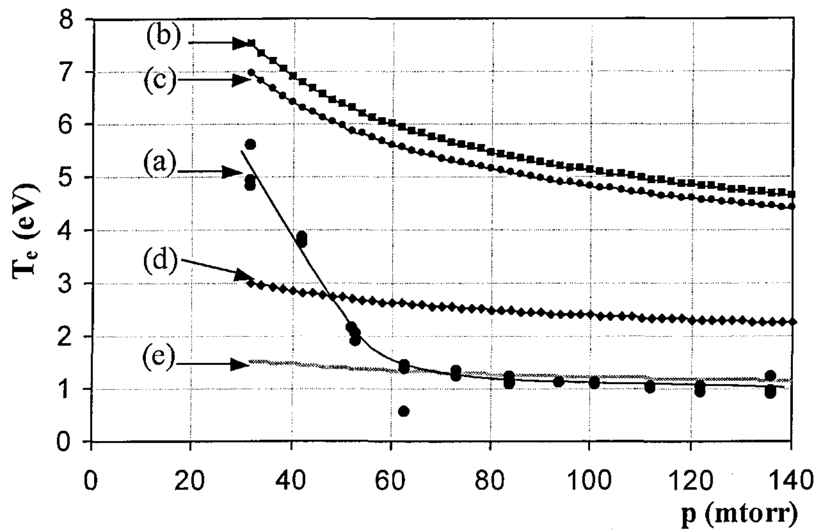

Fig. 2.12 Electron temperature T_e as a function of pressure p in hydrogen discharge.

(a)–experimental data from Fig.2.7, otherwise – theoretical curves with:

	(b)	(c)	(d)	(e)
V_i (V)	15.4	15.4	12.67	6.5
M_i (a.m.u.)	2	3	18	18

The model has not produced theoretical curve, which has a similar point of bending as the experimental one. It could be ascribed to the fact, that ion composition of the discharge changes with pressure (Fig. 2.8). On the contrary, the model doesn't account for presence of several different ions in plasma, no for the shift of their pressure dependent balance. In addition, stochastic heating of electrons, hence non-maxwellian EEDF, and non-uniformity of plasma density are significant at lower pressures. Coincidence of part of theoretical data (curve (e)) with experiment occurs at the ionisation threshold, which is much lower than the typical values for hydrogen and water. It points out at more complex ionisation mechanisms: step ionisation, requiring lower threshold values compared to electron ionisation of non-excited neutrals, or ionisation through neutral-ion collisions.

For the probe measurements in "argon" discharge it is possible to separate the real data for temperature and density. They are marked by solid lines on the Fig. 2.9. Starting from 40 mtorr, electron temperature rises, contradicting the formula (2.3). The possible explanation is a complete substitution of argon ions by water ionised species by 42 mtorr (Fir. 2.10). It leads to generation of higher harmonics, reflected in spreading of the probe data (Fig. 2.9). It will be demonstrated in chapter IV, that presence of higher RF harmonics benefit an effective electron heating by the sheath.

The strong decline with pressure of the energy and mass analysis probe signals in hydrogen and argon discharges (Fig. 2.8 and 2.10) seems contradictory to the formula, describing ionic flux to the substrate:

$$\Gamma_i = n_e \cdot \sqrt{\frac{e \cdot T_e}{m_i}}. \qquad (2.4)$$

where n_e - electron density, e - electron charge, T_e - electron temperature, m_i - ion mass. By using values of relative change of electron temperature and density in the range 30-100 mtorr in hydrogen (Fig. 2.7) it is estimated, that ion flux to the grounded electrode should increase 3.5 times. At the same pressure interval IEDF signal declines nearly by order of magnitude (Fig. 2.8). This phenomenon could be associated with the following two effects. First, the 50 μm sampling orifice of the probe allows in only ions with very small deflections from trajectories normal to the electrode surface. At higher pressures ions are scattered in collisions while passing through the sheath. Many of them are lost on the surfaces of the sampling orifice. Second, there could be redistribution of plasma density with pressure growth; density at the sheath boundary of the grounded electrode being a lose side.

2.8.2 Brief overview of impact reactions, forming hydrogen species

The plasma chemistry of hydrogen discharge is extremely complex. It is beyond the scope of this work to analyse it in detail. At the same time some general information is necessary in order to explain results of the energy and mass analysis probe. A number of collisional reactions [52], describing production of various hydrogen species, are presented in table 2.1. Complete graphs of collisional cross-sections and reaction rates of some reactions are presented in Appendix D.

As it could be seen from table 2.1, the probability of direct dissociation and dissociative ionisation of hydrogen (reactions (2.7) and (2.8)) in RF discharge is quite low, because of small cross-section values and high threshold energy (or ionisation potential)

for impacting electrons. The H_3^+ ion originates from the reaction (2.12). Its domination among hydrogen ions is based on highest cross-section value of the reaction and,

Reaction	E_{th} (eV)	σ_{max} (cm^2)	$<\sigma v>$ (cm^3s^{-1})	
$e + H(1s) \rightarrow e + H^+ + e$	13.6	$7 \cdot 10^{-17}$	$4 \cdot 10^{-10}$ (4)	(2.5)
$e + H^*(2s) \rightarrow e + H^+ + e$	3.4	$8 \cdot 10^{-16}$	$1.8 \cdot 10^{-7}$ (50)	(2.6)
$e + H_2 \rightarrow e + H_2^* \rightarrow e + H + H$	8.5	$3 \cdot 10^{-17}$	$4 \cdot 10^{-9}$ (17)	(2.7)
$e + H_2 \rightarrow e + H^+ + H + e$	~50	$7 \cdot 10^{-18}$	-	(2.8)
$e + H_2 \rightarrow (H_2^-)^* \rightarrow H^- + H$	0.1	$1 \cdot 10^{-15}$	$1 \cdot 10^{-8}$ (2)	(2.9)
$e + H_2 \rightarrow e + H_2^+ + e$	15.4	$1.01 \cdot 10^{-16}$	$7 \cdot 10^{-10}$ (4)	(2.10)
$H_2^+ + H_2 \rightarrow H_2 + H_2^+$	-	$2 \cdot 10^{-15}$ **	-	(2.11)
$H_2^+ + H_2 \rightarrow H_3^+ + H$	0	$4 \cdot 10^{-15}$ **	-	(2.12)
$e + H_3^+ \rightarrow e + H^+ + H + H$	14	$7.2 \cdot 10^{-16}$	$1 \cdot 10^{-9}$ (3)	(2.13)
$e + H_3^+ \rightarrow H + H + H$	-	$1 \cdot 10^{-14}$ **	$2 \cdot 10^{-7}$ (0.1)	(2.14)

Table 2.1 Impact reactions, producing various hydrogen species,
where σ_{max} - maximum value of cross-section, $<\sigma v>$ - reaction rate coefficient with energy of striking particle in brackets. Values, marked **, are for incident ion energy 0.1 eV

practically, no threshold barrier. But this reaction requires the H_2^+ ion, which originates from the reaction (2.10). Therefore (2.10) reaction stands at the beginning of reaction chains, producing hydrogen species on the discharge.

Production of atomic hydrogen could proceed through several reactions: (2.7), (2.8), (2.9), (2.12) and (2.14). Again, ion-atom reaction (2.14) has the highest cross-section. At the same time, cross-section of the electron impact reaction (2.9) is just four times lower, and involves low energy electrons. It is necessary to point out, that most of the electron reactions have maximum cross-section values between 50 and 100 eV electron energy (Appendix C). On the contrary, reaction (2.9) has its cross-section maximum just at

0.4 eV. Consequently, there should be negative ions in RF hydrogen discharge.

H^+ ions are produced by the reactions (2.5) and (2.6). Reaction (2.6) has higher cross-section and reaction rate together with a lower threshold due to excited state of the hydrogen atom. It is the most likely route in RF hydrogen discharge, having low electron temperature.

Summarising available information, it is possible to conclude, that domination of H_3^+ ions among hydrogen species arises from practically a zero energy threshold of the reaction (2.12). Majority of H_2^+ species are converted in H_3^+ even at weakest collisions with hydrogen molecules. Preference of ionisation route for hydrogen molecule (2.10) over the dissociation one (2.7) is attributed to the higher value of ionisation cross-section.

2.8.3 Formation of water ions in plasma discharge

The residual concentration of water vapour is quite low. At 0.1 torr of total pressure in the chamber it is less than or about 1% in hydrogen and in argon. Despite this ratio in the measurements, presented here, hydronium ions, mainly H_3O^+ and H_2O^+, form two thirds of all the ions in hydrogen discharges and a dominant part, around 99%, in argon discharges at the same pressure (Fig.2.11). A significant amount of hydronium ions in hydrogen RF discharges with increasing pressure was confirmed in [53]. The presence of hydronium ions in hydrogen and hydrogen-argon DC discharges was registered at the pressure 0.105 torr in [54]. Only little has been published about plasma chemistry, involving water molecules.

During the course of this work information about the cross-section of water ionisation by electron impact wasn't found. Water and carbon dioxide molecules are close in their effective size (Table 2.2) and are both strongly polarisable. Consequently the ionisation cross-section of water is probably similar to that of carbon dioxide. In this case a maximum value of the water ionisation cross-section exceeds that of argon by no more than 10%. At the same time the ionisation potential of water molecule is $\approx$3 V less than

potentials of argon and hydrogen (Table 2.2). These differences can not explain the domination of hydronium ions in both argon and hydrogen discharges, if their production is only by electron impact ionisation. But they permit effective hydronium ions production in reactions, originating from collisions of ions, atoms and molecules. It is possible to suggest reactions, based on the Penning effect, chemical bond rearrangement and charge transfer mechanisms.

Gas	Ionisation potential V_i (V)*	Effective molecular diameter d (10^{-8}cm) **	Maximum of ionisation cross-section σ_i (10^{-16}cm^2) ***
H_2	15.4	2.75	0.97
Ar	15.8	3.67	3.21
H_2O	12.67***	4.68	-
CO_2	13.8	4.65	3.53

Table 2.2 Ionisation potentials, effective diameters and ionisation cross-sections of selected molecules. (Data are taken from: *- [55], **- [56], ***- [57])

Penning ionisation reactions (2.17) and (2.19) (Table 2.3) are possible, because both hydrogen molecule and argon atom have metastable states with an excitation threshold of the order or exceeding ionisation potential of water molecule 12.67 eV. For hydrogen molecule it is $C^1\Pi_U$ state with 12.6 eV threshold, for argon - $3p^5$ states with thresholds in the range 12.76-12.89 eV. There is no information about rates and cross sections of these reactions. In [58] the cross section of the reaction (2.21) was measured, in which excited argon atom ($3p_{2.0}$ state) with 11.24 eV threshold passes excitation to water molecule with subsequent dissociation of the last. It is likely, that the reaction (2.19) has the similar value of cross section. Then the order of the reaction rate for (2.19) can be estimated by multiplying the cross section and relative velocity of colliding particles.

Chemical bond rearrangement reactions (2.16) and (2.20) can be sources of H_3O^+ ions. Thermal collisions of charged and neutral particles are dominated by the polarisation force. So, the maximum rate constants of the reactions are of the Langevin value [59]:

$$K_L = 8.99 \times 10^{-10} \times (\alpha_R / m_R)^{1/2} \quad , \text{cm}^3\text{s}^{-1} \qquad (2.15)$$

where α_R - relative polarisability (for water molecule α_R=9.8); m_R - reduced mass in atomic mass units, derived as $m_R = m_1 \cdot m_2 / (m_1 + m_2)$ from masses of colliding particles.

Reaction	**Rate constant** $\mathbf{cm^3s^{-1}}$	**Cross section** $\mathbf{cm^2}$	
Hydrogen discharge:			
$H_3^+ + H_2O \rightarrow H_2 + H_3O^+$	1.753×10^{-9}		(2.16)
$H_2^* + H_2O \rightarrow H_2 + H_2O^+ + e$			(2.17)
Argon discharge:			
$Ar^+ + H_2O \rightarrow Ar + H_2O^+$	$\sim 8 \times 10^{-10}$		(2.18)
$Ar^* + H_2O \rightarrow Ar + H_2O^+ + e$	8.12×10^{-10}	$\sim 10^{-14}$	(2.19)
$H_2O^+ + H_2O \rightarrow HO + H_3O^+$	9.37×10^{-10}		(2.20)
$Ar^* + H_2O \rightarrow Ar + H_2O^*$		$8\text{-}11 \times 10^{-15}$	(2.21)

Table 2.3 Hydronium ions production reactions

High probability of the reaction (2.18) originates from its exothermic character: the ionisation potential of argon exceeding the one of water ΔE=3.13 eV. Water molecules are greatly outnumbered by argon atoms with high internal energy. As a consequence almost all the water molecules are ionised. It is reflected in measurements by the energy and mass analysis probe (Fig. 2.10), which show water ions to be the second largest group after argon ions. This process can not be attributed to the class of resonant charge transfer reactions, that requires $\Delta E \approx 0$. So, the order of the reaction (2.18) rate constant has been estimated from the formula (2.15).

Summing up, it is possible to conclude that hydronium ions in hydrogen and argon discharges are produced mainly in collisions between heavy particles. Rate constants of these reactions are one-two orders higher than for ionisation by electron impact. This

determines preferable ionisation of the minor fraction of water molecules in mixtures with hydrogen and argon.

2.9 Conclusion

Residual water vapour is generally difficult to pump away. In the vacuum vessel (Fig. 2.1), designed for heated deposition experiments, multiple layers of the bottom heat shield, remaining in the chamber during plasma characterisation experiments, present a large area for water absorbtion. The pumpdown time has been observed to be considerably less, when the bottom heat shield assembly and the protective copper disk (Fig. 2.1, (11) and (4)) are removed from the chamber. In addition, deposition experiments resulted in growth of carbon films on various parts of the device. It is extremely difficult to clean away completely these deposits, especially from the heat shield. The porous structure of such films can be an ideal site for water attachment.

It can be concluded that the present configuration of the vacuum vessel has a feature of slow outgasing of residual vapour due to the multipurpose nature of the device. Residual water molecules play an active role in discharge plasma chemistry and can strongly influence plasma parameters. Nevertheless, it is possible to select regimes of discharge, where their effect will be minimal. In argon discharges it is below 25 mtorr and in hydrogen - below 50 mtorr. In hydrogen discharges the passive electrostatic probe implies lower boundary for measurements 30 mtorr. These pressure ranges are quite sufficient for conducting experiments on characterisation of plasma with injection-removal of electrons. In deposition experiments it is quite difficult to conduct monitoring of gas and plasma composition due to high temperature regimes 800-900°C. The energy and mass analysis probe can operate no higher than 400°C. Preheating of vacuum vessel is a common procedure for a rapid outgasing of residual water vapour; so, at this stage it is assumed that the problem with water impurities at high temperatures is somewhat lessened.

Chapter III.

"RF capacitive discharge with injection and removal of electrons"

3.1 Introduction

As it has been outlined earlier (Chapter I, section 1.8) electron injection looks like an attractive way of enhancing low pressure RF discharges. It allows the introduction into the plasma volume of an electron stream of preset energy. The energy of electrons in low-pressure RF plasmas is usually within the range 1-3 eV, which appears to be the main disadvantage of the RF discharge as an environment for diamond film growth (Chapter I, section 1.7). That is why an introduction in RF plasma of an electron stream in excess of 10-20 eV could be beneficial for this purpose.

On the other hand, the variation of electron temperature T_e and density n_e, resulting from the presence of the more energetic electron stream, can have a strong effect on other discharge parameters: plasma potential U_p and DC bias potential of the powered electrode $U_{dc\ bias}$. This rigid link between plasma parameters is determined by the balance of rates of charged particle production in the plasma bulk and their losses on electrode surfaces. For example, it has already been shown in Chapter II how a single variable, like gas pressure influence all the main plasma parameters.

It is important to know the effects, which result from electron injection. Such information will define to what extent this approach can be beneficial for carbon film deposition. So, the main target of this part is the investigation of the effect of electron injection on discharge plasma parameters and plasma composition.

3.2 Brief review of previous works on electron injection in plasma.

Injection of electrons into low-temperature plasma has quite a lengthy history. At the beginning of 50s an electron beam was used by Little and von Engel for measuring the electric field of a hollow cathode discharge [60]. The electron gun, used in that experiment, utilised thermionic effect for electron production. The hot emissive filament was

positioned between two copper hemispheres. The small hemisphere had an extraction orifice, connecting the volume of the electron gun with the main discharge chamber. The large hemisphere had a potential of a few hundred volts negative with respect to the filament, which was itself biased the grounded, small hemisphere. The emitted electric beam had energy up to 12 kV, but quite low current 10^{-9}A. The low current value was necessary to minimise ionisation by the electron beam in the main discharge plasma. The vacuum volume of the gun had a separate pumping system and was at a pressure below 1 mtorr.

In the 60s the necessity to operate DC sputter-coating reactors below 10 mtorr led to the development of the thermionically supported glow discharges, described by Maissel and Glang [61]. The scheme of this discharge presents a DC diode configuration with two additional electrodes: a second anode and a thermionic cathode. The thermionic cathode was based on electron emission from a heated tungsten filament. Also oxide-coated and thoriated filaments were in tested.

In the paper by Christensen [62] various schemes of thermionically enhanced DC and RF discharges were considered. Special attention was paid to the analysis of a triode system, which was described as an RF parallel plate electrode configuration with an additional DC biased electrode. A qualitative analysis is given for variation of potentials at all three electrodes. No plasma parameters were measured.

A detailed description of thermionically supported sputter-coating apparatus was given by Tisone and Cruzan in [63], where it had the name of a low-voltage sputtering (LVS) system. The basic plasma in this device was created between the thermionic cathode and the anode. A hot emissive filament was made of a pure Ta wire. Typical voltage and current of the discharge in Ar at a pressure $8 \cdot 10^{-4}$ torr were 90 V and 6 A respectively. The 540 W of discharge power together with 680 W of power for the filament heating required a special water-cooled confinement tube within the vacuum chamber. Another pair of

electrodes, a negatively biased sputter target and a substrate table, were positioned in openings of the confinement tube. An account of this work on sputter-deposition problems characterised the discharge system in terms of current-voltage characteristics. No direct measurements of plasma parameters were made.

A system, identical to the LVS one in its basic configuration, was used by Heinman and co-workers for high rate reactive ion etching of alumina and silicon in CCl_4 [64]. The etched material (Al_2O_3 or Si) was positioned on the negatively biased electrode. The main point of this work concerned problems associated with etching.

In the beginning of 70s a discharge device configuration was developed by Limpaecher and Mackenzie, which combined electron emission from a filament and plasma confinement by a magnetic field [65]. Emissive filaments were positioned directly in the main discharge volume; and a multipole cusp magnetic field along the surface of discharge chamber provided plasma confinement. The magnetic field was created by dipole permanent magnets. One of the first devices, based on this principle, had an 86 litre discharge chamber with 1252 bar magnets, mounted on walls. 48 filaments with bias between - 40 and -120 V performed the function of cathodes. The magnet pole faces served as anodes. A plasma density as high as $8 \cdot 10^{16}$ m^{-3} was achieved in this device in Ar at 1 mtorr and the emission current of filaments 20A. This configuration became the basis for numerous broad beam sources of ions and electrons. In this case one of walls of the discharge chamber was replaced by an extraction grid. For example, Intrator and co-workers described a triple plasma device [66]. It had two counterstreaming electron sources, producing beams of 30 cm diameter with energies up to 350 eV.

The configuration with locating the emissive filament in the main discharge plasma was utilised in some deposition experiments. Thus, Dehbi-Alaoui and co-workers developed a PVD system with enhancement by the emissive filament [67]. Carbon films were deposited on the RF or DC biased substrate. The filament with bias -100 V and

heating current 5 A was located at 25 cm from the substrate. Electron emission provided additional control of the current to the substrate and supported the discharge at pressures below 10 mtorr.

Some characterisation of plasma with injected electrons was performed by Ando and co-workers [68, 69]. The purpose of these works was to study potential formation in plasmas after the completion of gas breakdown. The injection of electrons was intended to imitate the process of secondary electron production on the cathode surface. The electron beam source consisted of a heated, oxide-coated cathode and a mesh grid, separating the cathode from the main discharge volume. The cathode was at a negative potential with respect to the mesh, up to - 40 V, and could operate in DC and pulsed regimes. The pressure of argon in the chamber was $(3\text{-}5)\cdot 10^{-4}$ torr. Temporal evolution of the spatial potential in the discharge volume was measured by means of an electron-emitting probe.

A number of works have been performed with electron beams used for probing RF or DC plasma sheaths. The beam energy in such systems was of the order of several kV. For example, Sato and Lieberman used the 8 kV electron beam for probing an RF capacitive discharge in Ar at 2.3 and 20 mtorr pressure [70].

A detailed description of an energetic (up to 3 kV) electron source was given Schatz and Ruzic [71]. Its function was as a secondary source of ionisation and an additional way of process control in an RF reactive ion etching reactor. The principle of operation of this source is based on secondary electron emission from the cold cathode and subsequent acceleration of electrons in the cathode potential fall. The maximum electron current 50 mA was achieved, when the reactor operated in O_2 or CF_6. In He the current was at the level of tens μA. This effect was explained by the formation of an oxide or a fluoride insulating layer on the cathode, which enhanced secondary electron emission. Attractive side of this source is its ability to operate at pressures as high as 50 mtorr. A cold cathode electron gun for X-ray spectrometry, having the similar design, was described by Legrand

and co-workers [72].

A more powerful electron source, developed for electron beam welding, was described by Galanski and co-workers [73]. The beam was formed by extracting electrons from a hollow cathode reflected discharge. The discharge was confined inside a cylindrical anode between a hollow cathode and a planar reflected cathode. Both cathodes were positioned opposite to each other at the but-ends of the anode. The reflector cathode had a 1 mm diameter channel for electron emission. Argon gas was supplied into the hollow cathode cavity and pumped away through the emission channel, maintaining the source pressure in the range 0.01- 0.5 torr. Axial magnetic field up to 0.1 T was applied to the discharge. The source was able to produce electron beam with the current up to 0.7 A. No data on the beam energy were presented. But from the current-voltage characteristic of the discharge it is possible to conclude, that it had the maximum value around 500 eV.

Recent works have started to address the issue of plasma parameters measurements. Early results of the experiments reported later in this chapter were presented in [74]. An RF deposition plasma with an external thermionic source was characterised by means of Langmuir probe and energy and mass analyser.

The influence of thermionic emission on a plasma, created by a screened RF coil, was investigated Schwager and co-workers [75]. The electron source consisted of an industrially manufactured, heated emissive disk, which was impregnated with barium calcium aluminum scandate. The disk was electrically insulated and directly exposed to the basic discharge plasma. Experiments were conducted in a hydrogen discharge at 11 mtorr. Plasma parameters and composition were diagnosed by a Langmuir probe and an energy and mass analyser. Probe measurements were performed in two positions: 20 mm in front of the emissive disk and with 70 mm shift to the side from the first position. Plasma potential, density and electron temperature were measured at two different temperatures of the emissive disk. Experimental data demonstrated that the effect of electron emission on

discharge plasma is localised in the vicinity of the emissive disk. This can be attributed to the low energy of emitted electrons, though the authors fail to make this point themselves. The only accelerating potential which affected the thermionic electron flux was the one between plasma and floating potentials. As a result, the injected electrons were localised near the emissive disk, and no charge multiplication was involved.

A more advanced scheme of electron source with controlled energy of the electron flux, was described by Sato and co-workers [76]. This work investigated the effect of electron injection on RF capacitive discharge. Powered and grounded electrodes were 110 mm in diameter and separated by 40 mm. The electron source was positioned behind the meshed grounded electrode, which separated an auxiliary plasma in the source from the main discharge. The auxiliary discharge was created in a DC cylindrical magnetron. The energy of injected electrons was controlled by biasing (up to 40 V) the magnetron with respect to the grounded electrode. A Langmuir probe provided data on plasma density and electron temperature, an emissive probe - on plasma potential. A multi-grid analyser was utilised for ion energy measurements. Experiments were conducted in argon at a pressure of 5 mtorr. Basic discharge parameters were quite moderate. RF voltage was just 40 V, resulting in a feeble plasma density of $2 \cdot 10^{13}$ m^{-3}. Injection of electron current up to 20 mA resulted in decrease of the plasma potential from 20 V to 3 V. Variation of maximum of ion energy, measured by the energy analyser, confirmed the decrease of plasma potential. Data on variation of plasma density and electron temperature were not presented.

Modelling of RF plasma with electron injection was described by Kushner and co-workers [77]. Two cold cathode electron beam sources, positioned at the opposite sides in RF discharge, were considered in order to compensate for asymmetry in bulk plasma parameters. Calculations of bulk distributions of plasma electron and injected electron densities, as well as of ion fluxes to the RF electrode were conducted.

Haas, Goodyear and Braithwaite studied injection of electron beam up to 100 eV energy in RF plasma both theoretically and experimentally [78]. Such effects, as cooling of the bulk electron temperature, increase of the bulk electron density and decline of plasma potential, were examined.

The reviewed publications demonstrate, that despite quite a long history of the method of electron injection into low-temperature plasma, there has been no systematic research of its physical effects on discharge conditions. Only during the last decade there has appeared several experimental programmes, looking at the relation between injected electron beam characteristics and plasma parameters.

The list of described publications with the main characteristics of electron sources is presentsd in the Table 3.1. It is not exhaustive, but it represents the main trends in development of electron sources for low-temperature plasma.

Table 3.1 Summary of the reviewed publications on electron sources and electron injection

Date	Ref.	Authors	Discharge	Electron source, I_e & E_e	Effects	Comments
1954	[60]	P.F.Little and A.von Engel	DC hollow cathode	Hot filament, 10^{-9} A, 12 keV	Negligeble effect on plasma	Discharge el. field was measured from diflection of e- beam
1970	[61]	L.I.Maissel and R.Glang	Thermionically sup. DC diode	Hot filament	Low pressure operat. <10mtorr	Oxide-coated and thoriated filaments were tested
1973	[65]	R.Limpaecher and K.Mackenzie	DC with magnet. insulated walls	48 filaments with net emis. current 6A	Creation of dense plasma $8 \cdot 10^{11}$ cm^{-3}	Filaments served as cathodes of the main discharge
1975	[62]	O.Christensen	DC and RF diodes	Hot filament	Variation of plasma potential	Qualitative analysis was given
1975	[63]	T.C.Tisone and P.D.Cruzan	DC sputter-coat. system	Tantalum filament, 6A	Low pressure operat. < 3 mtorr	Current-voltage characteristics of electrodes were measured
1980	[64]	N.Heiman, V.Minkiewicz and B.Chapman	DC sputter-coat. system	Hot filament, 4A	Etch. rate 10 times higher than DC diode	Reactive ion etching of silicon and alumina, using CCl_4
1984	[66]	T.Intrator, N.Hershkowitz and C.Chan	DC with magnetically insulated walls	Hot filament	Broad e-beam 350eV was extracted	Two counterstream e-beams gen. transverse EM radiat.

Table 3.1 (continued)

1986 1987	[68] [69]	K.Ando, T.Oshige, S.Yagura and H.Fujita	Pulsed e.injection into DC field	Heated oxide-coat. cath. behind grid	Negative potential is formed near e-source	Potential profile during discharge formation was studied
1990	[70]	A.H.Sato and M.A.Lieberman	RF diode	E. gun: oxide-coat. cath.; 10mA, 12 kV	No mentioned effect of e-beam on plasma	El. field in RF disch. was derived from deflec. e-beam
1990	[67]	A.Dehbi-Alaoui, A.S.James and A.Matthews	RF and DC PVD plasma device	Hot filament, pos. in discharge volume; 5A	Low pres. <1 mtorr discharge glow	Electron emisission allowed control of deposition current.
1991	[72]	P.B.Legrand, J.P.Dauchot and M.Hecq	E-source for X-ray spectrometry	Cold cathode, 150 μA, 1- 4 kV	E-beam spectr. with a peak ≈ disch. voltage	Source operation pressure up to 20 mtorr
1993	[71]	K.D.Schatz and D.N.Ruzic	RF reactive ion etch plasma	Cold cathode, 50 mA, 3kV	Increas. value of self-bias potential with el. injection	Strong variation of etch rate with distance from e-source.
1993	[75]	L.A.Schwager, W.L.Hsu and D.M.Tung	Inductively coupled RF discharge	Heated oxide disk, positioned in the discharge.	Plasma paramet. var. in the vicin of e-source	Meas. - Lang. pr.,energy and mass analyser at 11 mtorr H_2
1994	[73]	V.L.Galansky, V.A.Gruzdev, I.V.Osipov and N.G.Rempe	E-source for electron welding	Hollow cathode reflected discharge, 0.7 A	High density 10^{17} m^{-3} discharge in e-source	Pressure inside the e-source in the range 0.01-0.5 torr

Table 3.1 (continued)

1994	[74]	A.A.Goruppa, D.M.Grant and N.St.J. Braithwaite	RF capacitive discharge	Coated hot filament, 40 mA, 200V	Param. variat of discharge 30W, V_{rf}=300V at 30 mtorr H_2.	Meas.- Lang. pr., energy and mass anal. Control of IEDF for carbon film deposition.
1995	[76]	N.Sato, H.Kobayashi, T.Tanabe, T.Ikehata and H.Mase	RF capacitive discharge	DC magnetron with electron extraction through the mesh. 40V.	Param. variat of discharge in Ar at 5 mtorr, V_{rf}= 40V.	Meas.- Lang. pr., energy analyser. Control of ion energy at the ground. el-de.
1996	[77]	M.J.Kushner, W.Z.Collison and D.N.Ruzic	RF capacitive discharge	Cold cathode e-beam source, 60 mA, 1-3 kV.	Single and double sided injection of e-beam.	Electron density and ion flux to the substrate are calculated using two-dimensional model
1998	[78]	F.A.Haas, A.Goodyear and N.St.J.Braithwaite	RF capacitive discharge	Hot filament or discharge source, 100eV	Variation of plasma parameters (density, electron temperature and EDF) were meas. as functions of inject. electr. energy.	Meas.: Langmuir probe, energy and mass analysis probe.

3.3 Design of the electron source and the discharge volume configuration.

In order to implement electron injection in an RF capacitive discharge a special electron source was designed and manufactured. Thermionic electron emission from a heated filament was chosen for electron production. This choice was determined by the following considerations. The source should be compact in size for mounting inside the vacuum chamber between the side wall of the top hat electrode and the glass wall of the chamber (Fig. 2.6). Thermionic electron emission is a well established technology, which offers a selection of materials for the filament, allowing one to minimise its heating power. Too much thermal heating, produced by the filament, may damage the electric probe. The most important consideration was possibility of a straightforward regulation of electron energy flux by negative biasing of the filament. After a number of trials the electron source design depicted on Fig. 3.1 was developed.

The electron source assembly is mounted on a circular base made of machinable ceramic. The base acts as a fixing and insulating plate for the two electrical contacts of the filament and the body of the source. The body is a cylinder of 26 mm diameter and 40 mm length, spot-welded from 0.1 mm thick stainless steel. Its stiffness is provided by a quartz insert. The quartz tube also prevents a part of the emitted electron current from closing on the grounded body. The front part of the body is connected directly to the top hat grounded electrode of the main RF discharge. Between the source and the main chamber volume is a meshed window for extraction of the electron flux and protection of the filament from RF currents. The area of the window is approximately 2 cm^2. The mesh has density of 400 wires per inch with transparency of 69%. It is made from stainless steel. The emissive filament is positioned 3 mm behind the meshed window. It is made in the form of an helical spiral of 4 mm diameter and 13 mm length, formed from 0.325 mm diameter tungsten wire. At the rear side of the filament is a hemispherical reflector which is connected to the negative contact of the filament.

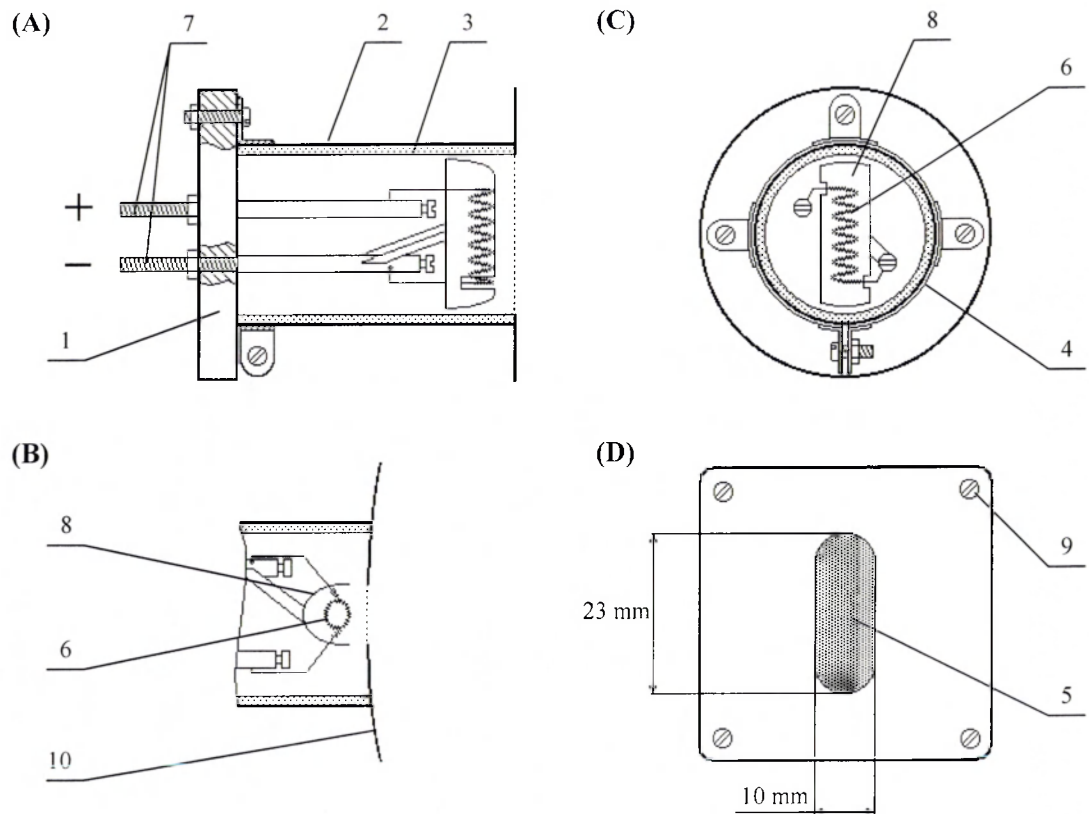

Fig. 3.1 Schematic diagram of the electron source.
(A) - Side section*, (B) - Plan*, (C) - Front section without mounting plate, (D) - Mounting plate.
*** - with longitudinal cross-section of the body**

1 -	Ceramic base	6 -	Emissive filament
2 -	Stainless steel body	7 -	Filament holders
3 -	Quarts tube	8 -	Reflector
4 -	Clamp	9 -	Fastening screw
5 -	Meshed window	10 -	Mounting plate

Geometric configurations of the semicircle reflector and the flat extracting mesh are close to the scheme of the Peers spherical electron gun with confocal flux [79]. So, it is assumed, that the dispersing electron flux from the quasi cylindrical emitting surface of the filament is transformed into a parallel flux at the exit of the source.

Effective thermionic emission from heated cathodes occurs at much lower temperatures, when they are coated by oxides of alkaline metals, than it does from pure

tungsten or molybdenum cathodes [80]. So, the tungsten emissive filament is coated with a powder mixture of equal parts of barium and strontium carbonates $(Ba,Sr)CO_3$. Barium and strontium carbonates are transformed into oxides during preheating of the filament in vacuum.

The problem of preserving the emissive layer on the filament surface for a sufficiently long time to study the injection of electrons into the RF plasma appeared to be the most difficult one. The barium-strontium carbonate powder was fixed by a blue mineral wax in the first prototypes. At the pressure range 10-40 mtorr in hydrogen or argon and the heating power of the filament 20-25 W the coating lasted no more than 30 min at most. The combined effect of heating and ion bombardment completely eroded the coating layer. In addition the emission from the filaments was very unstable.

Fixing of the emissive coating without the wax became possible, when quite an old technique, described in [81], was used. It uses electrophoresis, or electrochemical precipitation. A small amount of coating powder is stirred in acetone or amyl alcohol to the state of a turbid whitish liquid. Some solid phase in the liquid is acceptable. Two filaments, connected to a DC power source, are dipped into the mixture. Precipitation occurs on the positively biased filament. The process lasts 15-18 minutes at 180 V with a current up to 30 mA. Quite a uniform coating up to 0.5 mm thick is obtained all over the dipped surface. Although the electrophoresis method allows one to make a coating with good adhesion to the filament without the wax or other binder, it doesn't resolves the problem of erosion. The emissive layer deposited by the electrophoresis lasted just a few minutes at 30 mtorr in hydrogen.

The erosion problem has been eliminated by developing a porous-like cathode surface. Porous cathodes are sintered at high temperatures from coarse-grained powders of tantalum or molybdenum [82]. During electrophoresis emissive material penetrates into the pores of these structures. Such cathodes, impregnated with thorium and yttrium oxide, are

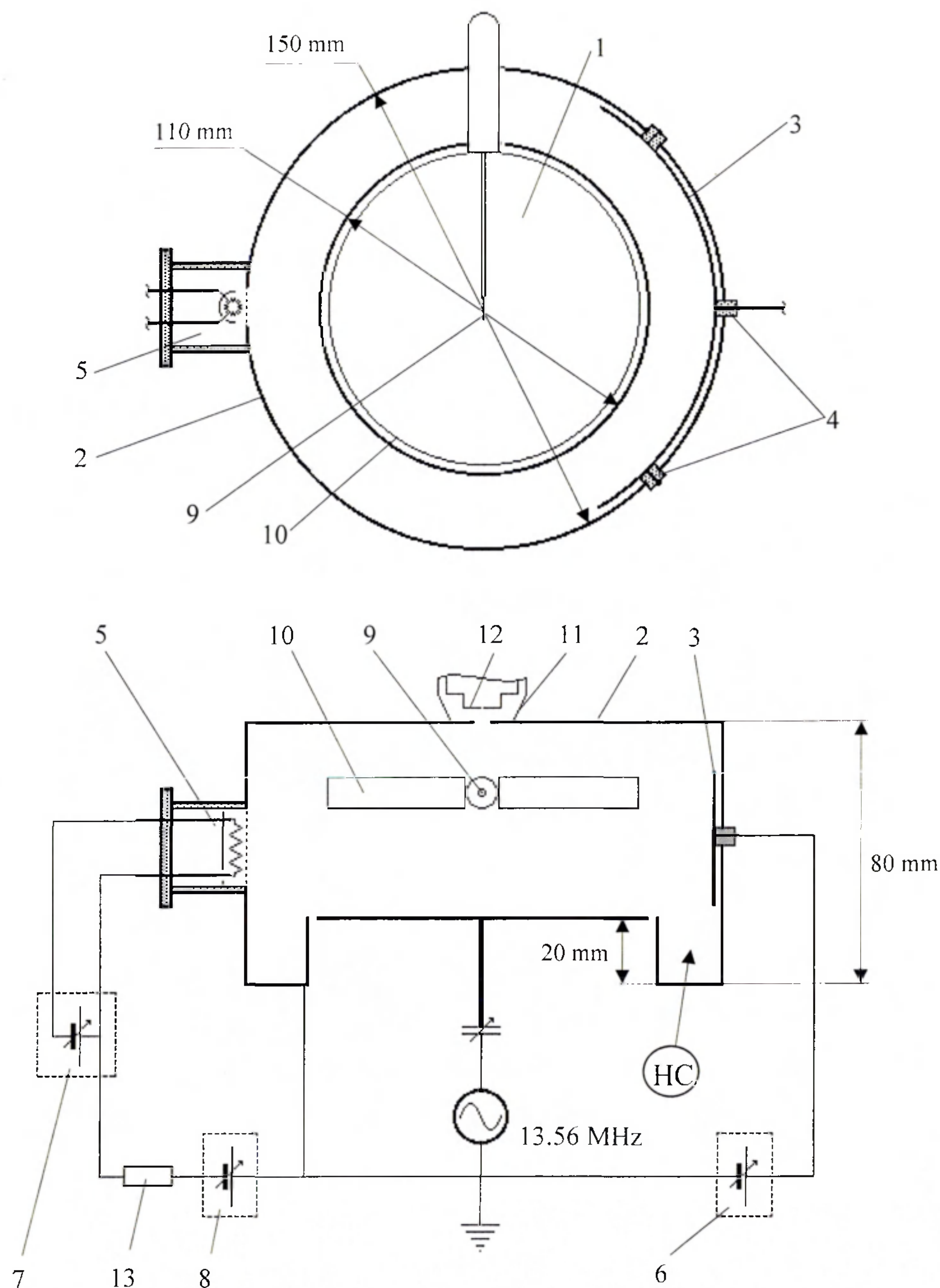

Fig. 3.2 Experimental configuration of the discharge volume: plan and side section.

1 -	Powered electrode	8 -	Filament bias power supply
2 -	Earthed electrode	9 -	Cylindrical electrostatic probe
3 -	DC bias electrode (DC anode)	10 -	Ring reference electrode
4 -	Insulating ceramic beads	11 -	Energy-mass analyser grounded shield
5 -	Electron source	12 -	Energy-mass analyser biased plate with sampling orifice
6 -	DC electrode power supply	13 -	Stabilising resistance; 988 Ω , 100 W.
7 -	Heated filament power supply	(HC)	Marking of the circular recess in the grounded electrode where the glow of "hollow cathode" type was observed

capable of providing an emission current density up to several $A \cdot cm^{-2}$ and are highly resistant to poisoning and ion bombardment. In order to mimic porous structures, the core tungsten wire used in this work was braided by 5-6 loose strands of a 0.025 mm diameter molybdenum wire. Afterwards it was shaped into the spiral filament and permeated by $(Ba,Sr)CO_3$, using electrophoresis. The filament with porous braiding has appeared to be both durable and stable.

The braided filament was preheated for about 10 min by a power of 12 W at $5 \cdot 10^{-6}$ torr in order to transform the impregnated carbonates to oxides by thermal decomposition. In the emission regime the filament is heated at arate of 15W (= 3A·5V) and negatively biased up to 200V. A source with such a filament has worked more than 3 hours in hydrogen at 45 mtorr.

The electron source is mounted on the side wall of the top hat grounded electrode with the bottom part of the extracting window 10 mm above the plane of the powered electrode (Fig. 3.2). In the early experiments, involving testing of the electron source, it was discovered that an additional positively biased DC electrode has a strong influence on plasma parameters. A small cirular DC electrode 2 cm in diameter was used originally. For the later experiments it has been replaced by the large rectangular one. So, the complete arrangement of electrodes includes the DC bias electrode, positioned opposite to the electron source. It has sizes 41mm×125mm
with its longer side curved along the circle of the grounded electrode. Three DC bench power sources are used to heat and bias the emissive filament and to power the positive DC electrode.

3.4 Operation of the DC bias electrode and the electron source

The current-voltage characteristics of the DC bias electrode operating in argon and hydrogen RF discharges are presented in Fig. 3.3 .

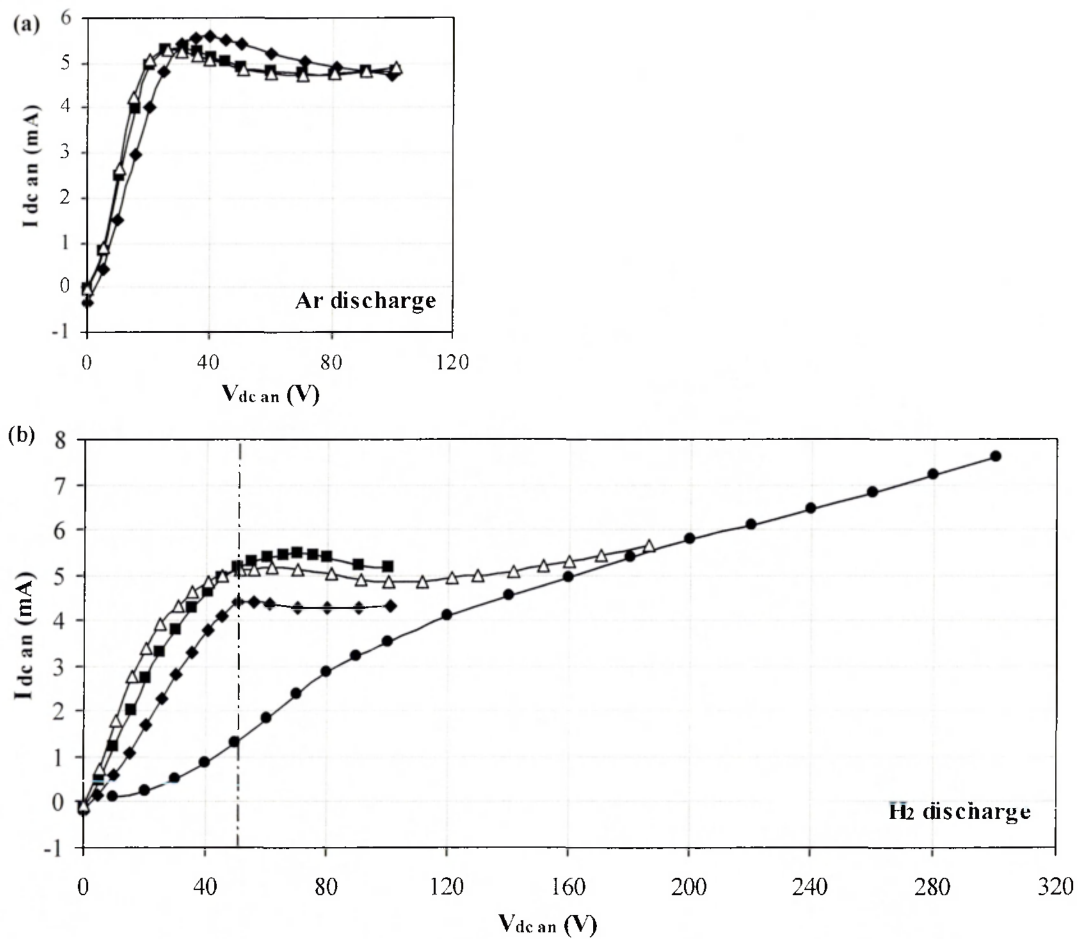

Fig. 3.3 Current – voltage characteristics of the DC bias electrode.
Discharge conditions for the large (51.25 cm^2) DC electrode:
(a) gas – argon; RF power – 30 W; pressure (mtorr) ◆- 15, ■ - 31, Δ- 47;
(b) gas – hydrogen; RF power –31 W; pressure (mtorr) ◆- 26, ■- 47, Δ- 68.
Symbols ● mark the characteristic of a small (3.14 cm^2) circular DC electrode : gas mixture – methane (5%) and hydrogen; RF power – 20 W; pressure – 30 mtorr.

Reading of the bias voltage marked $V_{dc\ an}$ was taken from the analog voltmeter of the DC power source; and reading of the current marked $I_{dc\ an}$ was taken from the digital meter in the circuit of the DC electrode. Current –voltage characteristics of the large DC electrode are qualitatively the same for argon and hydrogen. They start from a rising part which saturates in the interval 4.4 - 5.7 mA , depending upon the gas and its pressure. Further increase of the DC bias voltage first leads to approximately 5-10% decline of the collected current and than to its recurring growth but at a slower rate. The characteristic of the small electrode doesn't have a saturation region. Although the small electrode is sixteen times less than the large electrode in area it collects only 3 times lower current

compared with the saturation threshold current of the large electrode marked by the dotted line in Fig 3.3(b) . Further the current of the small electrode is eventually catching up with the one of the large electrode. It has to be noted that the conditions of operation of the large and small DC electrodes reflected in Fig. 3.3(b) were different in terms of gas composition and RF power. So, the gradual convergence of the current-voltage curves above 120 V is a coincidence. Nevertheless it is possible to analyse these data qualitatively using information from the electrostatic probe measurements. The fact that the small electrode appears more effective (in terms of current density) can be attributed to its time averaged sheath potential V_s (Fig 3.4(a)). It either diminishes almost to zero or changes from positive to negative already by 80 V bias.

As bias voltage is increased on the small electrode it forms an electron sheath during part of the RF cycle. In this way the small electrode collects electrons from all of the energy spectrum and for a longer fraction of the RF cycle than the large electrode, having as a result a higher current density.

The averaged sheath potential at the large electrode remains positive decreasing only by 20-25% at 30 V bias and almost restoring its original value at 55 V (Fig 3.4(b)).

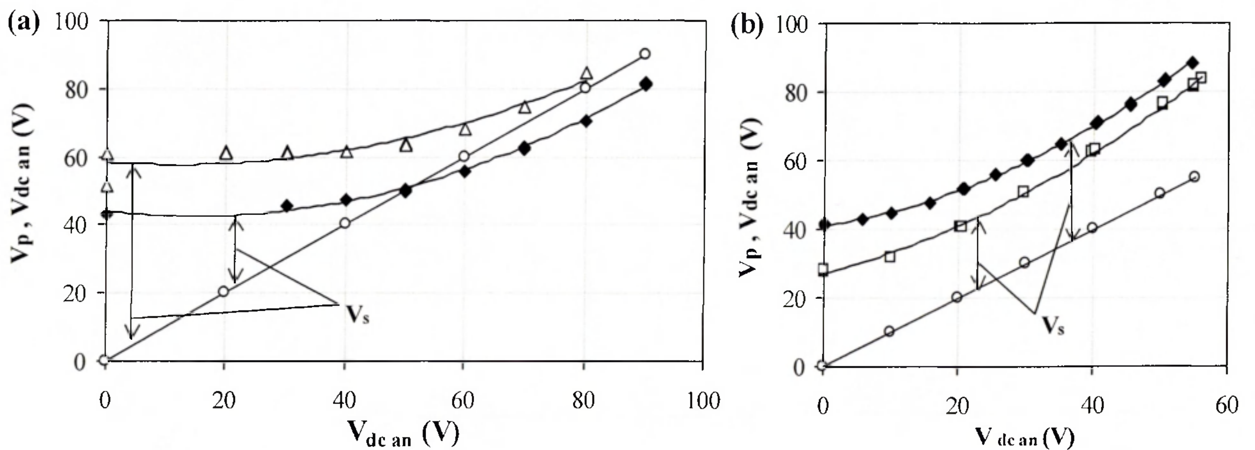

Fig. 3.4 Plasma potentials of RF discharge in hydrogen as a function of bias potential of (a) the small and (b) the large DC bias electrodes.
Markings on the graph:
(a) RF power – 20 W , gas pressure : △ - 31 mtorr , ◆ - 51 mtorr ;
(b) RF power: ◆ - 30 W, □ - 20 W; gas pressure: ◆ - 45 mtorr, □ - 70 mtorr.
Symbols o mark DC bias potential.

This recovery of the sheath potential contributes to the current saturation effect of the large electrode (Fig. 3.3(b)). At the same time variations of electron temperature and density can also play their part. It follows from the formula of instantaneous electron current to the surface based on the assumption of Maxwellian distribution:

$$i_e = \frac{1}{4} \cdot A \cdot \bar{\upsilon}_e \cdot n_e \cdot e \cdot \exp\left(-\frac{V_s(t)}{T_e}\right) \quad (3.1)$$

Here A – electrode area, $\bar{\upsilon}_e = \left(\frac{8 \cdot e \cdot T_e}{\pi \cdot m_e}\right)^{0.5}$ - average electron velocity, n_e – electron density, e – electron charge, m_e – electron mass, T_e – electron temperature, $V_s(t)$– time dependent sheath potential. For example the growth of the electron current can originate from an increase of electron temperature due to heating by the sheath of the grounded electrode. Measurements of plasma parameters were limited to 60 V bias at the large electrode due to growing stray noise in the electrostatic probe circuit. There were also problems in interpretation of the automated measurement system data, which will be discussed in the next section. The choice between two electrodes was made in favour of the larger one. It collected 3 times higher current at 60 V bias, having more effect on the main RF discharge.

The electron source bias circuit included a 988 Ohm stabilising resistance connected in series with the filament (Fig. 3.2). Voltage and current at the exit of the filament bias power supply were measured by its analogue current and voltage meters. Filament bias voltage was calculated by subtracting from the power source voltage a product of the bias circuit current and the value of the stabilising resistance. Current-voltage characteristics of the source are presented on the Fig. 3.5.

By plotting characteristics on a logarithmic scale it is possible to examine the source current-voltage relation. The straight line marked k=3/2 represents the Child-Langmuir space charge limited current equation (3.1), applied to the source geometry.

$$j = \frac{4 \cdot \varepsilon_0}{9} \cdot (2 \cdot e / m_e)^{\frac{1}{2}} \cdot \frac{V^{\frac{3}{2}}}{x^2} \qquad (3.2)$$

Here $\varepsilon_0 = 8.9 \cdot 10^{-12}$ F/m - permittivity of free space, $e = 1.6 \cdot 10^{-19}$ C - electronic charge, $m_e = 9.1 \cdot 10^{-31}$ kg - electronic mass, V (V) - potential difference between electrodes, x (m) - distance between electrodes.

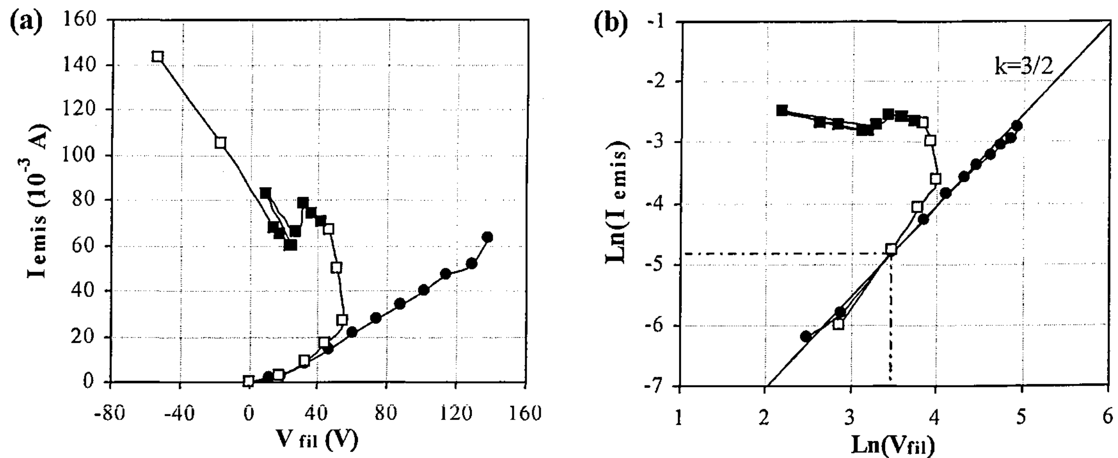

Fig. 3.5 Current - voltage characteristics of the emissive filament electron source: (a) – linear and (b) – logarithmic scales. Filament heating power - 15 W. Gas - hydrogen at pressures: • - 30 mtorr, ▫ and ▪ - 45 mtorr. Symbols ▪ mark the regime, when the DC bias electrode operated simultaneously with the electron source. Power of the main RF discharge - 30 W.

The current-voltage characteristic of the source at 30 mtorr conforms closely the Child-Langmuir equation (Fig. 3.5(b)). A small deviation at the beginning of the characteristic can be accounted for by uncertainty in the reading of small currents from the analogue current meter. A reduction of the source current in comparison with the k=3/2 line by the bias voltage 120 V might originate from the negative charge build up around the extracting mesh. Also at larger extraction currents the simple planar model is an increasingly poor representation of the filament/mesh region. Using the formula (3.1) and data of the characteristic it is possible to estimate the area of the emitted electron beam arriving to the extraction mesh. We take the source current and voltage values from the Child-Langmuir region of the source characteristic (dotted line on the Fig. 3.5(b)), and take the distance x equal to the 3 mm gap between the filament edge and the extraction mesh. Then by

dividing the measured emission current by the calculated current density we obtain the area $1.66{\cdot}10^{-4}\ \mathrm{m}^2$, which is a little less than the front section area of the reflector $10\ \mathrm{mm}{\cdot}20\ \mathrm{mm}\ (2{\cdot}10^{-4}\ \mathrm{m}^2)$.

At the higher pressure 45 mtorr the emission current starts to exceed the values allowed by the space charge limited relation above 40 V. More power from the DC bias generator led to growth of the emission current up to 70 mA with loss of the bias voltage from 54 to 40 V. Such behaviour of the emissive filament can be ascribed to a gradual development of breakdown inside the electron source. An internal plasma discharge was produced. It promoted growth of the filament emission current by neutralising the electron space charge in the source and by ion bombardment. At first when the DC bias electrode was activated the emission current grew up to 80 mA with loss of bias voltage down to 30 V. Then the filament emission became unstable falling to 64 mA. More power was supplied from the filament bias generator in order to compensate for the emission loss. Nevertheless further substantial growth of the emission current up to 143 mA became possible only when the DC electrode was switched off. The connection between the filament and the electrode was mediated by the main RF discharge plasma. The averaged plasma potential grew due to the effect of the DC electrode (Fig. 3.4(b)). It caused extra heating to the filament through higher energy ions penetrating through the meshed window. Also it led to erosion of the emission layer causing a reduction of the filament current. The change of filament polarity at emission currents above 80 mA culminating in positive 55 V at 143 mA can be ascribed to an effect similar to that of an emissive probe. A high enough electron current neutralises the positive sheath space charge formed near the filament by the secondary discharge. In this way the filament potential is pulled up or close to the discharge potential.

The two regimes of the electron source operation (with and without the internal discharge) affect the main RF discharge with different intensity. This can be illustrated by

the variation of electron density in the main discharge (Fig. 3.6). At 67 mA emission current for 30 and 46 mtorr the filament bias and hence the injected electron energy was three times higher at 30 than at 46 mtorr (Fig. 3.5(a)). But for the same filament emission current there was a five-fold increase of the main discharge electron density at 45 in comparison with 30 mtorr marked by the dotted line on the Fig. 3.6. It has to be noted that thermionic electrons could also gain extra energy while passing through the sheath of the main RF discharge narrowing the electron energy gap between 30 and 46 mtorr. A difference of ionisation cross sections, resulting from the difference in electron energy at these pressures, is unlikely to be more than 10-20% (Appendix C). So, the much stronger influence on the main discharge of the electron source at 46 mtorr can not be explained only by the 50% increase of the

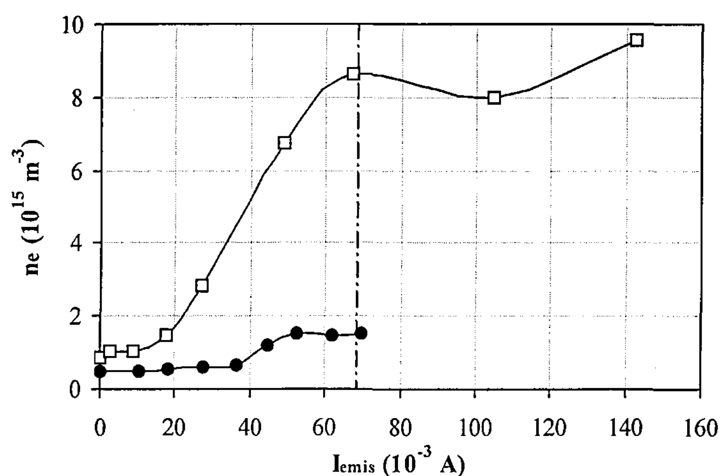

Fig. 3.6 Variation of electron density of the main plasma discharge as a function of the filament emission current. Gas – hydrogen; RF power of the main discharge – 30 W; pressure: • - 30 mtorr, ▫ - 46 mtorr.

neutral gas density combined with the 10-20% higher value of ionisation cross-section. It is proposed that the secondary discharge in the source promoted extraction toward the main discharge of a larger fraction of the emitted electrons. In the case of a pure electron sheath inside the source at 30 mtorr it is suggested that a substantial fraction of emitted electrons is reflected back by the negative potential distribution, formed in front of the electron source. This will be discussed further in section seven of this chapter. In order to check all

the assumptions about the operation of the electron source it is necessary to measure the actual injected current by the electron energy analyser [83]. Such an experiment was outside the resources of this project.

Saturation of electron density of the main RF discharge following electron injection (Fig. 3.6) can be caused by a balancing of the density increase by the growing losses of electrons to surfaces. It will be demonstrated in section seven of this chapter that the electron temperature and the averaged plasma potential decline with electron injection. So, according to the formula (3.1) electron current density increases because of the net effect of the increased density and the decreased plasma potential. Since the electron temperature is under the square root in expression (3.1), it has a weaker effect on the final result. A small dip in the saturation area at 45 mtorr appeared as the result of the source operating simultaneously with the DC electrode. The last two measurements were taken after turning-off of the DC electrode. Due to erosion of the emissive layer the filament produced less electron current, hence there was smaller electron density enhancement in the main discharge.

Attempts to operate the source in argon at 20 mtorr immediately resulted in the formation of a an arc with a peak current up to 3 A and led to the burning of hole in the meshed window. Interestingly, earlier versions of the source, which had a reflector in the form of a flat disc 8 mm behind the filament were capable of working in argon even at 30 mtorr. These facts confirm the role of reflector shape in forming a concentrated or expanding electron beam.

3.5 Interpretation of data from the electrostatic probe.

Measurements of plasma parameters were conducted by means of the passively compensated electrostatic probe. A brief description of the probe was given in section 3 of the previous chapter. Further information about its concept is given in the work by Annaratone and Braithwaite [49]. One of the main advantages is its simplicity of design.

An inductor chain is used to block RF signal from the probe tip, which is driven in phase with plasma potential by a reference ring. Experience of using the probe in this work has demonstrated that the filtering system of the probe was unable to block completely the RF signal in the probe circuit under certain conditions. Probe performance was dependent upon the input power to the RF discharge and to the pressure and nature of the gas. Probe measurements were more reliable above 30 mtorr, in Ar rather than in H_2 and preferably below 20 W input power. All the factors pointed out that the probe was prone to contamination by RF signal following large increases of RF potential in the plasma. It meant that the RF component, present in the electron current collected by the probe, resulted in a wider retardation region (Fig. 3.7).

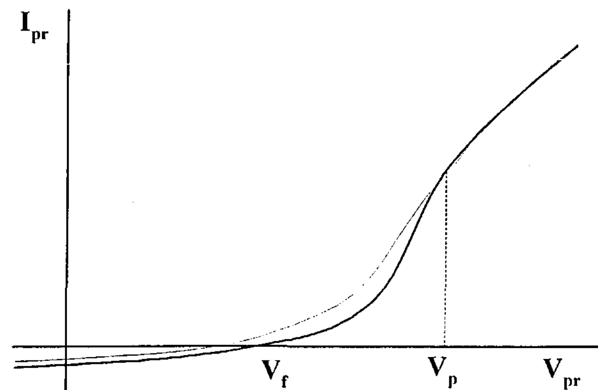

Fig. 3.7 Probe characteristic. Thick and thin lines mark signals with complete and insufficient RF compensation.

The most probable reason for insufficient RF filterring was a poor compensation of higher (3d, 4th and 5th) harmonics. A significant fraction of higher harmonics in the plasma could have originated from a comparatively high RF amplitude of input voltage: 380 V (30 W input power) in this work versus 100 V quoted in [49]. Also a specific configuration of the discharge volume (Fig. 3.2), capable of producing a "hollow cathode" effect, could promote higher harmonics.

Probe measurements were automatically processed by the "AEA Technology" data acquisition system. It consisted of an electronic unit connected to a personal computer. The unit provided probe biasing by a potential in the form of a few increasing and decreasing

ramps. Simultaneously the probe current was measured, converted into a digital format and passed to the computer. A dedicated software prepared probe signals for analysis implementing averaging and smoothing procedures. Typically in this work a cycle for measuring one data point was set to contain ten repetative measurements. Main plasma parameters were calculated by the software, using a chosen part of probe signal and a corresponding probe theory (Appendix A). For the current work, the retardation part of probe characteristic was used. The probe theory in use was based on the assumption of a Maxwellian electron energy distribution.

Processing of the retardation part worked as a preset default on the software main screen, automatically representing, after each measurement cycle, values of plasma potential, electron density and temperature. This regime was convenient for accumulating the large amounts of data, required while studying the effects of the DC bias electrode and electron injection on the main RF discharge. An alternative method to determine the electron temperature and density was by analysis of the probe characteristic above plasma potential, i.e. an orbital motion limited regime. This requires the probe radius to be small compared to the plasma Debye length. This condition was difficult to satisfy within the range of plasma regimes studied, so the orbital motion area was not used for analysis. At the same time a closer examination of the retardation area revealed that the software algorithm could sometimes produce incorrect values of electron temperature and density owing to contamination of the probe signal by RF current.

The first step in the calculation of plasma parameters was the determination of the time averaged plasma potential. It was identified as the point at which the second derivative of the probe current crosses zero between its' maximum and minimum. During subsequent checks of data, the second derivative was used to estimate the quality of the probe characteristic. The quality of the second derivative is much more sensitive to RF compensation than the characteristic itself. Typically in the case of adequate compensation

there is one clear narrow maximum (Fig. 3.9(b)). In the case of signal contamination there is a double maximum structure (Fig. 3.8(b)) or a distorted shape with a large maximum superimposed on a small one (Fig. 3.8(a) and 3.9(a)). Another indicator of satisfactory probe compensation relates to the distance between maximum and minimum in the second derivative, which should not be more than T_e measured in Volts.

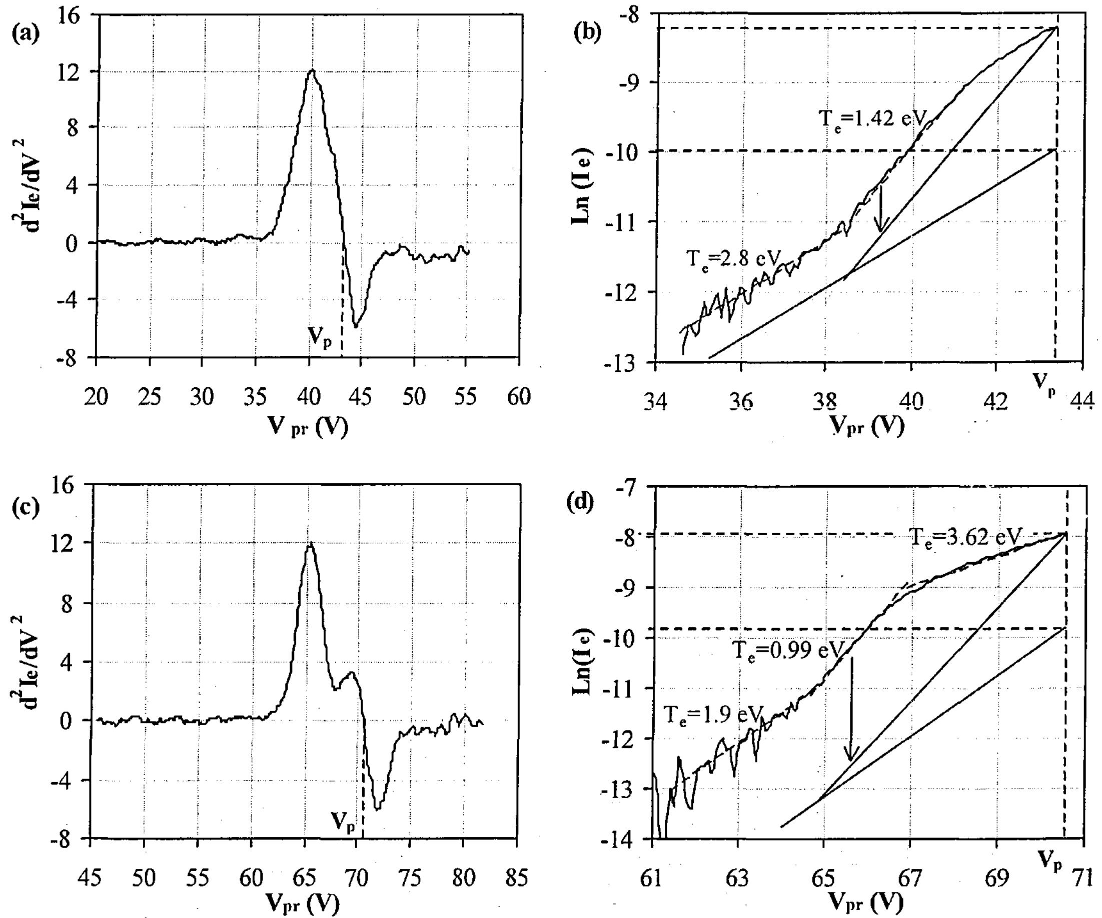

Fig. 3.8 Second derivative and natural logarithm of the probe electron current.

(a) and (b) – RF discharge in hydrogen at 51 mtorr, 20 W input power;
(c) and (d) – the same discharge with 80 V bias at the small DC electrode.
Straight solid lines on natural logarithm graphs mark corrected electron current signal, consisting of "cold" and "hot" electron groups.

For the probe configuration used in this work the uncertainty in the value of plasma potential was rarely less than 1 V. The two likely causes are residual RF and excessive smoothing of the software algorithm.

Since RF contamination of the probe signal was reckoned to be around 1-2 V the uncertainty in plasma potential was generally of this order. Plasma potential data were

verified by ion energy distributions, measured with the energy and mass analysis probe, and demonstrated uncertainty of a comparable amount. They correlated closely with a small potential offset at all plasma regimes and environments.

From the data of second derivative it could be seen that compensation of RF was barely sufficient for the basic RF discharges without modification (Fig.3.8(a) and 3.9(a)). Application of the DC bias potential made the situation worse, which was reflected in the double maximum structure (Fig. 3.8(c)). This was not surprising since the increase in plasma potential (Fig. 3.4(a)) is associated with an increase in the amount of RF in the plasma. Quite the opposite was the effect on the probe characteristic of electron injection - see Fig. 3.9. This led to a decrease of plasma potential from 44.47 V on (a) down to 7.72 V on (b). The probe RF filtering system had less RF to deal with at the lower plasma potential, resulting in a "purer" second derivative signal.

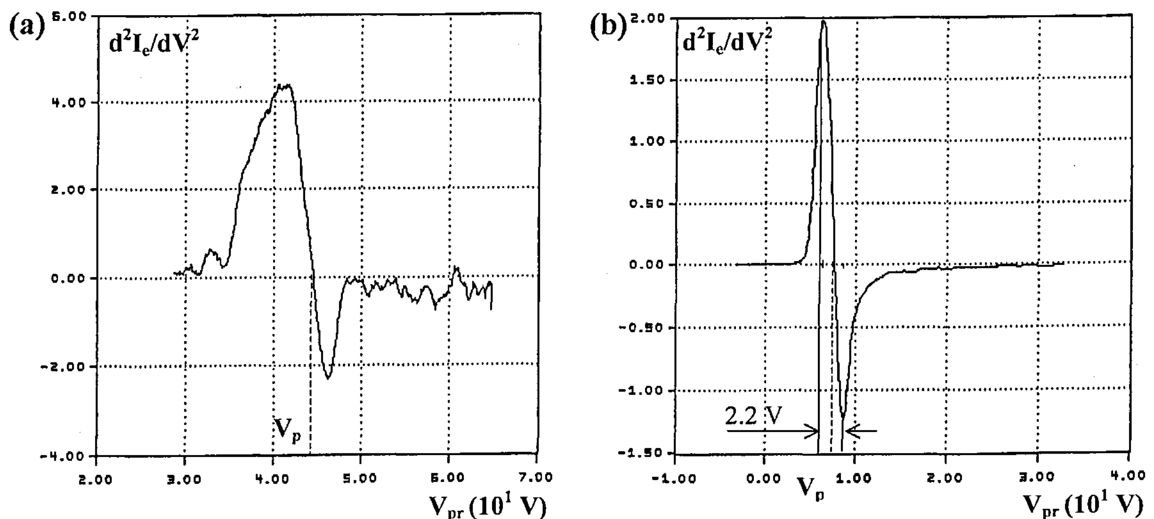

Fig. 3.9 **Second derivative of electron current to the probe**
(a) – RF discharge in hydrogen at 46 mtorr , input power 30 W;
(b) – the same discharge with electron injection, emissive filament current 143 mA.

The electron temperature was calculated by applying a sliding least square method to the natural logarithm of the electron current. The best linear fit was determined by locating the minimum of the associated chi-squared quality-of-fit parameter (in other words, by locating the longest linear part of the natural logarithm curve). Then the density was calculated from the electron current at plasma potential.

As it could be seen from the Fig. 3.8(b) the logarithm curve consists of three quasilinear parts, which was typical for probe signals in this work. The first part marked $T_e = 2.8$ eV represents a group of higher temperature or "hot" electrons. Their current could not be resolved well due to it's low value (the order of ion current) just above the floating potential. Even after the smoothing procedure it had a saw-like structure. So the algorithm ignored it in favour of a smoother linear part marked $T_e = 1.42$ eV, corresponding to cooler electrons named for simplicity "cold". The last, smoothly turning part of the logarithm curve appeared because of distortion of the probe signal close to plasma potential. This part was ignored also by the algorithm since it was much shorter than the "cold" electron part. Then the algorithm effectively subtracted (arrow mark on the Fig. 3.8(b)) the RF component from the probe electron current by calculating the density using the "cold" part of the logarithm curve at V_p. The bi-Maxwellian nature of the electron energy distribution was not taken into account in automatic calculations. It is possible to estimate the contribution of "hot" electrons to the total electron current by extending a corrected "hot" part up to the plasma potential. The "hot" electrons constitute typically 20% of the total current at the plasma potential. Then subtraction of the "hot" electron current from the total current singles out the "cold" electron component marked by $T_e = 1.42$ eV on the Fig. 3.8(b). Hand calculations of electron density and temperature for the bi-Maxwellian distribution give $1.84 \cdot 10^{15}$ m^{-3} for the "cold" and $0.25 \cdot 10^{15}$ m^{-3} for the "hot" electrons. For comparison the software electron density value was $2 \cdot 10^{15}$ m^{-3}. So, the algorithm on the basis of a single temperature Maxwellian approximation overestimated the "cold" electron temperature by approximately 15% and undervalued net electron density by 5%. This is acceptable as an uncertainty.

When the RF distortion of the probe signal was quite strong, the algorithm could mistakenly determine electron temperature from the wrong part of logarithm curve. For measurements in plasma with the high DC bias potential (Fig. 3.8(d)) automatic calculation

produced 3.62 eV electron temperature. This value originated from a distorted part of the logarithm curve since it was the longest linear part recognised by the software. In this case a correction by hand was needed, which produced a much lower value, 0.99 eV. An estimation of the "hot" electron component was also made, which gave 1.9 eV and constituted 17% of the total current at plasma potential. It has to be noted that this method of estimation of "hot" or tail electrons relies heavily on having adequately measured the probe current and having properly subtracted the ion contribution. This is especially important at and below floating potential. Such estimations have to be supported by more sensitive techniques such as a large area planar probe described in [84].

3.6 Some aspects of ion sampling by the energy-mass analyser

The principle of operation of the energy and mass analysis probe (model EQP300 manufactured by Hiden Analytical Ltd) is described in the Appendix B. A few comments have to be made here concerning problems linked with sampling of ions from a plasma by this device. In the period 1993-95, when the experimental part of this work was done, the EQP probe was supplied by the company with a standard set of electronic parameters (Appendix B). Setting of the extraction orifice potential for positive ions was recommended to be in the range minus 200-240 V. Since then there has appeared an opinion that such high extraction voltage, although providing high sensitivity for the device, risks distortion of the ion energy distribution through perturbation of the local plasma. Currently Hiden Analytical devices are operated at lower extraction potentials. For example in the 1999 publication by Jayaraman, McGrath and Hebner [85] a potential bias –20 V was mentioned. During the course of this research an attempt was made to verify the effect of the high extraction potential on plasma and distribution of ions. For this purpose a grounded 5 mm aperture, situated 4 mm in front of the sampling orifice, was covered with a high density (400 wires per inch) mesh. In this way plasma from the main discharge was separated from the biased plate with the sampling orifice. No visible change was

noticed in ion energy distribution or in the discharge plasma. Measurements presented in this work were made without this separating mesh. In general there are few publications, which study the effects of ion sampling by "Hiden Analytical" devices. In [86] the effect of scattering of low energy ions (≈1 eV) inside the analyser was estimated. For pressures 10-100 mtorr from 1 % to 12% of the sampled ions experienced collisions before detection. In [87] the effect of extractor voltage on acceptance angle and relative error of ion signal was studied for ion energy ranges 1- 500 eV and 50-500 eV accordingly. It is worth mentioning that the EQP analyser was positioned behind the powered electrode in that work. The acceptance angle for the extractor voltage –200 V increased from 1° to 2° with ion energy change from 100 eV down to 10 eV. In the range 10-1 eV the acceptance angle grew further up to 6°. As for the relative error in ion signal it changed very little in the range 50-100V for –200V extractor voltage, but changes from 10% to 0% in the range 100-320 V. As can be seen, the available information does not provide data directly applicable to the current work. The only value possible to quote is that for ion energies up to 100eV studied in this work the relative error is unlikely to be more than 10%. It is worth noting that in most of publications about ion sampling through electrostatic fields a SIMION software is quoted as the main tool for modelling (information on the website http://www.inel.gov/technology_transfer/products/simion.html).

3.7 Effect of the DC bias electrode on plasma parameters

Effects of positive biasing by the DC electrode on plasma parameters were studied by the electrostatic probe and by the energy and mass analysis probe described earlier in this chapter. Measurements were conducted in hydrogen and argon discharges. Data from the electrostatic probe measurements in hydrogen plasmas influenced by the small bias electrode are presented in Fig. 3.10. It was demonstrated in the previous section that the automatized software processing of probe characteristic could produce distorted values of electron temperature and density due to deformation of the characteristic by RF current.

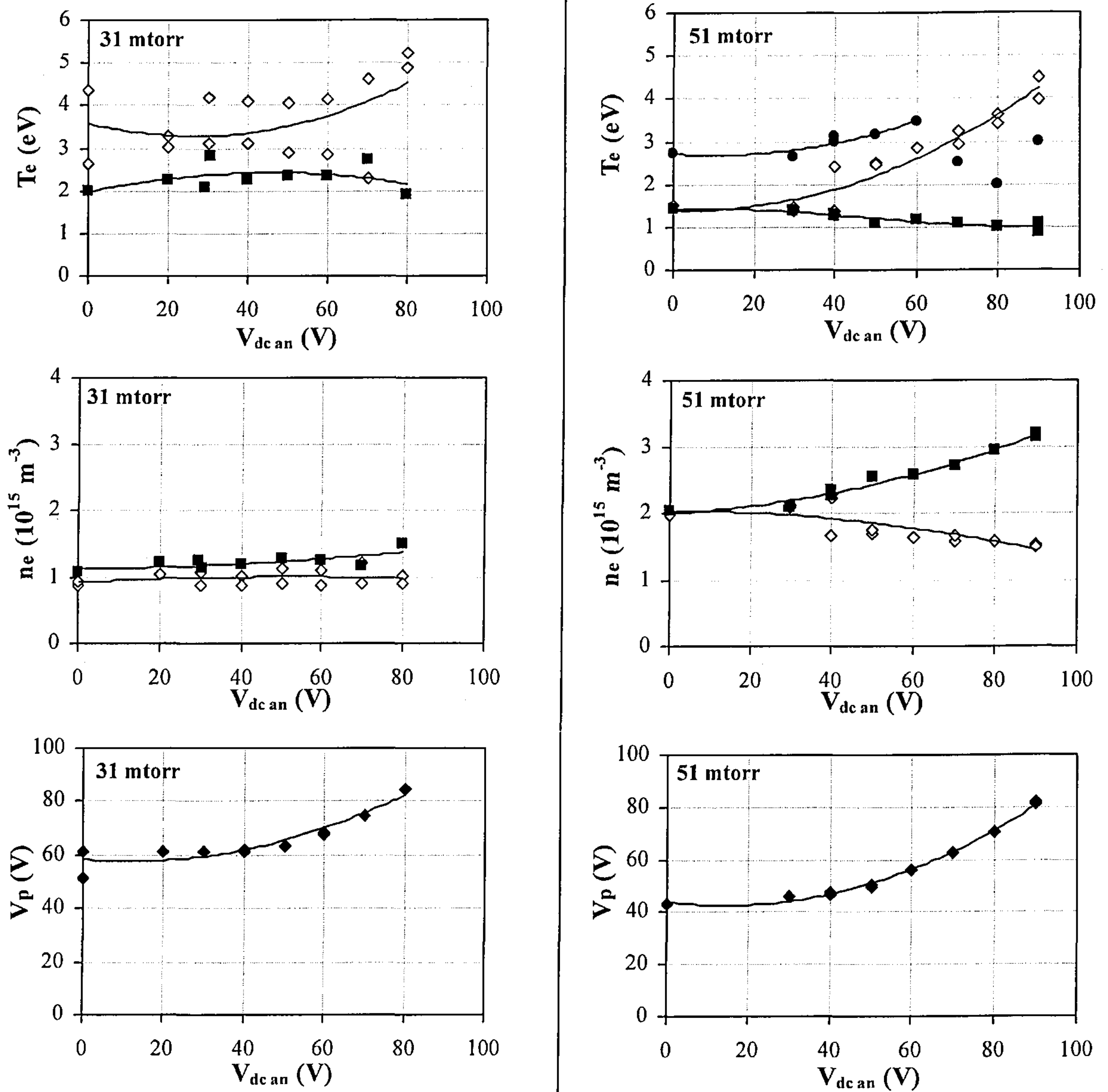

Fig. 3.10 Effect of the small (3.14 cm^2) DC anode on plasma parameters of RF discharge in hydrogen at 31 and 51 mtorr.
Input power – 20 W. Symbol marking:
◇, ◆ - data from automatic processing by software; ●, ■ - corrected data.

The data in Fig. 3.10 were corrected by using nondistorted sections of the probe signal. The natural logarithm of the probe electron current at 51 mtorr had a signal/noise ratio, which allowed the resolution of the temperature of a second, more energetic electron group from the characteristic section above floating potential (Fig. 3.8(b) and (d)). So, variation of the "hot" electrons temperature was traced in addition to that of the major "cold" group. At 31 mtorr signal/noise ratio of small electron currents was not good enough to perform the same operation.

The general trends of parameter variation can be described as a decrease of the bulk electron temperature, increase of the electron density and of the plasma potential. At 31 mtorr these trends were blurred for the electron temperature (practically a constant value) and were relatively weak for the electron density (25% increase) and the plasma potential (35% increase).

At 51 mtorr the bulk electron temperature decreased by 30% from 1.4 eV to 1 eV, the electron density increased 55% from $2 \cdot 10^{15}$ m^{-3} to $3.1 \cdot 10^{15}$ m^{-3} , the plasma potential increased almost 100% from 43 V to 82 V. The outlined growth of the temperature of "hot " electron group (from 2.8 eV to 3.5 eV at 60 V bias) at 51 mtorr didn't last until maximum bias of 90 V. Most likely this fluctuation of the "hot" electron temperature was due to a growing measurement uncertainty owing to the small level of current at the high bias voltages.

The effect of growing plasma potential originates from a changing balance of fluxes of charged particles to electrode surfaces. By drawing a net electron current from the plasma the positive DC electrode effectively increases the positive charge of the sheath between plasma and ground, causing a growth of its potential. The rate of this increase depends upon the DC electrode area as could be seen in Fig. 3.4, where the growth of plasma potential from 40 to 80 V requires 55 V bias of the large DC electrode versus 90 V bias of the small DC electrode. These responses of plasma potential are quite explainable since the large area DC electrode collects higher electron current than the small one (Fig 3.3), resulting in a stronger effect on the plasma potential. The overall importance of electron flux to the DC electrode as a basis of its effectiveness could be seen from the Fig. 3.10. In 31 mtorr hydrogen plasma without DC biasing electron density was smaller by a factor of 2 and the electron temperature was larger by the factor of 1.4 than in 51 mtorr plasma. Consequently, electron current available for collection from the plasma at 31 mtorr was approximately 1.5 less than at 51 mtorr. So, when positive biasing was applied, plasma

potential and other parameters were changed less intensively at 31 mtorr than at 51 mtorr.

3.8 Effect of simultaneous operation of the electron source and the DC bias electrode on plasma parameters

3.8.1 Impact of electron injection on RF plasma

The effect of electron injection and removal on plasma parameters has been studied by the electrostatic probe, described earlier in this chapter. When electrons are injected into an RF discharge at 30 mtorr (Fig. 3.11, left hand side graphs) the behaviour of the plasma parameters is quite predictable. The decline of plasma potential is associated with additional negative electric charge in the RF plasma brought in by injected electrons. This effect is confirmed by modelling in the next chapter. The increase of the plasma density is caused by ionisation of gas by fast injected electrons with maximum energy equal to the acceleration potential of the emissive filament (up to 145.8 eV). The gas density at pressure 30 mtorr is $1.061 \cdot 10^{21}$ m^{-3}. The ionisation cross-section of a hydrogen molecule by 130 eV electrons is $1.1 \cdot 10^{-20}$ m^2 (Appendix C), so the mean free path for these electrons is approximately 90 mm. Thus, every electron from the electron source produces at least one electron-ion pair while passing through the discharge volume. The decrease of the temperature of cold bulk electrons is associated with increased plasma density. The link between electron temperature and plasma density, mediated by the RF sheath, will be demonstrated in the next chapter.

It is worth specifying that the overall electron distribution in the part of discharge, through which injected electrons pass, consists of "cold" bulk electrons and (2-4 eV for 30 mtorr) and "hot" injected electron (30-145 eV). Only the "cold" group parameters are measured by the probe. Problems of automated measurement of plasma parameters were discussed in section five of this chapter. It was demonstrated that the probe measurements in a plasma with electron injection are reliable owing to the small amplitude of RF signal at

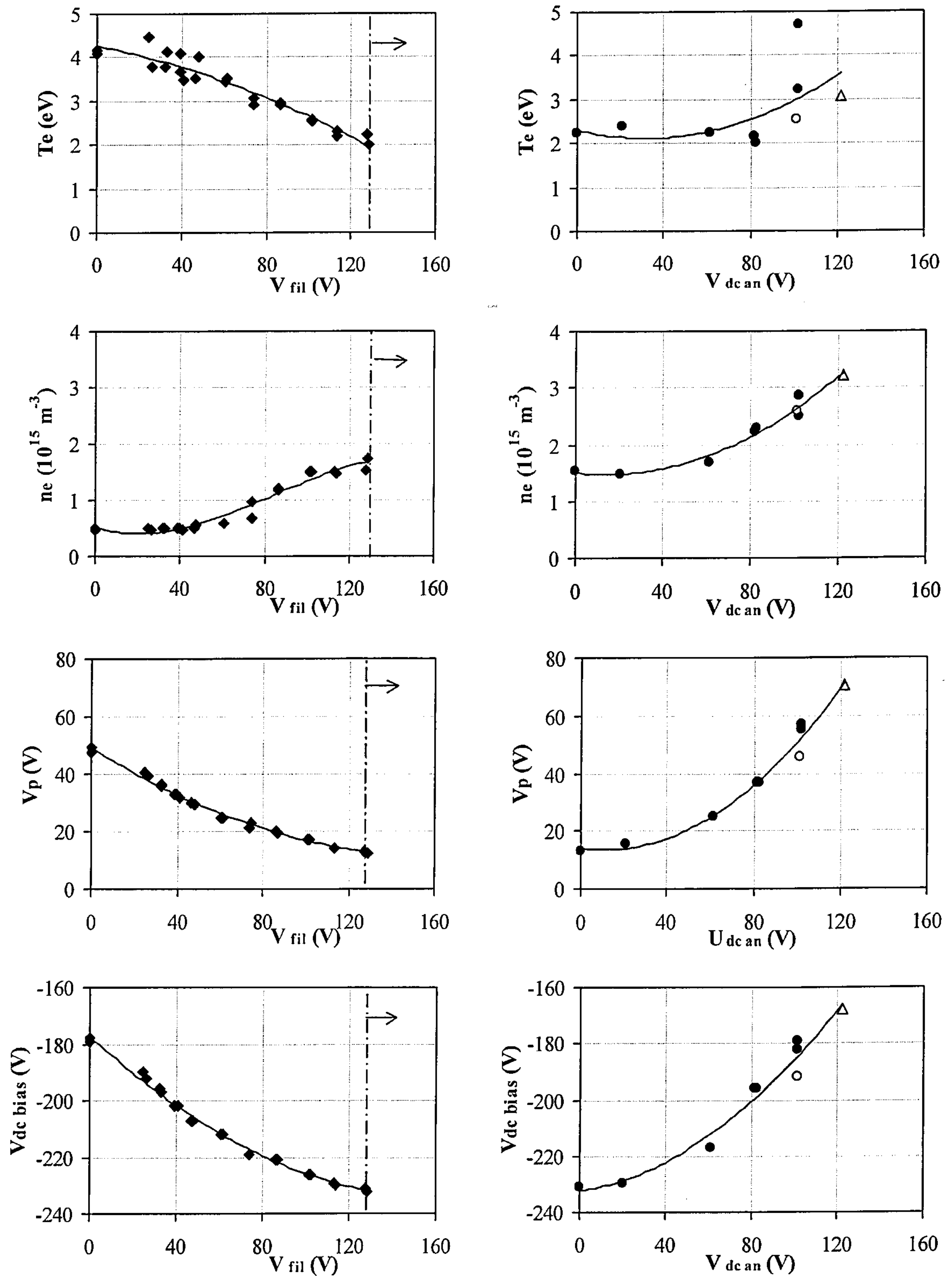

Fig. 3.11 Variation of plasma parameters with electron injection and removal in hydrogen discharge; RF power - 30 W, pressure - 30 mtorr.

♦- discharge operation with electron injection only. Dotted lines mark the stage when a DC anode was switched on. ●, ○, Δ- operation both with the electron source and the DC anode. Values of V_{fil}: ● - 127.7 V, ○ – 135.8 V, Δ - 145.8 V.

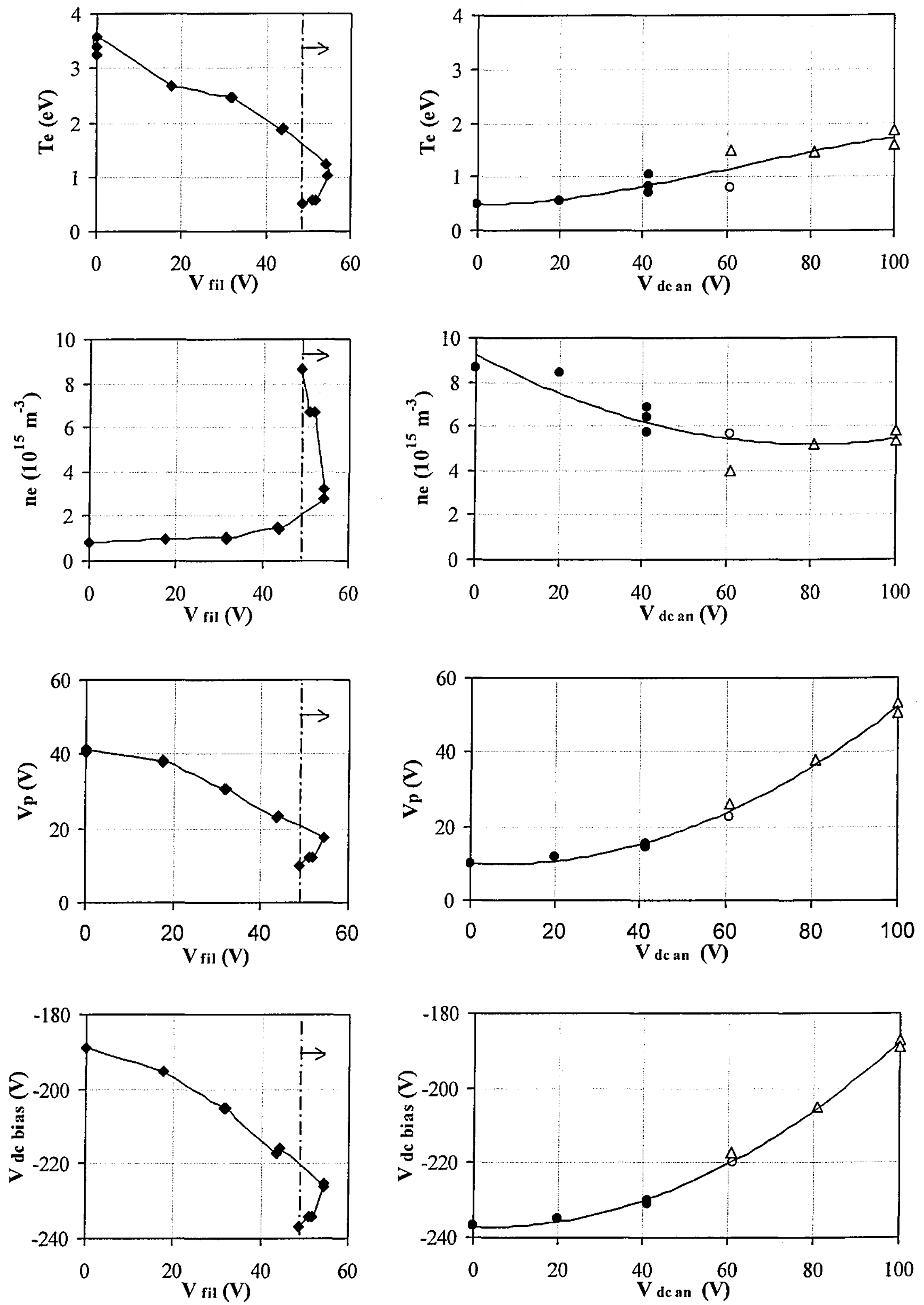

Fig. 3.12 Variation of plasma parameters with electron injection and removal in hydrogen discharge; RF power - 30 W, pressure - 46 mtorr.

♦ - discharge operation with electron injection only. Dotted lines mark the stage when the DC anode was switched on. ●, o, Δ - operation both with the electron source and the DC anode. Values of V_{fil}: ● - 48.9→ 30.9 V, o – 26.8 V, Δ - 24→ 14 V.

the probe. When the DC anode lifts up plasma potential, the probe circuitry cannot completely block out the RF potential. This leads to contamination of the probe signal, which is reflected in dispersion of measured electron temperature and density values above a DC bias 60 V. For the DC anode potential above 60 V, probe measurements are considered to be still reflecting trends in variation of plasma density and electron temperature, though there is less certainty in absolute values.

Plasma potential and electron temperature start rising, and electron density continue to rise (Fig. 3.11, right hand side graphs), when the DC anode is activated in addition to the electron source. Gradually, the increased potential of the DC anode pulls plasma potential upward by dragging net electron current from the discharge, thus leaving the grounded electrode sheath more and more positively charged. The growing potential of the grounded sheath causes stronger heating of the "cold" electron group, which in its turn elevates the plasma density through enhanced ionisation. The only contradiction in this scheme is the extent of the density increase, which in the 30 mtorr discharge cannot be solely caused by the DC anode. The DC anode without electron injection increases the density approximately by $0.3 \cdot 10^{15}$ m^{-3} (Fig. 3.10, left hand side graph), while with electron injection - by $1.5 \cdot 10^{15}$ m^{-3} (Fig. 3.11, right hand side graph). It is likely that the DC anode potential makes the ionisation process by injected "hot" electrons more effective. In order to clarify this process, it is worth testing the discharge configuration with one of its parameters changed, for example, with pressure increased.

The general trend of plasma parameter variation with electron injection at 46 mtorr is the same up to a filament bias of 55 V (Fig. 3.12, left hand side graphs). Further increase of potential of the filament power supply (marked 8 on the Fig. 3.2) leads to a reduction of the filament bias to 48.9 V, which is accompanied by a more than threefold increase of the plasma density (up to $8.8 \cdot 10^{15}$ m^{-3}). During this reversing of the filament bias, plasma

potential and electron temperature reach their lowest values: 10 V and 0.5 eV respectively. This effect, accompanied by the rapid change of the plasma parameters, is associated with the ignition of a discharge inside the electron source as described in section four of this chapter. Practically the filament acts as an emissive probe, pulling itself close to the local plasma potential. This regime is beneficial for increasing the plasma density in the main RF discharge, but is damaging for the filament. It leads to erosion of the emissive layer and an unstable current-voltage characteristic of the electron source (Fig. 3.5).

3.8.2 DC anode operation during electron injection

Application of positive potential to the DC anode increases the electron temperature and the plasma potential, but brings plasma density down (Fig. 3.12, right hand side graphs). Interestingly, simultaneous operation of the electron source and the DC anode affects the plasma density in qualitatively different ways at 30 and 46 mtorr. The DC anode initiates a decrease of density at 46 mtorr, while at 30 mtorr it causes a density increase. In order to verify these trends it is worth analysing ion energy distribution function (IEDF) data from the energy and mass analysis probe.

IEDFs of hydrogen ions H_3^+, H_2^+ and H^+, affected by electron injection and removal at 30 mtorr, are presented on the Fig. 3.13. Areas under the IEDF curves of H_3^+, H_2^+ and H^+ are in the ratio 19.76:5.71:1 in the unaffected plasma. This ratio reflects the balance of ionisation and loss for each ion species in the discharge. H_2^+ ions are produced by direct ionisation of hydrogen molecules. Low energy H_2^+ ions are transformed into H_3^+ ions in collisions with hydrogen molecule. This is a purely bulk plasma process, where ions have only thermal energy. It is obvious from the absence of any substantial tail of H_3^+ IEDF, which is normally associated with symmetric charge transfer reaction in plasma sheath. Such tails are well developed in H_2^+ and H^+ IEDFs. Ions, making up these tails, were "formed" within the plasma sheath and acquired less kinetic energy, when accelerating to the grounded substrate.

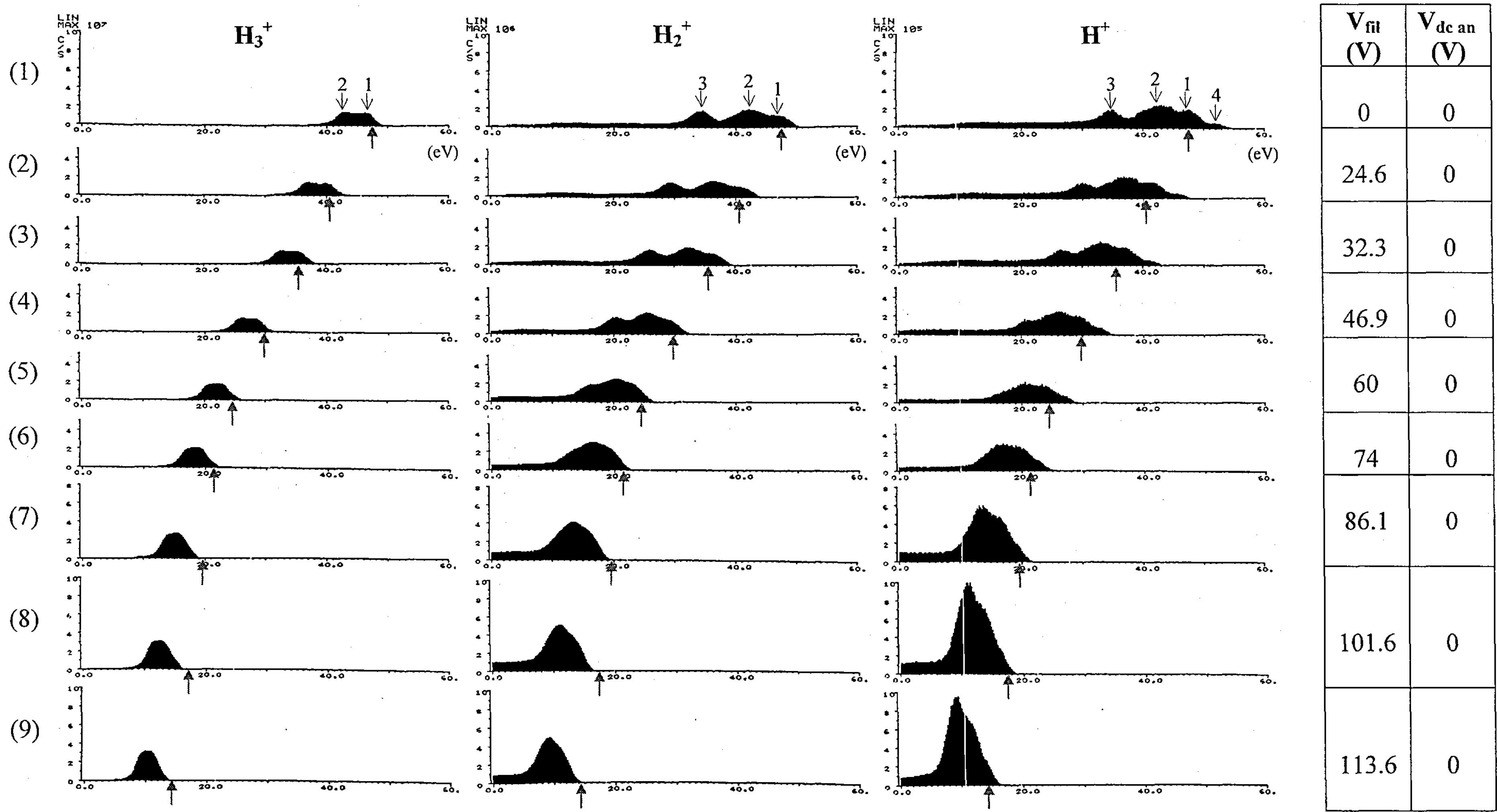

V_{fil} (V)	$V_{dc\ an}$ (V)
0	0
24.6	0
32.3	0
46.9	0
60	0
74	0
86.1	0
101.6	0
113.6	0

Fig. 3.13 Ion energy distribution at the grounded electrode in the H_2 discharge (30 mtorr) with electron injection

82

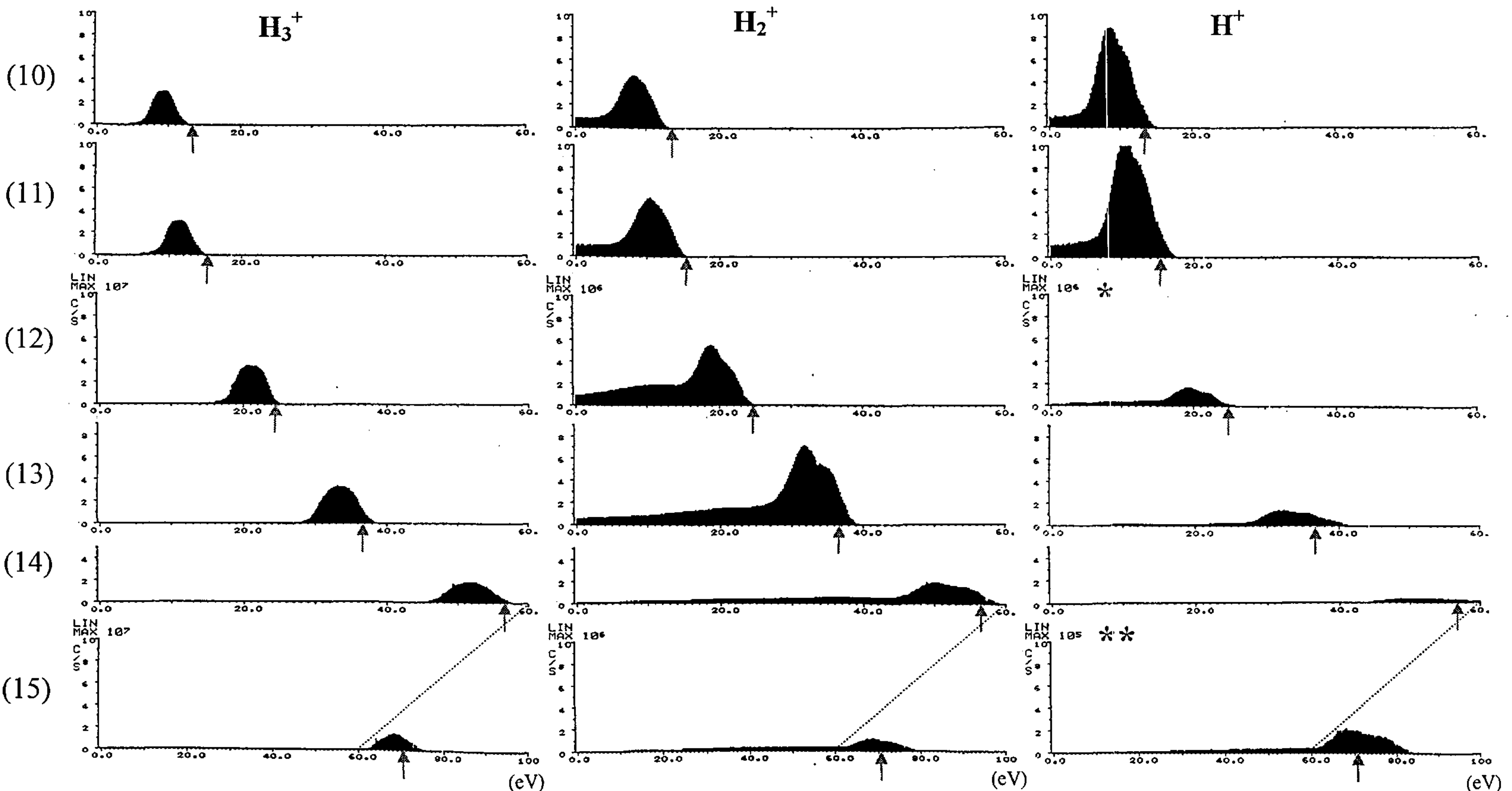

V_{fil} (V)	$V_{dc\ an}$ (V)
127.6	0
127.6	20
127.6	60
127.6	80
127.7	102
135.9	122

Fig. 3.13 (continued) **Ion energy distribution at the grounded electrode in the H_2 discharge (30 mtorr) with electron injection-removal; where U_{accel} – accellerating voltage of the electron source; U_{bias} – bias voltage of the DC electrode. ↑** - marking of plasma potential from probe measurement. Note the change in the energy scale from 60 to 100 eV at the last line graphs and the change in counts per second at the graphs marked * and **.

83

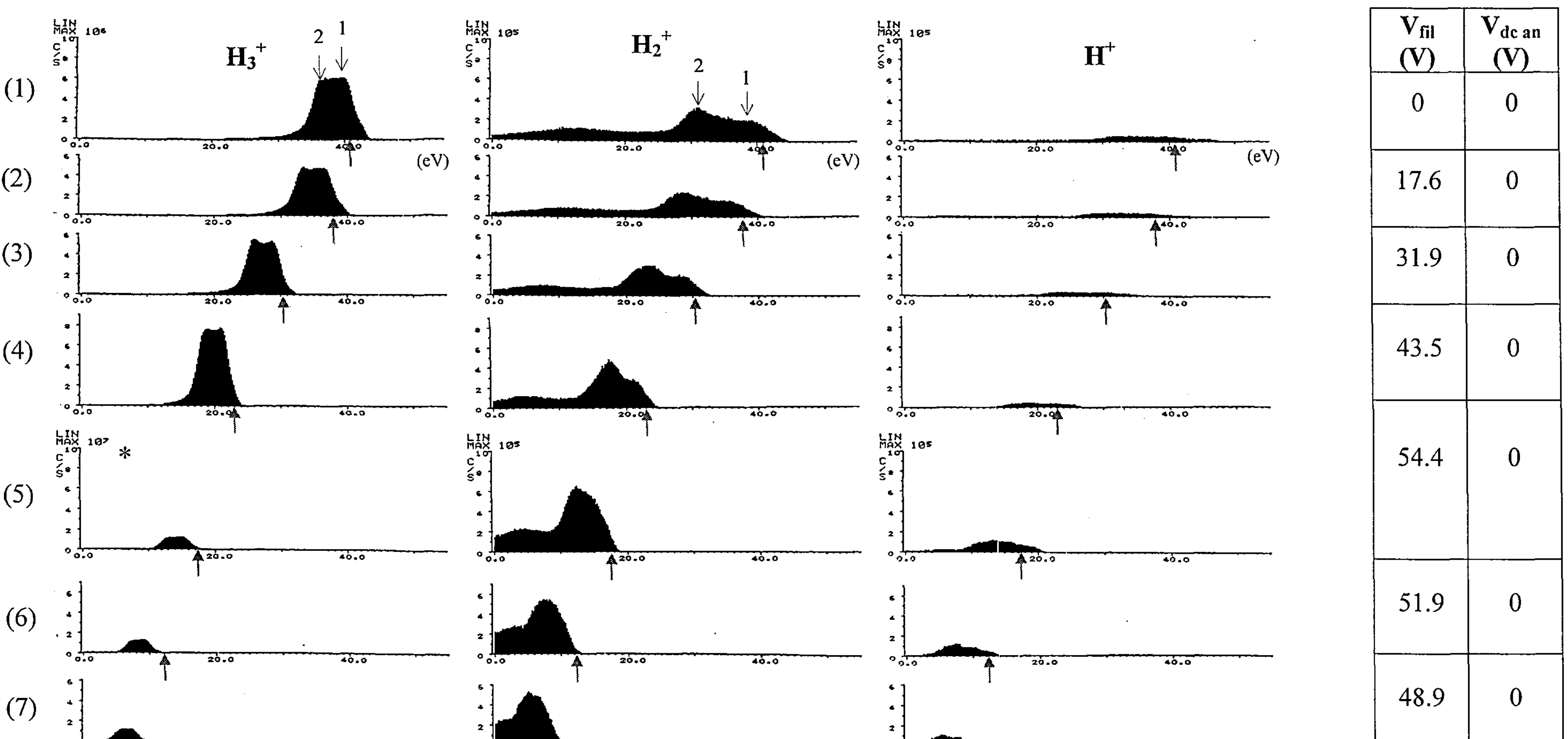

V_{fil} (V)	$V_{dc\,an}$ (V)
0	0
17.6	0
31.9	0
43.5	0
54.4	0
51.9	0
48.9	0

Fig. 3.14 **Ion energy distribution at the grounded electrode in the H_2 discharge (46 mtorr) with electron injection. ↑** - marking of plasma potential from probe measurement. Note the change in counts per second in the graph marked *.

84

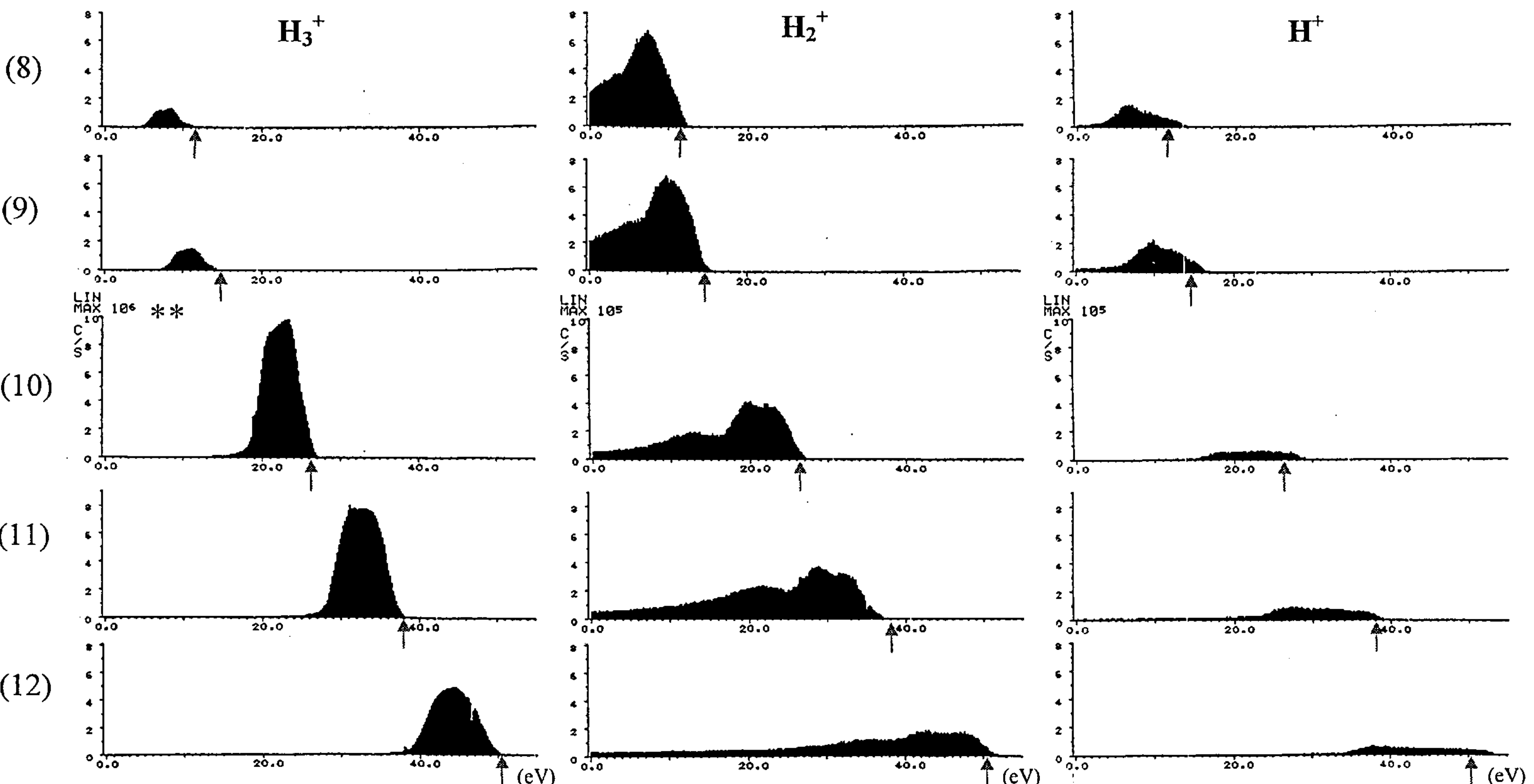

V_{fil} (V)	$V_{dc\ an}$ (V)
41.8	20
30.9	41.3
24.3	60.9
22.9	81.3
14.0	100

Fig. 3.14 (continued) **Ion energy distribution at the grounded electrode in the H_2 discharge (46 mtorr) with electron injection-removal; where U_{fil} – accellerating voltage of the electron source; $U_{dc\ an}$ – bias voltage of the DC electrode. ↑** - marking of plasma potential from probe measurement. Note the change in counts per second at the graph marked **.

85

In unperturbed discharges (i.e. without injection or removal of electrons) at 30 and 46 mtorr IEDFs of all hydrogen species exhibit structure with two or more gentle peaks (Fig. 3.13 and 3.14). Modulation of the IEDF is caused by RF components of the sheath potential. This process has been extensively studied in a number of works [83, 88, 89].

3.8.3 Time of ion transition through the sheath

A saddle-like structure of the ion distribution is associated with the flux of ions into the sheath at the maximum and minimum of the sheath potential being higher than during its intermediate values. This situation arises, when ions cross the sheath in a fraction of an RF cycle, i.e. transition time of ion through the sheath is less than RF period:

$$\tau_{ion} < \tau_{RF} \qquad (3.3)$$

A strongly structured IEDF is characteristic of plasma discharges at lower base frequencies, for example, 300 kHz [88]. The fact, that it happens in 13.56 MHz discharge in this work is a consequence of the low mass of hydrogen ions, and consequently their fast transition through the sheath.

The time of ion transition through the time-variable sheath can be expressed as:

$$\tau_{ion} = \int_0^{\bar{s}} \frac{dx}{\upsilon(x)} \qquad (3.4)$$

where $\bar{s}$ - time–averaged sheath thickness, $\upsilon(x)$ – ion velocity in the sheath. Ignoring initial ion velocity it is possible to express ion velocity in the sheath through the sheath potential as:

$$\upsilon(x) = \left(\frac{2 \cdot e \cdot V_s(x)}{m_i} \right)^{\frac{1}{2}} \qquad (3.5)$$

where e – electron charge, $V_s(x)$ – variable potential of the sheath and m_i – ion mass.

It is supposed that the conditions in the ion sheath are described by the Child-Langmuir law (3.2) and that the ion current density in the sheath is:

$$j_i = e \cdot n_e \cdot \upsilon_B \qquad (3.6)$$

where $\upsilon_B = \left(\frac{e \cdot T_e}{m_i}\right)^{\frac{1}{2}}$ - Bohm velocity, n_e – electron density at the edge of the sheath and T_e – electron temperature. Then by combining formulas (3.2) and (3.6) the sheath thickness could be expressed in terms of the sheath potential as:

$$x = A \cdot V_s^{\frac{3}{4}} \qquad (3.7)$$

where $A = \frac{2}{3} \cdot \left(\frac{2}{T_e}\right)^{\frac{1}{4}} \cdot \left(\frac{\varepsilon_o}{e \cdot n_e}\right)^{\frac{1}{2}}$. The first derivative of the expression (3.7) is:

$$dx = \frac{3}{4} \cdot A \cdot V_s^{-\frac{1}{4}} \cdot dV_s \qquad (3.8)$$

Using formulas (3.5) and (3.8) it is possible to substitute the integrand variable x in the expression (3.4) to V_s. Then with the integration limit $\bar{s}$ changed to a time-averaged sheath potential $\overline{V}_s$ the solution of the integral (3.4) is:

$$\tau_{ion} = 2^{\frac{3}{4}} \cdot \omega_{pi}^{-1} \cdot \left(\frac{\overline{V}_s}{T_e}\right)^{\frac{1}{4}} \qquad (3.9)$$

where $\omega_{pi} = \left(\frac{e^2 \cdot n_e}{\varepsilon_o \cdot m_i}\right)^{\frac{1}{2}}$ - ion plasma frequency. So, finally, it is possible to express time of ion transition through the sheath normalised to the number of RF cycles:

$$t_{ion} = \frac{\tau_{ion}}{\tau_{RF}} = \frac{1}{\pi} \cdot \frac{\omega_{RF}}{\omega_{pi}} \cdot \left(\frac{\overline{V}_s}{2 \cdot T_e}\right)^{\frac{1}{4}} \qquad (3.10)$$

where $\omega_{RF} = 8.52 \cdot 10^7$ the basic RF cyclic frequency. Taking the averaged sheath voltage to be equal to the plasma potential, the time of ion transition and the thickness of the sheath are calculated using density and temperature data from the probe measurements (Fig. 3.11 and 3.12).

As can be seen from the table 3.2 it takes hydrogen ions between 1.4 to 2.5 RF cycles, depending upon their mass, to pass through the sheath at 30 mtorr at the initial plasma conditions. The degree of modulation of IEDF is in inverse proportion to the

p (mtorr)	V_{fil} (V)	$V_{dc\ an}$ (V)	t_{ion}			$\bar{s}$ (mm)
			H^+	H_2^+	H_3^+	
30	0	0	1.442	2.04	2.498	3.433
	127.7	0	0.692	0.979	1.199	0.849
	135.9	122	0.658	0.931	1.14	1.872
46	0	0	1.084	1.533	1.877	2.398
	48.9	0	0.387	0.547	0.67	0.416
	14	100	0.555	0.785	0.961	1.361

Table 3.2 Time of ion transition through the sheath (number of RF cycles) and thickness of the sheath at different discharge conditions

transition time. The lightest ion H^+ has the shortest transition time and the strongest modulation (four peaks) of its IEDF, while the heaviest ion H_3^+ has just two peaks on its IEDF.

The 4 V separation of peaks in the H_3^+ IEDF (Fig 3.13, line 1) is relatively small, representing an intermediate case between a singly peaked IEDF and a pronounced saddle-like distribution. For comparison, Coburn and Kay [90] presented the energy distribution of residual H_3^+ ions with peak split of 105 V at the grounded electrode of 13.56 MHz discharge. The quoted disharge parameters were 100 W power and argon pressure 75 mtorr. The triple and quadruple peaks of an original H_2^+ and H^+ IEDFs (Fig. 3.12, line 1) can't be explained just by a simple sinusoid of sheath potential variation. The presence of higher harmonic components in the sheath potential, which increases complexity of ion dynamic in the sheath, may be their cause.

With electron injection on and increasing, RF modulation of the IEDFs becomes gradually smoothed (Fig. 3.13, lines 2-10), almost disappearing at 127.6 V filament bias. But at this level of electron injection the time of transition through the sheath for all hydrogen ions is decreased more than twice in comparison with the initial values (Table 3.2). This seeming contradiction is explained by a significant decline of the RF component

of the sheath potential. Reduction of RF in plasma with electron injection is confirmed by the decrease of the maximum energy of the IEDFs in line with the decreased value of plasma potential (Fig. 3.13, line 10). At the initial conditions RF modulation spreads the maximum ion energy above plasma potential. The maximum energy of the lightest H^+ ions exceeds plasma potential approximately by 7 V, while for heaviest H_3^+ ions it is just 1 V (Fig. 3.13, line 1). At 127.6 V filament bias the maxima of the IEDFs (Fig. 3.13, line 10) practically coincide with plasma potential, with the a small 1 V excess still present on the H^+ IEDF. So, the sheath of the grounded electrode behaves more like in case of direct current discharge. Nevertheless, signs of RF in the plasma could be still detected from the spreading of the full width at half maximum (FWHM) of the IEDFs. As was demonstrated in [83] the FWHM of non-modulated argon IEDF is of the order of $(0.3\text{-}1)\cdot T_e$ below 50 mtorr. Above 50 mtorr rapid pressure-dependent spreading of the IEDF occurs. IEDFs of H_3^+ and H_2^+ have FWHM of 3.5 V and 5 V respectively at 127.6 V filament bias (Fig. 3.13, line 10), which is 1.75 and 2.5 times the electron temperature of 2 eV, measured at this plasma condition (Fig. 3.11). As for H^+ IEDF, it still manifests RF modulation by having three very smooth peaks.

Subsequent activation of the DC anode (Fig. 3.13, lines 11-15) leads to recovery of modulation of the H_2^+ and H^+ IEDFs and broadening of the H_3^+ IEDFs. But this time RF modulation produces just two peaks at the H_2^+ and H^+ IEDFs despite further reduction of transition time of ions through the sheath (Table 3.2). The additional decrease of ion dwell in the sheath is attributed to a twofold increase of plasma density (Fig. 3.11). At a DC anode potential 122 V the sheath size is almost twice as low in comparison with the original value (Table 3.2), which produces a higher electric field in the sheath. So, ions experience stronger acceleration, while falling through the sheath. As a result, their time of transit slightly decreases even though the sheath expands. The lessened modulation of IEDFs in comparison with a discharge without electron injection and removal is ascribed to

a change of the sheath voltage. It is supposed, that higher harmonics are either suppressed or diminished with the DC anode on in presence of injected electrons.

At 46 mtorr transition times of ions through the sheath are generally shorter than at 30 mtorr: by 25% without electron injection or removal and by 45%, when electron injection is at maximum intensity (Table 3.2). This is linked with there being a denser plasma at 46 mtorr: almost double that in the original state and almost 6 times higher than that at maximum of electron injection (Fig. 3.11 and 3.12). A gradual decrease of plasma density with DC anode activation at 46 mtorr explains the almost threefold growth of the sheath thickness and increase of the ion transition times (Table 3.2).

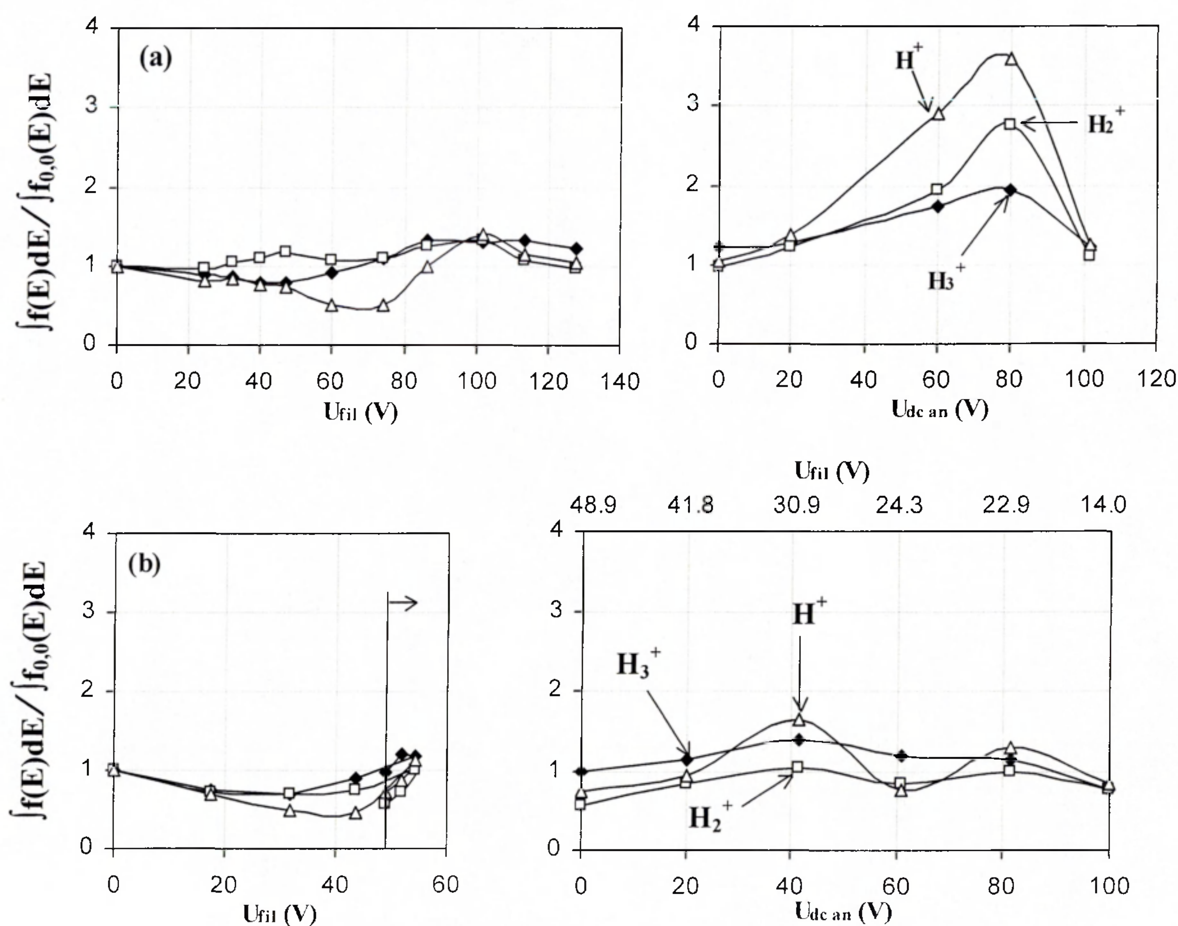

Fig. 3.15 Variation of IEDF area under the curve as a function of electron injection and removal at (a) – 30 mtorr and (b) – 46 mtorr. Area under the curve is normalised to its value at the original plasma condition ($V_{fil} = 0$, $V_{dc\ an} = 0$) for each ion.

Without injection or removal of the electrons H_2^+ IEDFs (Fig 3.14, line 1) exhibit less modulation than at 30 mtorr, having just two well defined peaks. This can be ascribed to a

reduction of higher harmonic components of the sheath voltage. In general, the effect of electron injection (Fig. 3.14, lines 1-7) and DC anode effect (Fig. 3.14, lines 8-12) on H_3^+, H_2^+ and H^+ IEDFs is qualitatively the same as at 30 mtorr.

The maximum energy of all IEDFs follows the variation of plasma potential, and electron injection causes reduction of modulation of IEDFs. A subtle difference between IEDFs at the two pressures could be traced, when areas under IEDF curves were calculated (Fig. 3.15).The area under the IEDF curve is proportional to the ion current reaching the surface of the grounded electrode. So, graphs in Fig. 3.15 demonstrate relative variations of those components of currents from the separate hydrogen ions, resulting from electron injection and removal.

The most obvious feature of the graphs is the maximum at 80 V DC anode bias, operating at 30 mtorr. So, the DC anode causes a stronger relative growth of the ion currents at 30 mtorr than at 46 mtorr. This supports the data of the electrostatic probe (Fig. 3.11 and 3.12), which show the beneficial effect of the DC anode on plasma density at 30 mtorr in contrast to 46 mtorr. It is suggested that at 30 mtorr the DC anode opens a "free way" for the injected electrons. Without the DC anode, injected electrons are slowed down and reflected back by a negative potential dip formed in front of the electron source (Fig. 3.16).

3.8.4 Potential structnres in the RF discharge with electron injection-removal

The appearance of negative potential structures in front of an electron source was registered by Ando and co-workers [68, 69] while studying pre-ignition conditions of DC discharges. A V-shaped potential dip was measured by an emissive probe ahead of the electron beam source, which was similar in its configuration to the source used in this work. Interestingly, the minimum of the dip potential corresponded to the energy of the electron beam, which was 30 V. The potential dip in front of the electron source existed only until ignition of the discharge; then it disappeared.

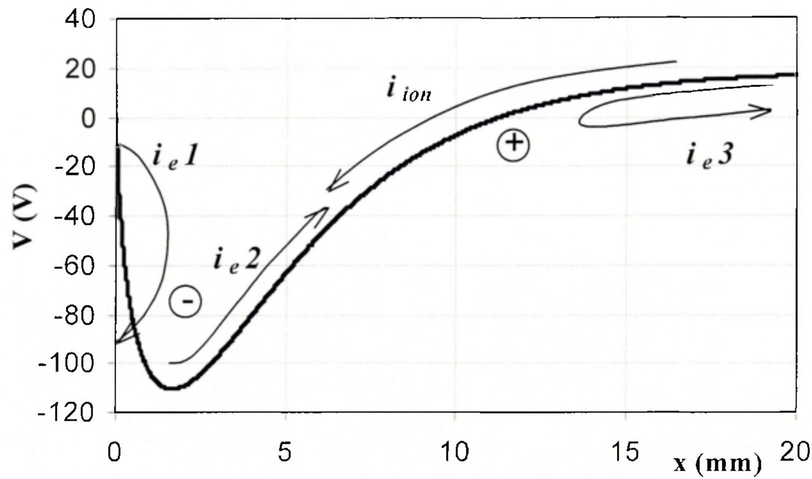

Fig. 3.16 Schematic time–averaged plasma potential profile in front of the electron source in RF discharge at 30 mtorr.

It is proposed that there is a similar potential structure formed ahead of the electron source in the discharge at 30 mtorr (Fig. 3.2). Having potential minimum equal or close to the accelerating voltage of the electron source acts as a potential barrier for the injected electrons. The electrons are deflected towards the grounded electrode surface, which surrounds the mesh of the electron source (Fig. 3.1(D)). In this way a substantial part of current of the electron source i_e1 (Fig. 3.16) is closed in its vicinity without penetrating the main discharge. The potential well acts as a virtual cathode and draws ion current i_{ion}. According to Hershkowitz [91] energetic ions transversing the potential well may be converted into slow ions due to charge exchange. Eventually, they could eliminate the well by neutralising its negative charge. In our case this scenario is unlikely due to a difference in current densities from the electron source and from the plasma. At the maximum current of electron source at 30 mtorr (Fig. 3.5), which is 63 mA, the electron current density is 315 A/m^2. Ion current at this plasma condition (Fig. 3.11), calculated using the formula (3.5), is just 2.17 A/m^2. Simply, the plasma is incapable of producing high enough ion current i_{ion} to compensate negative charge in front of the electron source. Plasma electron current i_e3 (see Fig. 3.16) is reflected back from the downward potential slope. So, in other words the negative potential well forms a double layer structure near the electron source.

Under the effect of RF variation of plasma potential it slightly expands and contracts. In this way some injected electrons, which appear to the right from the instantaneous potential minimum, are accelerated towards the main discharge, producing the current i_e2. This time they gain higher energy than in the electron source due to the contribution from the plasma potential. It is this group of "hot" electrons, which increases threefold the plasma density by ionisation (Fig. 3.11). Activation of the DC anode changes the distribution of plasma potential across the plasma volume to the DC-like one (Fig. 3.17).

When the DC anode is not activated, the distribution of potential inside the discharge plasma is quite flat (graph 1 on the Fig. 3.17). The electron source creates a potential dip, which prevents most of injected electrons from entering the main discharge. When DC anode potential is rising, a DC-like potential distribution appeares in plasma (graph 2 on the Fig. 3.17). This explains the electrostatic probe data (Fig. 3.11 and 3.12), which show values of the time-averaged plasma potential to be lower than the potential of the DC anode. On the contrary, when a flat RF-type potential distribution is implied, the time-averaged plasma potential is always higher

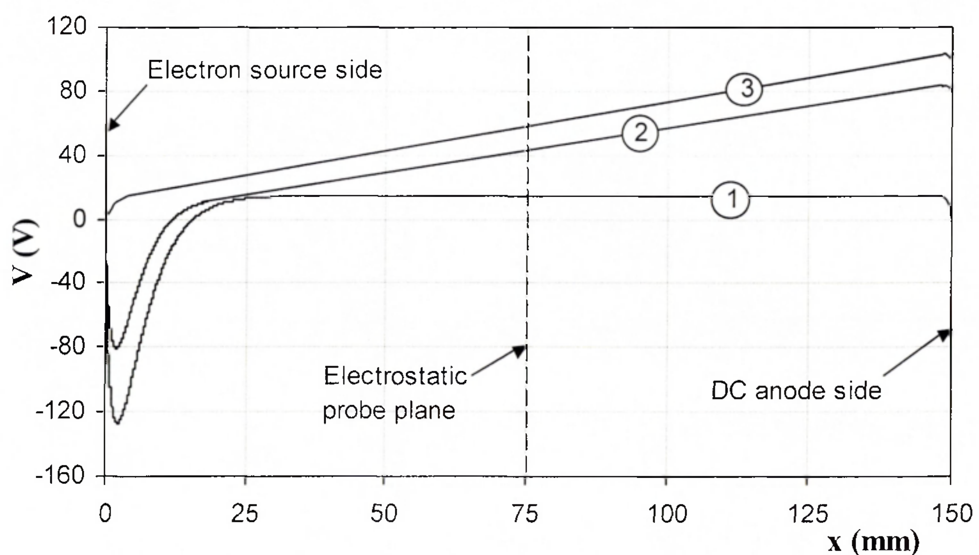

Fig. 3.17 Schematic variation of time-averaged potential in the discharge volume between the electron source and the DC anode at 30 mtorr.

than the one of the large DC anode (Fig. 3.4(b)). The resulting electrical field causes an increase of ion current towards the double layer. The potential dip minimum starts to rise, releasing more injected electrons in the discharge. This is indirectly confirmed by growth of plasma density measured by the probe (Fig. 3.11), and by increase of the area under the IEDF curve (Fig. 3.15). The area under the curve reaches it maximum at 80 V DC anode potential, then drops. This is associated with complete fading of the negative potential structure in front of the electron source (graph 3 on the Fig. 3.17). As a result there should be change in the bulk potential structure of the discharge, causing variation of plasma density near electrode surfaces. A sharp decrease of plasma density near the top side of the grounded electrode is thought to be responsible for the decline of the IEDF signal above 80 V DC anode potential.

Much smoother changes in area under the IEDF curve at 46 mtorr with DC anode operation are associated with the absence of any negative potential structures in front of the electron source. This is related to the internal discharge in the electron source, which prevents the formation of the double layer sheath ahead of the electron source. Electrons are injected in the discharge without obstruction. Hence, the increase of plasma density with electron injection at 46 mtorr is six time higher than at 30 mtorr (Fig. 3.6). With DC anode activation the distribution of plasma potential is qualitatively expressed by the graph 3 on the Fig. 3.17. This implies that no surplus electrons could be drawn from the electron source in comparison with the 30 mtorr case. Consequently, with the DC anode acting as an electron sink, plasma density decreases (Fig. 3.12).

Qualitative explanation of the effects of electron injection-removal and the appearance of the double layer sheath in front of the electron source are based on the time-averaged measurements of the elecrostatic probe and the energy and mass analysis probe. Although they provide a general insight into the processes of the discharge, a deeper understanding could be achieved by space- and time-resolved measurements of the

discharge parameters. These could reveal more fine mechanisms behind the discharge phenomena. For example, studies of double layer in DC discharges revealed effects of their oscillations at frequencies at kHz [92] and MHz [93] range. Gyergyek [92] demonstrated that DC anode potential could strongly effect the frequency of double-layer oscillations. In our case it would be interesting to trace oscillations of the double layer sheath in front of the electron source and to relate them to the discharge frequency and the DC anode potential. But this kind of research lies beyond the framework of the current research program.

Chapter IV. "Modeling"

4.1 Introduction

Probe measurements described in chapter III have demonstrated a clear division of plasma electrons into a "cold" major electron group and "hot" tail electrons. Such a distribution can be approximated by a two temperature Maxwellian one (Fig 3.8). Experiments on the effects of the DC electrode on RF plasma have established a growing divergence of temperatures of "cold" and "hot" electrons with the application of positive potential to the DC electrode (Fig 3.10). In order to understand this effect on the EEDF (Appendix E) it is necessary to retrace formation of the EEDF shape.

A bi-Maxwellian nature of EEDF in a low pressure RF discharge originates from interaction of electrons with the oscillating plasma-sheath boundary. Previously it has been studied both experimentally [94, 95] and theoretically [96, 97]. A term "stochastic heating" is commonly used to describe the interaction of electrons with an RF sheath. This reflects only part of the process, namely, the ascending part of the sheath cycle, when electrons gain energy from the sheath. During the descending part of the sheath cycle electrons lose energy. So, strictly speaking, the overall electron-sheath interaction could be called a heating-and-cooling cycle.

Typical models, calculating electron distribution in the vicinity of the sheath, use particle-in-cell or fluid approaches. In order to investigate the effect of a DC electrode on an EEDF a simple method of solving electron motion equation in the oscillating sheath field will be used. It will be demonstrated that a time-dependent shape of the sheath determines an extent of heating-cooling of electrons. The effect of ohmic heating will not be considered due to its minor role. In the low-pressure capacitive RF discharge its power constitutes less than 10% in comparison with stochastic heating [98]. A model, based on balance of currents to electrode surfaces, will be employed for investigation of the variation of the plasma potential with electron injection and removal.

4.2 Modeling of electron interaction with an RF sheath

4.2.1 Model

A basic case of an RF sheath acting on a single temperature Maxwellian electrons coming from plasma is considered. Figure 4.1 shows a schematic potential distribution between the powered and the grounded electrodes during a single RF cycle.

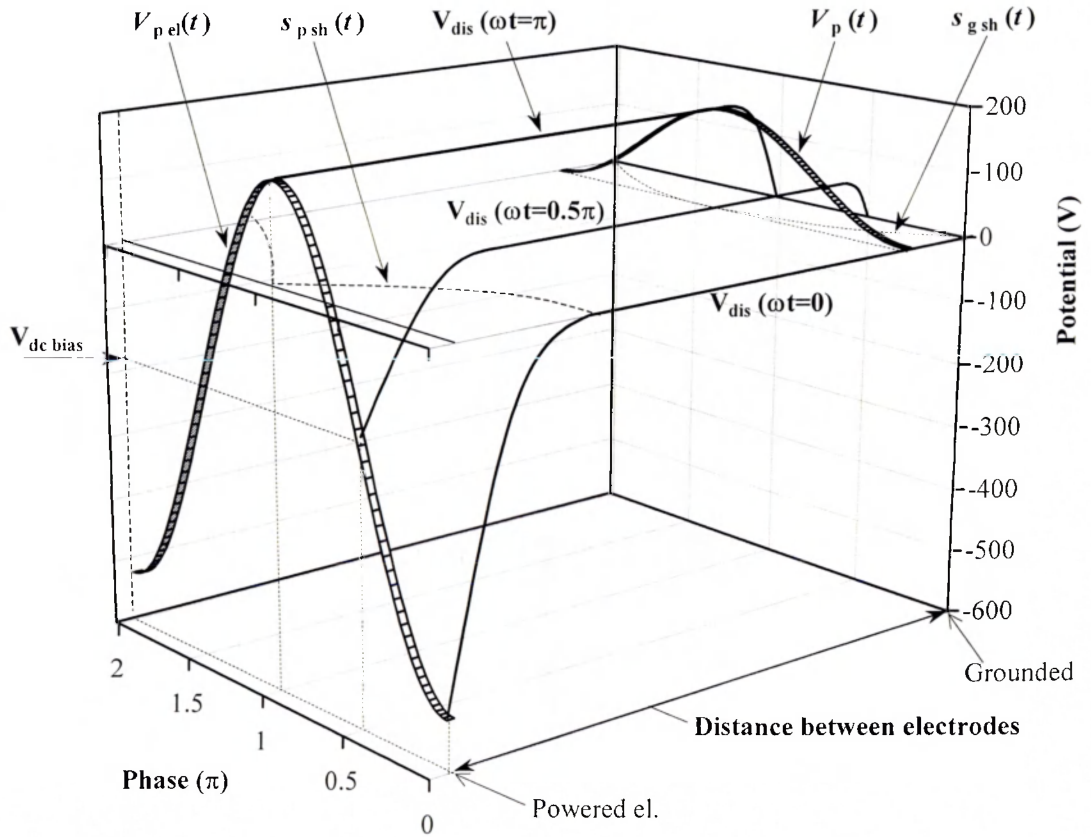

Fig. 4.1 Space- and time-dependent potentials of the discharge, where:
V_{dis} – distribution of potential between the electrodes, $V_{p\,el}(t)$ and $V_p(t)$ – time-dependent potentials of the powered electrode and plasma, $s_{p\,sh}(t)$ and $s_{g\,sh}(t)$ – time variation of the sheaths of the powered and grounded electrodes, $V_{dc\,bias}$ – self-bias potential of the powered electrode.

It is considered that at each moment the plasma potential is uniform across the bulk of discharge. Hence, the plasma potential is equivalent to the sheath potential of the grounded electrode. The time averaged energy distribution functions of electrons reflected into the plasma from grounded and powered electrode sheaths are calculated for different potentials of the DC bias electrode. The model is built using the following assumptions:

1. The sheath is one-dimensional and has a uniform ion density, i.e. it is a matrix sheath. So, the sheath thickness $s(t)$ and potential $V(t)$ are linked through by the formula

$$s(t) = \left(\frac{2 \cdot \varepsilon_0 \cdot V(t)}{\mathrm{e} \cdot \mathrm{n_e}} \right)^{\frac{1}{2}} \quad (4.1)$$

2. The sheath potential of the grounded electrode, being equal to the plasma potential, is assumed to have a sinusoidal form as in [99] for the grounded electrode

$$V_{g\,sh}(t) = \mathrm{V_0} \cdot (1 + \sin(\omega \cdot t + \varphi)) \quad (4.2a)$$

The powered electrode potential is set by the formula

$$V_{p\,el}(t) = \mathrm{V_{RF}} \cdot \sin(\omega \cdot t + \theta) + \mathrm{V_{dc\,bias}} \quad (4.2b)$$

where V_{RF} =340 V is an amplitude of a sinusoidal signal of RF generator, and $V_{dc\,bias}$ is a self-bias potential.

3. The electron motion in the sheath is described by the equation

$$\mathrm{m_e} \cdot \frac{\mathrm{d}^2 l}{\mathrm{d}t^2} = -\mathrm{e} \cdot \frac{\mathrm{d}E(t)}{\mathrm{d}t} \quad (4.3)$$

where l – distance of the electron from the electrode surface, $E(t)$ – sheath electric field determined as

$$E = -\frac{\mathrm{d}V}{\mathrm{d}s} \quad (4.4)$$

4. It is supposed that at any moment of time electrons from the plasma are described by Maxwellian EEDF (Appendix E):

$$\mathrm{f}(W) = \frac{2}{\sqrt{\pi}} \cdot W^{\frac{1}{2}} \cdot \mathrm{T_e}^{-\frac{3}{2}} \cdot \exp\left(-\frac{W}{\mathrm{T_e}} \right) \quad (4.5)$$

where W – electron energy (V), T_e – electron temperature (V).

5. The plasma is collisionless in the vicinity of the sheath.

6. The initial plasma parameters are the same as in the real discharge (Fig. 3.10): electron temperature T_e=1.4 eV, electron density $n_e=2 \cdot 10^{15}$ m^{-3}; but they don't change with variation of potential of the DC bias electrode.

The effect of DC bias potential is introduced through the equating of time-averaged potentials of the grounded electrode sheath to the plasma potential values taken from the probe measurements (Fig. 3.10). In this way V_0 values (formula 4.2a), are selected. The potential of the powered electrode sheath is calculated by subtracting the powered electrode potential equation (4.2) from the grounded sheath potential equation (4.2), given that they coincide at their maxima (Fig. 4.2).

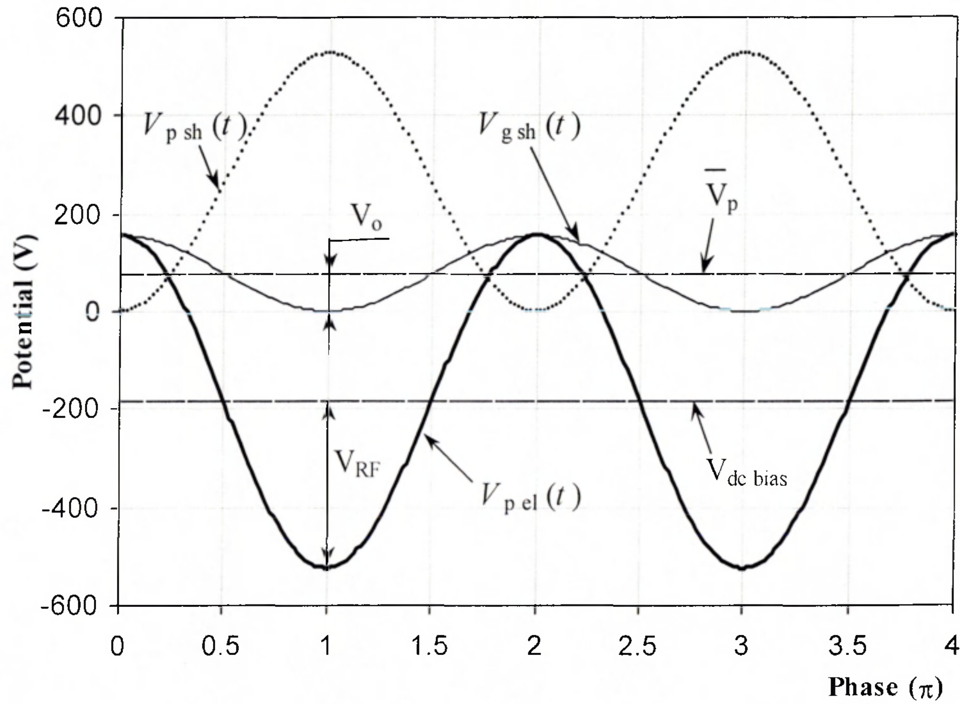

Fig. 4.2 Time-dependent potential settings, used in the model:

$V_{p\,sh}(t)$ – powered electrode sheath, $V_{g\,sh}(t)$ – grounded electrode sheath,

$V_{p\,el}(t)$ – powered electrode, $\overline{V}_p$ - time-averaged plasma potential.

Studies of RF discharges have demonstrated substantial gradients of plasma density, which typically declines from discharge center towards electrode surfaces. To account for this effect it is assumed that plasma density at the sheath boundary is approximately one quarter of its value in the center, as predicted in the model of Graves and Jensen [100] for hydrogen RF discharge.

In order to simplify solution of the electron motion equation (4.3) for the variable electric field, the RF period is divided into intervals $\Delta t = \dfrac{T}{2 \cdot 10^4}$. It is assumed that the sheath electric field is constant during each interval, changing abruptly its value at the

interval boundary. Then single and double integration of the equation (4.3) gives expressions for electron velocity (4.6) and position (4.7):

$$\upsilon_i = \upsilon_{i-1} - \frac{e \cdot E_i \cdot \Delta t}{m_e} \qquad (4.6)$$

$$l_i = l_{i-1} - \left(\upsilon_i \cdot \Delta t - \frac{e \cdot E_i \cdot \Delta t^2}{2 \cdot m_e} \right) \qquad (4.7)$$

Subscript i designates a number of the considered RF cycle interval with values of the previous interval used as boundary conditions. A range of successive calculations using formulae (4.6) and (4.7) gives an electron trajectory within the sheath. The electron exit energy is calculated, when its distance from the electrode surface becomes equal or larger than the sheath thickness $l_i \geq s_i$. Electrons reaching the electrode surface are not considered further. In order to trace the sheath effect on the whole spectrum of electrons (0-12 eV) the original EEDF is subdivided into 0.02 eV slots.

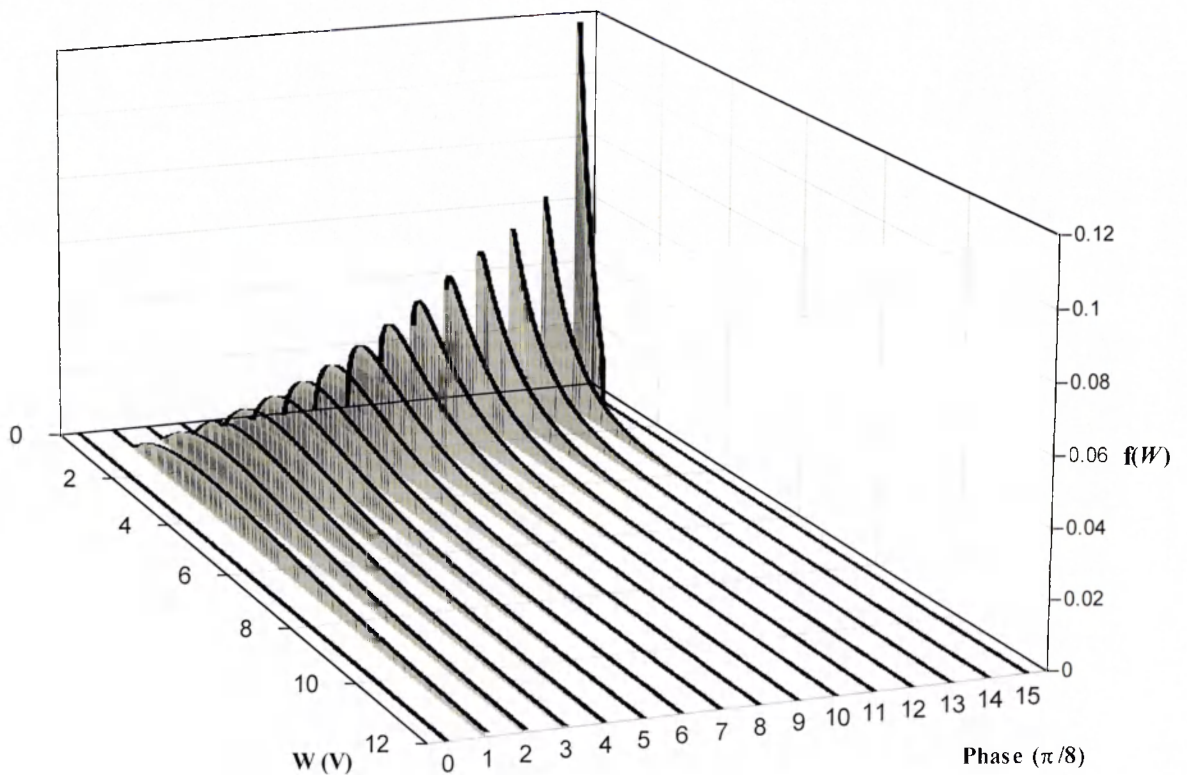

Fig. 4.3 Transformation of maxwellian electrons (T_e = 1.4 eV) during interaction with the matrix grounded electrode sheath over the period of RF cycle. $V_{dc\ an}$ = 0 V

Electron number conservation before and after interaction with the sheath is maintained by equalizing areas under the original and exit EEDF curves. The whole RF cycle is divided into 16 phases. For each phase a transformation of one sixteenth the original EEDF equation (4.5) is calculated (Fig. 4.3). Transformed EEDFs are summed up to obtain a time-averaged distribution function.

The algorithm for calculation of the EEDF transformation by the sheath at a given phase was written using programming functions of "Mathcad Professional" software. Then data were transferred to "Microsoft Excel" for calculation of the time-averaged EEDF and graphical presentation of the results.

4.2.2 Results and discussion

The cooling-heating effect of the RF sheath is apparent from the graphs in Fig. 4.3. During the sheath expansion ($\omega \cdot t = 0 \rightarrow \pi$) the EDFs of reflected electrons are elongated towards higher energies. The strongest heating occurs at $\omega \cdot t = \pi/8$, when electric field of the sheath is weak enough to allow deep penetration of electrons in the sheath without reaching electrode surface. At the point of maximum sheath expansion $\omega \cdot t = \pi$ the EDF of reflected electrons is changed very little compared with the original one. During the sheath recession ($\omega \cdot t = \pi \rightarrow 2 \cdot \pi$) the EDFs are shrunk towards smaller energies. The step is formed at the EEDF at $\omega \cdot t = \frac{15}{8} \cdot \pi$ due to collision of tail electron with the electrode.

Time-averaged EEDF and EEPF (Appendix E) of electrons reflected from grounded and powered sheaths are presented in Fig. 4.4. The model produces EEPF graphs (Fig. 4.4, (b) and (d)) with the smoothly curved "cold" part, which makes it difficult to assign it a certain value of electron temperature. As for the "hot" tail electrons, first, the powered sheath produces a hotter tail: 2.8 eV versus 2.0 eV (Fig. 4.2, (d) and (b)). Second, the DC electrode potential of 90 V affects the sheaths heating ability in the opposite ways. The tail temperature of EEDF is increased by 20% up to 2.4 eV for the grounded sheath (Fig. 4.2 (b)). At the same time, it is decreased by 14.3% down to 2.4 eV for the powered

sheath (Fig. 4.2, (d)). The effect of the DC electrode on the powered sheath contradicts the probe measurements. They indicate up to 50% increase of the tail temperature (Fig. 3.10).

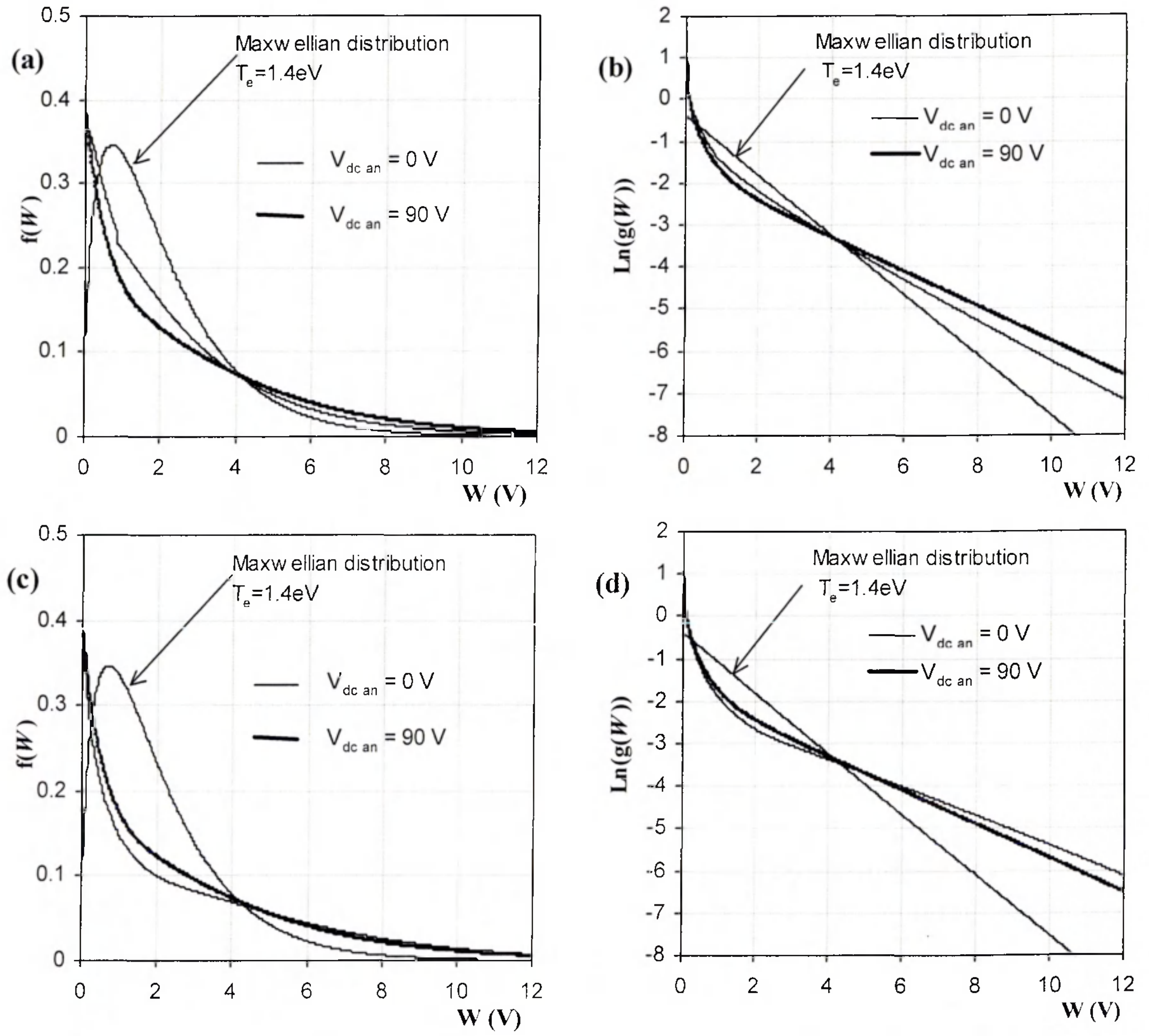

Fig. 4.4 EEDF and EEPF after interaction of Maxwellian electrons with the matrix grounded ((a) and (b)) and powered ((c) and (d)) electrode sheath affected by the positive DC electrode. The sheath voltage is set with the assumption of a single harmonic.

One of disadvantages of the basic matrix model is that it doesn't take into account a multi-harmonic nature of RF sheath. The problems of passive probe measurements described in the chapters 2 and 3, especially at the higher values of the DC electrode potential (Fig. 3.10) clearly point out at presence of several harmonics. It is well known that the plasma potential of RF excited plasmas contains various harmonics at significant levels [101]. To include harmonic terms one can express the grounded sheath potential containing four harmonics by the formula below:

$$V_g(t) = V_0 \cdot [A + \sin(\omega \cdot t + \varphi) + B \cdot \sin(2 \cdot (\omega \cdot t + \varphi)) + C \cdot \sin(3 \cdot (\omega \cdot t + \varphi)) + D \cdot \sin(4 \cdot (\omega \cdot t + \varphi))] \quad (4.8)$$

Values of coefficients are taken to be the following: A=1.3157732, B= -0.45, C=0.22, D = -0.1, as an example.

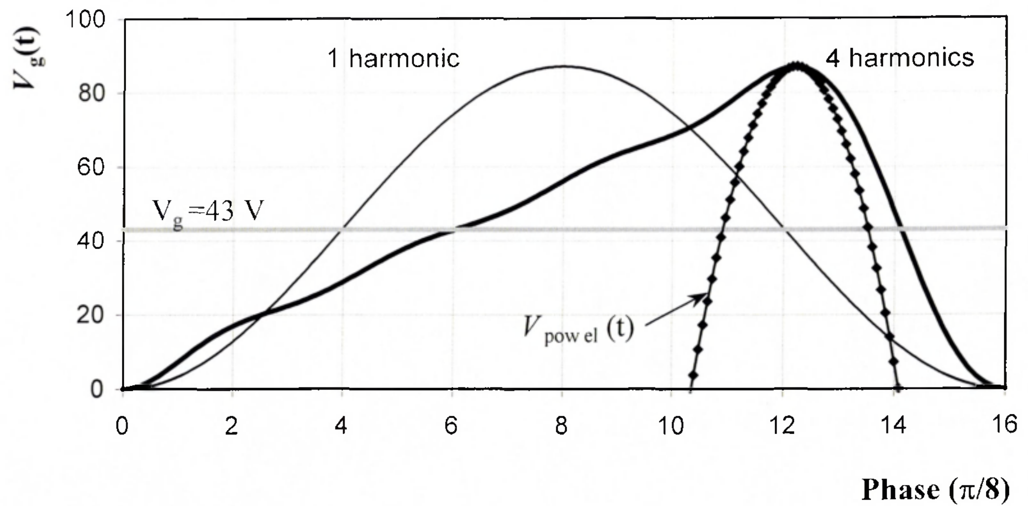

Fig. 4.5 Single and four harmonic potential curves of the grounded electrode sheath. The time-averaged sheath potential is 43 V; the DC bias electrode is grounded.

Of course, different values may apply across the range of conditions. In order to have zero phase of the potential curve (4.8) at its minimum (Fig. 4.5) the value of φ is chosen to be -0.764·π. Formula (4.8) has been used in place of (4.2a) in order to model the presence of potential harmonics across the sheath. The four harmonic sheath of the grounded electrode significantly reduces (below 0.5 eV on energy scale) a group of "cold" electrons in the resulting EVDF (Fig. 4.6 (b)). This could be expected since a larger part of oncoming electrons interacts with the sheath during its longer (3/4 of the cycle) ascending part (Fig. 4.5).

With the DC electrode at a potential of 90 V there is an increase of the "hot" tail temperature from 1.7 eV to 1.9 eV, which is just 12%. If the constraining assumption 5 of the model is partly eased, i.e. sheath boundary plasma density is allowed to vary with DC electrode potential, the resulting sheath effect on electrons can be quite the opposite. For example, variation of electron density at the sheath boundary from $0.25 \cdot n_e$ at 0 V up to $0.5 \cdot n_e$ at 90V DC electrode potential reduces the tail temperature down to 1.514 eV or by 10.8% (Fig. 4.6). This "net cooling" effect of the sheath is explained by a reduced sheath

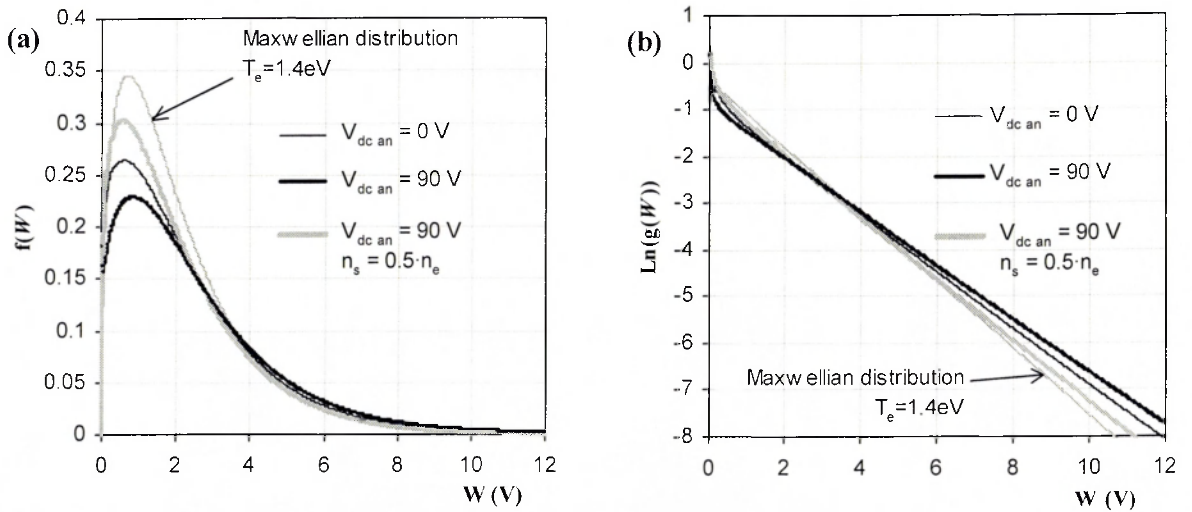

Fig. 4.6 EEDF (a) and EEPF (b) after interaction of maxwellian electrons with the matrix grounded electrode sheath affected by the positive DC electrode. The sheath voltage is set with the assumption of four harmonics.

thickness according to the formula (4.1). It leads to a stronger electric field in the sheath, hence shorter residence time of electrons in the sheath, hence weaker heating of reflected electrons.

The effect of the four harmonic powered electrode sheath (Fig. 4.7(b)) is stronger in comparison with the single harmonic sheath (Fig. 4.4(d)). Without the DC bias electrode it heats the tail electrons up to 3 eV, compared with 2.55 eV by the single harmonic sheath.

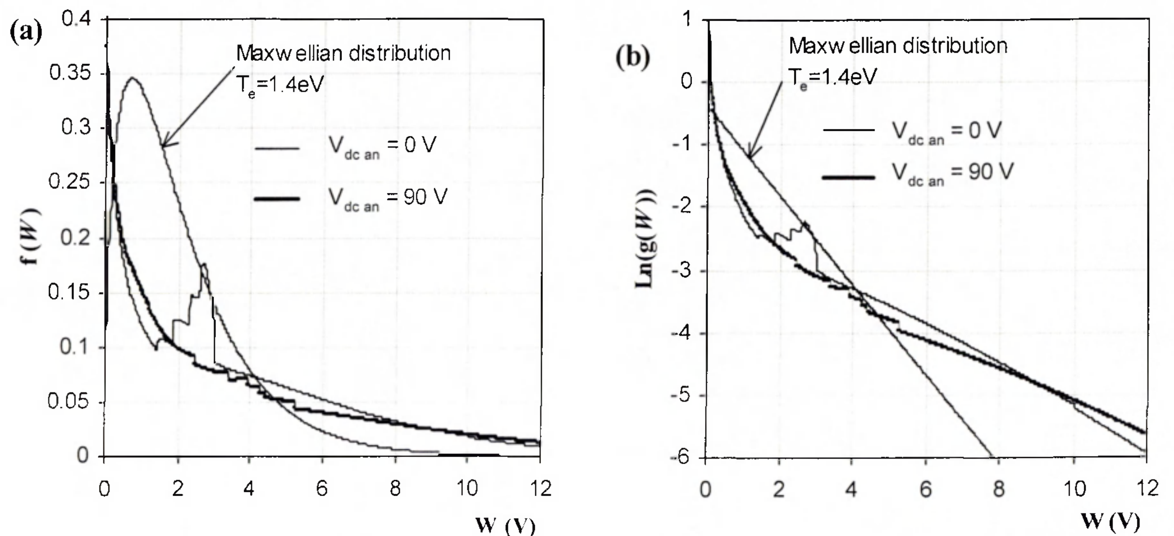

Fig. 4.7 EEDF (a) and EEPF (b) after interaction of the maxwellian electrons with the matrix powered electrode sheath affected by the positive DC electrode. The sheath voltage is set with the assumption of four harmonics. Double reflection of cooled electrons is taken into account.

At the DC bias potential 90 V the tail electrons are heated up to 4.26 eV: 42% gain in comparison with 8.2% for the single harmonic. This gain of the tail electrons temperature is close to the one measured by the probe (Fig. 3.10).

The origin of the harmonic effect of the powered electrode sheath could be seen from the variation of the sheath potential and electric field during RF cycle (Fig. 4.8). Biasing the DC electrode up to 90 V causes the growth of the powered sheath potential being delayed by approximately 1/16 of the cycle period (Fig. 4.8 (b)). It leads to formation of a dent in the ascending slope of the sheath electric field (Fig. 4.8 (c)).

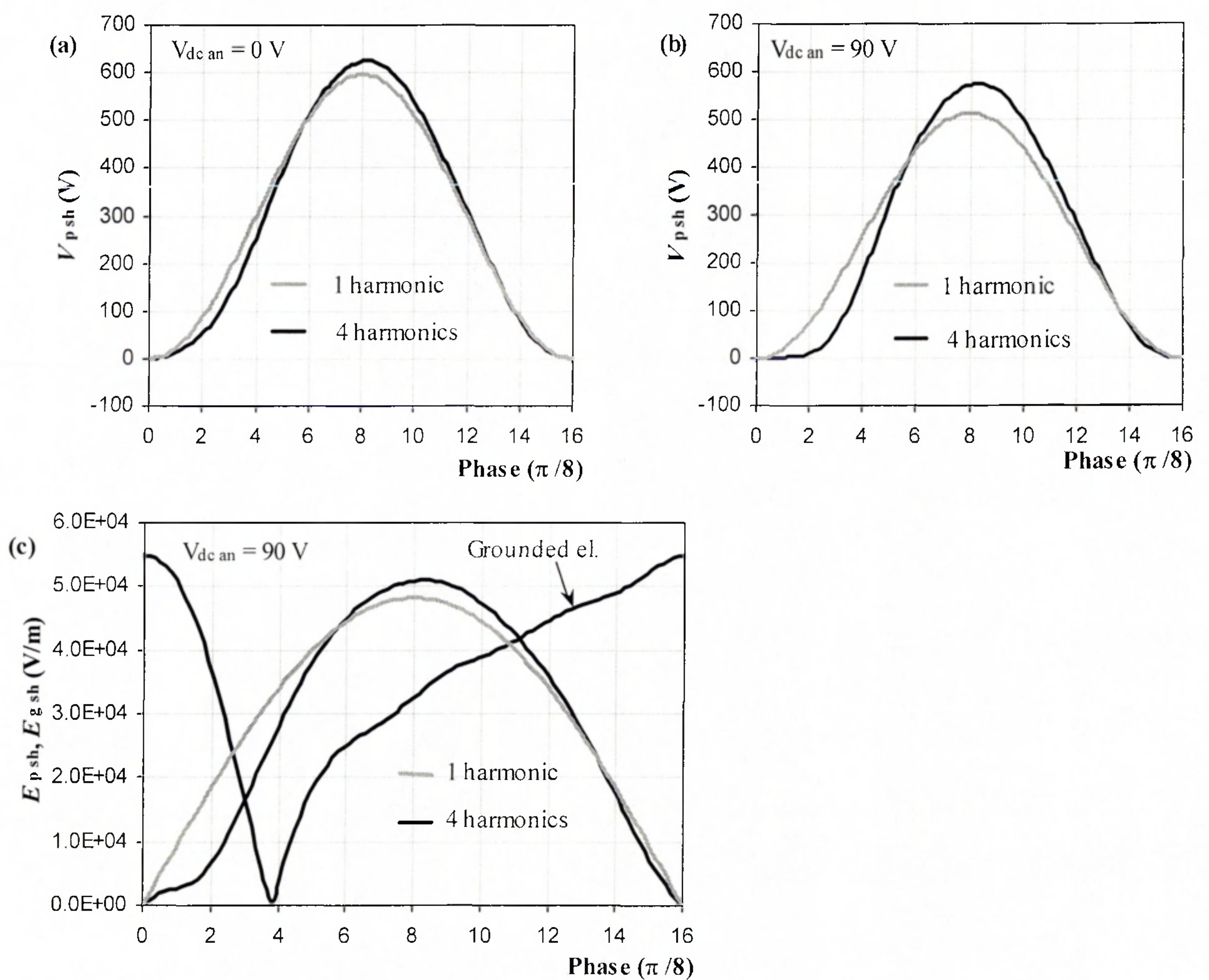

Fig. 4.8 Potential and electric field of the powered electrode in single and multiple harmonics cases. Subscript symbols *p sh* and *g sh* stay for powered and grounded electrode sheath.

This feature doesn't exist in the electric field curve of the single harmonic sheath. It is caused by a substantial increase of the multi-harmonic sheath potential of the grounded

electrode, when DC bias electrode is at 90 V. In this way the powered electrode sheath is affected. As a result, at the phase π/4, electrons can penetrate into the powered electrode sheath deeper (Fig. 4.7) than with DC electrode off. They stay longer in the sheath area and at the end gain higher energy from the sharp rise of the sheath potential, which starts right after the phase π/4 (Fig. 4.8 (b)).

The same reasons underlie advantage of the powered electrode sheath in comparison with the sheath of the grounded electrode. Despite approximately the same maximum values of electric fields (Fig. 4.8 (c)), hence repelling forces, of both sheaths, a stronger heating effect of the powered electrode (Table 4.1) is caused by a delayed rise of its sheath. On the contrary, the electric field of the grounded sheath has a strongest rate of growth straight after the sheath collapse, limiting in this way its heating effect. Actually, for the grounded sheath even a single harmonic ascending potential slope, which is steeper than the four harmonic one, produces more electron heating (Table 4.1).

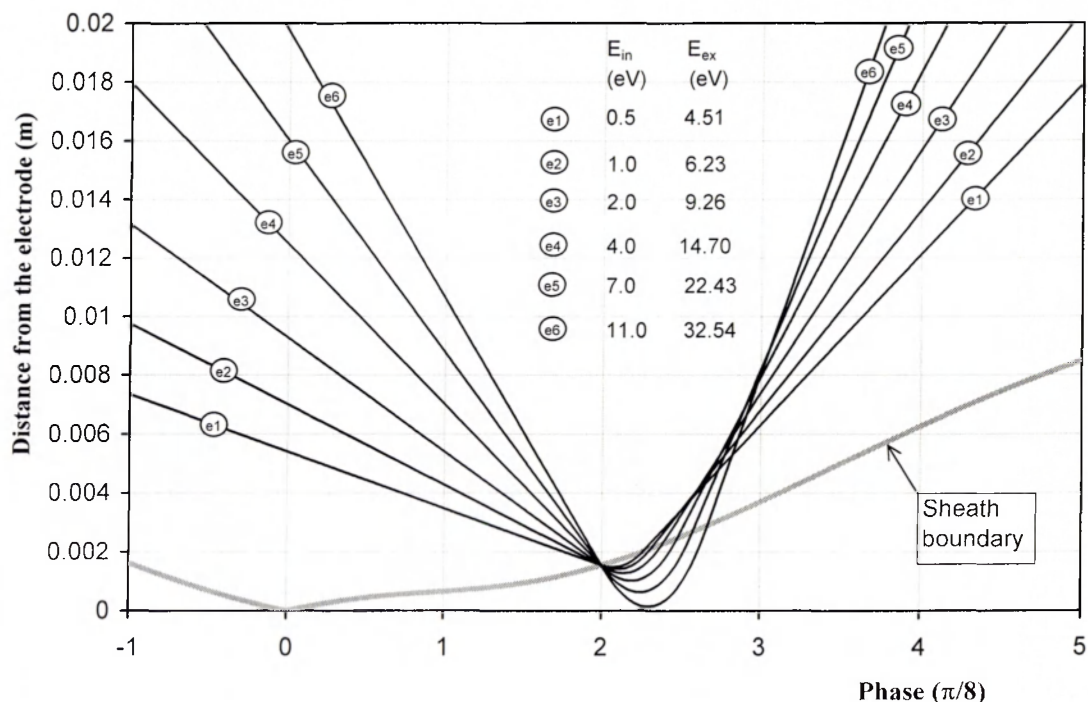

Fig. 4.9 Trajectories of electrons after the interaction with the matrix sheath of the powered electrode at $\frac{2}{8}\cdot\pi$ of RF cycle. The sheath voltage is set with the assumption of four harmonics and DC electrode voltage 90 V.

Indeed, of the ascending part of RF sheath the first half is most important for electron heating. This can be seen in Fig. 4.3, where EEDFs of reflected electrons are most elongated along the energy axis at the first quarter of RF cycle. The later part of the ascending slope accelerates electrons to a lesser degree, because of the strong electric field reflects electrons much faster. The commonly accepted approximation of a "brick wall" sheath-electron interaction is more justified here. So, in the case of the powered electrode sheath affected by the DC bias electrode it is the natural harmonic optimization of its' shape, that provides a stronger electron heating.

An interesting effect appears for colder electrons, if their trajectories are traced after interaction with the descending part of the sheath. Before departure from the sheath region some of the electrons, already being decelerated by the sheath, are caught again by the growing sheath boundary during the next RF cycle.

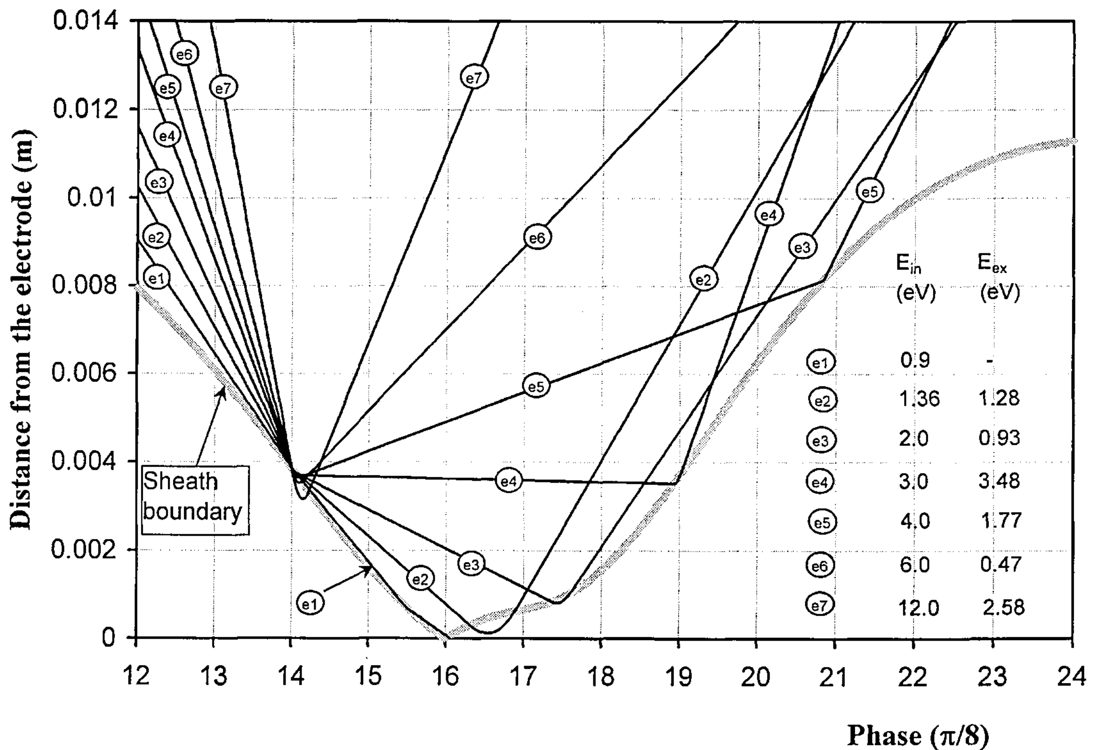

Fig. 4.10 Trajectories of electrons after the initial interaction with the matrix sheath of the powered electrode at $\frac{14}{8}\cdot\pi$ of RF cycle.

The sheath voltage is set with the assumption of four harmonics and positive DC electrode voltage 90 V.

As can be seen from the Fig. 4.8. a substantial fraction of electrons described by a Maxwellian EEDF, at least up to the initial energy 4 eV, has a double interaction with the powered electrode sheath. By taking into account this effect it is possible to build more accurate EEDFs and EEPFs for the part of colder electrons (Fig. 4.5 (a), (b)). It doesn't lead to an EEPF with a clear straight line for the "cold" bulk electrons, associated with a bi-Maxwellian distribution, but it points out the important limitation of the current model. Assumption 6 stated that the electron density at the sheath boundary doesn't vary with time. The double interaction electron-sheath effect breaks this assumption just after a single RF cycle. More sophisticated models [96, 97] account for a variable particle density at the sheath boundary by resolving in time the electron flux reflected from the opposite sheath. So, problems of the current model in verifying the "cold" part of EEDF are most likely caused by the constant boundary particle density.

The results of modeling of electron interaction with grounded and powered electrode sheath are summed up in the Table 4.1.

<table>
<tr><th></th><th>Grounded el. sheath (1 harmonic)</th><th>Powered el. sheath (1 harmonic)</th><th colspan="2">Grounded el. sheath (4 harmonics)</th><th>Powered el. sheath (4 harmonics)</th></tr>
<tr><td>T_e (eV) at $V_{dc\ an} = 0$ V</td><td>2.0</td><td>2.8</td><td colspan="2">1.697</td><td>3</td></tr>
<tr><td>T_e (eV) at $V_{dc\ an} = 90$ V</td><td>2.4</td><td>2.4</td><td>1.9</td><td>1.514*</td><td>4.26</td></tr>
<tr><td>$\frac{T_e(90) - T_e(0)}{T_e(0)}$</td><td>+ 0.2</td><td>-0.143</td><td>+ 0.12</td><td>- 10.8*</td><td>+ 0.42</td></tr>
</table>

Table 4.1 Effect of the DC bias electrode on the temperature of the tail electrons after interaction with RF sheath of the powered and grounded electrodes.
* Sheath boundary plasma density is $0.5 \cdot n_e$; otherwise $0.25 \cdot n_e$.

The most interesting part is highlighted by the thick boundary. First, the four harmonic sheath of the powered electrode affected by the DC bias electrode produces an EEDF tail heating of 42%, which is comparable with probe measurements. Second, the increase of plasma density at the sheath boundary of the grounded electrode, when the DC electrode is activated, causes cooling of EEDF by 10.8 %. It is again comparable with the actual probe measurements of the "cold" EEDF part. Since the four harmonic grounded sheath produces

a single Maxwellian EEDF, it is suggested that a combined net heating-cooling effect of both sheaths with four harmonics corresponds better for describing electron temperature variations, resulting from the DC electrode biasing. The preferential increase of plasma density near the grounded rather than near the powered electrode could be ascribed to the direction of closing of the DC current circuit. It happens only through the grounded electrode, since the circuit of the powered electrode has a blocking capacitor in the matching unit.

4.3 Modeling of plasma potential variation, caused by electron injection and removal.

It has been established in the previous section that the form of time-resolved plasma potential plays an important role in shaping electron EDF. The plasma potential, which was accepted to be equal to the sheath potential of the grounded electrode, was set using sinusoidal function by the formulas (4.2a) and (4.8) for the cases of single and multiple harmonics. In reality, the only sinusoidal signal in RF discharge, which could be verified reliably and easily, is the voltage of the powered electrode. Its reading is typically made by oscilloscope directly from the internal voltage probe of the matching unit. Consequently, it is important to trace formation and variation of the plasma potential, based on the initial experimental data: potential of the RF generator, self-bias potential of the powered electrode, potential of the DC bias electrode and injected electron current. The model is based on balancing net instantaneous currents to the discharge electrodes, described by Song, Field and Klemperer [102]. The similar approach was recently applied for investigation of the effect of electron injection in RF discharge by Haas and Braithwaite [103].

4.3.1 Model

It is considered that plasma electrons are described by a single temperature Maxwellian distribution. The electrode sheath is positively charged with no ionization or

recombination. The electron temperature and density don't vary during the RF cycle. The electrical circuit of the RF discharge is presented in Fig. 4.9. The powered electrode A_c is separated from the RF generator by a blocking capacitor. The biasing electrode A_b is maintained at a steady positive potential V_b by the DC generator. A simplified interpretation of electron injection is suggested. It is assumed that the electron beam doesn't acquire sufficient energy to produce additional ionization in the plasma and to affect the Maxwellian distribution of plasma electrons. It is represented by a DC electron

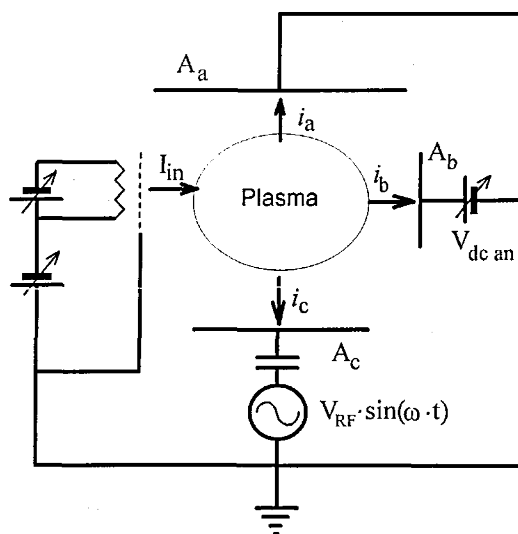

current I_e, entering the discharge plasma.

Fig. 4.11 Electrical circuit of the RF discharge with electron injection and removal

The model is built using the following mathematical definitions:

1. In general, the instantaneous conduction current at any plasma boundary is described using the Bohm sheath model. Ion and electron components are summarized to give a total current to an electrode of area A:

$$i = A \cdot \left[n \cdot e \cdot \upsilon_B - \frac{1}{4} \cdot n \cdot e \cdot \upsilon_e \cdot e^{-\frac{V_S(t)}{T_e}} \right] \qquad (4.9)$$

where $\upsilon_B = \left(\frac{e \cdot T_e}{m_i} \right)^{\frac{1}{2}}$ - Bohm speed, $\upsilon_e = \left(\frac{8 \cdot e \cdot T_e}{\pi \cdot m_e} \right)^{\frac{1}{2}}$ - mean electron speed, T_e – electron temperature in Volts, e - electron charge, m_i and m_e – ion and electron

mass, n = n_e plasma (or electron) density, $V_s(t)$ –sheath potential.

The current of secondary electrons is desregarded.

2. Plasma density is non-uniform over the discharge volume. Near the powered electrode it is higher than in the rest of plasma: $n_C = K \cdot n$ (4.10)

3. For convenience further calculations are conducted, using dimensionless variables:

$$\imath = \frac{i}{A_C \cdot n \cdot e \cdot \upsilon_B} \quad ; \quad \Phi = \frac{V}{T_e} \quad ; \quad \theta = \omega_0 \cdot t \qquad (4.11)$$

where A_C – surface area of the powered electrode, ω_0 – RF cyclic frequency.

Then normalized surface areas of the powered, grounded and bias electrodes are:

$$A_C = 1 \quad ; \quad A_A = \frac{A_A}{A_C} \quad ; \quad A_B = \frac{A_B}{A_C} \qquad (4.12)$$

4. The powered electrode potential is set by the formula

$$\Phi_{p\,el}(\theta) = \Phi_{RF} \cdot \sin\theta + \Phi_{dc\,bias} \qquad (4.13)$$

where Φ_{RF} is an amplitude of a sinusoidal potential of RF generator, and $\Phi_{dc\,bias}$ is a self-bias potential. The DC electrode has potential $\Phi_{dc\,an}$.

5. So, conduction currents to the powered, DC and earthed electrodes can be expressed in the following way:

$$\imath_C = K \cdot \left(1 - \alpha \cdot e^{-(\Phi_p - \Phi_{p\,el})}\right) \qquad (4.14a)$$

$$\imath_B = A_B \cdot \left(1 - \alpha \cdot e^{-(\Phi_p - \Phi_{dc\,an})}\right) \qquad (4.14b)$$

$$\imath_A = A_A \cdot \left(1 - \alpha \cdot e^{-\Phi_p}\right) \qquad (4.14c)$$

where $\alpha = \left(\frac{m_i}{2 \cdot \pi \cdot m_e}\right)^{\frac{1}{2}}$.

6. From the condition of quasineutrality of the discharge plasma at any moment of time it follows, that sum of all instantaneous conduction currents to the electrodes and a value of the current of injected electrons should be zero:

$$\iota_C + \iota_B + \iota_A + I_{in} = 0 \qquad (4.15)$$

where I_e – normalized current of injected electrons.

7. The formula of instantaneous plasma potential is derived from substitution of the formulae (4.14) into (4.15):

$$\Phi_p = \ln \frac{\alpha \cdot \left(K \cdot e^{\Phi_{pel}} + A_B \cdot e^{\Phi_{dc\,an}} + A_A \right)}{K + A_B + A_A + I_{in}} \qquad (4.16)$$

Then the time-averaged plasma potential is:

$$\Phi_p = \frac{1}{2 \cdot \pi} \cdot \int_0^{2\cdot\pi} \Phi_p d\theta \qquad (4.17)$$

8. Since there is a blocking capacitor in the circuit of the powered electrode, the net conduction current from plasma to the electrode over RF cycle should be zero:

$$\int_0^{2\cdot\pi} \iota_C = 0 \qquad (4.18)$$

Then substitution of (4.13), (4.14a) and (4.16) into (4.18) results in:

$$\int_0^{2\cdot\pi} \left(1 - \frac{\left(K + A_B + A_A + I_{in}\right) \cdot e^{\Phi_{RF} \cdot \sin\theta + \Phi_{dc\,bias}}}{K \cdot e^{\Phi_{RF} \cdot \sin\theta + \Phi_{dc\,bias}} + A_B \cdot e^{\Phi_{dc\,an}} + A_A} \right) d\theta = 0 \qquad (4.19)$$

Solution of the equation (4.19) provides the value of the self-bias potential of the powered electrode.

9. For comparison with the real RF plasma parameters of the model were set using data from the real discharge in hydrogen. Electron temperature and density (T_e = 3.2 eV, $n_e = 1.2 \cdot 10^{15}$ m^{-3}) were taken from the electrostatic probe measurements. Other discharge parameters, the amplitude of RF signal 440 V and the self-bias voltage of the powered electrode -195 V, were characteristic to the discharge at 30 W power and 45 mtorr pressure. Electrode areas were: of the powered electrode $8.332 \cdot 10^{-3}$ m^2, of the DC electrode $5.125 \cdot 10^{-3}$ m^2 and of the grounded electrode $6.53 \cdot 10^{-2}$ m^2. The main plasma ion was H_3^+.

4.3.1 Results and discussion

Initially, a case of the discharge without electron injection or removal was considered. At these conditions coefficient K was calculated from the equation (4.19), using the real discharge parameters. The solution gave the value K=4.6. This value was used unchanged for further calculations.

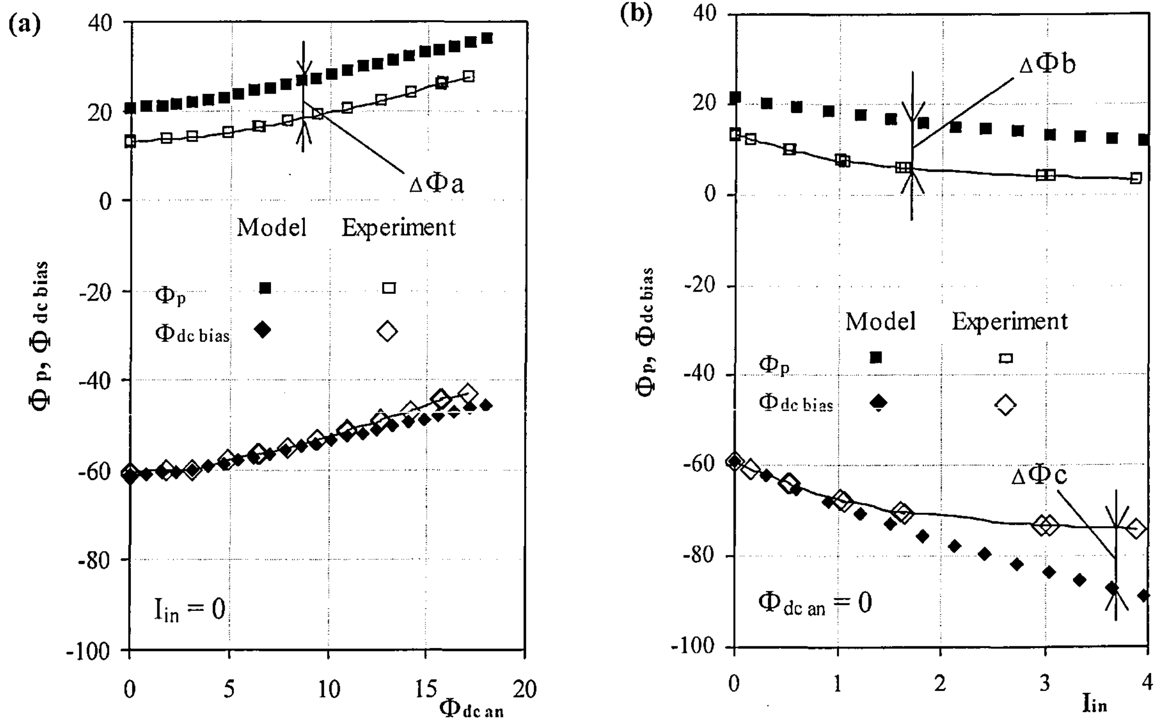

Fig. 4.12 Variation of the averaged plasma potential and the self-bias voltage of the powered electrode for the cases of: (a) - DC electrode and (b) - electron injection. It is assumed that all electrons, produced in the electron source (section 3.4, chapter III), are injected in plasma without losses: $I_{in} = I_{emis}$.

The time-averaged potential of the discharge and the self-bias voltage of the powered electrode were calculated, using the formulas (4.17) and (4.19), with electron removal or injection. These discharge conditions were regarded separately: variation of the potential of the DC electrode without electron injection, and variation of the current of injected electrons, when the DC electrode was earthed. The results of the model are presented together with experimental measurements in Fig. 4.12.

In both cases, variations of the theoretical and the experimental data are qualitatively the same. In general, the modeled plasma potentials are always higher than

the one, measured in RF plasma. Their excessive value, marked $\Delta\Phi a$ and $\Delta\Phi b$, is associated with the ion nature of the sheath, set in the model. Following the assumption (4.9), the plasma potential should always be positive in respect to the potential of the powered electrode or of the DC electrode. In the real discharge, during a short interval of the RF cycle there can be a reversal of electric field in the sheath of the powered electrode. For a brief moment, the sheath becomes an electron one. This effect was detected experimentally by Sato and Lieberman [77]. During a private communication, Prof N.Braithwaite has deduced a condition of the RF sheath changing its sign as

$$V_{RF} \geq T_e \cdot \sqrt{\frac{m_i}{2 \cdot \pi \cdot m_e}} \qquad (4.20)$$

where V_{RF} – amplitude of the RF signal of the powered electrode, T_e – electron temperature in Volts, m_i – electron mass and m_e – ion mass. In our case, for H_3^+ ions and Te = 3.2 eV, the right hand side of the condition (4.20) is equal 95 V, which is much less than 440 V RF amplitude of the powered electrode in the experiment. Therefore, in the real discharge the sheath of the powered electrode changes its sign at the experimental conditions, used for comparison with the model. Consequently, the time-averaged plasma potential, measured by the probe, is smaller than the potential, predicted by the model.

The difference between theoretical and experimental results for the self-bias potential ($\Delta\Phi c$, Fig. 4.12 (b)) increases with growth of injected electron current. This effect is ascribed to the fact that the model doesn't account for a considerable increase of plasma density, arising from ionization by injected electrons. In the real discharge, injected electrons can increase plasma density up to an order of magnitude (Fig. 3.12).

Time-resolved plasma potential, calculated from the formula (4.16), is equal to the potential of the sheath of the earthed electrode. Subtraction from it of the powered electrode potential (4.13) and of the potential of the DC electrode produces time-resolved values of the corresponding sheath potentials. They are presented in Fig. 4.11 for the case of $\Phi_{dc\ an} = 18.75$.

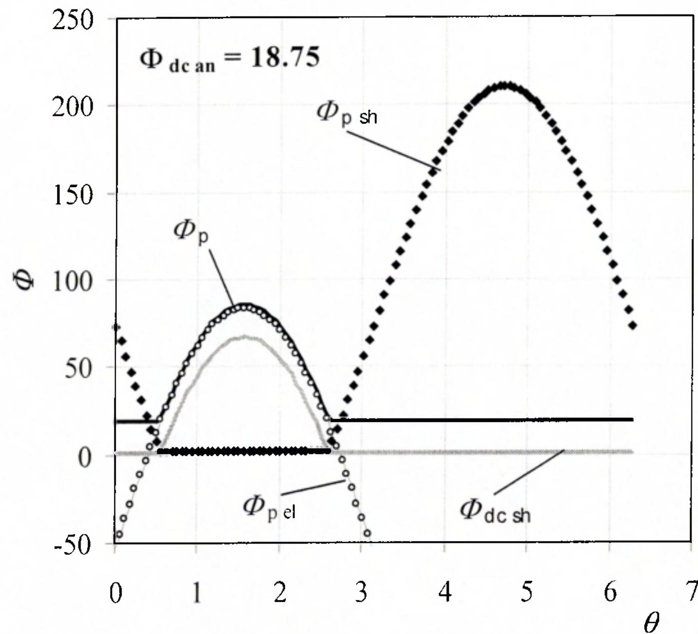

Fig. 4.13 Time-resolved potentials in the discharge at $\Phi_{dc\ an}$ = 18.75.

Φ_p – plasma potential, $\Phi_{p\ sh}$ – potential of the powered electrode sheath, $\Phi_{dc\ sh}$ – potential of the DC electrode sheath, $\Phi_{p\ el}$ – RF potential of the powered electrode.

Apart from having all the time positive values, as discussed on the previous page, all sheath potentials have a high degree of symmetry. It contradicts to the asymmetrical forms of the sheath potential, considered in section 4.2.2 of this chapter. This result of modeling was ascribed to limitation of the conduction current approach of this model. It didn't consider the whole RF circuit of the discharge. Therefore, displacement currents through plasma sheath and sheath capacitance were beyond the scope of analysis. These elements are crucial for investigation of the multi-harmonic asymmetrical sheath. The model, including both conduction and displacement currents through the RF sheath, was suggested by Dr P.Johnson. Its brief description is given in Appendix F.

Chapter V. "Deposition of carbon films, using various configurations of RF discharge"

5.1 Introduction

As has been demonstrated in the section 3.7, electron injection and removal by means of the electron source and the DC bias anode strongly influences the main plasma parameters of an RF capacitive discharge: density, electron temperature, plasma potential. It was beyond the technical capabilities of this work to measure a complete EEDF in plasma with injected electrons. It is believed that this EEDF includes "cold" bulk electrons and "hot" injected electrons.

The reaction of dissociation of hydrogen molecules by electron impact has a threshold 8.5 eV (section 1.5). Consequently, presence of "hot" electrons with energies up to 120 eV in RF plasma is beneficial for the production of atomic hydrogen. In its turn, during deposition of carbon films atomic hydrogen is crucial for preferential etching from the surface of carbon atoms, linked by weak sp^2 bonds. In this way, carbon atoms with a strong sp^3 bond are left, forming a diamond lattice.

Although information from the energy and mass analysis probe (section 3.7.2 and 3.73) has been solely about ionic components of hydrogen, it confirms indirectly the growth of atomic hydrogen density in a plasma with electron injection. Fig. 3.15 (a) reveals 3.7 times increase in density of H^+ species during simultaneous operation of the electron source and the DC bias anode. It has been demonstrated in section 2.9, that ionic hydrogen is produced mainly by electron impact of its atoms.

It is interesting to trace, how plasma conditions, modified by electron injection, affect coatings. So, deposition of carbon films from the RF discharge with electron injection will be described in this chapter. In addition, a hollow cathode configuration will be examined as an alternative scheme for bringing the RF discharge up to the conditions of diamond film deposition. Data on carbon coatings from the RF hollow cathode will also be presented.

5.2 Deposition of carbon coatings from an RF discharge with electron injection

5.2.1 Experimental conditions

The basic experimental system was the same as depicted in Fig. 3.2 of chapter III. Plasma diagnostics (the electrostatic probe and the energy and mass analysis probe) were removed from the discharge volume to prevent their contamination by carbon coatings.

Discharge conditions were the following. A gas mixture of methane, hydrogen and argon was used with flow rates 6, 20 and 20 sccm accordingly. The overall pressure of 70 mtorr was sustained in the discharge volume using a butterfly throttle valve. Incident RF power was 100W. Total deposition time was approximately one hour. No substrate heating was used.

The filament in the electron source was of the first prototype: with an emissive layer, attached by a blue mineral wax. The heating power of the filament was 30 W. The bias voltage of the filament was –134 V, resulting in an emission current of 93 mA. The fact of injection of electrons into the main discharge was indirectly confirmed by the variation of self-bias potential of the powered electrode. It declined from - 482 V without injection down to – 511 V during operation of the electron source. The same effect was confirmed both experimentally and theoretically in sections 3.7.1 and 4.2.2.

It was demonstrated in section 3.7.1 that the time-averaged plasma potential could decline two to three times as the result of electron injection, while the potential of the powered electrode sheath changes insignificantly. So, silicon and titanium deposition substrates were attached to the grounded electrode, where the strongest variation of plasma conditions was expected. For comparison one set of samples has been prepared with electron injection, another – without, keeping the other discharge conditions unchanged. The samples were analysed, using Raman spectroscopy (Appendix G).

5.2.2 Coating characterisation using Raman scattering

The Raman measurements of the samples from both experiments were conducted on a

Renishaw apparatus, which uses 515 nm Ar laser light. Spectra were recorded in the range 200 – 3200 cm^{-1} (Fig. 5.1).

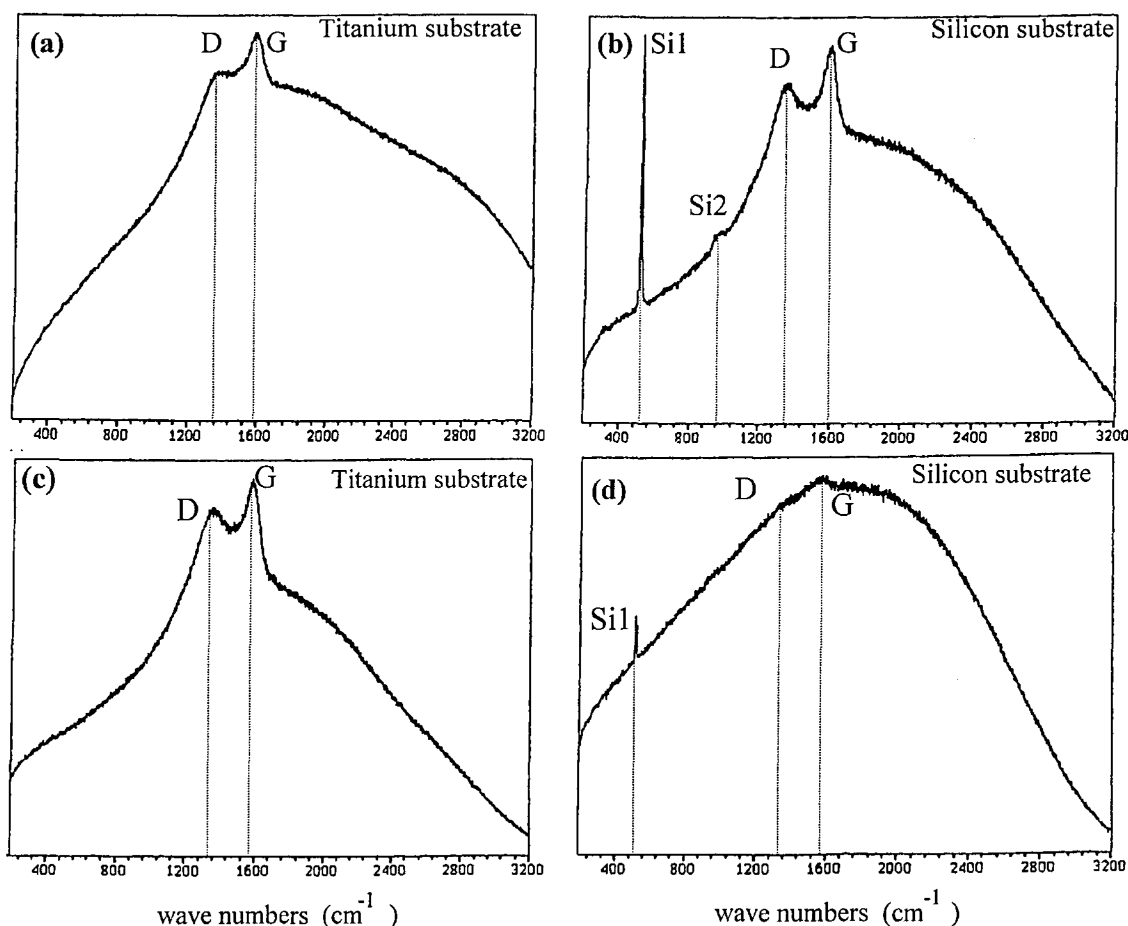

Fig. 5.1 Raman spectra of carbon coatings from the grounded electrode without (a, b) and with (c, d) electron injection in the RF discharge. (Courtesy of Dr D.Grant)

Specific peaks Si1 and Si2 (Fig. 5.1, (b, d)) are associated with 520 and 950 cm^{-1} peaks of Raman spectra of the silicon substrate [104]. The common features of all spectra are the two peaks, which are centred approximately at 1350 cm^{-1} (D peak) and 1590 cm^{-1} (G peak). Their labels suggest a state of carbon, producing a corresponding Raman scattering shift. G stands for graphite; and D stands for disordered, being associated with polycrystalline nature of graphite. More precise positions of these peaks, obtained from microcrystalline graphite sample, are 1355 cm^{-1} and 1575 cm^{-1} accordingly, as quoted in [105]. The difference of the location of the peaks on the Fig. 5.1 could be attributed to a number of factors. First, a small scale of the "wave numbers" axis on the Fig. 5.1 doesn't

allow accuracy higher, than 10 cm^{-1}. Second, the position of the G and D peaks could be affected by the hydrogen content of the film, by the presence of different carbon phases, such as graphite clusters and benzene ring clusters, and by stress in the film [105].

The effect of background signal on Raman spectra was attributed to luminescence. Yoshikawa and co-workers demonstrated Raman spectra of soft carbon coatings with superimposed luminescence signal [106]. They established, that luminescence intensified with increase of hydrogen content in the films. At 50-70% hydrogen content luminescence signal practically obscured Raman spectra [106]. This result was ascribed to large sp^3 carbon clusters and polymeric structure of the films.

It is suggested, that in our case the carbon coatings also contain large amount of hydrogen, causing substantial luminescence on all Raman spectra (Fig. 5.1). Electron injection reduced plasma potential and ion bombardment energy at the earthed electrode (Chapter III, sections 3.8.1 and 3.8.2). It promoted further polymerisation of the coating and growth of its luminescence signal (Fig. 5.1, (d)). Contrary decline of the luminescence signal on the titanium sample (Fig. 5.1, (c)) could be ascribed to roughness of its surface. It absorbed well laser light, which could cause decomposition of soft carbon coatings at laser power less than 10 mW [106].

5.2.3 Technical limitations of the configuration with electron injection and removal for depositing carbon films

Deposition of carbon coatings in the configuration, including the electron source and the DC anode (Fig. 3.2), has revealed a number of technical problems, which forced a revision of the program.

First, the DC anode could not be used because of fast growth of insulating carbon coating on its surface. In principle, alternative designs of the electrode, such as a rotating electrode or a remote electrode [65], could significantly reduce the problem. However, it was difficult to implement them because of limited space inside the vacuum bell jar (Fig. 2.1).

Second, at this time filaments of the electron source had the emissive layer, which was attached by a blue mineral wax. The design proved to be unreliable because of fast erosion of the emissive layer. For example, in order to conduct the experiment, described in the section 5.2.1 it was necessary to replace the filament three times. A more reliable design of the filament, described in the section 3.3, has been developed at the later stage of the project.

In addition, an interesting recommendation has been made by Dr B.Spitsyn, a discoverer of the CVD approach of diamond deposition (Section 1.2). During the the 4th International Conference on Diamond, Diamond-like and Related Materials (Portugal, 20-24/09/93) he has pointed out in private communication, that one of the process criteria of growing CVD diamond is discharge power densities at least 10 W/cm^3. It is unlikely, that the discharge configuration with electron injection–removal (Fig. 3.2) will be able to approach this value.

Therefore, following the technical and physical arguments, it was decided to look for an alternative configuration of RF discharge, which could reliably operate in methane-hydrogen gas environment, producing plasma with high-energy electrons and high power density.

5.3 Deposition of carbon coatings from RF hollow cathode configuration

5.3.1 Hollow cathode effect

The hollow cathode effect is a well-known phenomenon, which consists in confinement of discharge electrons in a potential well [107]. This potential structure is typically formed in cavities of a plane electrode, which could have cylindrical or linear, slot-like shape, or between parallel plates.

In low-pressure plasma discharges, sustained by means of electrodes, electrons either originate from ionisation processes inside the plasma or from secondary emission from the electrode surface, caused predominantly by ion bombardment. Secondary

electrons are accelerated through the electrode sheath, gaining energy equal to the sheath potential, sometimes, hundreds of Volts. Their role is important in DC discharges primarily, because they close the electron current circuit through the cathode sheath. In RF discharges they are a major source of ionisation at higher pressures, in the so-called γ-mode of discharge.

In the case of the hollow cathode, the original secondary electrons and electrons, produced in the sheath, are effectively trapped between the two sheaths. They traverse the discharge space until they are deflected from this pass by a single or several collisions. The EEDF of hollow cathode plasma could be qualitatively described in terms of "cold" bulk electrons and "hot" trapped electrons, as in the case of plasma with injected electrons (section 3.7.1). Measurement results of EEDF of the hollow cathode were presented in [108]. They are reproduced on the Fig. 5.2.

The trapped "hot" electrons produce multiple ionisations through collisions with neutrals, because their mean free path is much less than the total distance, they cover between the reflecting sheaths. Hence, hollow cathode plasma density could be

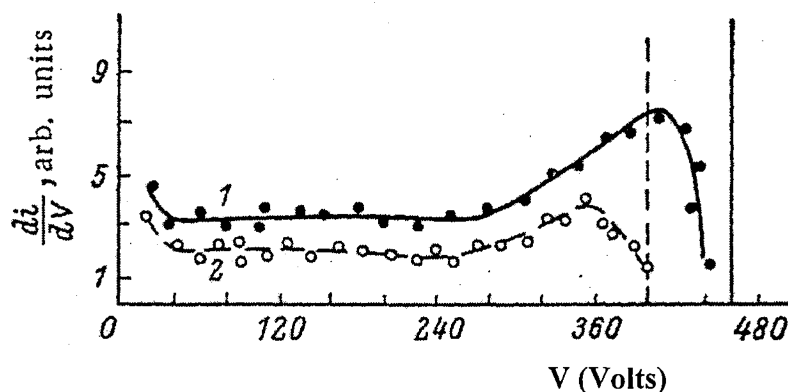

Fig 5.2 EEDF of the hollow cathode discharge in helium. Reproduction from the publication by Borodin and co-workers [108]. Hollow cathode diameter – 2 cm; pressure – 0.5 torr; discharge current: (1) – 100 mA, (2) – 50 mA. The vertical lines mark the cathode fall of potential: (1) – solid, and (2) - broken.

significantly higher, than in other types of low-pressure discharge. For example, in [109] there was measured $1.4 \cdot 10^{16}$ m^{-3} plasma density in RF hollow cathode discharge in argon at 45 mtorr, which was 20 times higher than in RF diode discharge at the same conditions.

In [110] there was reported $9 \cdot 10^{19}$ m^{-3} electron density for neon DC discharge in the copper hollow cathode. Practically, the density of hollow cathode plasma directly depends upon the power density of the discharge. From the data, published in [109] and [110] it is estimated that they correspond to power densities 0.42 $W \cdot cm^{-3}$ and 135 $W \cdot cm^{-3}$ accordingly.

High-density plasma of hollow cathodes was typically used for deposition or etching enhancement [111, 112] or as a light source, for example, in ion metal lasers [113]. Moreover, diamond films were successfully deposited from discharges, based on hollow cathodes of spiral [114] and tubular form [115, 116]. Interestingly, in [115] methane-hydrogen gas mixture was not supplied through the cathode. Nevertheless, the plasma plum between cathode and anode had sufficient plasma density to deposit diamond film. Another evidence of a very high power density in these discharges [114,115,116] was the absence of auxiliary heaters for deposition substrates. All of them were heated by energy transfer from hollow cathode and plasma.

5.3.2 Experimental configuration of RF hollow cathode discharge for carbon film deposition

In order to transform the diode RF discharge configuration (Fig. 2.1) into the hollow cathode one in the most economical way the changes were made only to the powered electrode unit (Fig. 5.3). A special stainless steel superstructure is screwed on top of the original 110 mm diameter powered electrode, preserving 6 mm gap. This superstructure consists of a circular plate, equal in diameter to the original electrode, and a puck-like body 76 mm diameter and 18 mm height, centred on its top. The puck has 7 orifices each of 18 mm diameter, passing also through the circular plate. The central orifice is blocked in the original experiments. The distance between the top of the powered electrode and the sample holder is 15 mm.

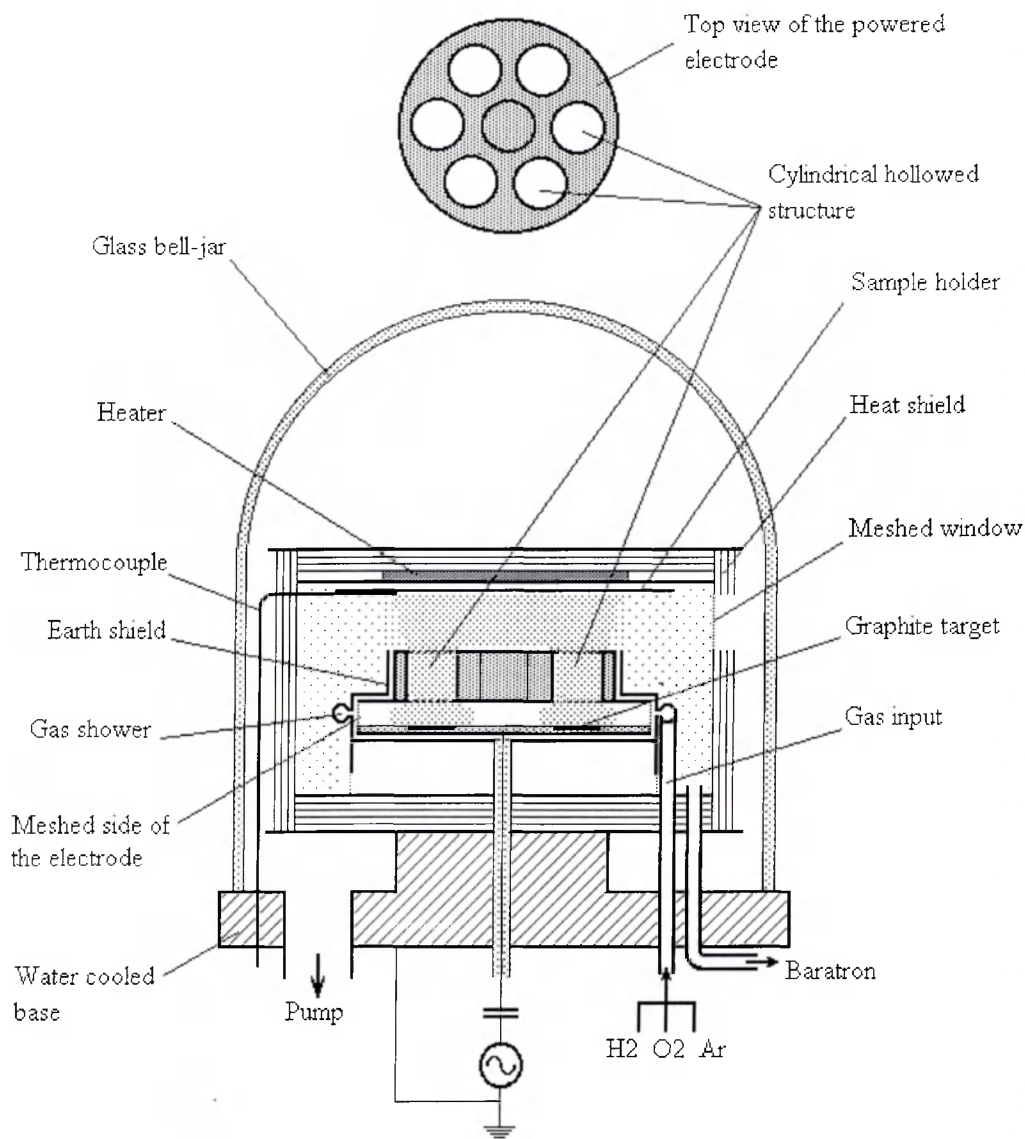

Fig. 5.3 Schematic diagram of the RF hollow cathode experimental device

The 6 mm gap between the original electrode and the superstructure is covered from the side by a stainless steel mesh, which is spot-welded. The mesh has density of 400 wires per inch with transparency of 69%. The whole electrode assembly is surrounded from the side by an earthed shield, with 2.5 mm separation approximately. The shield has orifices to allow gas in from the gas shower. After comparison of areas of the sheath separation and the meshed electrode side it is estimated, that 76% of the injected gas will pass through the hollowed structure of the powered electrode.

During the test runs of the system it was noticed that areas located at the bottom part of the hollowed structure were much lighter in colour. Hence, they were subject of

aggressive sputtering. To exploit this process for carbon introduction in the discharge and to suppress simultaneously the unwanted introduction of impurities graphite targets were positioned at the base of the hollowed structure at specially machined recesses.

Overall, configuration of the RF hollow cathode (Fig. 5.3) has proved to be successful for deposition of carbon films. It operated reliably in a wide range of gas pressures, up to 4 torr, for prolonged time. Even complete insulating carbon deposit all over the powered and grounded electrode surfaces did not obstruct operation of the discharge (Appendix H).

5.3.3 Experimental conditions

The general target of the first experimental series was to test the hollow cathode configuration (Fig. 5.3) at the discharge conditions, suitable for deposition of diamond film. In order to maximise power density of the discharge the output power of RF generator was set at maximum or close to maximum: 280 – 300 W. The sample holder was preheated to a temperature about 600° C. Plasma discharge heated it further, up to 790-830° C. Silicon samples, pre-polished by diamond paste, were attached to the holder in the centre and closer to its edge (Appendix H).

The vacuum chamber was typically evacuated to $8 \cdot 10^{-5}$ torr prior to admittance of gas mixture. Gas composition included hydrogen with a few percent of oxygen. In some experiments argon was added as well. Small amounts of oxygen lead to a decrease in the concentration of aromatics, oxidising hydrocarbon precursors in the gas phase. In addition, it promotes gasification (etching) of sp^2 surface carbon by OH radicals. Argon benefits the process by preventing polymerisation processes of carbon atoms in the gas phase. Hydrocarbon molecules are dissociated in collisions with argon ions and metastable atoms.

Deposition time lasted from 3 to 4.5 hours. Scanning electron microscope (SEM) micrographs of typical coatings are presented on the Fig. 5.4. Deposition parameters of these coatings are given in the Table 5.1.

Experiment label	H_2 flow (sccm)	Add. gasses (%)	Power (W)	$V_{dc\ bias}$ (V)	Pressure (torr)	Number of holes in the electrode
(A)	25	$O_2 - 3.5$	300	-131→-127	0.88	6
(B)	50	$O_2 - 3.3$ $Ar - 23.6$	300	-105→-98	1.05	6
(C)	50	$O_2 - 5$	280	-86→-85	1.32	3

Table 5.1 Deposition conditions

5.3.4 Results and discussion

Hardness of deposited films was estimated qualitatively: by scratching. A small force, applied by screwdriver, typically produced a visible scratch down to silicon substrate of the sample. The reason of soft nature of the coatings was in their morphology.

As it could be seen from the micrograph (A) on the Fig. 5.4, the film is quite porous, consisting of separate grains. The shape of grains is mainly irregular, and the size is from less than 100 nm up to 500-600 nm. The largest grains on the micrograph (B) are about 200 nm, but predominantly they are around 50 nm or less (Fig. 5.4 (B-1)). Coating on the micrograph (C) has grain size around 150 nm or less.

Etching of graphite targets in the gas mixtures, used in the experiments (Table 5.11), could originally produce various hydrocarbon molecules, radicals and ions [117] and carbon-oxide molecules and ions. By clustering and polymerisation they form large particles, creating an environment, which is known as dusty plasma [118]. Some typical phenomena of dusty plasma could explain deposition process in the RF hollow cathode. Conditions for dusty plasma are especially favourable in RF discharges because of trapping negative particles and ions between the positive time-averaged sheaths of the electrodes.

These conditions are practically ideal inside the hollow cathode with its centre-symmetrical distribution of potential. Dusty particles could acquire 10^2 to 10^6 negative elementary charges, growing to the sizes 0.01 to 1 μm accordingly. Diffusion of particles towards the deposition substrate occurs due to a combined effect of a directed flow of

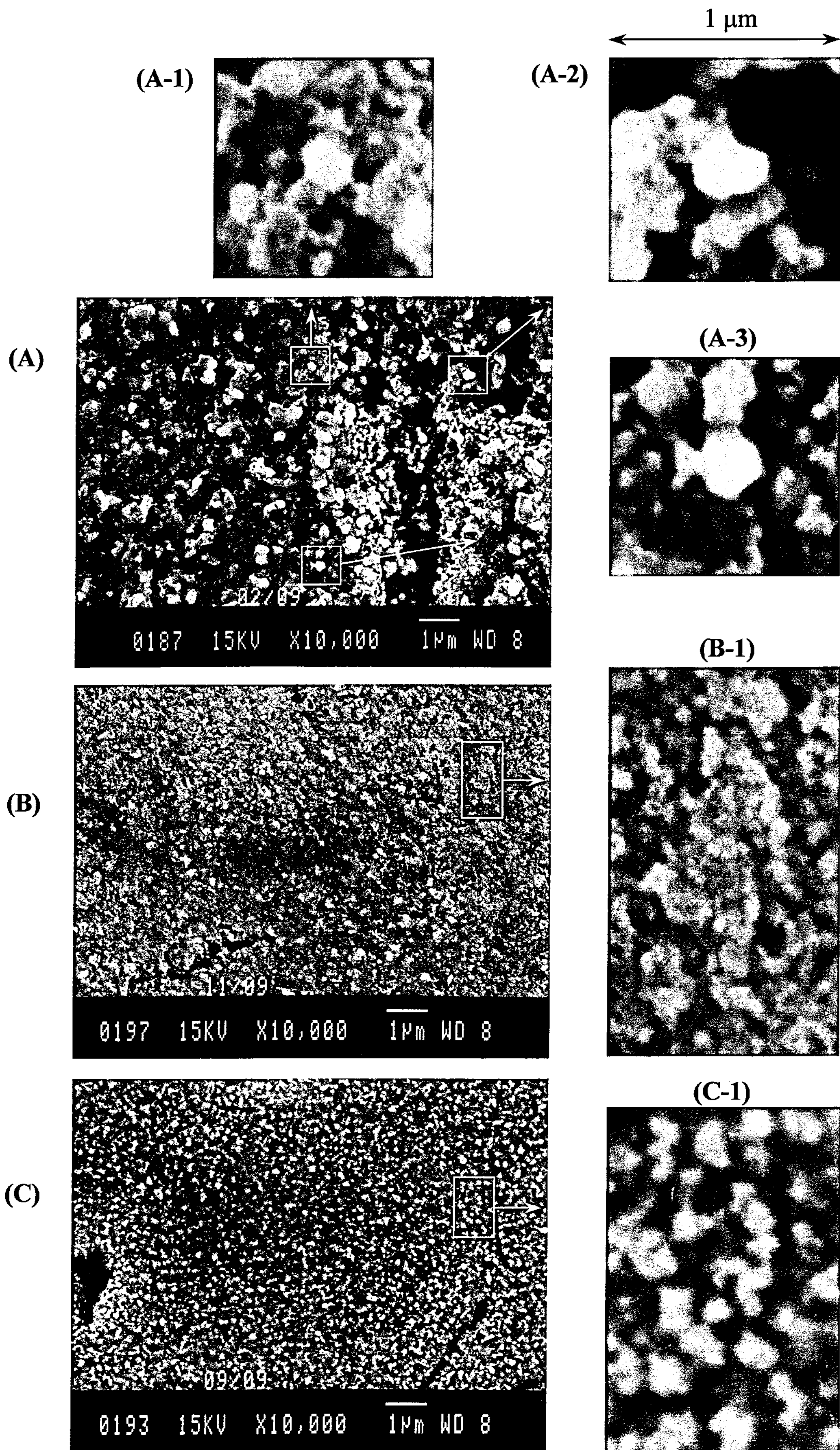

Fig. 5.4 SEM micrographs of carbon coatings

hydrogen species and interaction with other negatively charged particles. When their fractional amount starts exceeding 10^{-6}, the plasma potential is gradually depressed. This facilitates the arrival of negatively charged particles to the deposition substrate. Particles land on the substrate with little energy, which results in a porous, soft coating.

Interestingly, some of the particles on the micrograph (A) have a hexagon-like contour, which is clearly seen on the enlargements (A-1), (A-2) and (A-3) on the Fig. 5.4. Similar contour is characteristic to diamond microcrystals, grown from the gaseous phase (Chapter I, Fig. 1.3). It indicates the possibility of formation in the gas phase of sub-micron crystallites of diamond. In fact, such a process was described in [119] for laser heating of carbon vapours and for a high temperature flow of argon and acetylene.

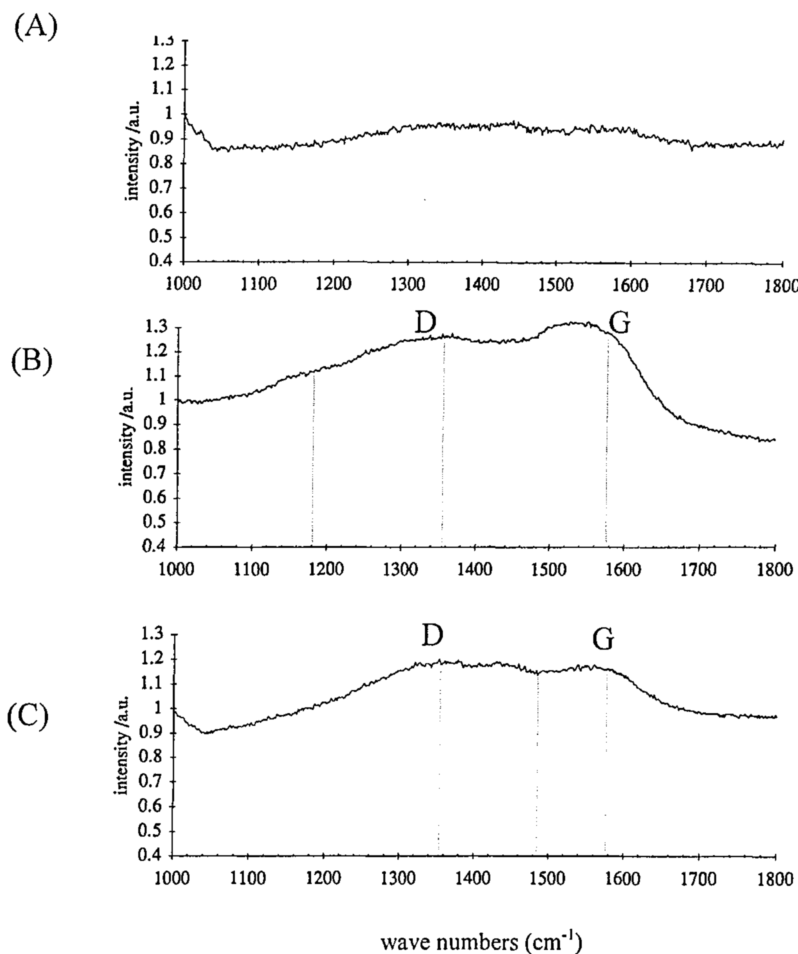

Fig. 5.5 Raman spectra of coatings from the RF hollow cathode configuration.
They correspond to the coatings on the Fig. 5.4 and conditions in the Table 5.1. (Courtesy of Renishaw Ltd)

Addition of argon in gas mixture together with increased hydrogen flow (Table 5.1,

line (B)) suppresses formation of large particles in the gas phase. It could be concluded, when micrographs (B) and (A) (Fig. 5.4) are compared. The first one has just a few particles, larger than 100 nm. Most of the film (B) is composed of aggregates of particles, which are 50 nm or less (Fig. 5.4, (B-1)). Their darker colour may be linked with their graphitic nature.

Indeed, this assumption is confirmed by the Raman spectra (B) on the Fig. 5.5. It has a well-developed peak structures near the Raman modes D and G, which are associated with graphite. The fact, that all the peak structures are quite broad, points out at the multiphase nature of carbon in these films. Superposition of different Raman active modes, associated with each phase, leads to broader effective line width. Some of the Raman modes of carbon [105], which could be used for interpretation, are indicated by dashed lines on the Fig. 5.5: 1180 cm^{-1} – sp^3 rich phase, 1486 cm^{-1} – stretch vibrations in benzene, 1355 and 1575 cm^{-1} – D and G modes of polycrystalline graphite.

Spectrum (C) (Fig. 5.5) also has a distinguished D and G peak structures. Graphitisation of this coating is caused by increase of the discharge power density, which was achieved by blocking three of six orifices in the electrode. In addition, concentration of oxygen was increased up to 5% (Table 5.1, line (C)). These conditions partly suppressed particle formation in the gas phase, resulting in deposition of particles no more than 150 nm in size (Fig. 5.4, (C-1)).

Although the first series of experiments with RF hollow cathode has not achieved diamond deposition conditions, it has emphasized the problem of dusty plasma for this configuration. This property of the hollow cathode could be beneficial for some other purposes. For example, in [120, 121] there were described experimental set ups for production of carbon clusters, based on hollow cathode effect. Alternatively, this experimental series has demonstrated ways of controlling formation of particles in plasma: by gas flow, gas composition and power density. Further research of the hollow cathode configuration has been concentrated primarily on the power density option because of a

particular drawback of the device, which had become clear after impedance measurements of its power line.

5.4 Deposition of carbon coatings from a single hollow cathode

5.4.1 Limitation of power in the discharge

During preparation of the first experimental series it was estimated, that the power density of the discharge inside the hollowed structure (Fig. 5.3) could be as high as 8-9 W/cm^3. One of the assumptions of this estimate was that most of RF power from the generator went into the plasma. RF power losses in the line were expected to be at the level 10-15%. There has appeared an opportunity to check these assumptions by the time of completion of the first experiments with the hollow cathode.

An electrical impedance probe [122] was developed within the framework of a different project under the supervision of Prof N.Braithwaite. The impedance probe, inserted in the RF power line, provided simultaneous time-resolved measurements of RF current and voltage. RF power, going in the discharge, could be calculated, using these data. In order to examine scope of this novel diagnostic an arrangement has been made to conduct a test run with the hollow cathode configuration. Measurements and processing of the data of the impedance probe were performed by Dr C. Mahony.

The results have demonstrated that only about 30% of the set power of the generator reached the discharge. The rest was absorbed by the matching unit and the part of the power line, which connected the matching unit with the electrode. This substantial loss in the power line is associated with insufficient diameters of the core wires in the atmospheric and vacuum coaxial cables, which were of the order 2-3 mm (Section 2.4, Chapter II). Only RF vacuum feedthrough had a transmitting rod 6 mm in diameter. The whole arrangement of the power line was a compromise solution, allowing seven other vacuum inputs for diagnostics and DC power in the water-cooled base plate (Section 2.2, Chapter II). However, the line could not transmit enough power for the multiple hollow

cathode structure of the electrode in order to achieve diamond deposition conditions.

5.4.2 Experimental configuration and conditions

To bypass the shortage of power in the discharge it was decided to concentrate plasma in a single hollow cathode structure of the electrode (Fig. 5.6). For this purpose, six holes in the powered electrode were blocked, while the central hole was opened. During the course of experiments a special graphite insert was positioned in the hollow cathode, which further increased power density of the discharge (Fig. 5.6).

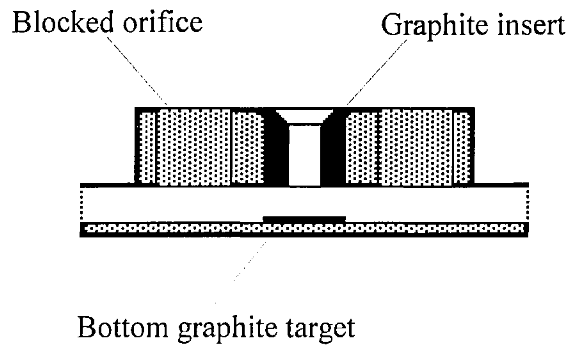

Fig. 5.6 RF powered electrode with a single hollow cathode structure

Experiment label	H_2 flow (sccm)	O_2 (%)	Power (W)	$V_{dc\ bias}$ (V)	t_{sub} C	Pressure (torr)	H/C diameter (mm)
(D)	40	3	290	-60→-64	842	1.63-1.67	18
(E)	79	-	280	-20→-23	856	3.04	8
(F)	79	2.2	280	-26→-28	800	3.0-3.21	8
(G)	79	1.3	285	-6→-13	823	3.07-3.42	5

Table 5.2 Deposition conditions of the single hollow cathode discharge

A 2 mm thick graphite sputter target was placed at the bottom of the hollow cathode.

In order to increase efficiency of hydrogen dissociation by the fast electrons it was decided to raise operational pressure up to a few torr. After trial runs it was discovered that above the pressure 5 torr the configuration is prone to ignite a parasitic local discharge in the gap between the earthed shield and the powered electrode (Fig. 5.3). Furthermore, local

discharge ignited, burning through the side mesh of the electrode, when hydrogen flow exceeded 100 sccm. Afterwards, the hollow cathode configuration was run with a safety margin for pressure and gas flow.

Deposition conditions of the most interesting experiments of the second experimental series are given in the Table 5.2. Typical duration of deposition process was three hours. Silicon was used as a deposition substrate. Two samples were attached to the heating stage opposite to the hollow cathode (Appendix H).

Considerably reduced discharge space and higher operation pressure required a special ignition procedure in this series. After the initial pumping down of the chamber the turbo pump was shut down; and vacuum was sustained only by the mechanical pump. First, argon gas was let in the chamber, and pressure was raised. At approximately 2 torr RF power was supplied to the electrode. Straight after the discharge ignition argon was substituted by hydrogen; pressure and power were set to the operation level.

5.4.3 Discussion

5.4.3.1 Morphology of deposition

The second series was started from the experiment at the conditions (D) (Table 5.2), using the single hollow cathode 18 mm in diameter. As it could be seen from the micrograph on the Fig. 5.7 the deposited film was qualitatively similar to the coatings from the first series (Fig. 5.4). It looked quite porous, and consisted of well-defined particles. The coating was easy to scratch.

It was assumed, that this film was deposited from dusty particles as described in the section 5.3.4. Another deposition experiment with the 18 mm single hollow cathode was conducted at 3.1 torr. However, it produced qualitatively the same type of coating. In order to overcome the effect of dusty plasma it was decided to increase further power density of the discharge. For this purpose, a graphite insert, having orifice of diameter 8 mm, was placed in the hollow cathode.

(D)

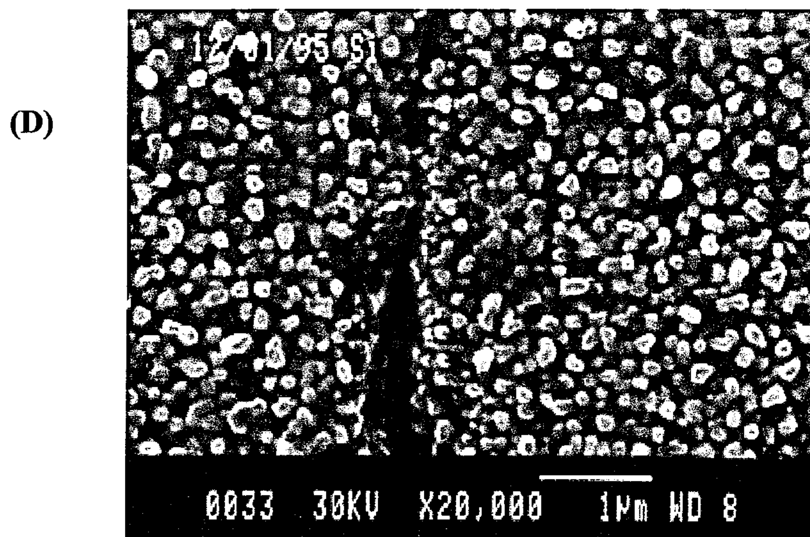

Fig. 5.7 SEM micrograph of coating for the conditions (D) in the table 5.2

Deposition experiments with graphite inserts (conditions (E), (F) and (G) in the Table 5.2) did not produce continuous coatings of silicon samples. Instead, results of deposition/nucleation process were noticeable mainly in the cavities, while the flat parts of substrate were kept pristine from deposition by plasma etching of carbon and even sputtering of silicon (Fig. 5.8 and 5.10). Discharge inside graphite inserts with internal diameters 8 and 5 mm had power density five and ten times higher, than inside the 18 mm hollow cathode. It is thought that the high power density resulted in production of sufficient amount of atomic hydrogen to suppress significantly particle formation in the gas phase. It led to a sufficiently high, of the order 130-140 V (Appendix I), plasma potential. Therefore, hydrogen ions, accelerated through the sheath, gained enough energy for sputtering and etching material from the deposition substrate.

Comparison of the masked and opened parts of the silicon substrate ((E-1) and (E-2) on the Fig. 5.8) demonstrates a significant transformation of the slopes of cavities. They became smoother and gentler after sputtering. This "opening" of cavities is thought to result from a substantial angular distribution of sputtering ions. Their sputtering effect decreases in the cavity from top to bottom due to a mutual "shading" of the opposite slopes (Fig. 5.9).

(E-1)

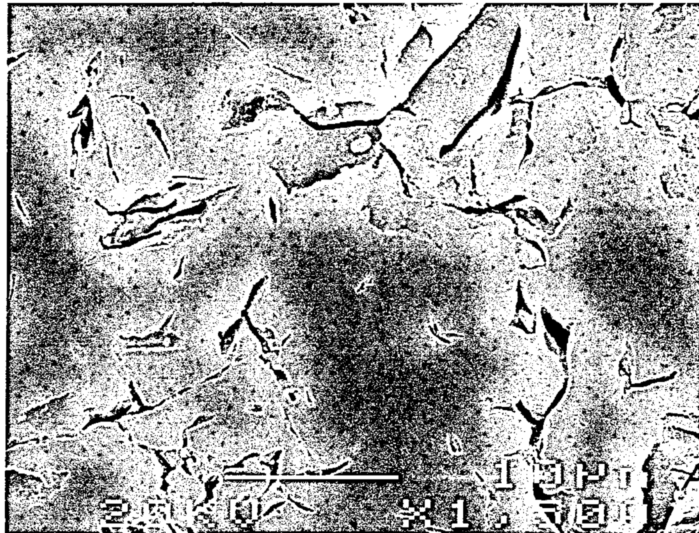

(E-2)

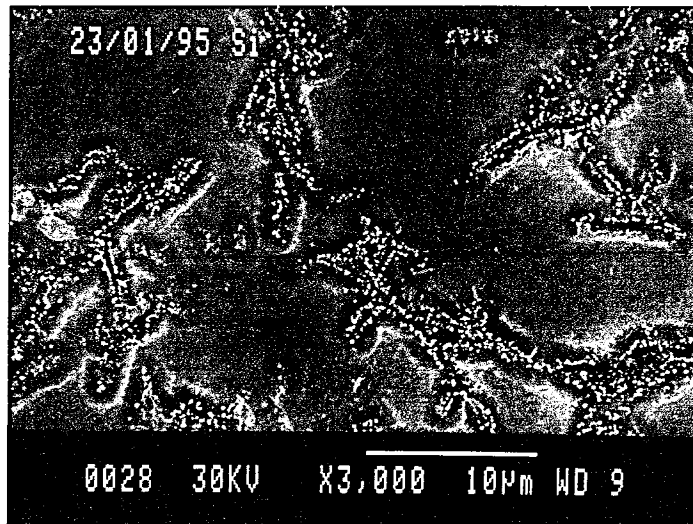

(E-3)

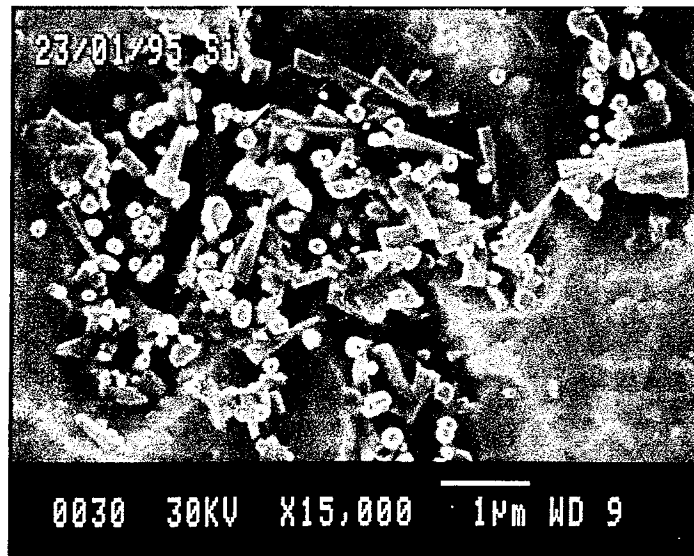

Fig. 5.8 SEM micrographs of the sample substrate for the conditions (E) in the Table 5.2. (E-1) – masked area, (E-2) and (E-3) – open area.

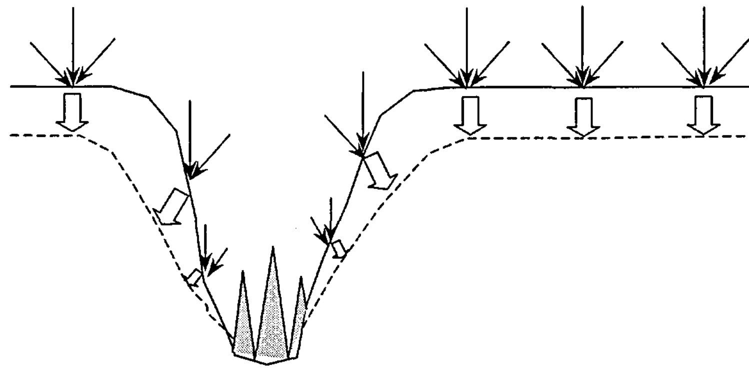

Fig. 5.9 Schematic of substrate transformation; where: solid line – profile of the original substrate, dashed line – profile of the sputtered substrate, small arrows – velocities of ions, block arrows – direction and intensity of sputtering, grey spikes – deposition structures.

As it could be seen from the micrographs (E-2) and (E-3) on the Fig. 5.8 deposition was mainly confined to bottom and adjacent areas of the cavities, which is explained by a reduced intensity of sputtering and etching in these parts. Although it was considered, that dusty plasma conditions were suppressed in this experiment, some fine soot was discovered on the samples after opening the chamber. Prior to examination of the samples by electron microscope, they were wiped out by tissue with alcohol. This procedure resulted in breaking off of some spike-like filaments, grown in the cavities. Some of the broken spike tops, which were pushed below their stump-like bases, lay normal to the line of view in the cavities (Fig. 5.8, (E-3)). They have length up to 1 μm with stump-like base diameter up to 0.2 μm.

Addition of 2.2% of oxygen to the discharge (Fig. 5.10, (F-1)), apart from increased sputtering of silicon substrate, promoted spreading of nucleation inside the cavities up to their edges. Position of some micro-crystallites clearly marked cavity edges, were carbide formation and, hence, nucleation of diamond phase proceeded faster. Further increase of nucleation density was achieved in the experiment, using the graphite insert with internal diameter 5 mm (Fig. 5-10, (G-1)). It is thought, that a higher power density inside the 5 mm hollow cathode elevated concentration of atomic hydrogen, which was a key factor in

deposition of the crystalline phase.

(F-1)

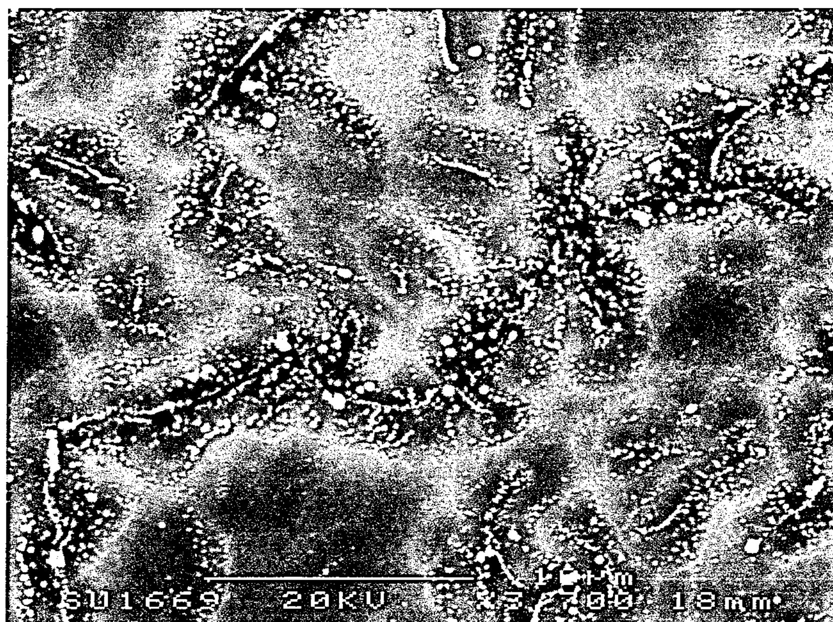

(G-1)

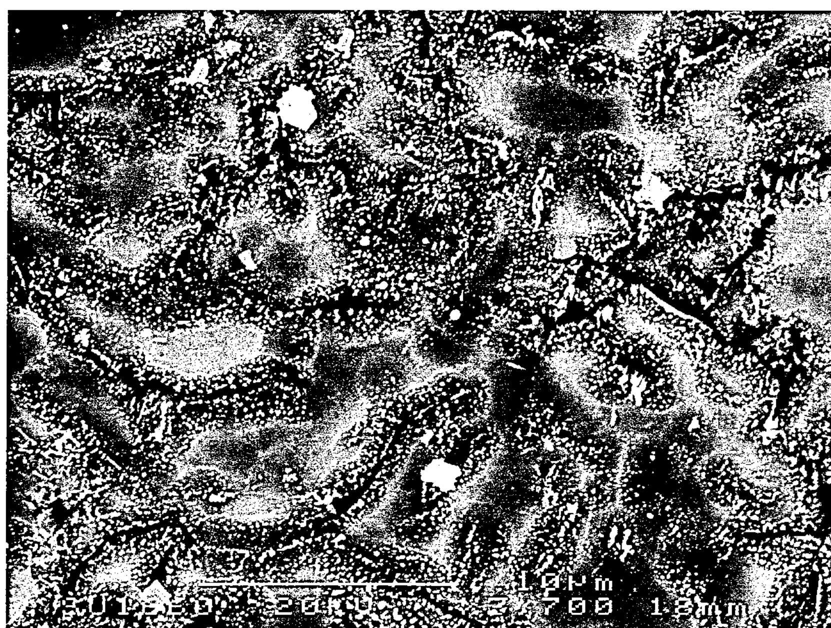

Fig. 5.10 SEM micrographs of sample substrates for the conditions (F) and (G) in the Table 5.2.

It was difficult to resolve shape of microcrystallites, when a higher SEM magnification of the areas, presented on the Fig 5.10, was attempted. Images of crystallites were typically very bright and blurred due to their negative charging. This problem was largely neutralised on the SEM images of the tilted substrates (Fig. 5.11, (F-2) and (G-2)). Micrographs of the tilted samples revealed, that the shape of all well-developed crystallites was spike-like.

(F-2)

(G-2)

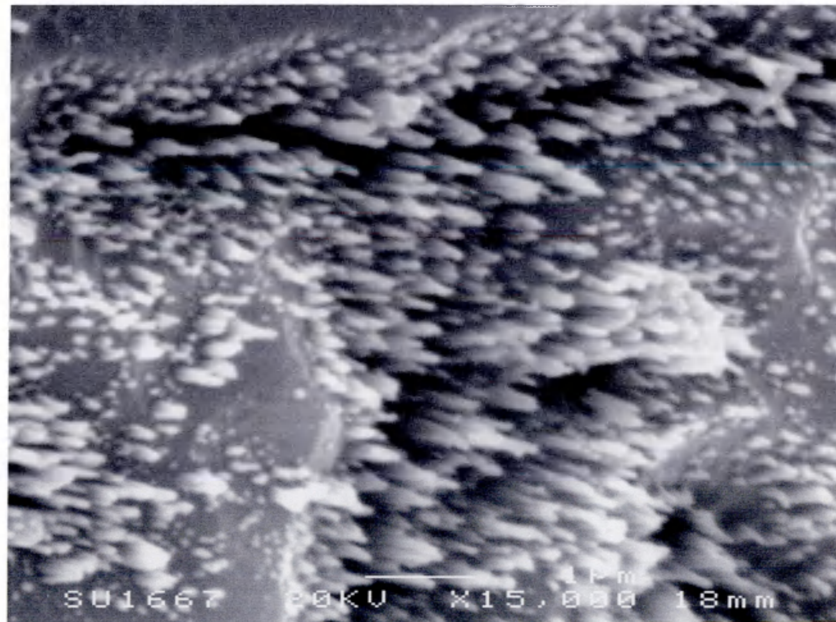

Fig. 5.11 SEM micrographs of sample substrates with tilt 26° for the conditions (F) and (G) in the Table 5.2.

Usually, the large crystallites filled central, deepest parts of the cavities, and small one spread over the cavity slopes (Fig. 5.11, (G-2)). It confirmed the assumption, made earlier (Fig. 5.9), about the initial nucleation at the bottom part of the cavities. Fence-like formation (Fig. 5.11, (F-2)) of crystallites was associated with primary nucleation at the edge of the deeper crack-like part of the cavities (Fig. 5.12).

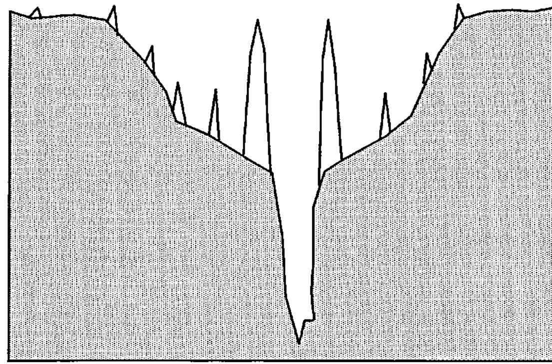

Fig. 5.12 Suggested cross-section of a cavity with fence-like formation of crystallites

On the Fig. 5.10 these "fence" formations could be seen as chains of crystallites, sometime merging into white lines, aside of the black curves of the deeper narrow parts of the cavities.

(F-3)

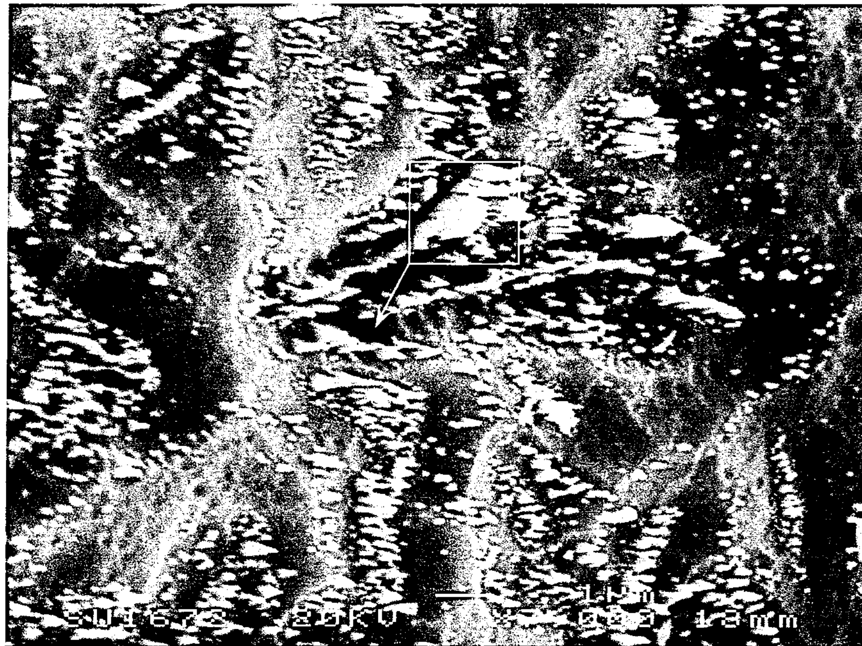

(F-4)

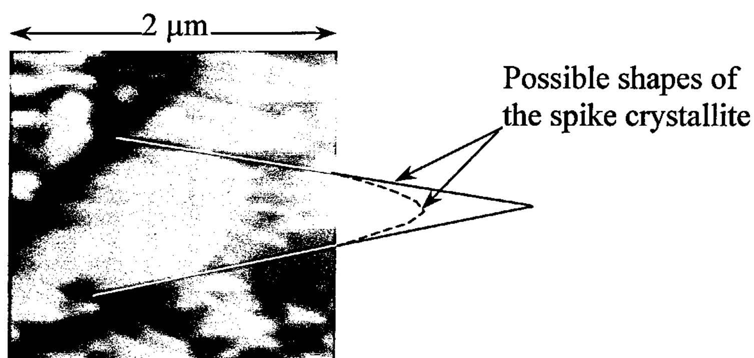

Fig. 5.13 SEM micrograph of the tilted (26°) sample for the conditions (F) in the Table 5.2

On average, the largest microcrystallites had the height up to 1.7-2 μm. Nevertheless, some features on the SEM micrographs pointed out that even higher spikes had been deposited. For example, on the Fig. 5.13 there is a stump-like base of the broken crystallite, which has a larger axis of its nearly oval cross-section around 900 nm. It could be speculated, that, if previously it was a completed spike crystallite, its vertical size was 4.5 - 6.4 μm (Fig. 5.13, (F-4)).

5.4.3.2 Composition of deposited crystallites

The phenomenon of deposition of carbon filaments (whiskers, cones) from the gas phase is well known. For example, a catalytic pyrolysis of acetylene, using Ni powder as a catalyst, produced coiled carbon whiskers dozens micrometers in length [123]. Contrasting small height of carbon spikes in our case is the result of a strong etching effect by energetic ions. Similar results for other plasma discharges were reported. Biased deposition in methane/hydrogen microwave plasma, which lasted for 2 hours, formed 0.5 μm carbon cone-like structures [124]. They were called conic diamonds, and were very like the spike crystallites, deposited in our experiments. Three hour etching of glass-like carbon by DC biasing of hydrogen microwave discharge resulted in growth of 1 μm carbon fibres on the same substrate because of back scattering [125]. The last datum points out at the possible way of re-deposition of silicon in the experiments (E), (F) and (G). Back scattering of sputtered silicon could contribute to forming silicon carbide composition of the spikes.

Samples from the second experimental series were not examined by Raman spectroscopy. Nevertheless, it is suggested that the spike microcrystallites, deposited in the experiments (E), (F) and (G), may contain a diamond phase. This assumption could be made on the bases of comparison with available data from other sources.

First, similar looking conical diamonds, described in the publication by Y.T.Trong and co-workers [124], produced two Raman peaks at 1332.5 and 1580 cm^{-1}. The first peak indicated presence of crystalline diamond; the second one was a slightly shifted G peak of

graphitic phase (section 5.2.2). It was concluded, that the cone–shaped diamond contained graphite components, possibly, between diamond grain boundaries. Second, crystallites, grown in the masked areas of some of the samples (Fig. 5.14 and 5.15), also corresponded to known morphologies of CVD diamond.

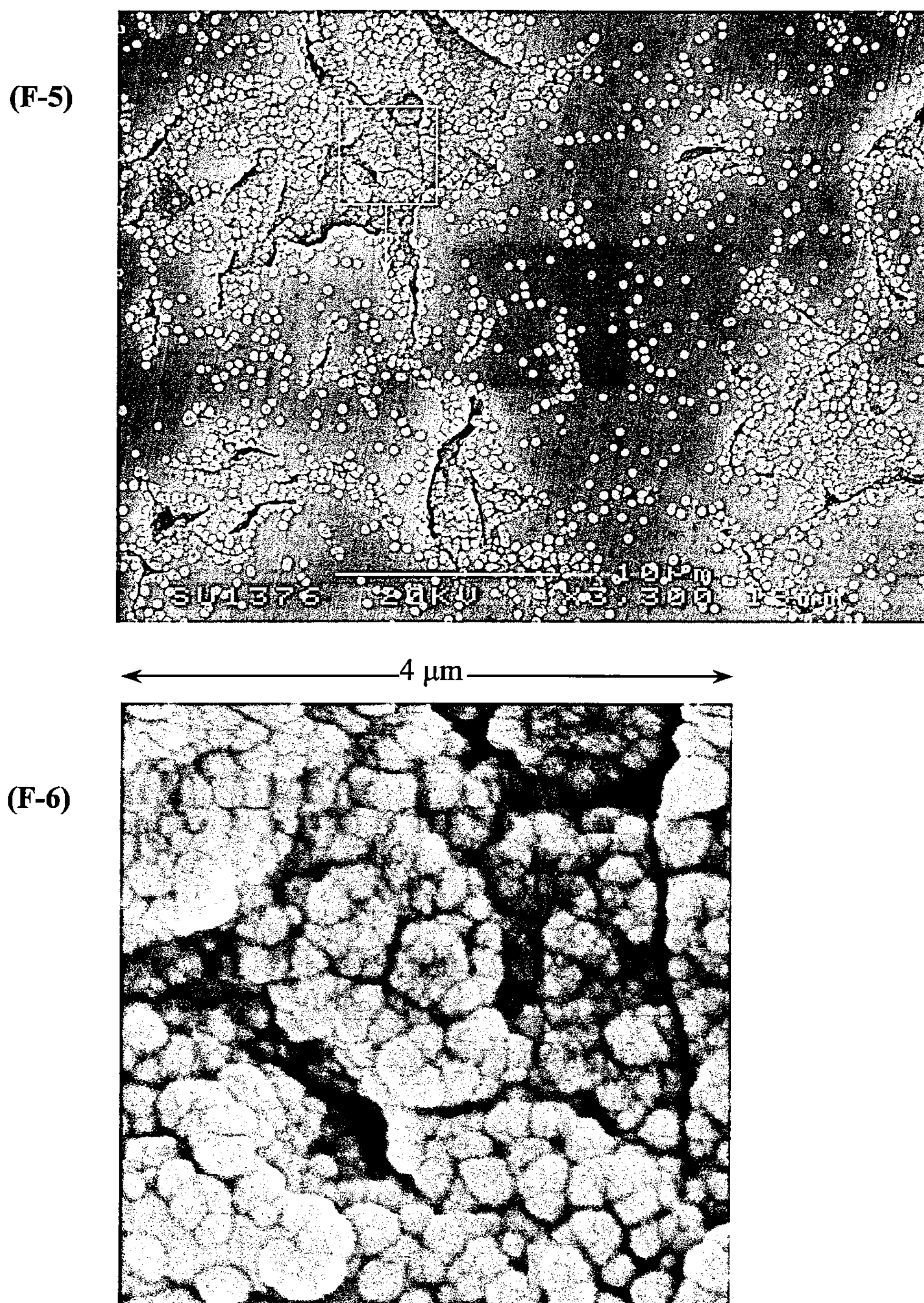

Fig. 5.14 SEM micrographs of the masked area of the cavity-rich substrate

As it could be seen on the photograph of the deposition substrate in the Appendix F, silicon samples were fastened to the substrate by thin metal strips. It appeared that at least one of

the strips did not adjoin tightly to the silicon surface. There was a gap, through which processing gas, containing hydrocarbon components, could flow freely under the strip and over the masked area of the sample. As a result, growth of crystallites occurred in the masked area without etching by plasma ions. Signs of the similar process could be seen on the micrograph (E-1) on the Fig. 5.8. Dark dots on the flat surface indicate primordial nucleation sites. Masked areas with crystallite growth were discovered on the samples from the experiments (F) and (G) (Table 5.2). Cauliflower-like crystallites formed practically continuous coating inside the cavities (Fig. 5.14, (F-6)) of the sample from the experiment (F). The polished surface of the same masked area (Fig. 5.14, (F-5)) was covered only by separate ball shaped crystallites. A similar pattern of crystallite distribution could be seen on the masked area of the highly polished sample from the experiment (G) on the Fig. 5.15. A deep scratch was overfilled by a highly segmented and densely packed crystallite phase, consisting of multiple spheroid-like shapes from less than 0.1 up to 0.4 μm in size. At the same time surrounding polished surface had only rare crystallites approximately 0.4 μm in diameter.

(G-3)

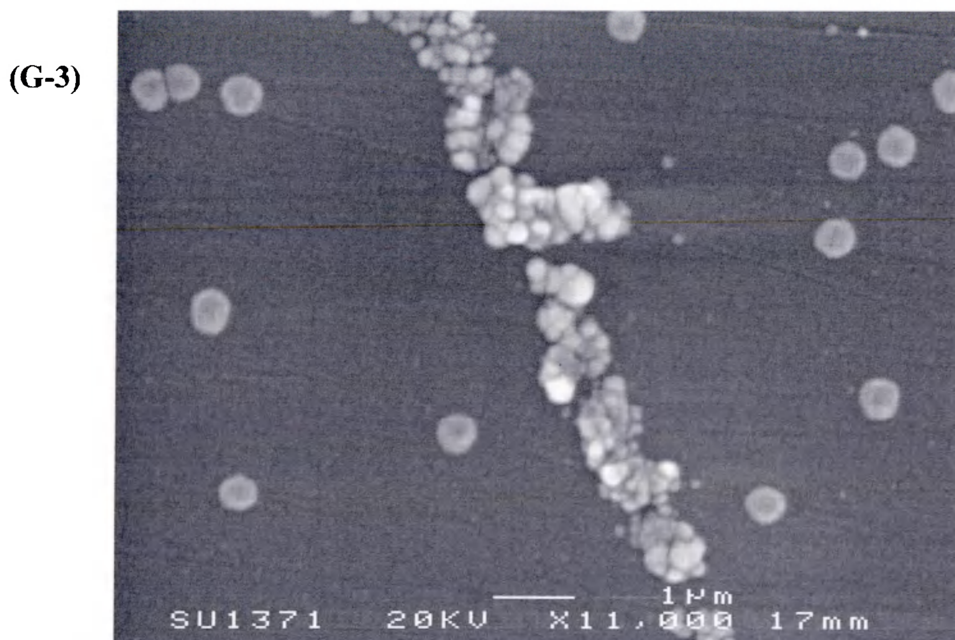

Fig. 5.15 SEM micrograph of the polished substrate

Both morphologies were described earlier by Zhu and co-workers [25]. They established that morphologies of diamond films, deposited from microwave plasmas, depend upon substrate temperature, methane concentration and gas flow rate. "Cauliflower" and "ball" morphologies appeared, when concentration of methane exceeded 4%, but at the different substrate temperatures: 850°C and 1020°C respectively. Although this information confirms in general diamond origin of the crystallites in the experiments with the hollow cathode, it could not be applied directly. The deposition systems were quite different.

In our case, ball crystallites did not form a continuous coating and grew at the same temperature as the "cauliflower" phase. Most likely they were overdeveloped embryo crystallites, which grew to a relatively large spherical size in the absence of "competitive" adjacent growth sites. Development of the "cauliflower" morphology at substrate temperatures, lower by 30 - 50° C than quoted in [25], could be attributed to a lower temperature threshold in our experiments because of added oxygen.

5.5 Conclusion

A number of deposition experiments have been conducted, using RF plasmas with "hot" electrons. The concept of plasma with "hot" electrons was implemented by electron injection at the pressure 70 mtorr. At pressures close to 1 torr and higher this concept was realised in the hollow cathode discharge configuration.

Electron injection demonstrated its viability for controlling deposition process primarily through variation of plasma potential. Effective input of "hot" electrons in discharge chemistry was achieved in the hollow cathode configuration. It is associated with high degree of hydrogen dissociation, resulting from frequent collisions of "hot" electrons with hydrogen molecules at elevated pressures, characteristic to the hollow cathode regime. The direct consequence of producing a large amount of atomic hydrogen in the plasma was etching of the silicon substrates and deposition of the micro-crystallites.

An important parameter, which affected the deposited carbon coatings, was the power density of the discharge. Mixed phase, non-diamond carbon coatings were deposited from the configurations of the RF powered electrode, having six, three or one hollowed structures 18 mm in diameter. Sub-micron particle morphology of these coatings was related to the dusty plasma condition in the hollow cathode discharge. Deposition of the micro-crystallites was achieved only when the internal diameter of the single hollowed structure was reduced to 8 mm and below by means of the graphite inserts. It was associated with increase of discharge power density inside the hollowed structure of the powered electrode, resulting in more effective dissociation of hydrogen.

Conical, "cauliflower" and "ball" morphologies of carbon crystallites were deposited. The first one was linked with presence, others – with absence, of etching effect from plasma energetic ions as well as with topography of silicon substrate and the concentration of hydrocarbon species in the gas phase more than 4%.

General conclusion

The results of the work on this thesis are the following.

A special multi-purpose plasma rig has been designed and built. Its concept has been specifically aimed at combination of plasma diagnostic facilities (electrostatic probe and energy and mass analysis probe) and deposition of carbon films in the wide range of conditions. In the deposition configuration the rig has operated normally with heating of samples above 800° C.

A special electron source for injection of electron current in RF discharge has been designed and built. It was based on the electrically heated tungsten filament with "porous" molybdenum overlayer, filled with barium and strontium carbonate. The filament operated evenly in hydrogen environment for several hours with emission current up to 140 mA.

A range of experiments has been conducted on measurement of the basic characteristics and ionic and neutral composition of hydrogen and argon plasma, sustained by RF capacitive discharge. A considerable presence in plasma of water based ions has been detected, linked with water absorbed on the developed surface of the heat shield.

A range of experiments has been conducted on characterisation of the RF hydrogen plasma with injection and removal of electrons. Electron injection/removal has been found to control strongly plasma potential and maximum of ion energy at the grounded electrode, reducing them to less than 10 V or increasing above 90 V accordingly. Related changes of electron temperature and density have been measured, with plasma density being increased up to an order of magnitude by electron injection. This effect has been linked with a regime, when hot filament instigates discharge inside of an electron source.

Two models were suggested for investigation of the variations of plasma parameters. One was based on the analysis of electron movement in the RF matrix sheath. It was applied for analysis of origin of a non-Maxwellian electron energy distribution in RF plasma in cases of a single-harmonic and a multi-harmonic sheath. Another model considered an approach of conduction currents from the discharge plasma to the electrodes.

It was used for studying time-averaged and time-dependent variations of plasma potentials with electron injection and removal.

Deposition experiments were conducted from both discharge configurations. Carbon coatings were analysed by means of Raman spectroscopy and scanning electron microscope (SEM). Raman spectra of coatings from the plasma with injected electrons revealed a polymeric-like nature of the coatings. SEM study of carbon films from the RF hollow cathode configuration demonstrated a wide variety of coating morphology: from porous films, consisting of separate particles, to nucleation of conical, spherical and cauliflower-like carbon phases.

The following prospective developments of the effects, highlighted in this thesis, could be suggested. It has been demonstrated that the cause of the problems with electron injection in hydrogen plasma at 30 mtorr was a negative potential well in front of the electron source, forming a plasma double layer. Activation of the positive DC anode has gradually suppressed this double layer, increasing plasma density over the discharge volume in the non-linear way. It is thought that a certain combination of parameters of the electron source and the DC anode could benefit more uniform spreading of injected electrons in plasma, than in the case of a single electron source. Further work in this direction could be conducted along the lines of mapping of a spatial distribution of the injected electrons by a portable energy analyser.

Modelling of electron interaction with RF sheath indicated that electron heating is most effective during the first quarter of the RF cycle. It is suggested that increasing frequency of the basic RF signal up to four times, together with changing its shape into trapeze or saw-like could increase effectiveness of RF heating of electrons.

Deposition experiments from the RF hollow cathode demonstrated that diamond growth conditions from the RF plasma could be achieved for a cost of a large deposition area. This limitation could be overcome by using a long, slot-like hollow cathode in combination with the deposition substrate moving above it.

Appendix A. Electrostatic probe measurements

Langmuir introduced the technique of measuring plasma parameters by electrostatic probes in 1924. Since then electrostatic probes are quite often referred to as Langmuir probes. The experimental arrangement of this technique is quite simple. It consists of a bare wire probe, immersed into plasmas, and an external electrical circuit. A second connection to the plasma through, for instance, a large grounded surface completes the citcuit.

Most often the probe has cylindrical or flat geometry. Cylindrical probes are usually made of a tungsten, tantalum, platinum or molybdenum wire of diameter of the order from a few 10s to 100s μm. The size of the wire is dictated by a necessity to minimise disturbances of the plasma. Different analyses are available depending on the size of the probe compared with the Debye length λ_D.

$$\lambda_D = \left(\frac{\varepsilon_0 \cdot T_e}{n_e \cdot e^2} \right)^{1/2} \qquad (A.1)$$

where ε_0 - permittivity of free space, T_e - electron temperature (eV), n_e -electron density (m^{-3}), e - electron charge. Debye length defines a distance of shielding disturbances in plasma. Probe measurements have an important advantage of being local and not averaged over a large volume of plasma.

The electrical circuit of the probe contains a power supply, biasing the probe negative or positive with respect to the plasma. Analysis of the resulting current-voltage characteristic provides information about plasma parameters. A typical probe characteristic is presented on the Fig.A.1. At the voltage, equal to plasma potential V_p, no electrical field is created around the probe. Charged particles move to the probes tip due to their thermal velocities. Since $T_e > T_i$ the probe collects at this point predominantly electron current. With the probe voltage, higher than V_p no ion current reaches the probe surface. An excess of negative charge is built up around the probe, causing electron current to saturate (area A).

But it can still grow, depending on the probe geometry, due to increasing of range of influence as the probe potential rises. When the probe voltage becomes more negative relative to V_p , the balance between

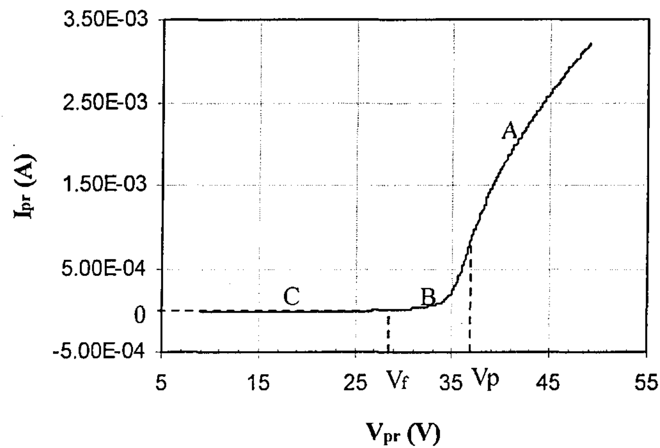

Fig. A.1 Current-voltage signal from the tantalum 0.25 mm diameter 5.6 mm length probe. RF discharge parameters: Ar gas flow – 40 sccm, power - 30 W, pressure - 30 mtorr.

electron and ion currents change in favour of ions owing to the repelling of electrons. Positive charge is built around the probe. This part of characteristic (area B) is known as electron retardation area. At the point V_f, known as floating potential, electron and ion currents are equal, resulting in zero net current. With further decrease of the probe voltage virtually all electrons are repelled, and ion current saturates (area C).

A variety of theories have been developed for calculating plasma parameters from the probe characteristic. The most commonly used methods will be outlined here. All basic probe theories assume Maxwellian electron energy distribution in the plasma.

Plasma potential corresponds to the boundary between regions A and B of the probe characteristic, where there is a "knee". Often the bending point is hard to recognise as on the Fig. A.1. The most reliable method in this case is the second differential of the probe signal, which gives a self-evident value of the plasma potential at the point of crossing zero.

Orbital motion limited (OML) theory is used for deriving electron number density from the part A of the characteristic by the Langmuir formula:

$$I_e = 2 \cdot e \cdot n_e \cdot r \cdot l \cdot \left(\frac{2 \cdot e \cdot |V_p - V_{pr}|}{m_e} \right)^{1/2} \qquad (A.2)$$

where e - electron charge, n_e -electron density, m_e -electron mass, r & l - probe radius and length, V_p & V_{pr} - plasma potential and probe voltage.

OML theory is valid on condition of thick, collisionless sheath $\lambda_e > s > r$, where λ_e - electron mean free path, s - probe sheath thickness, r - probe radius. It is easily seen that the square of the electron current versus probe sheath voltage gives a linear function. Electron number density is derived from its slope. OML theory cannot be reliably applied to the ion saturation region, because orbital ion motion is destroyed by collisions in the sheath.

Conventional Langmuir probe theory interprets the part B of the probe characteristic – the retardation area. The area of it's application covers also the case of collisionless thin sheath $\lambda_e > r > s$. Electron current to the probe in the retardation area is described by the formula:

$$I_e = \frac{1}{4} \cdot e \cdot n_e \cdot A_p \cdot \bar{v}_e \cdot \exp\left(-\frac{V_p - V_{pr}}{T_e} \right) \qquad (A.3)$$

where new symbols are A_p - probe surface area, $\bar{v}_e$ - electron mean speed, electron temperature T_e is in Volt units. Turning to the current density and taking the natural logarithm, the following formula is obtained:

$$\ln j_e = \ln \frac{e \cdot n_e \cdot \bar{v}_e}{4} - \frac{V_p - V_{pr}}{T_e} \qquad (A.4)$$

The formula (A.4) predicts that the natural logarithm of the electron current density is linearly dependent upon the difference of plasma and probe potential. So, electron temperature is derived from the slope of $\ln j_e$, then electron density is easily calculated from the expression (A.3).

The ion saturation region C of the probe characteristic is used for calculation ion density. ABR theory, named after the authors Allen, Boyd and Reynolds, gives a graphical form of an ion current as a function of electron temperature and ion density. Appearance of the electron temperature in the ABR model arises from the effect of the presheath, that pulls ions into the probe due to the potential difference, determined by the electron temperature. Taking T_e from the retardation region leads to determination of ion density. Chen made extension of the ABR theory to the case of cylindrical probe. Description of other positive ion current theories can be found in [127].

Appendix B. Energy and mass analysis probe

Analysis of the positive ions and neutral gas components, incident to the grounded electrode, is conducted by the commercial energy and mass analysis spectrometer EQP300, manufactured by Hiden Analytical Ltd (Fig. B.1).

The spectrometer is pumped differentially by a 60 l/s turbopump with the internal pressure maintained below $(3\text{-}4)\cdot 10^{-7}$ torr while the plasma gas pressure is less than 100 mtorr. The EQP analyser has the energy range 0-100 eV and the mass range up to 300 amu. Energy resolution is 0.25 eV FWHM and mass resolution is 1 amu at 5% peak height throughout the mass range.

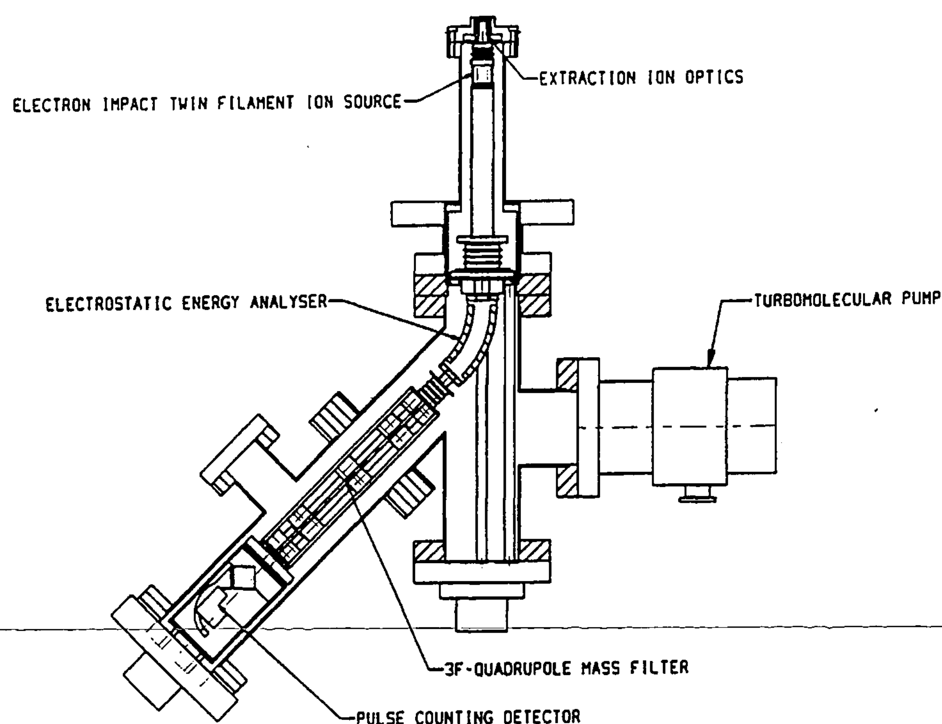

Fig. B.1 Schematic of the EQP300 energy and mass analysis probe
(reproduced from the manual, supplied by Hiden Analytical Ltd)

Ions and neutrals are sampled through the 50 μm diameter sample orifice. The sampling orifice is laser drilled in the metal plate and can be DC biased for ion extraction or be earthed while sampling neutrals. Neutral species are ionised while passing through the electron impact ionisation source, which is located behind the sampling orifice. This procedure is necessary for their subsequent analysis in the quadrupole mass filter. First, all

the ions enter the 45° sector field energy analyser. An energy scan is conducted by shifting the reference potential of the whole spectrometer against ground to accelerate/decelerate ions to the energy required for passing through the energy analyser. Prior to entering the quadrupole mass filter all ions are decelerated to the same energy in order to conduct mass analysis. The quadrupole mass filter has a mass dependent transmission, which added to a mass dependent sensitivity of the chaneltron signal detector results in up to two orders of magnitude signal loss for 300 amu. But for the masses below 50 amu this effect is not significant. The chaneltron detector operates in the high rate (up to 10^7 c/s) pulse counting mode. In addition, the EQP analyser includes several focusing and energy setting ion lenses which condition the ion flux for passing through each of the main parts. During the experimental program, the EQP analyser has been operated with the major electronic parameters set by the manufacture (Table B.I).

Table B.I Electronic parameters values of the EQP 300 analyser

EMISS	0 μA * 200 μA **	VERT	0% * 20% **
EXTRCT	-240 V * 0 V **	CAGE	0 V * 4.5 V **
1STDYN	-1200 V	HORIZ	0%
E-ENERGY	0 V * 70V **	LENS 1	-15 V * 0 V **
MUTHT	1900 V	AXIS	-40 V
FOCUS2	-200V	ENERGY	25 V * 0.5 **
PLATES	7.7 V	QUAD	0% * 10% **
LENS 2	-110 V * -90 V **		

* - values set for the regime of plasma ions sampling

**- values set for the regime of neutrals sampling

Appendix C. Ionization and particle loss model

The idea of the approach, formulated below, is described in the monograph by Lieberman and Lichtenberg [51].

The plasma density n_e is assumed uniform all over the discharge volume. Electron energy distribution is a Maxwellian one. In addition, it is considered that ionization happens only due collision of electron with a non-excited atom or molecule. Than, electron temperature T_e could be derived from balancing the total volume ionization and total surface particle loss. In other words, the rate of production of charged particles in the discharge volume is equalised to the rate of their loss on the electrode surfaces:

$$K_{iz} \cdot n_g \cdot n_e \cdot \mathcal{V}_{pl} = n_e \cdot \upsilon_B \cdot S_{loss} \qquad \text{(C.1)}$$

where K_{iz} – ionisation coefficient, n_g – density of background gas, n_e – electron dencity, $\mathcal{V}_{pl}$ – plasma volume (assumed equal to the discharge volume), υ_B – Bohm velocity, S_{loss} – area of particle loss (assumed equal to the electrode area).

The effective size of plasma could be defined as:

$$d_{eff} = \frac{\mathcal{V}_{pl}}{S_{loss}} \qquad \text{(C.2)}$$

Bohm velocity is expressed as:

$$\upsilon_B = \left(\frac{e \cdot T_e}{m_i}\right)^{\frac{1}{2}} \qquad \text{(C.3)}$$

Assuming Thomson cross-section for describing ionisation by electron-neutral collision, the ionization coefficient could be expressed as:

$$K_{iz} = 4 \cdot \sigma_{max} \cdot \overline{\upsilon}_e \cdot \left(1 + \frac{2 \cdot T_e}{V_i}\right) \cdot \exp\left(-\frac{V_i}{T_e}\right) \qquad \text{(C.4)}$$

where σ_{max} – maximum of ionisation cross section (m^2), $\overline{\upsilon}_e$ - mean electron speed, V_i – ionisation potential. The mean electron speed is:

$$\overline{\upsilon}_e = \left(\frac{8 \cdot e \cdot T_e}{\pi \cdot m_e}\right)^{\frac{1}{2}} \qquad \text{(C.5)}$$

For convenience of using the final formula, we substitute background gas density by gas pressure:

$$n_g = \frac{0.13332 \cdot p}{k \cdot T_g} \qquad (C.6)$$

where p – gas pressure (mtorr), k – Boltzmann constant.

Than, after substituting formulas (C.2) - (C.6) into (C.1) and regrouping the factors we obtain:

$$\alpha \cdot \left(1 + \frac{2 \cdot T_e}{V_i}\right) \cdot \sigma_{max} \cdot M_i^{\frac{1}{2}} \cdot p \cdot d_{eff} \cdot T_g^{-1} \cdot \exp\left(-\frac{V_i}{T_e}\right) = 1 \qquad (C.7)$$

where $\alpha = \frac{0.13332}{k} \cdot \left(\frac{1}{2 \cdot \pi}\right)^{\frac{1}{2}} \cdot \left(\frac{m_p}{m_e}\right)^{\frac{1}{2}} = 1.651 \cdot 10^{23}$, M_i – ion mass (a.m.u.).

Taking natural logarithm of the formula (C.7) and rearranging the factors, the final expression is:

$$T_e \cdot \ln\left(1.651 \cdot 10^{23} \cdot \left(1 + \frac{2 \cdot T_e}{V_i}\right) \cdot T_g^{-1} \cdot M_i^{\frac{1}{2}} \cdot \sigma_{max} \cdot p \cdot d_{eff}\right) - V_i = 0 \qquad (C.8)$$

This is a transcendental equation. It could be solved numerically to obtain a dependence $T_e = F(p)$, when values of V_i, T_g, M_i, σ_{max}, d_{eff} are preset. In this work, the equation (C.8) has been solved, using the *root* function of the Mathcad software (section 2.8.1, chapter II).

Appendix D. Chemical reactions, describing impact collision processes with hydrogen

A selection of graphs, representing cross section σ (dashed curve) and the corresponding reaction rate coefficient <σv> (solid curve), are presented in this appendix for impact collision reactions with hydrogen. The graphs are reproduced from the publication [128].

In the reactions between electrons and heavy particles (Fig. C.1-C.5, C.8, C.9) energy of heavy particle is taken to be zero. For the reactions between heavy particles (Fig. C.6 and C.7) the target particle energy can be important. Therefore, curves of reaction rate coefficient are presented for several energies (in eV) of the target particle, specified by number above the graph.

Fig. D.1

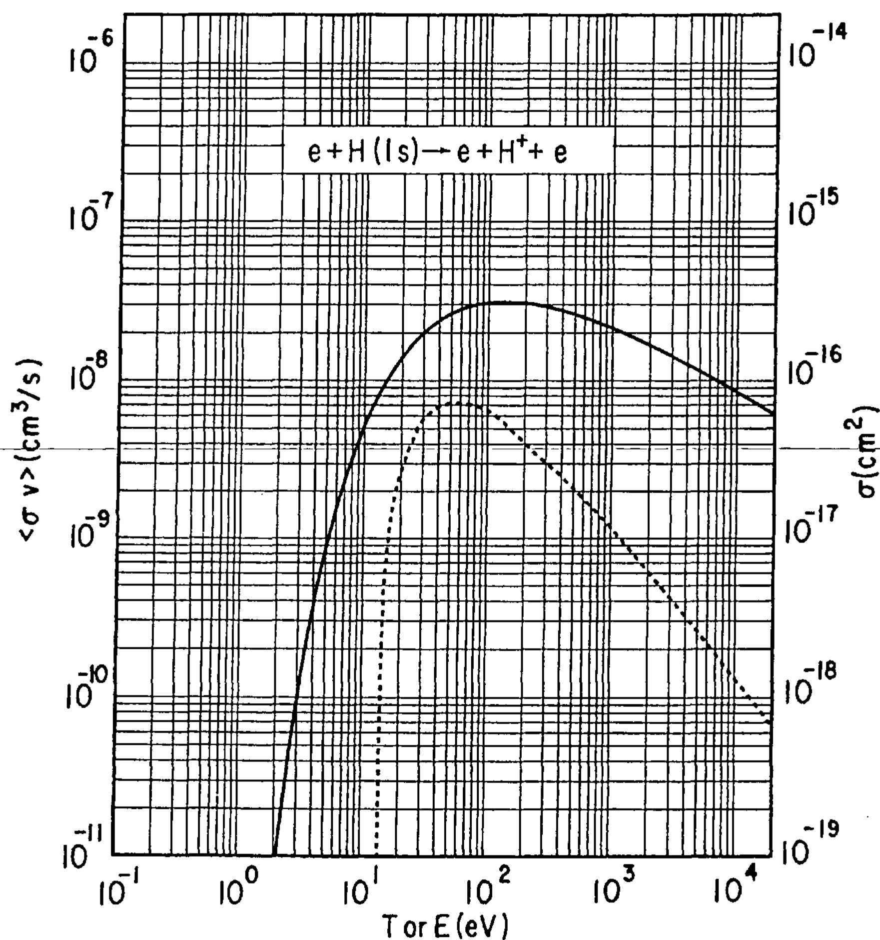

Fig. D.2

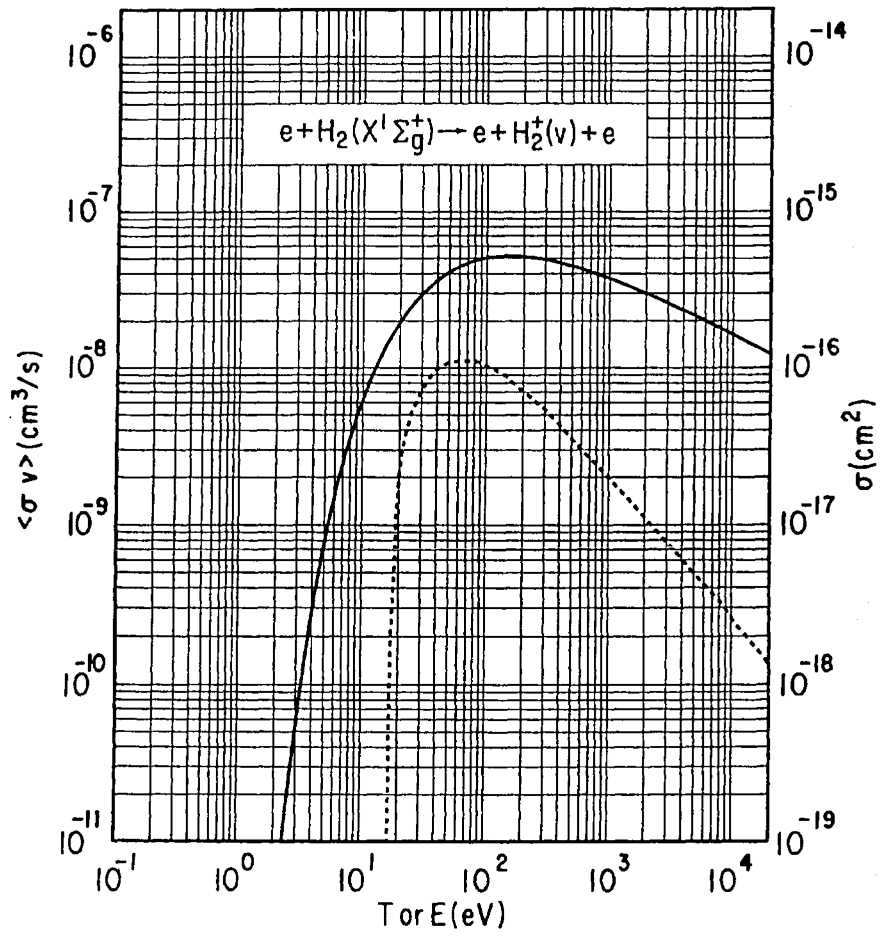

Fig. D.3

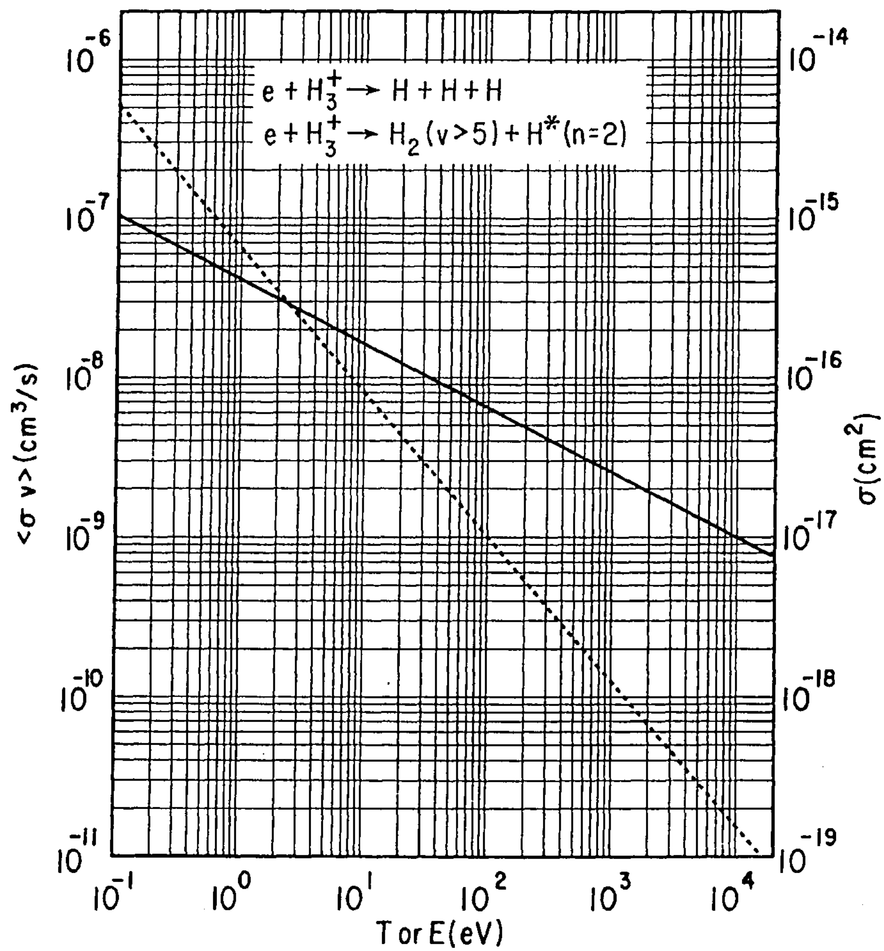

Fig. D.4

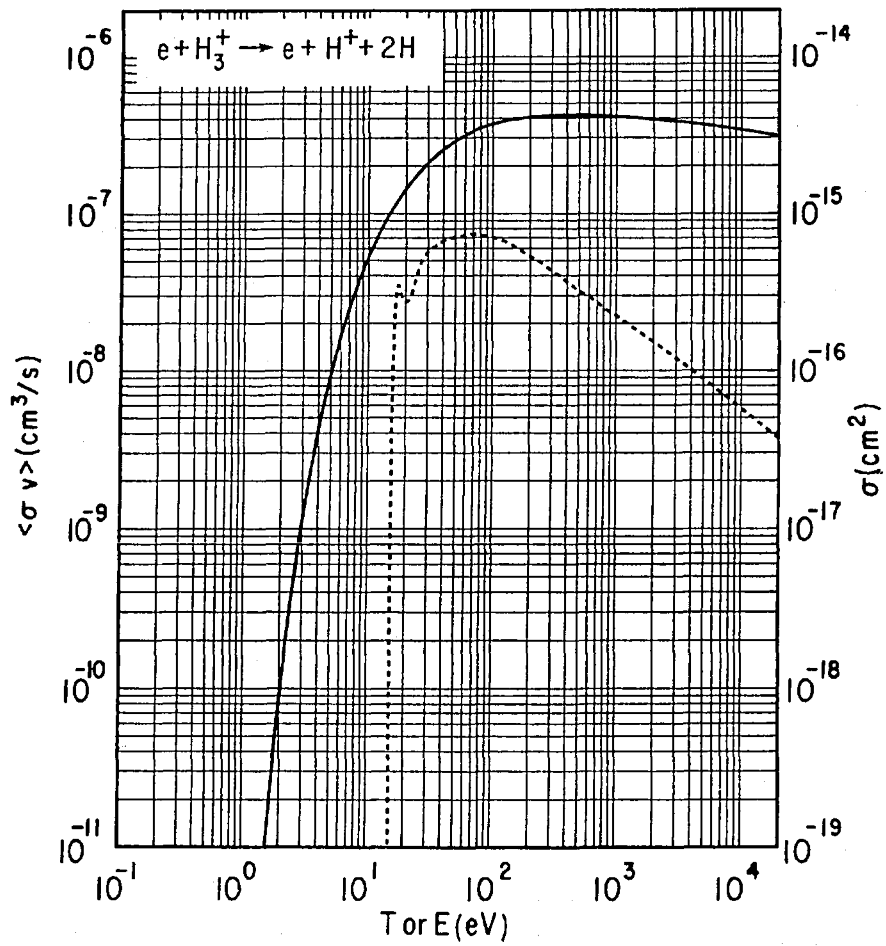

Fig. D.5

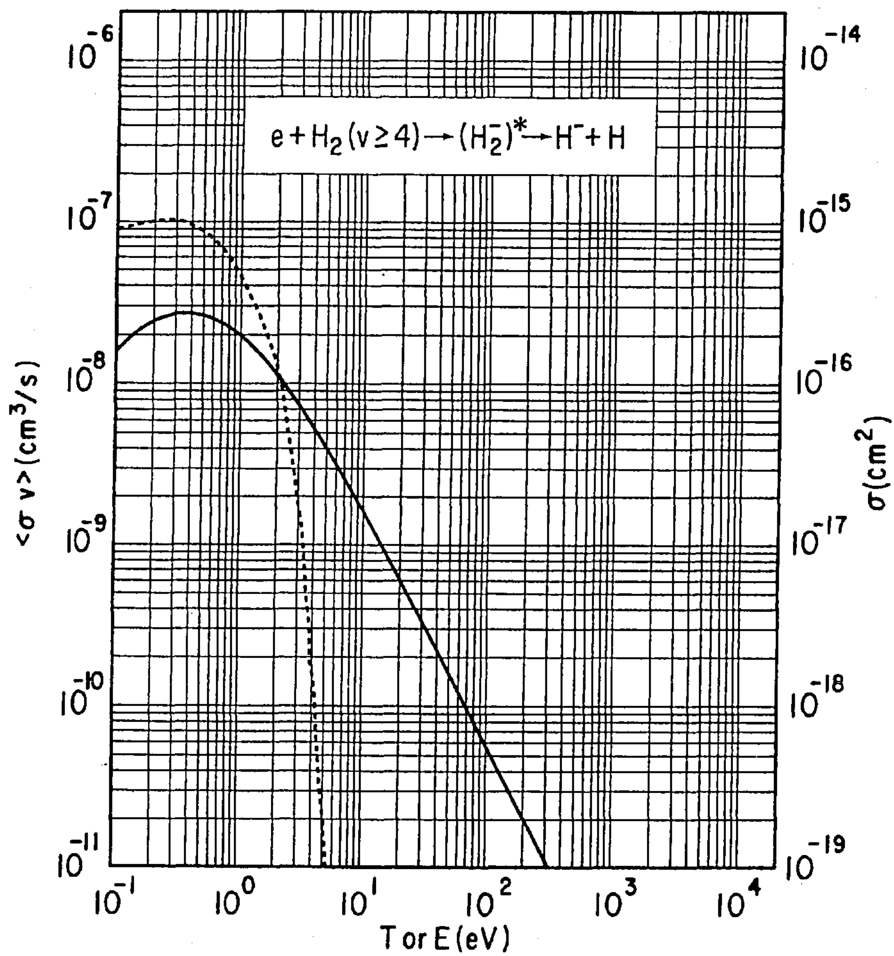

Fig. D.6

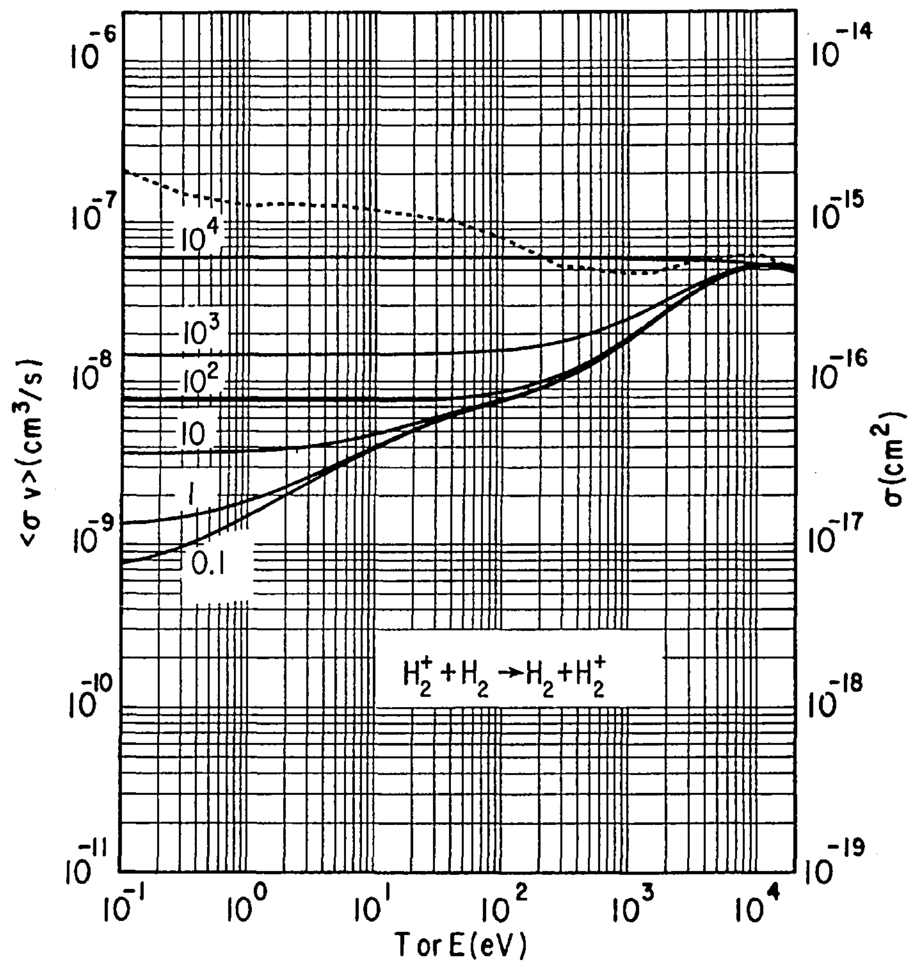

Fig. D.7

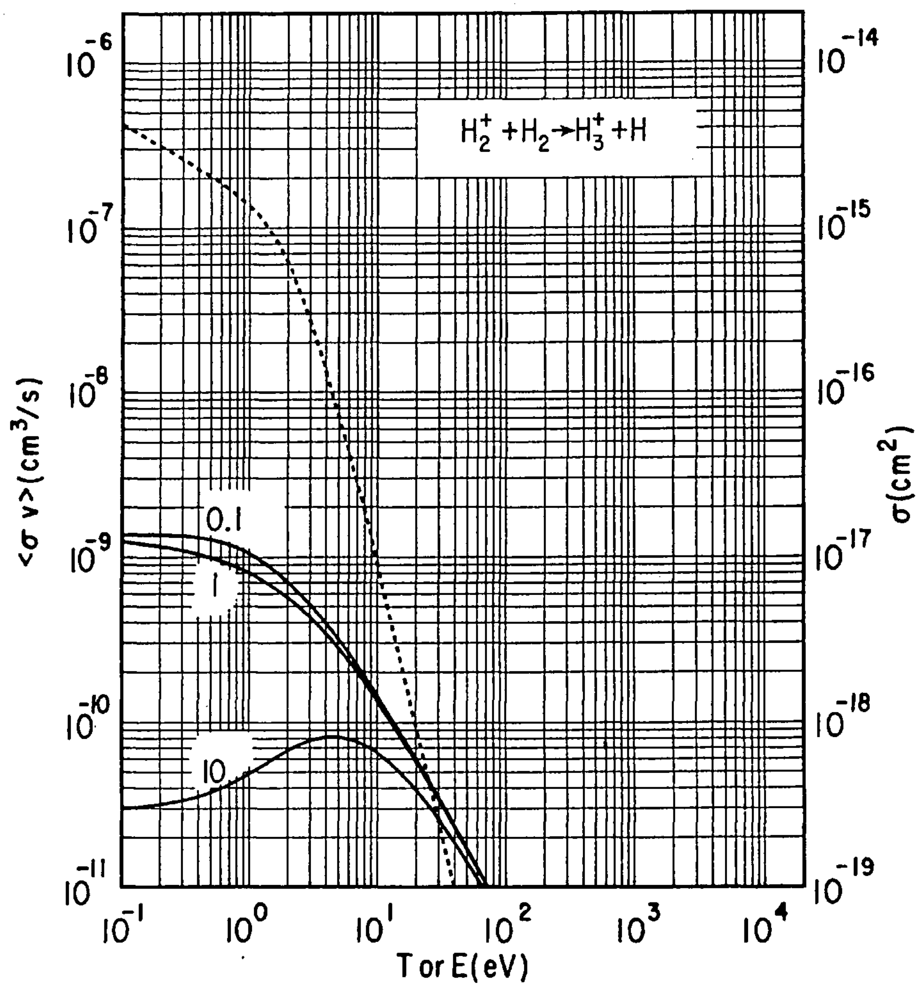

Fig. D.8

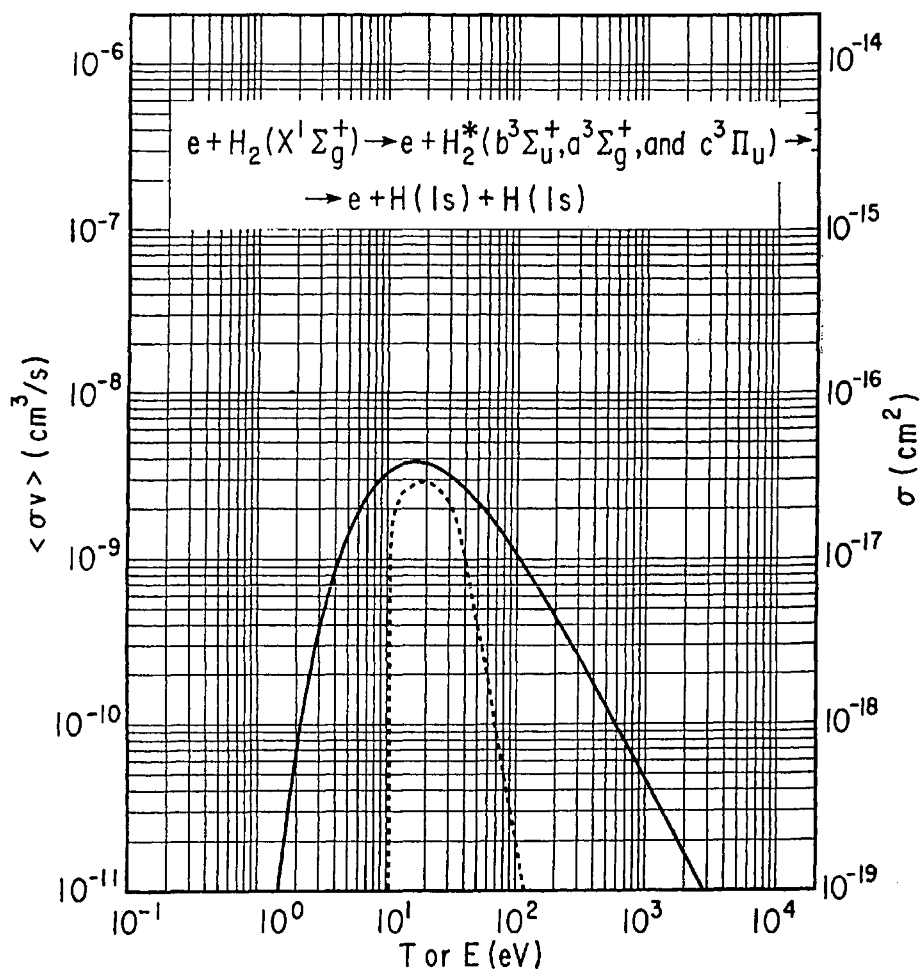

Fig. D.9

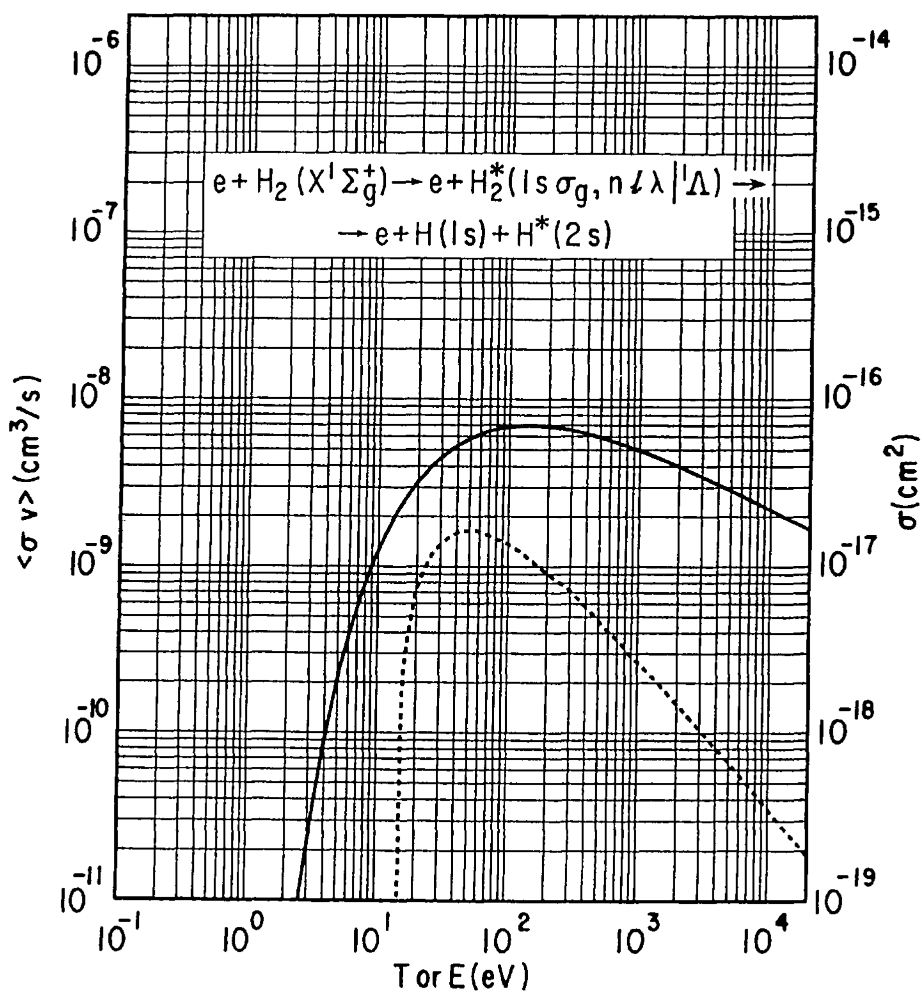

Appendix E. Electron energy distribution

Electron energy distribution describes dependence of electron density upon their velocity or energy. Maxwellian distribution is often used for describing velocity/energy spreading of electrons in low pressure plasma. Originally, it was derived by Robert Maxwell for ideal gas in state of thermal equilibrium:

$$dn = n \cdot \left(\frac{m_a}{2 \cdot \pi \cdot k \cdot T} \right)^{\frac{3}{2}} \cdot \exp\left(-\frac{m_a \cdot \upsilon^2}{2 \cdot k \cdot T} \right) \cdot 4 \cdot \pi \cdot \upsilon^2 d\upsilon \qquad (E.1)$$

where dn – number of atoms, which has velocity in the interval υ to $\upsilon + d\upsilon$, m_a – atom mass, T – thermodynamical temperature, υ - atom velocity. A convenience of Maxwellian distribution is concluded in describing velocity/energy states of all considered particles by a single parameter T. The formula (E.1) could be re-written as:

$$\frac{dn}{n} = f(\upsilon) d\upsilon \qquad (E.2)$$

$f(\upsilon)$ is known as velocity distribution function of atoms:

$$f(\upsilon) = \left(\frac{m_a}{2 \cdot \pi \cdot k \cdot T} \right)^{\frac{3}{2}} \cdot \exp\left(-\frac{m_a \cdot \upsilon^2}{2 \cdot k \cdot T} \right) \cdot 4 \cdot \pi \cdot \upsilon^2 \qquad (E.3)$$

Electron energy distribution function (EEDF) could be written down in the same way. It is quite convenient to use EEDF in terms of energy, expressed in Volts. Kinetic energy of electron could be put down as:

$$W[V] = \frac{m_e \cdot \upsilon^2}{2 \cdot e} \qquad (E.4)$$

where e – elementary charge, m_e – electron mass. Electron temperature, expressed in Volts, will be:

$$T_e[V] = \frac{k \cdot T}{e} \qquad (E.5)$$

Substituting (E.4) and (E.5) in (E.1) and conducting necessary transformations, we obtain:

$$\frac{dn}{n} = f(W) dW \qquad (E.6)$$

where EEDF is:

$$f(W) = \frac{2}{\sqrt{\pi}} \cdot W^{\frac{1}{2}} \cdot T_e^{-\frac{3}{2}} \cdot \exp\left(-\frac{W}{T_e} \right) \qquad (E.6)$$

Quite useful is another form of distribution function (E.6), which is known as electron energy probability function (EEPF):

$$g(W) = \frac{f(W)}{W^{\frac{1}{2}}} \tag{E.7}$$

Natural logarithm of g(*W*) is linearly dependent of *W*:

$$\ln(g(W)) = \ln\left(\frac{2}{\sqrt{\pi}} \cdot T_e^{-\frac{3}{2}}\right) - \frac{W}{T_e} \tag{E.8}$$

It is helpful to build a ln(g(*W*)) graph to check the nature of a modelled EEDF. If the graph has a straight line form, EEDF is Maxwellian. It is not an equally good check during processing an electrostatic probe signal. It could contain RF components, resulting in a highly distorted EEPF graph. As a result, for probe data it is more practical to use graphs of natural logarithm of electron current (Fig. 3.8, (b) and (d)). The non-distorted part of the $\ln(I_e)$ graphs (Fig. 3.8) has the shape, which could be approximated by a broken straight line, interpreted by a two temperature Maxwellian distribution. As an example, EEPF graph (Fig. E.1, (b)), consisting of straight lines with bending joint, could be built. Summing up two Maxwellian distributions, determined by different temperatures and electron densities, makes:

$$dn = n_{e1} \cdot f_1(W)dW + n_{e2} \cdot f_2(W)dW \tag{E.10}$$

The general EEDF for the distribution (E.10) is:

$$f_\Sigma(W) = \left(1 + \frac{n_{e2}}{n_{e1}} \cdot \left(\frac{T_{e1}}{T_{e2}}\right)^{\frac{3}{2}} \cdot \exp\left(\frac{W}{T_{e1}} - \frac{W}{T_{e2}}\right)\right) \cdot \frac{2}{\sqrt{\pi}} \cdot W^{\frac{1}{2}} \cdot T_{e1}^{-\frac{3}{2}} \cdot \exp\left(-\frac{W}{T_{e1}}\right) \tag{E.11}$$

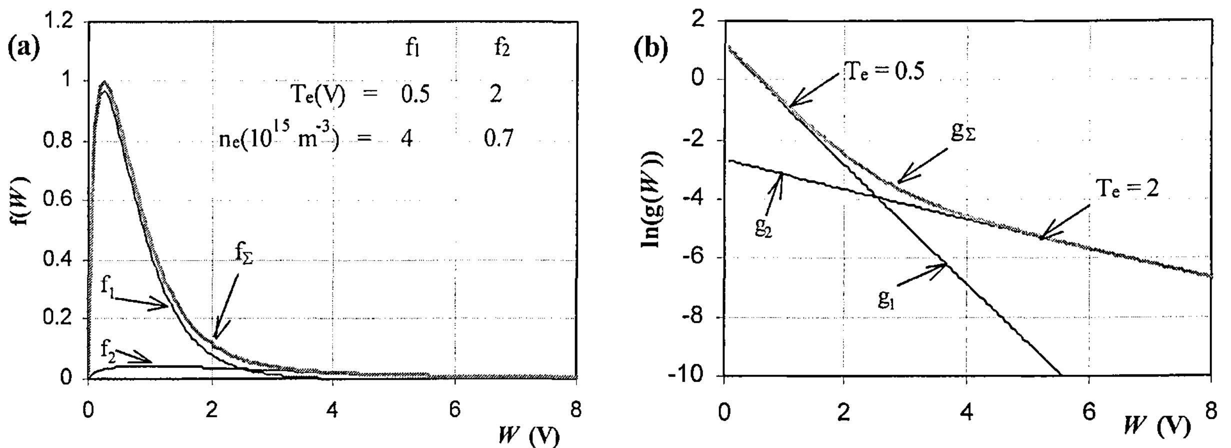

Fig. E.1 EEDF (a) and EEPF (b) of two temperature Maxwellian distribution

Appendix F. Model of particle balance, including conduction and displacement currents.

Dr Peter Johnson has suggested the following approach, based on balancing of conduction and displacement currents to all discharge electrodes.

F.1 Model assumptions

The model assumptions are the following:

1. The sheath is one-dimensional and has a uniform ion density, i.e. it is matrix sheath. Hence double integration of Poisson's equation gives dependence of sheath potential V from its size x: $$V = \frac{e \cdot n}{\varepsilon_0} \cdot \frac{x^2}{2} \qquad \text{(D.1)}$$ where $n = n_e = n_i$ is plasma density, e – electron charge and ε_0 – electrical constant.
2. Conduction current is described using Bohm sheath model. Ion and electron components are summarized to give total conduction current to the electrode surface A: $$i_{con} = A \cdot \left[n \cdot e \cdot \upsilon_B - n \cdot e \cdot \upsilon_e \cdot \exp\left(-\frac{e \cdot V}{k \cdot T_e} \right) \right] \qquad \text{(D.2)}$$ where $\upsilon_B = \left(\frac{k \cdot T_e}{m_i} \right)^{\frac{1}{2}}$ - Bohm speed, $\upsilon_e = \left(\frac{k \cdot T_e}{2 \cdot \pi \cdot m_e} \right)^{\frac{1}{2}}$ - mean electron speed, T_e – electron temperature, k – Boltsman constant, m_i and m_e – ion and electron mass.
3. Displacement current is described regarding sheath as a capacitor with varying plate separation x: $$i_D = A \cdot \frac{dQ}{dt} \qquad \text{(D.3)}$$ where $Q = e \cdot n \cdot x$ – surface charge density. Using formula (D.1) surface charge density can be expressed as $Q = (2 \cdot \varepsilon_0 \cdot e \cdot n)^{\frac{1}{2}} \cdot V^{\frac{1}{2}}$. Substituting it in (D.3) gives: $$i_D = A \cdot \frac{(2 \cdot \varepsilon_0 \cdot e \cdot n)^{\frac{1}{2}}}{2} \cdot V^{-\frac{1}{2}} \cdot \frac{dV}{dt} \qquad \text{(D.4)}$$

4. Current i, potential V and time t are normalised as

$$\imath \rightarrow \frac{i}{A \cdot e \cdot n \cdot \upsilon_B}, \quad \Phi \rightarrow \frac{e \cdot V}{k \cdot T_e} \text{ and } \theta \rightarrow \omega_0 \cdot t \quad \text{(D.5)},$$

where $\omega_0 = 2 \cdot \pi \cdot f$ - basic RF frequency (f=13.56 MHz).

After substituting dimensionless units (D.5) the formula for conduction current (D.2) is transformed in:

$$\imath_{con} = 1 - \alpha \cdot \exp(-\Phi) \quad \text{(D.6)}$$

where $\alpha = \left(\frac{m_i}{2 \cdot \pi \cdot m_e} \right)^{\frac{1}{2}}$. The same procedure for the displacement current (D.4) modifies the formula into:

$$\imath_D = \left(\frac{\varepsilon_0 \cdot m_i}{e^2 \cdot n} \right)^{1/2} \cdot \left(\frac{1}{2 \cdot \Phi} \right)^{1/2} \cdot \omega_0 \cdot \frac{d\Phi}{d\theta} \quad \text{(D.7)}$$

In the expression (D.7) the second factor is reverse proportional to the plasma ion frequency $\omega_i = \left(\frac{e^2 \cdot n}{\varepsilon_0 \cdot m_i} \right)^{1/2}$. Finally, the displacement current can be expressed as

$$\imath_D = \frac{\beta}{\sqrt{2}} \cdot \Phi^{-\frac{1}{2}} \cdot \frac{d\Phi}{d\theta} \quad \text{(D.8)}$$

where $\beta = \frac{\omega_0}{\omega_i}$. Than, the total current, consisting of the conduction and displacement components, is expressed as:

$$\imath = 1 - \alpha \cdot \exp(-\Phi) + \frac{\beta}{\sqrt{2}} \cdot \Phi^{-\frac{1}{2}} \cdot \frac{d\Phi}{d\theta} \quad \text{(D.9)}$$

F.2 Model

RF plasma discharge, having grounded electrode of an area A_A, powered electrode of an area A_C and DC bias electrode of an area A_B, is considered. Plasma boundary is assumed equipotential with potential V. Equivalent circuit of the discharge is presented in Fig. D.1.

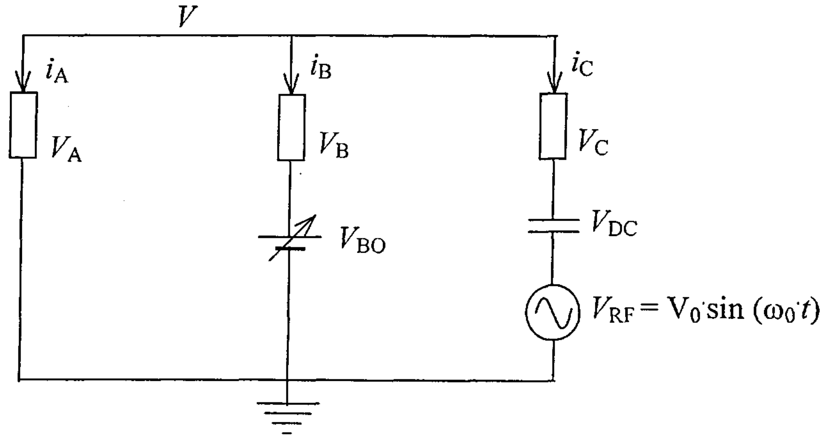

Fig. F.1 Equivalent circuit of RF discharge with DC bias electrode
where: $V_{A,B,C}$ – potentials across plasma sheaths, V_{DC} – potential across blocking capacitor C_{DC}, V_{BO} – DC bias potential at the bias electrode.

The circuit equations could be written as:

$$V = V_A = V_B + V_{BO} = V_C + V_{DC} + V_{RF} \quad \text{(D.10)}$$

$$i_A + i_B + i_C = 0 \quad \text{(D.11)}$$

Furthermore, potential across the blocking capacitor varies in time:

$$\frac{dV_{DC}}{dt} = \frac{1}{C_{DC}} \cdot i_C \quad \text{(D.12)}$$

Areas of the electrodes are normalised by the area of the powered electrode:

$$A_C = 1,\ A_A = \frac{A_A}{A_C},\ A_B = \frac{A_B}{A_C} \quad \text{(D.13)}$$

Than, after normalising equations (D.10), (D.11) and (D.12) we obtain:

$$\Phi = \Phi_A = \Phi_B + \Phi_{BO} = \Phi_C + \Phi_{DC} + \Phi_{RF} \quad \text{(D.14)}$$

$$\iota_A + \iota_B + \iota_C = 0 \quad \text{(D.15)}$$

$$\frac{d\Phi_{DC}}{d\theta} = \frac{e^2 \cdot n}{(k \cdot T_e \cdot m_i)^{\frac{1}{2}}} \cdot \frac{A_C}{\omega_0 \cdot C_{DC}} \cdot \iota_C \quad \text{(D.16)}$$

Expression (D.16) is re-written, using Debye length $\lambda_D = \left(\frac{\varepsilon_0 \cdot k \cdot T_e}{e^2 \cdot n}\right)^{\frac{1}{2}}$ and ion plasma

frequency $\omega_i = \left(\frac{e^2 \cdot n}{\varepsilon_0 \cdot m_i}\right)^{1/2}$ as:

$$\frac{d\Phi_{DC}}{d\theta} = \frac{\omega_i}{\lambda_D} \cdot \frac{\varepsilon_0 \cdot A_C}{\omega_0 \cdot C_{DC}} \cdot \imath_C \qquad \text{(D.17)}$$

The notion of characteristic capacitance of the powered electrode sheath is introduced as :

$$C_C = \frac{\varepsilon_0 \cdot A_C}{\lambda_D} \qquad \text{(D.18)}$$

Further, time derivative of potentials will be expressed as Φ' in order to simplify formulas. After substituting (D.9) and (D.18) into (D.17) we obtain:

$$\Phi_{DC}' = \gamma \cdot \left(1 - \alpha \cdot \exp(-\Phi_C) + \frac{\beta}{\sqrt{2}} \cdot \Phi_C^{-\frac{1}{2}} \cdot \Phi_C'\right) \qquad \text{(D.19)}$$

where $\gamma = \frac{C_C}{C_{DC}} \cdot \frac{\omega_i}{\omega_0}$.

Derivatives of the sheath potentials (D.14) are written as:

$$\Phi_A' = \Phi' \qquad \text{(D.20)}$$

$$\Phi_B' = \Phi' \qquad \text{(D.21)}$$

$$\Phi_C' = \Phi' - \Phi_{DC}' - \Phi_0 \cdot \cos\theta \qquad \text{(D.22)}$$

Than, using expressions (D.9), (D.14), (D.20), (D.21) and (D.22), it is possible to write down formulas of total current to each of electrodes:

$$\imath_A = A_A \cdot \left(1 - \alpha \cdot \exp(-\Phi) + \frac{\beta}{\sqrt{2}} \cdot \Phi^{-\frac{1}{2}} \cdot \Phi'\right) \tag{D.23}$$

$$\imath_B = A_B \cdot \left(1 - \alpha \cdot \exp(-(\Phi - \Phi_{BO})) + \frac{\beta}{\sqrt{2}} \cdot (\Phi - \Phi_{BO})^{-\frac{1}{2}} \cdot \Phi'\right) \tag{D.24}$$

$$\imath_C = A_C \cdot \left(1 - \alpha \cdot \exp(-(\Phi - \Phi_{DC} - \Phi_0 \cdot \sin\theta)) + \frac{\beta}{\sqrt{2}} \cdot (\Phi - \Phi_{DC} - \Phi_0 \cdot \sin\theta)^{-\frac{1}{2}} \cdot \left(\Phi' - \Phi'_{DC} - \Phi_0 \cdot \cos\theta\right)\right) \tag{D.25}$$

After substitution of (D.23), (D.24) and (D.25) in (D.15) the following differential equation is derived:

$$\begin{aligned} & A_A + A_B + A_C - \alpha \cdot \exp(-\Phi) \cdot \left[A_A + A_B \cdot \exp(\Phi_{BO}) + A_C \cdot \exp(\Phi_{DC} + \Phi_0 \cdot \sin\theta)\right] - \frac{\beta}{\sqrt{2}} \cdot \Phi_0 \cdot \cos\theta \cdot A_C \cdot (\Phi - \Phi_{DC} - \Phi_0 \cdot \sin\theta)^{-\frac{1}{2}} + \\ & + \Phi' \cdot \frac{\beta}{\sqrt{2}} \cdot \left[A_A \cdot \Phi^{-\frac{1}{2}} + A_B \cdot (\Phi - \Phi_{BO})^{-\frac{1}{2}} + A_C \cdot (\Phi - \Phi_{DC} - \Phi_0 \cdot \sin\theta)^{-\frac{1}{2}}\right] - \Phi'_{DC} \cdot \frac{\beta}{\sqrt{2}} \cdot A_C \cdot (\Phi - \Phi_{DC} - \Phi_0 \cdot \sin\theta)^{-\frac{1}{2}} = 0 \end{aligned} \tag{D.26}$$

Another differential equation is obtained by substituting (D.14) and (D.22) in (D.19):

$$\begin{aligned} & \gamma - \gamma \cdot \alpha \cdot \exp[-(\Phi - \Phi_{DC} - \Phi_0 \cdot \sin\theta)] - \frac{\gamma \cdot \beta}{\sqrt{2}} \cdot \Phi_0 \cdot \cos\theta \cdot (\Phi - \Phi_{DC} - \Phi_0 \cdot \sin\theta)^{-\frac{1}{2}} + \Phi' \cdot \frac{\gamma \cdot \beta}{\sqrt{2}} \cdot (\Phi - \Phi_{DC} - \Phi_0 \cdot \sin\theta)^{-\frac{1}{2}} - \\ & - \Phi'_{DC} \cdot \left[\frac{\gamma \cdot \beta}{\sqrt{2}} \cdot (\Phi - \Phi_{DC} - \Phi_0 \cdot \sin\theta)^{-\frac{1}{2}} + 1\right] = 0 \end{aligned} \tag{D.27}$$

164

Equations (D.26) and (D.27) are reduced to a symbolical form:

$$A + B \cdot \Phi' + C \cdot \Phi'_{DC} = 0 \qquad \text{(D.28)}$$

$$D + E \cdot \Phi' + F \cdot \Phi'_{DC} = 0 \qquad \text{(D.29)}$$

This is a system of two first order differential equations with non-linear coefficients:

$$A = A_A + A_B + A_C - \alpha \cdot \exp(-\Phi) \cdot [A_A + A_B \cdot \exp(\Phi_{BO}) + A_C \cdot \exp(\Phi_{DC} + \Phi_0 \cdot \sin\theta)] - \frac{\beta}{\sqrt{2}} \cdot \Phi_0 \cdot \cos\theta \cdot A_C \cdot (\Phi - \Phi_{DC} - \Phi_0 \cdot \sin\theta)^{-\frac{1}{2}}$$

$$B = \frac{\beta}{\sqrt{2}} \cdot \left[A_A \cdot \Phi^{-\frac{1}{2}} + A_B \cdot (\Phi - \Phi_{BO})^{-\frac{1}{2}} + A_C \cdot (\Phi - \Phi_{DC} - \Phi_0 \cdot \sin\theta)^{-\frac{1}{2}} \right]$$

$$C = \frac{\beta}{\sqrt{2}} \cdot A_C \cdot (\Phi - \Phi_{DC} - \Phi_0 \cdot \sin\theta)^{-\frac{1}{2}}$$

$$D = \gamma - \gamma \cdot \alpha \cdot \exp[-(\Phi - \Phi_{DC} - \Phi_0 \cdot \sin\theta)] - \frac{\gamma \cdot \beta}{\sqrt{2}} \cdot \Phi_0 \cdot \cos\theta \cdot (\Phi - \Phi_{DC} - \Phi_0 \cdot \sin\theta)^{-\frac{1}{2}}$$

$$E = \frac{\gamma \cdot \beta}{\sqrt{2}} \cdot (\Phi - \Phi_{DC} - \Phi_0 \cdot \sin\theta)^{-\frac{1}{2}}$$

$$F = \frac{\gamma \cdot \beta}{\sqrt{2}} \cdot (\Phi - \Phi_{DC} - \Phi_0 \cdot \sin\theta)^{-\frac{1}{2}} + 1$$

165

The equations (D.28) and (D.29) could be changed into:

$$\Phi' = \frac{D \cdot C - A \cdot F}{B \cdot F - E \cdot C} \qquad (D.30)$$

$$\Phi'_{DC} = \frac{D \cdot B - A \cdot E}{C \cdot E - B \cdot F} \qquad (D.31)$$

This system of equations could be solved numerically for a suitable initial conditions.

F.3 Solution

The system of the equations (D.28) and (D.29) has been solved, using a fourth order Runge-Kutta numerical method in Mathcad software. The program algorithm has been developed by Dr Peter Johnson.

The initial discharge conditions were the following: hydrogen molecular ion mass $M_i = 3$, $T_e = 2.62$ eV, $n_e = 1.2 \cdot 10^{15}$ m^{-3}, area of the powered electrode $A_C = 7.854 \cdot 10^{-3}$ m^2, dimensionless areas of the electrodes $A_C = 1$, $A_A = 7.84$, $A_B = 0.615$, potential of the RF generator $\Phi_0 = 70$, potential of the DC bias electrode $\Phi_{BO} = 0$ and 3. These conditions have been set close to the real RF discharge. The only difference was in the value Φ_0, which in the real discharge was of the order 240. It has been impossible to find a solution of the equations (D.28) and (D.29) for the values
$\Phi_0 >> 70$ and $\Phi_{BO} >> 3$. Time-averaged potential values from the conduction currents model (Fig.4.12) have been used as initial conditions for the total currents model. Results of calculations are presented in Fig. D.2.

It could be seen that potentials during RF cycle have more realistic shape than the one from the conduction current model (Fig. 4.13). Plasma potential shapes (Fig. D.2 (a) and (b)) clearly indicate presence of higher harmonics. Nonetheless, the total currents model doesn't allow increase of RF potential in plasma with growth of Φ_{BO}. It contradicts experimental results. In particular, problems of compensation of RF signal at the electrostatic probe (Sections 3.5 and 3.7, chapter III) point out at the opposite effect.

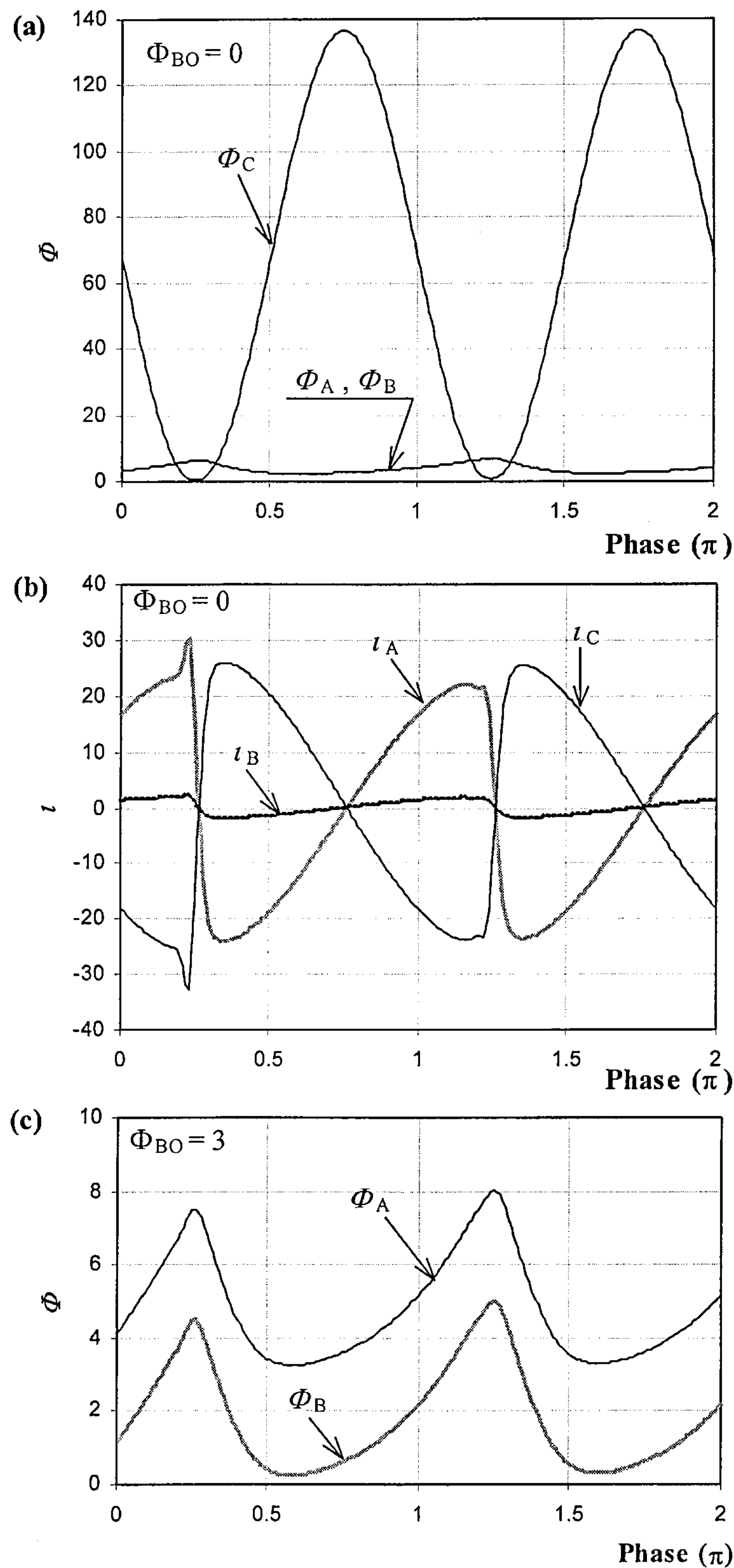

Fig. F.2 Variations of potentials and currents during RF cycle.

It is suggested that the purely electron sheath, set in the total currents model, limits its capability in describing the real plasma conditions. If electric field in electrode sheaths could be set to reverse during part of RF cycle, the model, most likely, will work with higher values of Φ_0 and Φ_{BO} as well as portray more realistic RF potentials in plasma. This could be the next stage in development of the model.

Appendix G. Raman Spectroscopy

The Raman effect arises when the incident light excites molecules in the sample, which subsequently scatter the light. While most of this scattered light is at the same wavelength as the incident light, some is scattered at a different wavelength. This *inelastically* scattered light is called Raman scatter. It results from the molecule changing its molecular motions.

The energy difference between the incident light (E_i) and the Raman scattered light (E_s) is equal to the energy involved in changing vibrational state of the molecule (i.e. getting the molecule to vibrate, E_v). This energy difference is called the Raman shift.

$$E_v = E_i - E_s$$

Several different Raman shifted signals will often be observed; each being associated with different vibrational or rotational motions of molecules in the sample. The particular molecule and its environment will determine what Raman signals will be observed.

A plot of Raman intensity versus Raman shift is called a Raman spectrum.

Appendix H. Hollow cathode deposition chamber

In the first experiments there was used a hollow cathode with a holed structure, having nine orifices. In order to save time it has been manufactured from

(a)

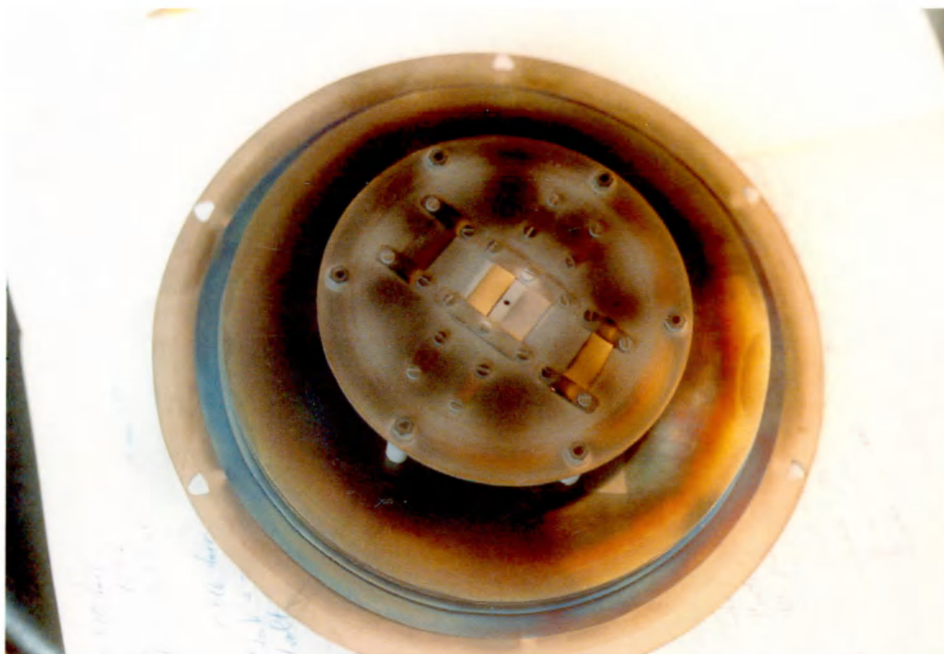

(b)

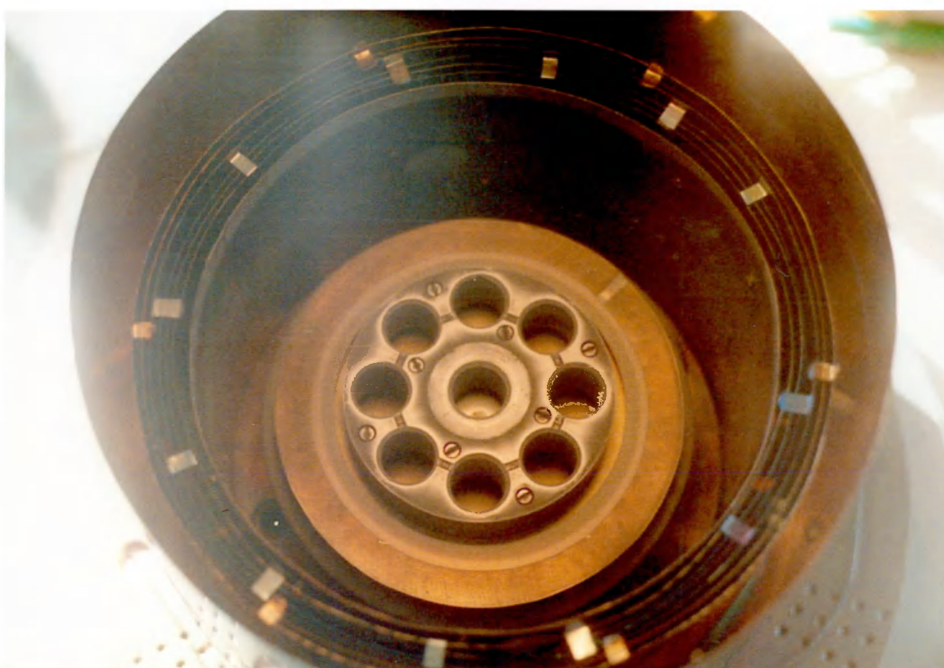

Fig. H.1 Hollow cathode discharge chamber after trial deposition experiments (a) – deposition substrate, (b) – hollow cathode unit, surrounded by the heat shield

the outdated vacuum flange. Hence, it had nine holes instead of seven in the later model. Trial experiments, using nine-hole model, have revealed some features of hollow cathode

discharge. First, it was discovered, that the stainless steel body of the cathode was actively etched. A light grey colour of the holes base and shining metal surface around the holes edges indicate the places of the most active etching (Fig. F.1). Second, hollow cathode glow was always brighter in the central hole. It indicates a higher discharge density in this part of the electrode. This non-uniform distribution of glow among the holes was linked with non-uniformity of gas flow plus, possible, difference in electrode structure heating. In the experiments with the seven-hole model the central hole was blocked. Alternatively, six outside holes were blocked and covered by the grounded shield, when it was necessary to work with a single hole structure.

Appendix I. Plasma potential of the hollow cathode discharge

Plasma potential has been estimated, using the information of time resolved voltage of the powered electrode. Qualitative reading of the voltage was taken from the oscilloscope screen, displaying sample signal from the matching unit during the deposition experiment (F) (Chapter V, Table 5.2). The signal had a split peak structure, which was associated with high values of second and third harmonics (Fig. G.1). Maximums of the peaks were equal approximately 420 and 350 V; while the minimum between them was about 250 V. Coefficients in the formula (G.1) were selected to match approximately the maximums and the minimum of the RF signal.

$$V_{RF}(t) = 400 \cdot \sin(\omega \cdot t) + 30 \cdot \sin(2 \cdot \omega \cdot t) + 150 \cdot \sin(3 \cdot \omega \cdot t) \qquad (G.1)$$

Than, potential of the powered electrode could be calculated using formula (G.2):

$$V_{pow\ el}(t) = V_{RF}(t) + \mathrm{V}_{\mathrm{dc\ bias}} \qquad (G.2)$$

The initial value of the self-bias potential of the powered electrode $V_{dc\ bias}$ in the experiment (F) was –26 V.

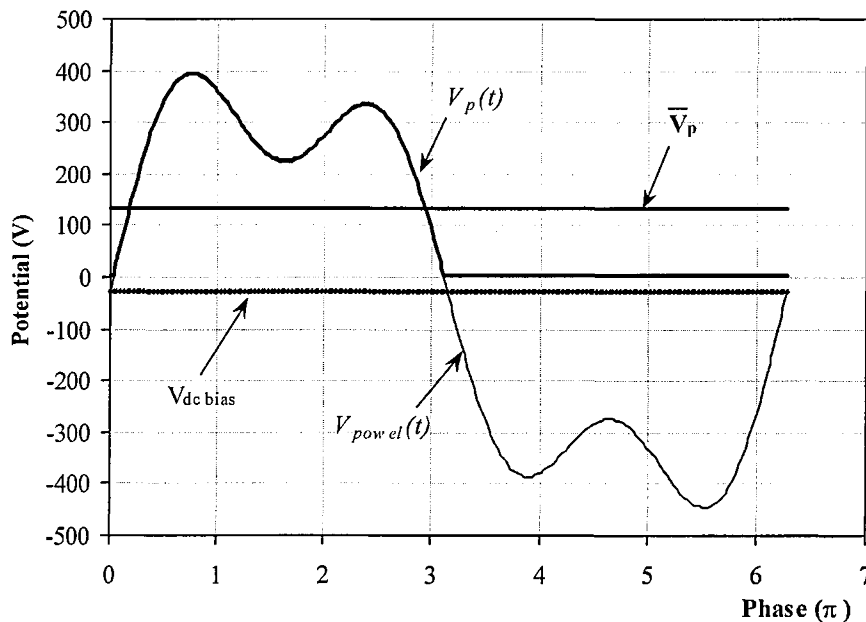

Fig. I.1 Time-resolved potentials in the RF hollow cathode discharge

The time-resolved plasma potential was approximated as

$$V_p(t) = \begin{cases} V_{pow\ el}(t) + \Delta V, & V_{pow\ el}(t) > 0 \\ \Delta V, & V_{pow\ el}(t) < 0 \end{cases} \qquad (G.3)$$

where

$$\Delta V = T_e \cdot \ln\left(\frac{M_i}{2 \cdot \pi \cdot m_e}\right)^{\frac{1}{2}} \qquad (G.4)$$

The electron temperature T_e of the "cold" electron group was assumed to be equal 1 eV. The dominant ion in plasma was accepted to be H_3^+. Therefore the ration M_i/m_e was equal thrice the proton electron mass ratio 1836.2 .

Then, from the expression (G.3) the time-averaged plasma potential $\overline{V}_p$ was calculated to be 132 V.

References

1. O.I.Leipunski, "Synthetic diamonds", Usp. Khim., 8 (1939), 1519-1534.
2. P.K.Bachmann, "Diamonds from vapour phase", Phys. World, 4 (1991), 32-36.
3. J.Wilks and E.Wilks, "Properties and applications of diamond", 1991, Butterworth-Heinemann, Oxford, 16.
4. L.S.Polak, "Electrochemistry in discharge plasmas", in Proc. 10th Int. Conf. on Phenomena in Ionised Gases, Oxford, Donald Parsons, 1971, 113-191.
5. J.C.Angus, "Development of low-pressure diamond growth in the United States", in "Synthetic diamond: emerging CVD science and technology", ed. by K.E.Spear and J.P.Dismukes, 1994, John Wiley & Sons. Inc., New York, 21-40.
6. B.V.Deriagin and D.B.Fedoseev, "The synthesis of diamond at low pressure", Sci. Amer., 233 (1975), 102-108.
7. B.V.Deriagin, B.V.Spitsyn, L.L.Bouilov, A.A.Klochkov, A.E.Gorodetski and A.V.Smolyaninov, "Synthesis of diamond on non-diamond substrates", Dokl. Akad. Nauk SSSR, 231 (1976), 333-335.
8. B.V.Spitsyn, L.L.Bouilov and B.V.Deriagin, "Vapour growth of diamond on diamond and other surfaces", J. Cryst. Growth, 52 (1981), 219-226.
9. Ref. 5, p. 35.
10. S.Aisenberg and R.Chabot, J. Appl. Phys., 42 (1971), 2953.
11. D.S.Whitmell and R.Williamson, Thin. Sol. Films, 35 (1976), 253.
12. L.Holland and S.M.Ohja, Thin. Sol. Films 38 (1976), L17.
13. S.Matsumoto, Y.Sato, M.Kamo and N.Setaka, "Vapour deposition of diamond particles from methane", Jpn. J. Appl. Phys., Part 2, 21 (1982), L183-L185.
14. S.Matsumoto, Y.Sato, M.Tsutsumi and N.Setaka, "Growth of diamond particles from methane-hydrogen gas", J. Mater. Sci., 17 (1982), 3106-3112.
15. M.Kamo, Y.Sato, S.Matsumoto and N.Setaka, "Diamond synthesis from gas phase in microwave plasma", J. Cryst. Growth, 62 (1983), 642-644.
16. Y.Matsui, S.Matsumoto and N.Setaka, "TEM-electron energy loss spectroscope study of the diamond particles prepared by chemical vapour

deposition from methane", J. Mater. Sci. Lett., 2 (1983), 532-534.

17. P.K.Bachman, "Microwave plasma CVD and related techniques for low pressure diamond synthesis", in Thin Film Diamond, ed. by A.H.Lettington, and J.W.Steeds, 1994, Chapman & Hall, London, 31-54.

18. K.E.Spear and M.Frenklach, "Mechanisms for CVD diamond growth", in "Synthetic Diamond: Emerging CVD Science and Technology", ed. by K.E.Spear and J.P.Dismukes, 1994, John Wiley & Sons. Inc., New York, 243-304.

19. A.H.Lettington, "Applications of diamond-like carbon thin films", in "Thin Film Diamond", ed. by A.H.Lettington and J.W.Steeds, 1994, Chapman & Hall, London, 117-126.

20. "Diamond and diamond-like films and coatings", ed. by R.E.Clausing, L.L.Horton, J.C.Angus and P.Koidl, NATO ASI Series B: Physics, 1991, Plenum Press, New York, Vol. 226.

21. "Thin Film Diamond", ed. by A.H.Lettington and J.W.Steeds, 1994, Chapman & Hall, London.

22. "Synthetic Diamond: Emerging CVD Science and Technology", ed. by K.E.Spear and J.P.Dismukes, 1994, John Wiley & Sons. Inc., New York.

23. S.Matsumoto and Y.Matsui, "Electron microscopic observation of diamond particles grown from the vapour phase", J. Mater. Sci., 18 (1983), 1785-1793.

24. A.van der Drift, Philips Res. Rep., 22 (1967), 267.

25. W.Zhu, A.R.Badzian and R.Messier, "Morphological phenomena of CVD diamond (Part 1)", in Proc. SPIE Diamond Optics III, edit. by A.Feldman and S.Holly, Bellingham, WA: SPIE – The Int. Society for Optical Eng., vol. 1325, 1990, 187 – 201.

26. B.V. Deryagin and D.V.Fedoseev, "Growth of Diamond and Graphite from the Gas Phase", Nauka, Moscow (1977).

27. N.Setaka, in "Chemical Vapour Deposition", Proc. 10th Int. Conf. on Chem. Vapour Deposition, ed. by G.W.Gullen and J.Brocher, The Electrochemical Society, Pennington, NJ, 1987, 1156-1163.

28. B.B.Pate, Surf. Sci., 165 (1986), 83.

29. K.E.Spear and M.Frenklach, in "Diamond and diamond-like films", ed. by A.J.Purdes, J.C.Angus, R.F.Davis, B.M.Meerson, K.E.Spear and M.Yoder, The Electrochemical Society, Pennington, NJ, 1989, 122-138.

30. M.Frenklach, J. Appl. Phys., **65** (1989) 5142.

31. J.C.Angus, A.Argoitia, R.Gat, Z.Li, M.Sunkara, L.Wang and Y.Wang, "Chemical vapour deposition of diamond", in ref. 21, 1-14.

32. M.Frenklach, "Theory and models for nucleation and growth of diamond films", in ref. 20, 499-524.

33. B.Lux and R.Haubner, "Nucleation and growth of low pressure diamond", in ref. 20, 579-610.

34. B.R.Stoner, G.H.M.Ma, S.D.Wolter and J.T.Glass, Phys. Rev. B, 45 (1992), 11067.

35. D.P.Monaghan, K.C.Laing, P.A.Logan, P.Teer and D.G.Teer, Surf. Engin., (1993), 347.

36. J.Robertson, "Structure and electronic properties of diamond-like carbon", in ref. 20, 331-356.

37. Y.Catherine, "Preparation techniques for diamond-like carbon", in ref. 20, 193-228.

38. A.Bubenzer, B.Dischler, G.Brandt and P.Koidl, "RF plasma deposited amorphous hydrogenated hard carbon films: preparation, properties and applications", J. Appl. Phys., 54 (1983), 4590.

39. D.R.McKenzie, D.Muller and B.A.Pailthorpe, Phys. Rev. Lett., 67 (1991), 773.

40. J.Robertson, "Deposition of diamond-like carbon", in ref. 21, 107-116.

41. M.Weiler, R.Kleber, K.Jung and H.Ehrhardt, Diamond Related Mater., 1 (1991), 121.

42. M.A.Tamor, W.C.Vassell and K.R.Carduner, Appl. Phys. Lett., 58 (1991), 592.

43. J.C.Angus, Diamond Related Mater., 1 (1991), 61.

44. I.R.McColl, D.M.Grant, S.M.Green, J.V.Wood, T.L.Parker, K.Parker, A.A.Goruppa and N.St.J.Braithwaite, "Low temperature plasma-assisted chemical vapour deposition of amorphous carbon films for biomedical-

polymeric substrates", Diamond Relat. Mater., 3 (1993), 83-87.

45. K.Donnely, D.P.Dowling, T.P.O'Brien, A.O'Leary, T.C.Kelly, R.Cheshire, K.F.Al-Assadi, W.G.Graham, T.Morrow, V.Kornas, V.Schulz-von der Gathen and H.F.Döbele, "Quantitative measurements of atomic hydrogen during the deposition of diamond-like carbon films", Diamond Related Mater., 4 (1995), 324-327.

46. M.M.Millard and E.Kay, J. Electrochem. Soc., 129 (1982), 160.

47. A.Rousseau, A.Grainer, G.Gousset and P.Leprince, "Microwave dischage in H_2 – influence of H atom density on the power balance", J. Phys. D: Appl. Phys., 27 (1994), 1412–1422.

48. J.C. Ward and J.E. Allen, J. Phys. E: Scien. Instr., 3 (1970), 534.

49. B.M. Annaratone and N.St.J. Braithwaite, "A comparison of a passive (filtered) and an active (driven) probe for RF plasma diagnostic", Meas. Sci. Technol., 2 (1991), 795-800.

50. J.D. Swift and M.J.R. Schwar, Electrical Probes for Plasma Diagnostics, Iliffe Books Ltd, London (1970).

51. M.A. Lieberman and A.J. Lichtenberg, "Principles of Plasma Discharges and Material Processing", John Wiley & Sons, Inc., NY (1994), 79 and 306-308.

52. P.K.Janev, W.D.Langer, K.Evans,Jr. and D.E.Post, Jr., "Elementary processes in hydrogen-helium plasmas", Springer-Verlag, Berlin, 1987.

53. J. Freisinger, M. Faufmann and W.Kraus, in Proc. 7th Int. Conf. on Plasma Chemistry - ICPC 85, ed. by C.J.Timmermans, Eindhoven, 1985, 605.

54. D. Heim and H. Störi, J. Appl. Phys., 72 (1992), 3330.

55. Yu.P. Raizer, Gas Discharge Physics, Springer-Verlag, Berlin, 1991, 63.

56. L.I.Maissel and R.Glang, "Handbook of Thin Film Technology", McGraw Book Co., New York, 1970, 1-24.

57. H.S.W. Massey, E.H.S. Burhop and H.B. Gilbody, "Electronic and Ionic Impact Phenomena", vol. I and II, Clarendon Press, Oxford, 1969.

58. J.W. Sheldon and E.E. Muschlitz, J. Chem. Phys., 68 (1978), 5288.

59. Ref. 51, p. 63.

60. P.F.Little and A. von Engel, "The hollow cathode effect and the theory of glow

discharges", Proc. Roy. Soc. A, 224 (1954), 209-227.

61. L.I.Maissel and R.Glang, Handbook of Thin Film Technology, McGraw-Hill Book Co., New York, 1970, 4-(7-8).

62. O.Christensen, "Sur quelques facteurs intervenant dans le bombardement de couches pulverisees", Thin Sol. Films, 27 (1975), 63-81.

63. T.C.Tisone and P.D.Cruzan, "Low-voltage triode sputtering with a confined plasma. Part II: Plasma characteristics and energy transport", J. Vac. Sci. Technol., 12 (1975), 1058-1066.

64. N.Heiman, V.Minkiewicz and B.Chapman, "High rate reactive ion etching of Al_2O_3 and Si", J. Vac. Sci. Technol., 17 (1980), 731-734.

65. R.Limpaecher and K.MacKenzie, "Magnetic multipole containment of large uniform collisionlessquiescent plasmas", Rev. Sci. Instrum., 44 (1973), 726-731.

66. T.Intrator, N.Hershkowitz and C.Chan, "Experimental observations of nonlinearly enhanced $2\omega_{UH}$ electromagnetic radiation excited by steady-state colliding electron beams", Phys. Fluids, 27 (1984), 527-534.

67. A.Dehbi-Alaoui, A.S.James and A.Matthews, "A comparison of properties of hard carbon films produced by direct gas deposition and plasma-assisted evaporetion", Surf. Coat. Technol., 43/44 (1990), 88-94.

68. K.Ando, T.Oshige, S.Yagura and H.Fujita, "Influence of electron-beam injection on pre-discharge state in low pressure gas", Jpn. J. Appl. Phys., 25 (1986), 299-300.

69. K.Ando, T.Oshige, S.Yagura and H.Fujita, "Temporal evolution of potential formation in a discharge created by pulsed electron beam injection in a low-pressure argon gas", J. Phys. D: Appl. Phys., 20 (1987), 45-49.

70. A.H.Sato and M.A.Lieberman, "Electron beam probe measurements of electric fields in rf discharges", J. Appl. Phys., 68 (1990), 6117-6124.

71. K.D.Schatz and D.N.Ruzic, "An electron-beam plasma source and geometry for plasma processing", Plasma Sources Sci. Technol., 2 (1993) 100-105.

72. P.B.Legrand, J.P.Dauchot and M.Hecq, "Study of an electron cold cathode tube for soft x-ray spectrometry", Rev. Sci. Instrum., 62 (1991), 1539-1541.

73. V.L.Galansky, V.A.Gruzdev, I.V.Osipov and N.G.Rempe, "Physical processes in plasma electron emitters based on a hollow-cathode reflected discharge", J. Phys. D: Appl. Phys., 27 (1994), 953-961.

74. A.A.Goruppa, N.St.J. Braithwaite and D.M.Grant, "Direct electrical control of

diamond-like carbon growth by plasma-enhanced CVD", Diamond and Rel. Mat., 3 (1994), 1223-1226.

75. L.A.Schwager, W.L.Hsu and D.M.Tung, "Effects of cold electron emission on the plasma sheath", Phys. Fluids B, 5 (1993), 621-630.

76. N.Sato, H.Kobayashi, T.Tanabe, T.Ikehata and H.Mase, "Control of ion energy for low-damage plasma processing in RF discharge", Jpn. J. Appl. Phys., 34 (1995), 2158-2162.

77. M.J.Kushner, W.Z.Collison and D.N.Ruzic, "Electron-beam controlled radio frequency discharges for plasma processing", J. Vac. Sci. Technol. A, 14 (1996), 2094-2101.

78. F.A.Haas, A.Goodyear and N.St.J.Braithwaite, "Tailoring of electron energy distribution in low temperature plasmas", Plasma Sources Sci. Technol., 7 (1998), 471-477.

79. J.P.Pierce, "Theory and design of electron beams", Van Nostrand, Princeton, 1954.

80. C.L.Hemenway, R.W.Henry and M.Caulton, "Physical electronics", John Wiley & Son, Inc., New York, 1967, 64.

81. I.G.Herrmann and P.S.Wagener, "The oxide-coated cathode", Chapman & Hall Ltd., London,1951, 41.

82. "Electronics encyclopaedia", Soviet Encyclopaedia, Moscow, 1991, (in Russian), 338.

83. S.G.Ingram and N.St.J.Braithwaite, " Ion and electron energy analysis at asurface in an RF discharge", J. Phys. D: Appl. Phys., **21** (1988) 1496-1503.

84. N.St.J.Braithwaite, J.P.Booth and G.Cunge, "A novel electrostatic probe method for ion flux measurements", Plasma Sources Sci. Technol., 5 (1996) 677-684.

85. R.Jayaraman and R.T.McGrath, "Ion and neutral species in C_2F_6 and CHF_3 dielectric etch discharges", J. Vac. Sci. Technol. A, 17 (1999), 1545-1551.

86. J.K.Olthoff, R.J.Van Brant, S.B.Radovanov, J.A.Rees and R.Surowiec, "Kinetic-energy distributions of ions sampled from argon plasmas in a parallel-plate, radio-frequency reference cell", J. Appl. Phys., 75 (1994), 115-125.

87. M.Zeuner and H.Neumann, "Ion energy distributions in a dc biased rf discharges", J. Appl. Phys., 81 (1997), 2985-2994.

88. S.G.Ingram and N.St.J.Braithwaite, "RF modulation of positive ion energies in low pressure discharge", J. Phys. D: Appl. Phys., 68 (1990), 5519-5527.

89. E. Kawamura, V.Vahedi, M.A.Lieberman and C.K.Birdsall, "Ion energy distribution in RF sheaths; review, analysis and simulation", Plasma Souces Sci. Technol., 8 (1999), R45-R64.

90. J.W.Coburn and E.Kay, "Positive-ion bombardment of substrates in rf diode glow discharge sputtering", J. Appl. Phys., 43 (1972), 4965.

91. N.Hershkowitz, "How does the potential gets from A to B in plasma?", IEEE Trans. Plas. Science, 22 (1994), 11-21.

92. T.Gyergyek, "Experimental study of the nonlyner dynamics of a harmonically forced double layer", Plasma Phys. Control. Fusion, 41 (1999) 175-190.

93. D.Diebold, C.E.Forest, N.Hershkowitz, M.-K.Hsieh, T.Intrator, D.Kaufman, G.-H.Kim, S.-G.Lee and J.Menard, "Double-layer-relevant laboratory results", IEEE Trans. Plasma Science, 20 (1992), 601-606.

94. G.Dilecce, M.Capitelli and S.De Benedictis, "Electron-energy distribution function in capacitively coupled RF discharge", J Appl Phys, 69, 1991, 121-128.

95. V.A.Godyak, "Electron energy distribution in low pressure RF discharge" in Proc. of the XX Int. Conf. On Pheomena in Ionised Gases (Invited papers), Il Ciocco, Italy, July 1991, 162-171.

96. M.Serendra and D.B.Graves, "Particle simulation of radio frequency glow discharge", IEEE Trans Plasma Science, 19, 1991, 141-157.

97. B.P.Wood, part of thesis reproduced in "Principles of plasma discharges and material processing" by M.A.Lieberman and A.J.Lichtenberg, J.Wiley &Sons, Inc,. New York, 1994, 362-363.

98. M.A.Lieberman and A.J.Lichtenberg, "Principles of plasma discharges and materials processing", John Wiley & Sons, New York, 1994, 348.

99. A.F.Stekolnikov, N.St.J.Braithwaite, Proc of the 8th Int. Conf. On Gas Discharges and Their Application, Venice, 1988, 391.

100. D.B.Graves and K.F.Jensen, "A continuum model of DC and RF discharges", IEEE Trans Plasma Science, 14, 1986, 78-91.

101. M.A.Sobolewski, "Electrical characteristics of argon radio frequency glow discharges in an asymmetric cell", IEEE Trans Plasma Science, 23, 1995, 1006-1022.

102. Y.P.Song, D.Field and D.F.Klemperer, "Electrical potentials in RF discharges", J. Phys. D: Appl. Phys., 23 (1990), 673-681.

103. F.A.Haas and N.St.J.Braithwaitr, "Modelling the effects of an electron beam

on the potential distribution in a low pressure parallel electrode discharge", J. Phys. D: Appl. Phys., 33 (2000), 1-8.

104. M.A.Tamor and W.C.Vassell, "Raman "fingerprints" of amorphous carbon films", J. Appl. Phys., 76 (1994), 3823-3830.

105. J.Schwan, S.Ulrich, V.Batori, H.Ehrhardt and S.R.P.Silva, "Raman spectroscopy on amorphous carbon films", J. Appl. Phys., 80 (1996), 440-447.

106. M.Yoshikawa, G.Katagiri, H.Ishida and A.Ishitani, "Raman spectra of diamondlike amorphous carbon films", J. Appl. Phys., 64 (1988), 6464-6468.

107. M.E.Pillow, "A critical review of spectral and related physical properties of the hollow cathode discharge", Spectrochimica Acta, 36B (1981), 821-843.

108. V.S.Borodin, Yu.M.Kagan and R.I.Lyagushchenko, "Investigation of a hollow cathode discharge. II.", Sov. Phys. Tech. Phys. (In English), 11 (1967), 887-889.

109. D.Korzec, M.Schott and J.Engemann, "Radio-frequency hollow cathode discharge for large-area double-sided foil processing", J. Vac. Sci. Technol., A13 (1995), 843 – 848.

110. E.M.van Veldhuisen and F.G. de Hoog, J. Phys. D: Appl. Phys., 17 (1984), 953.

111. J.H. Coleman, US Patent No 4,741,801.

112. C.M.Horwitz, S.Boronkay, M.Gross and K.Davies, "Hollow cathode etching and deposition", J. Vac. Sci. Technol., A6 (1988), 1837 – 1844.

113. D.C.Gerstenberger, R.Solanki and G.J.Collins, "Hollow cathode metal ion lasers", IEEE J. Quant. Electronics, QE-16 (1980), 820 – 834.

114. P.J.Kung and Y.Tzeng, "Growth of diamond thin films by spiral hollow cathode plasma-assisted vapour deposition", J. Appl. Phys., 66 (1989), 4676 – 4684.

115. B.Singh, O.R.Mesker, A.W.Lewine and Y.Arie, "Hollow cathode plasma assisted chemical vapour deposition of diamond", Appl. Phys. Lett., 52 (1988), 1658 – 1660.

116. J.Stiegler, S.Roth, K.Hammer, O.Stenzel, B.Mainz and W.Scharff, "Plasma-assisted CVD of diamond films by hollow cathode arc discharge", Diamond and Rel. Mat., 2 (1993), 413 – 416.

117. A.A.Haasz, J.W.Davis, O.Auciello, P.C.Stangeby, E.Vietzke, K.Flaskamp and V.Philipps, "Synergistic methane formation on pyrolytic graphite due to combined H^+ ion and H^0 atom impact", J. Nuclear Mat., 145-147 (1987), 412-

416.

118. A.Garscadden, “Particles in plasmas”, in proceedings of XX International Conference on Phenomena in Ionised Gasses, 8-12 July, 1991, Pisa, Italy, Invited papers, 147- 154.

119. D.V.Fedoseev, “Summary of research on diamond growth from the gas phase in Russia”, in ”Synthetic diamond: emerging CVD science and technology”, ed. by K.E.Spear and J.P.Dismukes, J.Wiley & Sons, Inc., New York, 1994, 47-50.

120. H.-G.Busmann, H.Gaber, T.Müller and I.V.Hertel, “Production of carbon cluster beams and their characterisation by time-of-flight mass spectroscopy”, in “Diamond and diamond-like films and coatings”, Ed. by R.E.Clausing, L.L.Horton, J.C.Angus and P.Koidl, NATO ASI Series, Plenum Press, New York, 1990, 289-296.

121. S.Ahmad, “Carbon cluster formation in regenerative sooting plasma”, Phys Let. A, 261 (1999), 327-331.

122. N.St.J.Braithwaite, “Internal and external electrical diagnostics of RF plasmas”, Plasma Sources Science & Tech., 6 (1997), 133-139.

123. H.Iwanaga, M.Kawaguchi and S.Motojima, “Growth mechanisms and properties of coiled whiskers of silicon-nitride and carbon”, Jap. J. Appl. Phys. (Part 1), 32 (1993), 105 –115.

124. Y.T.Trong, H.C.Hsieh and C.F.Chen, “Fabrication of nano-size conic diamond arrays by bias assisted PCVD”, Diamond Relat. Mater., 8 (1999), 772 – 780.

126. K.Kobashi and T.Tachibana, “Formation of fibrous structures on glass-like carbon by hydrogen plasma treatment under DC bias”, Carbon, 39 (2001), 303 – 306.

127. F.F.Chen, “Electric probes”, in “Plasma diagnostic techniques”, ed. by R.H.Huddlestone and S.L.Leonard, Academic Press, New York (1965). 113-200.

128. P.K.Janev, W.D.Langer, K.Evans,Jr. and D.E.Post, Jr., “Elementary processes in hydrogen-helium plasmas”, Springer-Verlag, Berlin, 1987.

Reproduced with permission of copyright owner. Further reproduction prohibited without permission.